

UC San Diego

UC San Diego Electronic Theses and Dissertations

Title

Synthetic biology in yeast : reconstructing the galactose network to probe the role of feedback induction in response to metabolic stimuli

Permalink

<https://escholarship.org/uc/item/7p38h49q>

Author

Ferry, Michael Stephen

Publication Date

2010

Peer reviewed|Thesis/dissertation

UNIVERSITY OF CALIFORNIA, SAN DIEGO

**Synthetic biology in yeast: Reconstructing the galactose network to probe the role
of feedback induction in response to metabolic stimuli**

A dissertation submitted in partial satisfaction of the requirements for the degree
Doctor of Philosophy

in

Bioengineering

by

Michael Stephen Ferry

Committee in Charge:

Jeff Hasty, Chair
Stuart Brody
Tracy Johnson
Bernhard Palsson
Lev Tsimring
Kun Zhang

2010

Copyright

Michael Stephen Ferry, 2010

All rights reserved.

The dissertation of Michael Stephen Ferry is approved, and it is acceptable in quality and form for publication on microfilm and electronically:

Chair

University of California, San Diego

2010

DEDICATION

*Thanks to Kristen for her support and love,
to Nathaniel for demonstrating what's important in life,
to Matthew for bringing even more joy into our lives,
to my family for supporting me from my first day of school to my last,
and to everyone else who has assisted me in my endeavors.*

TABLE OF CONTENTS

Signature Page	iii
Dedication	iv
Table of Contents	v
List of Abbreviations	ix
List of Figures	xi
List of Tables	xv
Acknowledgements	xvii
Vita	xix
Abstract of the Dissertation	xxi
Chapter 1 Introduction	1
Chapter 2 Circadian Rhythms in <i>Neurospora crassa</i> : Dynamics of the clock component frequency visualized using a fluorescent reporter	7
2.1 Introduction	7
2.2 Materials and Methods	11
2.2.1 Strain and culture conditions	11
2.2.2 mCherry optimization	12
2.2.3 Production of MFNC1: a strain with the <i>cgc2</i> promoter driving mCherryNC	14
2.2.4 Construction of a yeast recombination plasmid directly transformable into <i>Neurospora</i>	17
2.2.5 Production of His3 targeted FRQ-mCh fusion constructs	18
2.2.6 Cloning steps for modified “HyTK Blaster” technique	21
2.2.7 Insertion of the mCh gene at the native <i>frq</i> locus using a modified “tk-blaster” technique	22
2.2.8 Fluorescence microscopy	25
2.2.9 Confocal live-cell imaging	26
2.3 Results	26
2.3.1 Expression of the RFP mCherry under the control of the <i>cgc-2</i> promoter in <i>N. crassa</i>	26
2.3.2 Kinetics of the protein FRQ under the control of the <i>cgc-2</i> promoter in <i>N. crassa</i>	29

2.3.3	Kinetics of the protein FRQ under the control of the <i>frq</i> promoter in <i>N. crassa</i>	32
2.3.4	Clock effects in the <i>N. crassa</i> constructs	36
2.4	Discussion	39
2.5	Acknowledgements	43
Chapter 3	Microfluidics for synthetic biology: from design to execution	44
3.1	The design of a microfluidic chip	44
3.1.1	Mixing in microchemostat devices	45
3.1.2	Calculating flow rates and pressure drops	47
3.1.3	Designing a microchemostat chip	55
3.1.4	Design of an improved DAW junction	66
3.1.5	Calibration of the DAW junction	69
3.1.6	Design of an improved yeast cell trap	71
3.2	A parallel DAW device	73
3.3	Cell tracking	78
3.4	Acknowledgements	89
Chapter 4	Reconstructing the galactose network: the role of feedback induction	90
4.1	Introduction	90
4.2	The <i>S. cerevisiae</i> galactose utilization pathway	91
4.2.1	Structural elements of the galactose utilization pathway	92
4.2.2	Regulation of the galactose utilization pathway	92
4.2.3	Growth under inducing conditions	94
4.2.4	Growth under repressing conditions	94
4.2.5	Growth under non-inducing conditions	95
4.3	Project overview	97
4.3.1	Primary question and general motivation	97
4.3.2	Additional examples of networks containing positive and negative feedback	97
4.3.3	The importance of activating positive and negative feedback in response to stimulus	98
4.3.4	Primary hypothesis	100
4.3.5	Approaches taking to test the primary hypothesis	102
4.4	Strain construction and promoter testing	102
4.4.1	Promoter testing	104
4.4.2	Calibration of the flow cytometer	106
4.4.3	Results of the promoter strength experiments	110
4.4.4	Cloning work for necessary strains	112
4.5	Experimental results for the engineered strains	114
4.5.1	Flow cytometry results	114
4.5.2	The ratio of Gal3 to Gal80	126
4.6	Probing the Gal network with a dynamic environment	135

4.7	The significance of induced negative feedback	150
Chapter 5	Summary	154
Appendices	157
Appendix A	Yeast Strains	158
A.1	Complete strain list	158
Appendix B	Microfluidics for synthetic biology	162
B.1	DAW Hardware and software	162
B.1.1	Hardware	162
B.1.2	Software - <i>iDAW</i>	165
B.2	Photolithography	167
B.2.1	Cleaning the wafer	175
B.2.2	Applying the cleaning agents	176
B.2.3	Drying the wafer	176
B.2.4	Centering the wafer on the spinner	176
B.2.5	Dispensing photoresist	177
B.2.6	Spin coating	177
B.2.7	Soft-baking at 95°C	177
B.2.8	Alignment of photomask and UV exposure	178
B.2.9	Post exposure baking (PEB) at 95°C	179
B.2.10	Developing	179
B.2.11	Cleaning	179
B.2.12	Examining the wafer	180
B.2.13	Measuring feature height	180
B.2.14	Hard-baking at 200°C	180
B.3	Soft Lithography	184
B.3.1	Aluminum holder	185
B.3.2	Applying release agent (for new wafers only)	185
B.3.3	Preparing PDMS	186
B.3.4	Degassing PDMS	186
B.3.5	Pouring PDMS	186
B.3.6	Curing	186
B.4	PDMS processing	187
B.4.1	Removing PDMS layer	187
B.4.2	Cutting PDMS	189
B.4.3	Punching ports	189
B.4.4	Cleaning ports	189
B.4.5	Cleaning chips	190
B.4.6	Cleaning coverslips	190
B.4.7	Bonding chips to coverslips	190

B.4.8	Troubleshooting	191
B.5	Experimental setup for <i>E. coli</i>	191
B.5.1	Overnight culture	192
B.5.2	Cell growth	195
B.5.3	Wetting the chip	195
B.5.4	Preparing syringes	196
B.5.5	Connecting syringes	199
B.5.6	Setting up DAW software	199
B.5.7	Spinning down cells	199
B.5.8	Loading cells	199
B.5.9	Starting experiment	200
B.5.10	Checking on cells	200
B.6	Method to setup a MDAW microfluidic experiment	201
B.6.1	Pre-experiment preparation	201
B.6.2	Cell Growth	203
B.6.3	Media preparation	203
B.6.4	Air removal from the chip	204
B.6.5	Connecting DAW reservoirs to the device	204
B.6.6	Processing and loading cells	205
B.6.7	Microscope setup	206
References	209

LIST OF ABBREVIATIONS

A.U.	arbitrary units
bd	band mutation
bp	base pair
<i>ccg-2</i>	clock controlled gene two
CT	Circadian time
DNA	deoxyribonucleic acid
<i>E. coli</i>	<i>Escherichia coli</i>
Eq.	equation
fig.	figure
FL	fluorescence
FP	fluorescent protein
<i>frq</i>	frequency gene
FRQ	frequency protein
FRQ-mCh	frequency - mCherry fusion protein
FSC	forward scatter
FUDR	5-Fluoro-2'-deoxyuridine
GFP	green fluorescent protein
hrs.	hours
kb	kilobase
LB	lysogeny broth
mRNA	messenger ribonucleic acid
MW	molecular weight
nl/s	nanoliters per second
<i>N. crassa</i>	<i>Neurospora crassa</i>
NLS	nuclear localization signal
no.	number
OD	optical density

ODE	ordinary differential equation
PCR	polymerase chain reaction
PDMS	poly(dimethylsiloxane)
PIV	particle image velocimetry
<i>Re</i>	Reynolds number
<i>S. cerevisiae</i>	<i>Saccharomyces cerevisiae</i>
T μ C.....	Tesla microchemostat
UTR	untranslated region
UV	ultraviolet
VMM	Vogel's Minimal Medium
YFP	yellow fluorescent protein
WCC	white collar complex
%w/v	percent weight per volume (concentration)

LIST OF FIGURES

Figure 2.1: Plots depicting the fluorescence excitation and emission ranges for the mCherryNC protein	13
Figure 2.2: Graphical overview of the promoter constructs driving the mCherryNC protein used to transform <i>N. crassa</i>	16
Figure 2.3: Figure showing the structure of the pMFP28 plasmid.	19
Figure 2.4: Diagram depicting the modified “tk-blaster” technique.	24
Figure 2.5: Phenotype of strain MFNC9 (Pccg2-mCheryyNC) of <i>N. crassa</i>	27
Figure 2.6: Expression of mCh driven by the <i>ccg-2</i> promoter during colony development of <i>N. crassa</i> , strain MFNC9.	29
Figure 2.7: Profile of fluorescence intensity of the protein mCh driven by the <i>ccg-2</i> promoter during the circadian cycle of <i>N. crassa</i> , strain MFNC9	30
Figure 2.8: Nuclear entrance of FRQ-mCh under the <i>ccg-2</i> promoter in vegetative hyphae of <i>N. crassa</i> , strain MFNC23	31
Figure 2.9: Nuclear entrance of FRQ-mCh under the <i>frq</i> promoter in vegetative hyphae of <i>N. crassa</i> , strain MFNC30.	33
Figure 2.10: Accumulation of FRQ-mCh in cytoplasm and nuclei of <i>N. crassa</i> , strain MFNC30.	34
Figure 2.11: Variation of fluorescence intensity in nuclei of the protein mCh driven by the <i>frq</i> promoter during the circadian cycle of <i>N. crassa</i> , strain MFNC30	35
Figure 2.12: Nuclear localization of FRQ-mCh in <i>N. crassa</i> , strain MFNC30.	37
Figure 2.13: Control showing the expression of mCh alone driven by the <i>ccg-2</i> promoter in individual hyphae of <i>N. crassa</i> , strain MFNC9.	38
Figure 3.1: Overview of how to conceptually setup microfluidic flow problems.	50
Figure 3.2: Overview of the mask design process for microchemostat devices.	56
Figure 3.3: Overview of the an alignment pattern for microchemostat devices.	58
Figure 3.4: Overview of the MFD005 _a chip and components.	63

Figure 3.5: Comparison of a nodal analysis tool (moca) and Comsol (finite element analysis package).	65
Figure 3.6: Comparison of a T-junction to the improved DAW junction.	68
Figure 3.7: Performance of the DAW junction.	70
Figure 3.8: Graphic of the individual subexperiments in the MDAW microfluidic device.	76
Figure 3.9: Graphic of the MDAW microchemostat device.	77
Figure 3.10: Comparison of different cell parameters for a population of yeast cells.	80
Figure 3.11: Comparison of phase contrast and differential interference contrast (DIC) imaging with regards to cell tracking.	81
Figure 3.12: Segmentation of yeast phase contrast imagery.	84
Figure 3.13: Different cases which need to be handled in cell tracking.	87
Figure 3.14: Overview of the cell tracking process.	88
Figure 4.1: Overview of the Leloir pathway which converts galactose into a form suitable for central metabolism	93
Figure 4.2: Depiction of the conceptual galactose regulation model outlined in the text.	96
Figure 4.3: General carbon source detection problem as described in the text. . . .	101
Figure 4.4: General strategy for strain construction to test the hypothesis given in the text.	103
Figure 4.5: Power law relationship between a sample's fluorescence mean and cytometer voltage	107
Figure 4.6: Power law scaling for a variety of tested promoters	109
Figure 4.7: Flow cytometry analysis of constitutive promoters	111
Figure 4.8: Flow cytometry analysis for tested inducible promoters	112
Figure 4.9: Flow cytometry analysis for inducible promoters grown in glucose and galactose media	113

Figure 4.10: Gal1 induction for the wildtype and controllable Gal80 strain at several concentrations of galactose and Gal80.	116
Figure 4.11: Histograms and scatter plots which demonstrate bimodality in the Gal80 controllable strain, but not the wildtype strain, at full induction	119
Figure 4.12: Gal1 induction profiles, representing the distribution of cellular fluorescence, for the Gal80 controllable and wildtype strains.	121
Figure 4.13: Galactose induction curves for Gal3 and Gal80 in the wildtype strain	123
Figure 4.14: Galactose induction curves for Gal3 and Gal80 in the Gal80 controllable strain	125
Figure 4.15: Fold change of the Gal1 and Gal3 proteins between inducing and uninducing conditions for the wildtype and controllable Gal80 strains	126
Figure 4.16: Comparison of Gal3 and Gal80 in the wildtype strain and the controllable strain with an intermediate level of Gal80.	127
Figure 4.17: Histograms of the Gal3/Gal80 ratio for the wildtype and controllable Gal80 strains at several levels of galactose.	129
Figure 4.18: Plot of the Gal3/Gal80 mode locations as a function of galactose in the wildtype and controllable Gal80 strain.	130
Figure 4.19: Scatter plot of Gal1 fluorescence versus the log of the Gal3/Gal80 ratio for the wildtype and the controllable strain: low galactose concentrations . .	133
Figure 4.20: Scatter plot of Gal1 fluorescence versus the log of the Gal3/Gal80 ratio for the wildtype and the controllable strain: high galactose concentrations. .	134
Figure 4.21: A comparison of the cell fields of the wildtype and Gal80 inducible strains grown in the MFD005 _a microfluidics chip	136
Figure 4.22: A comparison of two induction signals using the MFD005 _a microfluidics chip.	138
Figure 4.23: Single cell trajectories generated from the controllable Gal80 strain subjected to a square wave drive with a four hour period.	140
Figure 4.24: Comparison of periodic to random drive signals.	142

Figure 4.25: Comparison of the phase space explored by a periodic signal compared to the random drive signal	143
Figure 4.26: Scatter plot of single cell Gal1-yCCFP fluorescence means versus time for the wildtype and Gal80 controllable strain.	145
Figure 4.27: Scatter plot of single cell Gal3-yCCFP fluorescence means versus time for the wildtype and Gal80 controllable strain.	146
Figure 4.28: Gal3/Gal80 ratio under driven conditions	148
Figure B.1: Linear actuator setup for DAW.	164
Figure B.2: Screenshot of <i>iDAW</i> software.	166
Figure B.3: Overview of the fabrication process.	168
Figure B.4: Graph of SU-8 formulation vs percent solids.	171
Figure B.5: Graph of SU-8 formulation vs percent solids.	172
Figure B.6: Sample layer alignment technique.	183
Figure B.7: Vacuum pump and desiccators.	187
Figure B.8: Syringe towers.	193
Figure B.9: Experimental setup.	194
Figure B.10: Making connection pins.	197
Figure B.11: Experimental line and syringe techniques.	198

LIST OF TABLES

Table 2.1: Period length and growth rate of the <i>N. crassa</i> strains used in this study.	12
Table 2.2: Primer sequences used in this study.	14
Table 2.3: Description of the primer structure used in the yeast fusion procedure.	15
Table 2.4: Plasmids produced in this study.	16
Table 2.5: Strains produced in this study.	17
Table 3.1: Typical physical parameter values for microchemostat devices used in synthetic biology.	45
Table 3.2: Diffusion coefficients for ions and molecules commonly used in microfluidic chemostats.	46
Table 3.3: General guidelines for channel dimensions in microchemostat chips.	61
Table 3.4: Role and pressures for each port in the MFD005 _a device.	62
Table 3.5: Sample yeast cell tracking output.	85
Table 4.1: Relevant strains produced in this study for which extensive experimental data was collected.	114
Table A.1: Table of <i>S. cerevisiae</i> strains made for this project.	158
Table B.1: Hardware required for DAW actuator setup	165
Table B.2: SU-8 2000 photoresists formulations	170
Table B.3: Calculated and experimental exposure times.	175
Table B.4: Sample table of wafer fabrication parameters.	175
Table B.5: Sample alignment datasheet.	182
Table B.6: Photolithography Equipment, chemicals and supplies.	184
Table B.7: Soft lithography equipment, chemicals and supplies.	188
Table B.8: PDMS processing equipment, chemicals and supplies.	192
Table B.9: Experimental equipment, chemicals and supplies.	201
Table B.10: Experimental equipment, chemicals and supplies.	203

Table B.11: Components of Nikon *Ti* automated fluorescence microscope. 208

ACKNOWLEDGEMENTS

I want to especially thank Dr. Jeff Hasty for all the support, guidance and friendship he has given me over the years I have been in his lab. His expertise and knowledge have allowed me to gain new perspectives in the field of synthetic biology that would have been impossible without his help. Furthermore his consistent and unwavering belief in me strengthened my resolve when times became difficult. I also would like to thank Dr. Stuart Brody who welcomed me into his lab soon after my arrival at UCSD and introducing me to the intriguing world of *Neurospora crassa* circadian rhythms. I will always have fond memories of the time I spent there and at the several conferences I attended. I would also like to thank my co-advisor Dr. Lev Tsimring for his insight and interest in my work. The tomato experiment I conducted with his help is one I am sure I will not forget. My time at UCSD would have been much different were it not for the help and camaraderie I have received from my fellow co-workers in the Hasty and Brody labs. I am particularly indebted to Will Mather whose advice and friendship are as boundless as his knowledge in seemingly all subjects. I would also like to thank Scott and Natalie Cookson, two of the most intelligent, helpful and downright kind people I have ever met, Martin Kolnik for his natural skill and Ivan Razinkov for his talent with manufacturing and design. Finally I would like to thank the National Science Foundation's Graduate Research Fellowship program for their funding and support of my graduate work.

Chapter 2 contains material originally published as Castro-Longoria, E.*, Ferry, M.*, Bartnicki-Garcia, S., Hasty, J., and Brody, S., 2010: Circadian rhythms in *neurospora crassa*: dynamics of the clock component frequency visualized using a fluorescent reporter. *Fungal Genet Biol*, **47**(4), 332-341. (*equal contribution). Copyright permission to republish here was granted by Elsevier Limited.

Chapter 3 contains material originally published as Ferry, M.*, Razinkov, I.*, and Hasty, J., 2010: Microfluidics for synthetic biology: From design to execution. *Methods in Enzymology*, accepted (*equal contribution). Copyright permission to re-

publish here was granted by Elsevier Limited.

VITA

- 2002 Bachelor of Science in Molecular, Cellular and Developmental Biology
University of California Los Angeles
- 2007 Master of Science in Bioengineering
University of California, San Diego
- 2010 Doctor of Philosophy in Bioengineering
University of California, San Diego

PUBLICATIONS

Peer Reviewed Journal Articles

Lu, T., **Ferry, M.**, Weiss, R. and Hasty, J., 2008: A molecular noise generator. *Phys. Biol.* **5**: 36006.

Castro-Longoria, E.*, **Ferry, M.***, Bartnicki-Garcia, S., Hasty, J. and Brody, S., 2010: Circadian rhythms in *Neurospora crassa*: dynamics of the clock component frequency visualized using a fluorescent reporter. *Fungal. Genet. Biol.* **47**: 332-341. (*equal contribution).

Baumgartner, B., Bennett, M., **Ferry, M.**, Tsimring, L, and Hasty, J., 2010: Competitive protein synthesis regulates adaptation to new growth environments. *Cell*, under review.

Ferry, M.*, Razinkov, I.*, and Hasty, J., 2010: Microfluidics for synthetic biology: From design to execution. *Methods in Enzymology*, accepted (*equal contribution).

Book Chapter

Ostroff, N., **Ferry, M.**, Cookson, S., Johnson, T., and Hasty, J., 2008: Synthetic Biology: Bioengineering at the Genomic Level. *An Introductory Text to Bioengineering*, World Scientific Publishing Co., 427-451.

FIELDS OF STUDY

Major Field: Bioengineering (Synthetic Biology)

Studies in Biological Dynamics
Professor Jeff Hasty and Dr. Lev S. Tsimring

ABSTRACT OF THE DISSERTATION

Synthetic biology in yeast: Reconstructing the galactose network to probe the role of feedback induction in response to metabolic stimuli

by

Michael Stephen Ferry

Doctor of Philosophy in Bioengineering

University of California, San Diego, 2010

Jeff Hasty, Chair

With the expanding interest in cellular responses to dynamic environments, microfluidic devices have become important experimental platforms for biological research. Microfluidic “microchemostat” devices enable precise environmental control while capturing high quality, single cell gene expression data. For studies of population heterogeneity and gene expression noise, these abilities are crucial. I have developed a microchemostat device optimized for capturing data from thousands of cells in multiple sub-experiments. The device is robust, easy to use and capable of generating precisely controlled dynamic environments. The device uses an integrated fluidic junction, coupled to linear actuators, to modulate the external port pressures as a function of time. In this way the concentration of an inducer compound can be tightly controlled without the use of mechanical mixing devices. To analyze the large amounts of data generated, I have developed a method for automated cell tracking, focusing on the special problems presented by *Saccharomyces cerevisiae* cells. I have used these tools to probe the

response of a natural genetic circuit, the Gal system of *S. cerevisiae*. I have altered the regulation of the native Gal system, replacing the transcriptional positive and negative feedback loops with artificial promoters. Looking at these modified strains, I have determined that induced negative feedback is essential for tuning the cell's genetic response to the external galactose concentration. Moreover, without *induced* negative feedback, the system exhibits bistability, with subpopulations of responding and non-responding cells. When observing these cells in a dynamic environment, I have found that the Gal network is optimized to respond sharply to changes in the inducer concentration, regardless of the network's original induction state.

Chapter 1

Introduction

The field of genetics has always attempted to understand how an organism's genes directed the production of the observable traits, or phenotype of that organism. In humans, this relationship can often be understood for diseases that are inherited in a simple Mendelian fashion. Typically a specific defect in a gene is correlated to the loss of a proteins function, resulting in a disease phenotype. However for many human traits such as height, intelligence, propensity for heart disease, etc. the relationship between genotype and phenotype is not so clear (Hartman et al., 2001; Guarente, 1993). This has traditionally been blamed on our limited knowledge of how multiple genes interact to create a complex phenotype.

Increasingly interactions between genes are becoming the focus of modern genetics (Hartman et al., 2001; Guarente, 1993) and understanding these relationships is central to all aspects of human health research and biology. Historically the relationships in complex biological networks have been described in words, cataloguing the qualitative effects perturbations of a genetic system have on an organism's phenotype. However genome projects have revealed that eukaryotes have on the order of 10^3 to 10^4 genes making a narrative description of the entire genetic system infeasible. Ideally genetic interactions could be described mathematically, using basic principles and these ideas could be expanded to cover networks of increasing size.

Recent successes describing synthetic genetic networks mathematically have given credibility to this idea and shed light on areas needing improvement (Hasty et al., 2002a,b; Elowitz et al., 2002; Elowitz and Leibler, 2000). Such a description is desirable because it would lead to quantitative predictions about how genetic networks are constructed and would allow one to predict the phenotypic consequences of a genetic perturbation with increasing accuracy. This would enable improved diagnoses for complex human diseases and the construction of synthetic genetic circuits in microbial organisms. The potential applications of these circuits are diverse and include: the detoxification of environmental contaminants, the low cost production of novel chemicals, the improved treatment of wastewater and increased production of biofuels to name a few.

The construction of rationally designed, novel genetic circuits has generally come under the field of synthetic biology. While there is no strict definition governing just what synthetic biology represents, generally the term refers to the combination of mathematical modeling and genetic experimentation to design new and improved genetic circuits. A recent demonstration of the utility of this approach is the synthesis of large amounts of the previously expensive antimalarial drug artemisinin (Martin et al., 2003) which may fundamentally alter the economics of treating one of the most deadly diseases on earth. Additionally synthetic biology will likely contribute to the creation of improved microbial strains for biofuel production from terrestrial crops such as corn (Stephanopoulos, 2007) and unconventional sources like algae (Oswald, 1995).

In general synthetic biology borrows from the disciplines of molecular biology, physics, engineering and non-linear science. Since synthetic biology problems and approaches require a broad base of knowledge, it is critical that participants interact beyond the traditional confines of their disciplines. While synthetic biologists risk becoming generalists, with less highly targeted knowledge than a specialist would have, the tradeoff is being able to approach new problems from angles not possible before. The overarching theme of synthetic biology is attempting to describe biological networks within a mathematical framework, something that has a long history in and of itself.

Perhaps one of the earliest examples was Thomas Malthus' description of populations displaying exponential growth, while food supplies grow at a smaller rate (Malthus, 1817). While there is still debate about Malthus' ideas today, often previous efforts to model biological networks were hampered by the limited available experimental techniques. Before some of the technologies in common use today for synthetic biology, few options were available to generate data with the temporal resolution necessary to adequately test mathematical models of gene function.

One such technology which has enabled a rapid growth in synthetic biology, is microfluidic technology. This technology has enjoyed considerable success and interest in recent years. Microfluidic devices have been used for everything from miniaturization of molecular biology reactions, to platforms for cell growth and analysis. A driving factor for increased use of microfluidics is the potential for more productive experiments, ie accomplishing the same or more using fewer resources (primarily less reagents, consumables and time). Furthermore microfluidic devices offer the unrivaled ability to precisely control and perturb the environment of single cells while capturing their behavior using high resolution microscopy. Later I will discuss how to design, build, operate and analyze data from single cells growing in the chambers of high throughput microfluidic devices. I will focus primarily on a device built to monitor the growth of *Saccharomyces cerevisiae* (yeast) in a dynamically changing environment as a case study. This device is known in our lab as the MDAW or multiple dial-a-wave device.

In our lab we strongly believe in the importance of acquiring single cell trajectories from our experimental runs. This requires the ability to track single cells over the course of an experiment, which generally lasts from 24-72 hours. Indeed of all technologies available in molecular biology, microfluidics alone offers the ability to track the behavior of a large number of individual cells over the course of an experiment. While other technologies, such as flow cytometry, allow the acquisition of single cell data, the experimenter cannot track each individual cell in time. This leads to "snap shots" of how the population as a whole changes in time, but cannot tell you how individual cells progress in time over the course of an experiment.

The difference between the techniques can be illuminated easily if one thinks of a population of cells containing a desynchronized genetic oscillator. In this case much depends on the waveform of the oscillator. For oscillators with sinusoidal output, the population will appear bimodal with a large portion of the cells spread between the two modes. However for an oscillator with output similar to a triangle wave, the cells will be uniformly distributed between all phases of oscillation and therefore the population will have a fairly evenly distributed set of fluorescent values. Of course the behavior of a real oscillator can be somewhere between these extremes, but the point is that looking at the progression of a population as a whole does not tell you everything about its dynamics. For example in each of the cases mentioned above, other explanations are possible, such as the transient of a bistable switch, or even a genetically mixed population of cells. In contrast using a microfluidic device to follow the temporal dynamics of single cells in such a population would allow one to easily see if any cells were oscillating.

While microfluidics is powerful, flow cytometry has the ability to capture a large amount of data quickly, much more quickly than can be done in traditional microfluidics. For this reason microfluidic and flow cytometry should be thought of as complimentary, instead of competing, technologies. We often find it useful to first characterize our genetic circuits using flow cytometry, testing as many media or inducer concentrations as possible, to look for behavior indicative of interesting dynamics. Once these conditions are determined we follow up with the more powerful, but involved microfluidic experiments.

Thus in the context of this report I will be talking about microfluidic chips designed to capture single cell data over the 1-3 days of the experiment. Unfortunately this limits the architecture of such a chip due to the difficulty of tracking cells. Regrettably cells such as yeast and especially *E. coli*, have few unique features which can be used to distinguish them from their brethren. The full details of this will be discussed in a later section describing cell tracking, but suffice it to say that the only truly unique characteristic that all cells have visible by phase contrast microscopy is their position in time. Cells such as yeast or *E. coli* are so fast growing that they can quickly fill up a trap and

the cameras field of view and begin to move quickly as their growth exerts pressure on the cell traps walls.

This means that phase contrast images of a colonies growth must be taken often, usually every 30 seconds to a minute to ensure that cells do not move more than about one cell diameter between images. This imposes a physical limit to the size of the chip, which is usually determined by the speed of the microscope hardware. Even state of the art, fully automated microscope hardware cannot autofocus, acquire phase contrast and 3-4 fluorescent images, and then move to a new stage location in less than 4-5 seconds and sometimes as many as 7-10 seconds depending on the acquisition parameters. This limits the number of chambers and hence the number of independent experiments to at most 10-15 if the one minute interval between phase images is followed. Of course one also has to worry about overexposing cells to fluorescent excitation light, which can easily kill even the hardiest of cells rather quickly. Thus while phase contrast images are acquired every minute, we normally only capture fluorescent images every 5 minutes. Since 4 out of 5 acquisitions will not contain fluorescence capture (usually the longest step) this decreases the overall acquisition time somewhat. However, even if the phase contrast interval is lengthened somewhat the scope hardware will end up being the limiting factor in determining how large a chip can become. Of course microfluidic chips have been created with thousands of chambers, however these devices cannot capture the type of high quality, single cell trajectory data that smaller devices can, at least with current microscope technology.

Automation of most microscope tasks is critical, such as stage movement, phase ring and fluorescent cube changing, and shutter control. Moreover taking images every minute for days on end requires an automated focus routine, which luckily most microscope manufactures can readily provide. This also requires large amounts of hard disk space and equally important a rigorous method for space management, with backup procedures in place to prevent catastrophic data loss. Moreover the sensitivity of the camera used is extremely important. While the background fluorescence signal (which determines the minimal detectable signal) of yeast and *E. coli* cells is easily observed

using CCD cameras even a decade old, one should always use the most sensitive camera available to minimize the exposure time and hence phototoxicity caused by the fluorescent excitation lamp. The overall idea is that while older hardware may allow you to capture some data like that we discuss here, newer hardware will allow you to capture more data with a higher quality and with less damage to your cells.

Chapter 2

Circadian Rhythms in *Neurospora*

***crassa*: Dynamics of the clock**

component frequency visualized using a fluorescent reporter

2.1 Introduction

Circadian rhythms are a widely-occurring part of the biological landscape, particularly for eucaryotic organisms. The generally agreed upon features of a circadian rhythm are: 1) a period of 24 hrs (circa-dian); 2) an endogenous or self-sustaining rhythm when all external stimuli, such as light/dark cycles, are removed; 3) entrainability by external signals such as a daylength of 24 hrs; and 4) a period that remains relatively constant with respect to ambient temperature, particularly in those organisms that cannot regulate their internal temperature. The occurrence of circadian rhythms has been documented from micro-organisms both procaryotic (Dunlap et al., 2004) and eucaryotic all the way up the taxonomic scale to humans (Aschoff, 1965). The occurrence of circadian rhythms in fungi has been known for some time (Dunlap and Loros, 2006;

Lakin-Thomas and Brody, 2004; Loros and Dunlap, 2001; Bell-Pedersen et al., 1996b; Sargent et al., 1966).

For circadian rhythms, the most widely-studied fungus has been *Neurospora crassa*, primarily because of its well-known genetics and biochemistry. Significant advances in understanding the mechanism of a core oscillator as well as its input and output components have been extensively documented (Lee et al., 2000; Liu et al., 2000; Aronson et al., 1994). The *Neurospora* clock is expressed on solid agar media as a series of conidiating rings (asexual spore formation) designated as “bands” alternating with areas of thin filamentous growth. The macroscopic effect of this binary developmental lifestyle is to produce on agar media, either in long linear glass tubes (race tubes) or in Petri plates, bands that develop 22 hrs apart. Moreover, since periods can be measured for many days, a large number of cultures can be simultaneously monitored and manipulated. The *Neurospora* clock system has all of the properties of the circadian rhythm definition listed above and is one of the handful of organisms where a reasonable amount of molecular understanding is known (Dunlap, 2006; Bell-Pedersen et al., 2001a,b; Loros and Dunlap, 2001). All of the formal aspects of the *Neurospora* clock have been worked out from cultures growing on the surface of an agar medium, either in race tubes or plates, and most of the details of the molecular biology of the *Neurospora* clock system have been obtained from a mycelial disk system in a shaking liquid culture (Nakashima, 1981). Despite the differences in culture conditions in liquid and solid cultures, the clock keeps the same time in both instances (Perlman et al., 1981). However, since growth is often limited in liquid cultures, the traditional *Neurospora* clock output phenotype (conidiation) is suppressed by the submerged growth environment. While developmental pathways are suppressed intentionally to examine only the circadian cycling of clock components, the conditions of the disk are unlike any fungi normally encounter. Consequently this has led some to question whether the data gained through such experiments can be directly applied to those when *Neurospora* is cultured on agar media. Furthermore, although macroscopic development is suppressed, it is interesting that many clock-controlled genes are still expressed in the disk system, including those

involved in the formation of conidia (*ccg-2*). Thus although the final morphological output of the clock, conidiating regions of a culture, is not seen in the disk culture system, many of the downstream processes still are.

Increasingly it will be important to address what differences, if any, occur in the *Neurospora* clock between the surface and submerged systems if the clock regulation of the output processes, such as conidiation, are to be understood. To gain insight into the dynamics of the *Neurospora* clock gene components, newer online reporter tools (Gooch et al., 2008; Morgan et al., 2003) have been developed allowing the assessment of some clock components while the culture is growing on the surface of an agar media. Other studies on the *Neurospora* clock (Ramsdale and Lakin-Thomas, 2000; Brody and Harris, 1973) have involved extracting and analyzing components directly from surface-grown cultures. However, although the output of the circadian rhythm can be followed at a macroscopic level using clock-controlled production of luciferase, for example, no previous tool has been able to follow the dynamics of a *N. crassa* clock gene at the *cellular* level. Consequently our fusion protein has allowed us to determine the cellular localization of the FRQ protein in aerobic conditions with higher temporal resolution than previous techniques could achieve.

The system we have developed is based on a fluorescent protein fused in frame to the core oscillatory protein Frequency (FRQ). FRQ was chosen due to its critical importance in generating the *Neurospora* clock's rhythms since deletion of the *frq* gene abolishes all circadian rhythms in *Neurospora* (Aronson et al., 1994). Moreover certain mutations in the *frq* gene retain expression but can alter the period of the rhythm from as low as 16 hours to as much as 29 hours (Feldman and Hoyle, 1973). Due to its importance, the temporal profile of the expression of FRQ has been extensively studied in the liquid disk system. However the spatial and temporal distribution of FRQ in an actively-growing, aerobic *Neurospora* culture has been difficult to determine due to the previously mentioned problems. The fluorescent fusion system we describe here is an attempt to overcome these limitations and is useful for determining *frq* gene dynamics both spatially and temporally. Advantages of this system include reporter output for

more than two days of an actively-growing culture, allowing correlations with the visible conidiation rhythm. The system is an aerobic one, has high sensitivity, and can be sampled with high temporal resolution. Furthermore the response of the clock to phase shifting stimuli or other environmental changes can be rapidly observed.

The approach employed for the fluorescent labeling of clock proteins was a multi-faceted one. The first step was to use a fluorescent protein, mCherry, that emits in the red wavelengths of the visible spectrum and whose excitation wavelength is far away from the blue light range, which would have reset the *Neurospora* clock (Liu et al., 2003). Unfortunately, the more commonly used GFP (green fluorescent protein) variants have this as a built-in limitation. The second step was to optimize the codons of mCherry for expression in *Neurospora* since there have been numerous reports about poor translation efficiencies for foreign genes in this organism (Gustafsson et al., 2004; Kinnaird et al., 1991). The third step was to drive the mCherry protein with various promoters in order to assess the time course, strength, and localization of the signal. The fourth step was to localize the FRQ protein and observe its kinetics by fusing the mCherry reporter to the C-terminal end of the FRQ protein (we call this fusion FRQ-mCh). The fifth step was to put FRQ-mCh under the control of different promoters, i.e. *ccg-2* or *frq*. The *ccg-2* promoter was chosen since it is one of the strongest promoters of *N. crassa* and would serve as a useful control to ensure that FRQ-mCh was detectable. However an argument could be made that data obtained with the *ccg-2* promoter driving FRQ-mCh is complicated to decipher since there may be feedback from a clock protein being regulated by a clock promoter. Therefore our final step was to fuse the mCherry gene to the native *frq* gene using a novel technique based on the “tk blaster” method (Pratt and Aramayo, 2002). This technique allowed us to study the dynamics of the *frq* gene in its native genomic context with no disruption to its promoter, 5’ or 3’ UTR. Consequently our results with this strain removed any doubt about the functionality of our fusion protein since the circadian rhythm had a period near that of the wild type.

At the cellular level, our objective was to analyze the dynamics and spatial localization of the FRQ-mCh fusion protein to determine possible novel organelle local-

ization, localization in tips vs. older areas, and if these processes were under circadian control. We were particularly interested in this promoter's spatial specificity (i.e. aerial hyphae vs. mycelia) and when it was activated during the circadian cycle and the conidiation process. Furthermore we have described previously (Castro-Longoria et al., 2007) some of the intracellular details of the *Neurospora* conidiation rhythm and these fluorescent strains gave us a new dimension to employ for this type of study. Using these tools we have discovered that the FRQ protein makes a second, previously-unknown entry into the nucleus during the circadian cycle. This entry appears to be related to the conidiation process due to its timing and thus is evidence of the utility of our system for studying the *Neurospora* clock in an aerobic environment.

2.2 Materials and Methods

2.2.1 Strain and culture conditions

Neurospora crassa strains used in this study are listed in Table 2.1. Unless otherwise stated, *N. crassa* strains were cultured and maintained in Vogel's minimal medium N (VMM) (Vogel, 1956) with 2% sucrose as a carbon source and 1.5% agar. Strains MFNC23 and MFNC30 were grown in Petri plates at 28°C to obtain a higher expression of fluorescence. To determine the fluorescence signal from whole Petri plate cultures, the plates were illuminated using a halogen spot light bulb and a band pass excitation filter (580nm \pm 20nm). The fluorescent emission signal was captured using a standard digital camera (Canon A510) with an emission filter (610nm \pm 10nm) placed in front of the lens. Hyphal extension rate and period of strains were calculated from cultures on race tubes. Cultures in special chambers were grown at 25°C as previously described (Castro-Longoria et al., 2007). All cultures were incubated in a VWR® Diurnal Growth Incubator, Model 2015. Cloning steps necessary to produce the Pccg2-mCh, Pccg2-FRQ-mCh and Pfrq-FRQ-mCh constructs are given in the supplementary methods. Moreover complete lists of the strains and plasmids produced in this study are

given in Tables 2.4 and 2.5 respectively.

Table 2.1: Period length and growth rate of the *N. crassa* strains used in this study.

Strain	Promoter	Protein	Period(hrs.)(n)	Growth rate (mm/h)
<i>bd</i> (control)	<i>frq</i>	FRQ	22.4±3.2 (41)	1.2
<i>bd</i> (MFNC9)	<i>cgc-2</i>	mCherryNC	21.1±2.0 (17)	1.0
<i>bd</i> (MFNC23)	<i>cgc-2</i>	FRQ-FLEX-mCh	16.4±1.8 (26)	0.9
<i>bd</i> (MFNC22)	<i>frq</i>	FRQ-FLEX-mCherryNC (<i>his-3</i> ectopic integration)	19.6±2.1 (21)	1.0
<i>bd</i> (MFNC30)	<i>frq</i>	FRQ-FLEX-mCherryNC	24.5±2.0 (18)	1.1

2.2.2 mCherry optimization

The mCherry protein was created by the Tsien lab at UCSD as a monomeric variant of the dsRed protein (Shaner et al., 2004). This fluorescent protein contains 236 amino acids and has several advantages over dsRed. These include a rapid folding time (15 minutes), the protein is a monomer rather than a dimer, it is resistant to photobleaching and it has been optimized to tolerate fusion proteins. The protein was optimized by the Tsien lab for expression in mammalian systems and therefore largely reflected the GC rich codon bias of *Neurospora*. However five codons were found to be suboptimal (arbitrarily defined as occurring with a frequency less than 20% for that amino acid in predicted coding sequences of the *Neurospora* genome) and these were altered to more favorable codons by site directed mutagenesis. Site directed mutagenesis was carried out using the Stratagene QuikChange Site-Directed Mutagenesis kit. We call this codon optimized version mCherryNC (or mCh) and the plasmid containing it pMFP5. The peak of excitation and emission of the protein mCherryNC was determined from conidia expressing fluorescence and from a wild type strain as a control. Conidia from *N. crassa* strains MFNC9 and wild type (FGSC#2489) were harvested and diluted to 5.0×10^6 per ml and then measured with a Perkin Elmer LS 55 Luminescence Spectrometer (see Fig. 2.1).

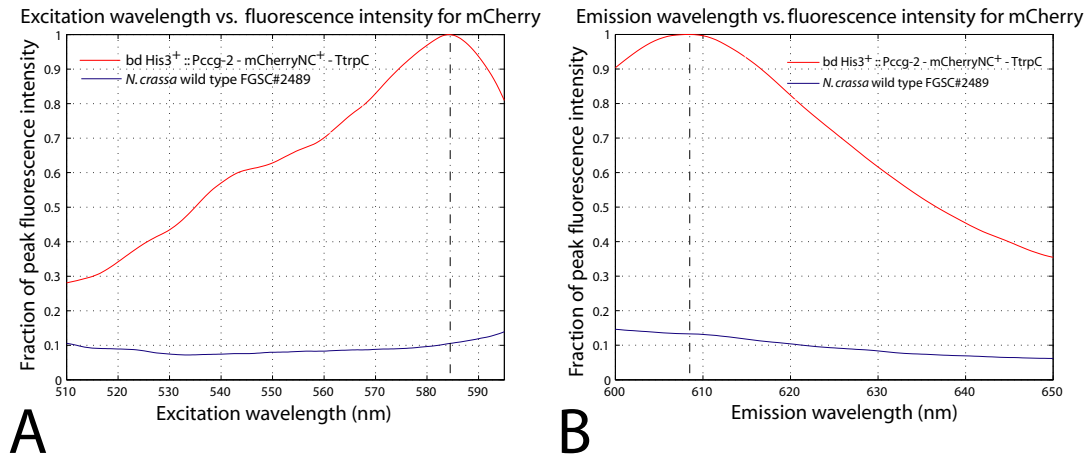


Figure 2.1: Plots depicting the fluorescence excitation and emission ranges for the mCherryNC protein (**A**) This is a plot of the emission intensity measured at 630nm over a range of excitation wavelengths. Conidia from a bd His3⁺ :: Pccg-2 - mCherryNC⁺ - TrpC strain and from a *N. crassa* wild type FGSC#2489 strain were diluted to 5.0×10^6 per ml and then measured with a Perkin Elmer LS 55 Luminescence Spectrometer. The excitation peak is indicated by the vertical dashed line and occurs at 584.5 nm. (**B**). The assay conditions in this plot are the same as in part A, except we are measuring the emission intensity at a variety of wavelengths while keeping the excitation wavelength constant at 550nm. The peak is found at 608.5 nm.

2.2.3 Production of MFNC1: a strain with the *ccg2* promoter driving mCherryNC

The construct required to make this strain was prepared by PCR amplifying the -2066 to -1 region of the *ccg2* promoter using primers P15.1 - P15.2 (see Table 2.2 for a list of primers and Table 2.3 for an overview of the homologous regions of each primer) from *Neurospora* wild-type DNA (FGSC#2489). The mCherryNC gene was amplified from the codon optimized version in the pMFP5 plasmid using primers P4.4 - P4.8 and the TrpC terminator amplified from plasmid pCSN44 using primers P15.7 - P15.8. All PCR reactions were carried out using Phusion high-fidelity DNA polymerase (New England Biolabs) to minimize the risk of PCR induced mutations. These primers, along with those subsequently listed, were designed for the yeast fusion PCR procedure (Wendland, 2003; Oldenburg et al., 1997). This procedure provides a convenient way to link PCR products which share homologous ends through site specific recombination.

Table 2.2: Primer sequences used in this study. Primers that contain both upper case and lower case text were used in the yeast fusion procedure. The upper and lower case text are used to designate the regions of the primer homologous to different DNA sources, see Table 2.3 for more information

Name	Description	Sequence
P4.1	pRS426-FRQ fusion primer	gcgcgtaatacagactcactatagggcgaatCCGCCCGGTGGTGTCAGTT
P4.2	FRQ-FLEX linker-mCherry fusion primer	cttgctcaccatgagggcggcgccgtcgccCGAGGATGAGACGTCCTCCA
P4.3	mCherry - FLEX linker fusion primer	cgccggcctcATGGTGAGCAAGGGCGAGEA
P4.4	mCherry amplification primer	cttgtacagctcgtccatgccgcc
P4.5	mCherry - FRQ fusion primer	ctccaccggcgcatggacgagctgtacaagTGAGACCTGAGTGGGTATTTTTCTATGTGA
P4.6	pRS426-FRQ fusion primer	ggctgcaggaattcgatatcaagcttatcgGAGCGTAATACGACGCAGAA
P4.7	FRQ amplification primer	ccaggttacaagcagattgagatacacc
P4.8	mCherry amplification primer	atggtgagcaagggcgagga
P15.1	pRS426-pCCG2 fusion primer	caccgcggtggcgccgctctagaactagtCTTTGCATGCTCTGACTCCA
P15.2	mCherry-pCCG2 fusion primer	catgttatcctcctcgcccttgctcaccatTTGGCGGTGGGGGTTT
P15.3	pRS426-pQA2 fusion primer	caccgcggtggcgccgctctagaactagtAGGAGGGAATGAAGCACACA
P15.4	mCherry-pQA2 fusion primer	catgttatcctcctcgcccttgctcaccatTGTGTTGGTACCTCTGGTT
P15.5	pRS426-pTrpC fusion primer	caccgcggtggcgccgctctagaactagtTTCGACAGAAGATGATATTGAAGGA
P15.6	mCherry-pTrpC fusion primer	caccgcggtggcgccgctctagaactagtTTCGACAGAAGATGATATTGAAGGA
P15.7	mCherry-tTrpC fusion primer	caccgcgcatggacgagctgtacaagtgaTTAATAGCTCCATGTCAACAAGAAAT
P15.8	pRS426-tTrpC fusion primer	gacggtatcgataagcttgatatcgaattcGAAAGAAGGATTACCTCTAAACAAGT
P15.9	pRS426-pBM61 fusion primer 1	gtaacgcccagggttttcccagtcacgacgAAGCTTGCCATCTCCACCAT
P15.10	pRS426-pBM61 fusion primer 2	gcggataacaattttcacacaggaaacagcAATGCGGATGGATTCCGCTCA
P21.1	pMFP28-pFRQ fusion primer	ctaattaacctcactaaagggaaacaaaagGTGGCTGGCTATGACCGTAT
P21.2	pMFP28-pCCG2 fusion primer	ctaattaacctcactaaagggaaacaaaagCTTTGCATGCTCTGACTCCA
P21.3	FRQ amplification primer (from atg)	atggcggatagtggggataa
P21.4	pCCG2-FRQ fusion primer	gcctgggatttatcccactatccgccatTTTGGCGGTGGGGGTTT

The PCR products were combined using this technique and the transformants

Table 2.3: Description of the primer structure used in the yeast fusion procedure. Each primer used in this procedure was homologous to at least two DNA sources. The first source is listed in the homology 1 column and the second in the homology two column. The homologous sequences are also listed. Note that P4.7, P4.8 and P21.3 were not designed for use in the yeast fusion procedure and thus are not listed here.

name	homology 1	sequence 1	homology 2	sequence 2
P4.1	pRS426	gcgcgtaatacgactcactatagggcgaat	FRQ	CCGCCGGTGGTGTCCAGTT
P4.2	mCherry-FLEX linker	cttgcaccatgaggccggcgcgcgcgcc	FRQ	CGAGGATGAGACGTCCTCCA
P4.3	FLEX linker	cgccggcctc	FRQ	ATGGTAGCAAGGGCGAGGA
P4.4	mCherry	cttgtacagctcgtccatgccgcc		
P4.5	mCherry	ctccaccggcggcatggacgagctgtacaag	FRQ	TGAGACCTGAGTGGGTATTTTTCTATGTGA
P4.6	pRS426	ggctgcaggaattcgatatcaagcttatcgat	FRQ	CGCGCCAGCAGCAACCT
P15.1	pRS426	caccgcggtggcggcgcgctctagaactagt	pCCG2	CTTTGCATGCTCTGACTCCA
P15.2	mCherry	catgttatcctcctcgcccttgctcaccat	pCCG2	TTTGGCGTTGGGGGTTT
P15.3	pRS426	caccgcggtggcggcgcgctctagaactagt	pQA2	AGGAGGGAATGAAGCACACA
P15.4	mCherry	catgttatcctcctcgcccttgctcaccat	pQA2	TGTGTTGGTACCCTCTGGTT
P15.5	pRS426	caccgcggtggcggcgcgctctagaactagt	pTrpC	GTCGACAGAAGATGATATTGAAGGA
P15.6	mCherry	catgttatcctcctcgcccttgctcaccat	pTrpC	GATCGAGGCTGGGTAGAATAG
P15.7	mCherry	caccgcgggcatggacgagctgtacaagtga	tTrpC	TTTAATAGCTCCATGTCAACAAGAAT
P15.8	pRS426	gacggtatcgataagcttgatcgaaattc	tTrpC	GAAAGAAGGATTACCTTAAACAAGT
P15.9	pRS426	gtaacgccagggtttcccagtcacgacg	pBM61	AAGCTTGCCATCTCCACCAT
P15.10	pRS426	gcgataacaatttcacacaggaacacagc	pBM61	AATGCGGATGGATTTCGCTCA
P21.1	pMFP28	ctaattaaccctcactaaaggaacaaaag	pFRQ	GTGGCTGGCTATGACCGTAT
P21.2	pMFP28	ctaattaaccctcactaaaggaacaaaag	pCCG2	CTTTGCATGCTCTGACTCCA
P21.4	FRQ	gccctgggattttatcccactatccgccat	pCCG2	TTTGGCGTTGGGGGTTT

screened for the desired construct using PCR. DNA was extracted from positive colonies using the yeast smash and grab DNA prep (Amberg et al., 2005) and electroporated into *E. coli*. Plasmid DNA was prepared from *E. coli* transformants using standard techniques (Sambrook and Russell, 2001) and the plasmid identity was confirmed through restriction digestions and sequencing. The finished plasmid containing the Pccg2 - mCh - tTrpC construct was named pMFP22 (Fig. 2.2A). Additionally we made similar constructs using two additional promoters, the qa-2 promoter and the trpC promoter from *Aspergillus niger*. However, upon microscopic investigation we found that the strongest signal was obtained using the *ccg-2* promoter and the other constructs were not investigated further (although they will be made available by request). Please see Table 2.4 for a list of all plasmids created in this study.

To transform *N. crassa*, the DNA fragment containing Pccg2-mCh-tTrpC was moved from pMFP22 into the His3 targeting vector pBM61, (Margolin et al., 1997). To accomplish this the pMFP22 plasmid was digested with EcoRI and the 3.28 kb fragment containing the Pccg2-mCh-tTrpC construct was gel purified. Next the pBM61 plasmid

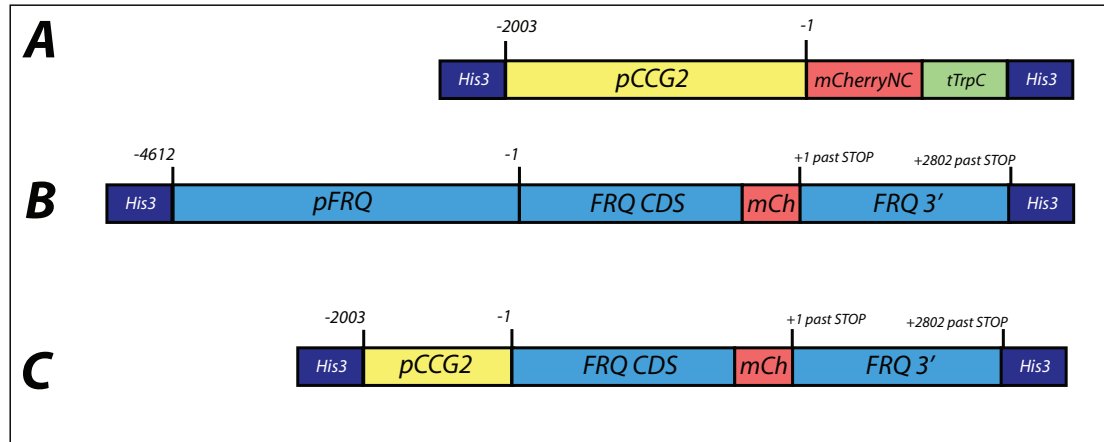


Figure 2.2: Graphical overview of the promoter constructs driving the mCherryNC protein used to transform *N. crassa*. The numbers above each graphic refer to the base pair distance from the promoter boundary to the start site of translation. (A) Construct with the *ccg2* promoter driving mCherryNC in the pMFP22 plasmid. (B) Insert in plasmid pMFP29 used to transform *Neurospora* at the *his-3* locus with the *frq* gene promoter driving the FRQ-mCh construct. (C) Insert in plasmid pMFP30 containing the FRQ-mCh construct driven by the *ccg-2* promoter, also used to transform *Neurospora* at the His3 locus.

Table 2.4: Plasmids produced in this study. The name and a description of the plasmid are given. The base plasmid refers to the parent plasmid used for construction.

name	description	base plasmid
pMFP2	Contains the mCherryNC <i>Neurospora</i> optimized version of mCherry	pRS426
pMFP5	Contains the a linker sequence preceding the mCherryNC gene	pRS426
pMFP10	Contains a partial amount of the FRQ coding sequence fused to the FLEX linker and the mCherryNC gene	pRS426
pMFP12	Contains the mCherryNC gene in the pBluescript KS+ plasmid	pBluescript KS+
pMFP15	Contains the mCherryNC - HyTK - mCherryNC construct	pBluescript KS+
pMFP16	Contains a partial amount of the FRQ coding sequence fused to the FLEX linker and the mCherryNC gene	pBluescript KS+
pMFP18	Contains the FRQ-FLEX-mCherryNC-HyTK-mCherryNC construct in the pBluescript KS+ plasmid	pBluescript KS+
pMFP20	Contains the pQA2-mCherryNC-tTrpC construct	pRS426
pMFP22	Contains the pCCG2-mCh-tTrpC construct	pRS426
pMFP23	Contains the pTrpC-mCh-tTrpC construct	pRS426
pMFP24	Contains the pQA2-mCh-tTrpC construct in the pBM61 <i>Neurospora</i> His3 targeting vector	pBM61
pMFP25	Contains the pTrpC-mCh-tTrpC construct in the pBM61 <i>Neurospora</i> His3 targeting vector	pBM61
pMFP26	Contains the pCCG2-mCh-tTrpC construct in the pBM61 <i>Neurospora</i> His3 targeting vector	pBM61
pMFP28	Fusion of the pRS426 and pBM61 plasmids. Useful for yeast cloning; can directly transform <i>N. crassa</i>	pRS426
pMFP29	Contains the pFRQ-FRQ-FLEX-mCh construct which can be targeted to the <i>Neurospora</i> His3 locus	pMFP28
pMFP30	Contains the pCCG2-FRQ-FLEX-mCh construct which can be targeted to the <i>Neurospora</i> His3 locus	pMFP28

was digested using EcoRI and the 5' phosphates were removed using Antarctic Phosphatase (New England Biolabs). The 3.28 kb DNA fragment was then ligated into the pBM61 plasmid to create plasmid pMFP26 whose identity was confirmed by restriction digestion and sequencing. The pMFP26 plasmid was linearized using SspI and used to transform FGSC strain #9716 (His3-A) by electroporation (Aramayo and Metzenberg,

1996; Vann, 1995). The transformants were then screened for the correct integration by PCR. Positive isolates were examined using fluorescent microscopy and one was renamed MFNC1 (His3::Pccg2-mCh-tTrpC derived from FGSC #9716). MFNC1 was then crossed to a *bd frq7* a strain (SG#7465) and the progeny were screened for the *bd*, *frq7* and His3::Pccg2-mCh-tTrpC genotypes by monitoring of the circadian rhythm using growth in race tubes and fluorescence microscopy. Isolates from this cross led to the production of the following strains MFNC5 through 9 (*bd*, His3::Pccg2-mCh-tTrpC) and MFNC10 through 17 (*bd*, *frq7*, His3::Pccg2-mCh-tTrpC). Please see Table 2.5 for a list of all strains produced in this study.

Table 2.5: Strains produced in this study. Note those listed as from DBP originally were provided by Dr. Deborah Bell-Pedersen.

strain	genotype	derived from	creation steps
MFNC1	His3::pCCG2-mCh-tTrpC	FGSC #9716 (His3-A)	pMFP26 transformed
MFNC2	His3::pQA2-mCh-tTrpC	FGSC #9716 (His3-A)	pMFP24 transformed
MFNC3	His3::pTrpC-mCh-tTrpC	FGSC #9716 (His3-A)	pMFP25 transformed
MFNC4	Δ mus-51 bar a+, FRQ-FLEX-mCh	FGSC #9718 SG7500(Δ mus-51 bar a+)	pMFP18 transformed, streaked onto FUDR media
MFNC5-9	<i>bd</i> , His3::pCCG2-mCh-tTrpC	<i>bdfrq7a</i> (SG#7465) x MFNC1	Isolates of cross MFIII
MFNC10-17	<i>bd</i> , <i>frq7</i> , His3::pCCG2-mCh-tTrpC	<i>bdfrq7a</i> (SG#7465) x MFNC1	Isolates of cross MFIII
MFNC18-19	His3::pFRQ-FRQ-FLEX-mCh-tFRQ	FGSC #9716 (His3-A)	pMFP29 transformed
MFNC20-21	His3::pCCG2-FRQ-FLEX-mCh-tFRQ	FGSC #9716 (His3-A)	pMFP30 transformed
MFNC22	<i>bd</i> , His3::pFRQ-FRQ-FLEX-mCh-tFRQ	<i>bdHis3a</i> #28 (from DBP)	pMFP29 transformed
MFNC23	<i>bd</i> , His3::pCCG2-FRQ-FLEX-mCh-tFRQ	<i>bdHis3a</i> #28 (from DBP)	pMFP30 transformed
MFNC24	<i>bd</i> , <i>we-1</i> Δ , His3::pFRQ-FRQ-FLEX-mCh-tFRQ	<i>bd,we-1</i> Δ , <i>his3A</i> (from DBP)	pMFP29 transformed
MFNC25	<i>bd</i> , <i>we-1</i> Δ , His3::pCCG2-FRQ-FLEX-mCh-tFRQ	<i>bd,we-1</i> Δ , <i>his3A</i> (from DBP)	pMFP30 transformed
MFNC26	<i>bd</i> , <i>frq7</i> , <i>eas</i> , His3::pCCG2-FRQ-FLEX-mCh-tFRQ	<i>bd,frq7,eas,his3A</i> (from DBP)	pMFP30 transformed
MFNC27	<i>bd</i> , <i>frq9</i> , His3::pFRQ-FRQ-FLEX-mCh-tFRQ	<i>bd,frq9,his3</i> #33 (from DBP)	pMFP29 transformed
MFNC28	<i>bd</i> , <i>frq9</i> , His3::pCCG2-FRQ-FLEX-mCh-tFRQ	<i>bd,frq9,his3</i> #33 (from DBP)	pMFP30 transformed
MFNC29	<i>bd</i> , <i>basR</i> , FRQ-FLEX-mCh	MFNC4a x <i>bdA</i> SG#2105	Isolate of cross 614
MFNC30	<i>bd</i> , <i>basS</i> , FRQ-FLEX-mCh	MFNC29 x <i>bdA</i> SG#2105	Isolate of cross 640

2.2.4 Construction of a yeast recombination plasmid directly transformable into *Neurospora*.

The yeast recombination technique utilizes yeast's high frequency of homologous recombination to fuse multiple PCR fragments together (Wendland, 2003; Oldenburg et al., 1997). In section 2.2.3, two cloning steps were needed before transformation of *Neurospora*: the first being yeast recombination cloning and the second being move-

ment of the recombinant DNA into the His3 targeting vector pBM61. To make this process faster we decided to combine the pRS426 and pBM61 plasmids so that a *Neurospora* transformable plasmid could be made after just the yeast recombination cloning step. To accomplish this we amplified the His3 containing regions of the pBM61 plasmid with primers P15.9 and P15.10. These primers each contained regions of homology to the pRS426 plasmid. The pRS426 plasmid was digested with SacI and KpnI and the 5.6 kb band was gel purified. The pBM61 PCR product and the digested pRS426 vector were combined and used to transform the FY834 yeast strain. DNA was isolated from transformant yeast as previously described and electroporated into *E. coli*. The identity of the recombinant molecule was confirmed by restriction digestion and sequencing of the fusion junctions. This molecule was named pMFP28 and a diagram of the plasmid is shown in Figure 2.3.

2.2.5 Production of His3 targeted FRQ-mCh fusion constructs

To create fusion constructs between *frq* and mCh we amplified a portion of the *frq* coding sequence with primers P4.1 - P4.2 and 2.8 kb of the *frq* 3' UTR using primers P4.5 - P4.6 (DNA from strain FGSC#2489 used as template). We amplified the mCh gene with primers P4.3 - P4.4 and pMFP5 plasmid template. To link the FRQ protein to mCh we introduced the flexible linker sequence described in (Sheff and Thorn, 2004) into the P4.2 - P4.3 primers. These PCR fragments were combined in the yeast fusion PCR procedure and transformants screened as previously described. The resulting plasmid was named pMFP10 and used as an intermediary to build two additional plasmids, one containing the native *frq* promoter and the other containing the *ccg-2* promoter driving FRQ-mCh.

After the pMFP10 plasmid's creation we amplified the *frq* promoter using the primers P21.1 - P4.7 with FGSC #4200 DNA as template (note this template was used for all *N. crassa* genomic PCR reactions described in this section). This product contained the *frq* promoter sequence starting from -4612 bp upstream of the start site of

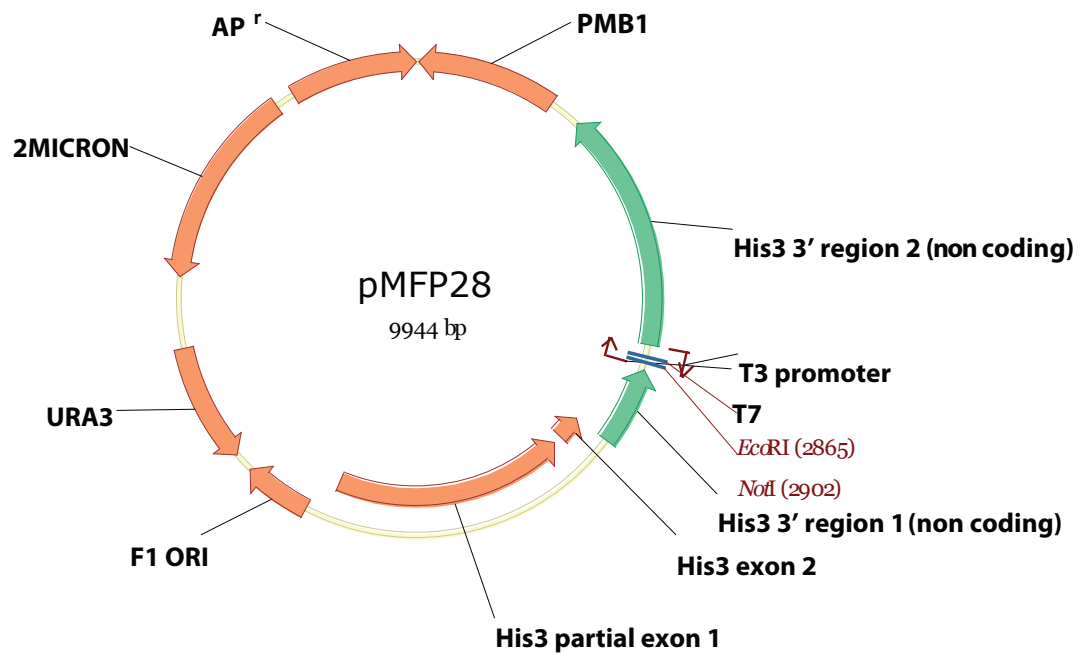


Figure 2.3: Figure showing the structure of the pMFP28 plasmid. This plasmid is a combination of the pRS426 and pBM61 plasmids, expanding the functionality of each. The *E. coli* and yeast origins of replication and selectable markers are retained from plasmid pRS426, while the multiple cloning site has been removed. The *Neurospora* His3 sequences and the multiple cloning site from pBM61 have been retained. We recommend using EcoRI or NotI to linearize this plasmid for yeast recombination cloning. To linearize the plasmid for *Neurospora* transformation we recommend using the SspI enzyme, which cuts three times in the pRS426 derived sequences, none of which are necessary for *Neurospora* transformation.

translation. We chose this boundary position since it had been used previously for *frq* constructs (see the ABC1 construct in (Froehlich et al., 2002) and the *Cla*I site of plasmid pCRM102 in (McClung et al., 1989)). In parallel to work with the *frq* promoter, we created an analogous *cgg2* promoter version using primers P21.2 - P21.4. These primers amplified the *cgg2* promoter's -2066 to -1 region which is the same region included in plasmid pMFP22, see section S2. After both promoters had been processed, the *frq* coding sequence was amplified from +1 to +1476 using the primers P21.3 - P4.7. Finally the pMFP10 plasmid was digested using the *Xho*I, *Not*I and *Xmn*I restriction enzymes and the 5.9 kb fragment containing the FRQ-mCh construct was gel purified.

For the *frq* promoter construct, the P21.1 - P4.7 PCR product, 5.9 kb restriction fragment, and *Eco*RI linearized pMFP28 were combined using the yeast recombination procedure. To create the *cgg2* promoter construct, the two PCR products generated using the P21.2 - P21.4 and P21.3 - P4.7 primers along with the 5.9 kb restriction fragment were combined with *Eco*RI linearized pMFP28 and used in the yeast recombination procedure. DNA was isolated from recombinant yeast as previously described and the identity of each plasmid confirmed. The plasmid containing the the FRQ promoter driving FRQ-mCh was named pMFP29 (Fig. 2.2B), while the *cgg-2* promoter version was named pMFP30 (Fig. 2.2C). Note that each of these constructs contained the full FRQ coding sequence and 2.8 kb of the FRQ 3' UTR (only the promoters are different). The pMFP29 plasmid was linearized using *Nsi*I and used to transform strains FGSC #9716 (*his-3 A*), *bd his-3 a #28*, *bd wc-1Δ his-3 A*, *bd frq7 eas his-3A*, *bd frq9 his-3 #33* (all except FGSC #9716 obtain from Dr. Deborah Bell-Pedersen) by electroporation (Aramayo and Metzenberg, 1996; Vann, 1995). The pMFP30 plasmid was linearized using *Psi*I and used to transform these same strains by the same methods. Transformants were screened for the correct integration by PCR. Isolates from this transformation are listed in Table 2.3.

2.2.6 Cloning steps for modified “HyTK Blaster” technique

Essentially this procedure called for flanking the HyTK marker with two copies of the mCh gene and then placing the combined DNA at the end of the *frq* gene. Upon transformation of *N. crassa* with this construct, recombination between the mCh repeats would be selected for, yielding the desired insertion. To create the necessary targeting construct we first cloned the mCh gene into the pBluescript KS+ plasmid since this plasmid had more favorable restriction sites. We accomplished this by digesting the pMFP2 plasmid (a plasmid related to pMFP5 and also carrying the mCh gene) with BamHI and EcoRI and gel purifying the 0.7 kb mCh fragment. This fragment was then ligated into the similarly digested pBluescript KS+ plasmid and used to transform chemically competent *E. coli* cells. The resulting transformants were screened for the proper insert and named pMFP12.

To create the direct repeat, a triple ligation reaction was carried out inserting an additional copy of mCh and the HyTK gene into the pMFP12 plasmid. To accomplish this, SacI and XhoI were used to digest the pMFP12 plasmid and the 0.79 kb mCh fragment was gel purified. Next the pHyTK plasmid was digested with XhoI and NotI and the 3.0 kb band containing the HyTK gene was gel purified. Finally the pMFP12 vector was digested with SacI and NotI in a separate reaction and the 3.65 kb band containing the vector was gel purified. These 0.79kb and 3.0kb DNA fragments were ligated to the digested pMFP12 vector and the resulting DNA electroporated into competent *E. coli*. The identity of this plasmid, named pMFP15, containing the mCh-HyTK-mCh construct was confirmed through restriction ligation and sequencing. Next the mCh repeat in pMFP15 had to be combined with the FRQ-mCh fusion in pMFP10. To accomplish this the FRQ-mCh construct was moved from pMFP10 to the pBluescript KS+ vector by digesting pMFP10 with the NotI, XhoI and XmnI restriction enzymes. The resulting 5.91 kb fragment containing the FRQ-mCh construct of interest was then gel purified and ligated into NotI-XhoI digested pBluescript KS+. and the reaction products were electroporated into *E. coli*. The transformants were screened by restriction digestion and

the resulting plasmid named pMFP16.

To make the desired FRQ-mCh-HyTK-mCh construct an additional cloning step was necessary using the pMFP15 and pMFP16 plasmids. The SbfI enzyme digests the pMFP16 plasmid once, in the middle of the mCh coding sequence and this enzyme was used to linearize this plasmid. The pMFP15 plasmid was digested with SbfI to release the 3.81 kb fragment containing the mCh-HyTK-mCh construct. The digested pMFP16 plasmid was then treated with antarctic phosphatase and the 3.81 kb fragment from pMFP15 was ligated into it. The ligation reaction was used to transform *E. coli* by electroporation. Plasmid DNA was isolated from the transformants using standard techniques and the identity confirmed using restriction digestions and DNA sequencing. This confirmed that the plasmid created contained the desired FRQ-mCh-HyTK-mCh construct and this plasmid was named pMFP18.

2.2.7 Insertion of the mCh gene at the native *frq* locus using a modified “tk-blaster” technique

Since the regulation of the *frq* gene is complex, containing regulatory elements both 5' and 3' of the actual FRQ coding sequence (Colot et al., 2005; Crosthwaite, 2004), we decided to fuse mCh to the FRQ gene in its native genomic locus. We reasoned this fusion gene might capture the intricate regulation of FRQ more completely than an ectopic FRQ construct like that described in the supplementary methods section. Moreover our strategy allowed for the selectable marker gene's complete removal, resulting in a minimum of DNA being added to the genome (essentially being only a linker and mCh sequences). Our strategy was similar to the “tk-blaster” strategy described in (Pratt and Aramayo, 2002), which itself is based on the URA-blaster strategy of *Saccharomyces cerevisiae* (Alani et al., 1987). The “tk-blaster” strategy is essentially a technique to knockout a gene without a permanent marker being left behind. This enables the recycling of the marker gene in subsequent knockout experiments and is therefore useful in building strains with multiple gene knockouts. We have extended

this technique beyond knockouts by modifying it to fuse fluorescent protein genes to the genomic copy of a gene of interest. Unlike a knockout, this strategy retains the function of the native gene and allows the fusion gene's regulation to be studied in its native context with a minimal amount of inserted DNA. Importantly this removes any ambiguity about regulation being altered by an ectopic genome location.

To accomplish this fusion, our method, like the “tk-blastar” technique, makes use of the hygromycin-thymidine kinase fusion gene from the plasmid pHyTK (Lupton et al., 1991). This construct confers resistance to hygromycin B and sensitivity to 5-Fluoro-2'-deoxyuridine (FUDR) and thus enables dominant positive and negative selection of transformants (Pratt and Aramayo, 2002). In the “tk-blastar” technique a sequence is placed flanking the marker sequence on both the 5' and 3' ends, creating a direct repeat. This construct is then targeted to the genomic region of interest, selecting for hygromycin resistance. In the next step, marker removal is selected by plating cells on media containing FUDR. This removal process occurs due to the high frequency of mitotic recombination between direct repeats in the genome of *Neurospora* and other organisms (Pratt and Aramayo, 2002). In the “tk-blastar” strategy of (Pratt and Aramayo, 2002), one of the repeat sequences remains as essentially unwanted DNA after the marker's removal in (Pratt and Aramayo, 2002) this sequence was known as a “lambda scar”). In our strategy we have made the mCh fusion sequence itself the repeat, hence when the marker gene is removed all that remains is the desired fusion sequence and no extraneous DNA is leftover. Importantly the most minimal disturbance to the native gene possible is made: the end result is an insertion of the fluorescent protein gene only between the second to last codon of the gene and the stop codon; no other part of the gene, including the promoter, 5' or 3' UTR, is altered. In our case with the *frq* gene, we ended up inserting only 711 base pairs into the *N. crassa* genome at the end of *frq*. An overview of our strategy is shown in (Fig. 2.4) and a detailed overview of the cloning steps taken to produce the required construct is given in the supplementary methods.

These cloning steps eventually yielded plasmid pMFP18 containing appropriate targeting vector with repeating copies of mCh flanking the HyTK marker. To trans-

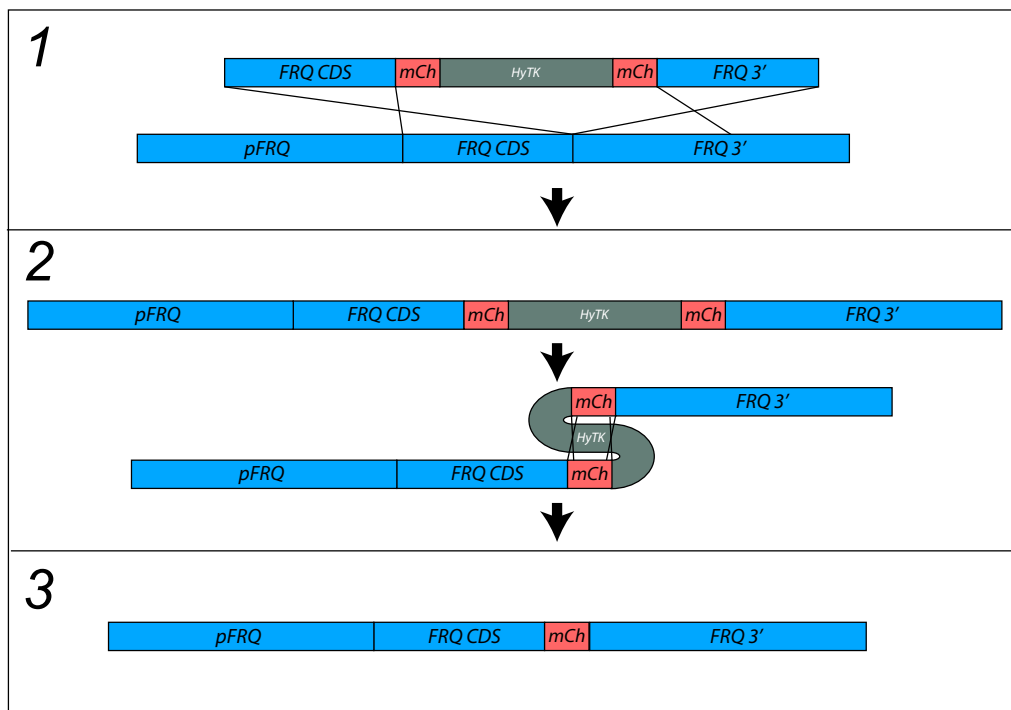


Figure 2.4: Diagram depicting the modified “tk-blaster” technique. (A) The construct containing the HyTK marker gene flanked by two repeating sequences (in this case the mCh gene) is targeted to the genomic FRQ locus of *Neurospora*. Integration of this construct creates the FRQ-mCh fusion gene followed by the HyTK resistance gene and another copy of the mCh gene. (B) Mitotic recombination between the two mCh repeats is selected by plating conidia on FUDR containing media. Only those cells that have removed the HyTK gene from their genome will be able to survive in this media. (C) The final result is an insertion of only the mCh gene following the FRQ gene. No other DNA, such as a marker, is inserted. Moreover the promoter, 5' UTR and 3' UTRs remain intact.

form *Neurospora* the pMFP18 vector was linearized with the XmnI restriction enzyme and used to transform *Neurospora* strain FGSC #9718 (Δ mus-51 bar a+) by electroporation. The resulting *Neurospora* colonies were transferred to 10x75 mm test tubes and screened for the presence of the pMFP18 derived construct by PCR. Conidia from positive isolates were streaked onto plates containing FUDR to select those that had undergone recombination between the mCh repeats. Colonies were transferred to 10x75 mm test tubes and screened for the recombination event by PCR. The PCR products from isolates positive for the desired recombination product were then cloned into the pCR-Blunt vector (Invitrogen) and sequenced. The sequencing reaction indicated the desired recombination had occurred perfectly in at least some of the isolates. We named one of these isolates MFNC4 (FRQ-FLEX-mCh, Δ mus-51 bar a+) and crossed it to the bd strain (bd A SG#2105) to remove the Δ mus-51 bar marker, add the bd allele, and generate a homokaryon. Please note that FLEX refers to the linker used to fuse FRQ to mCh and is described in the supplementary methods. The cross yielded 72 isolates, which were screened for basta resistance (conferred by the Δ mus-51 bar marker), the bd allele and the presence of the FRQ-mCh fusion gene. One isolate was chosen from this cross and named MFNC29 (bd, FRQ-mCh, Δ mus-51 bar). This strain was then back crossed to bd A SG#2105 to generate MFNC30 (bd FRQ-FLEX-mCh).

2.2.8 Fluorescence microscopy

Expression of fluorescence (strain MFNC9) was monitored from live cultures grown in special chambers (Castro-Longoria et al., 2007) under epifluorescence microscopy (Carl Zeiss Axiovert 200M inverted microscope) equipped with a Texas Red filter and in complete darkness. Observations of vegetative hyphae were done each hour at low magnification (using a 10X objective) once the colony had grown and formed the first conidiation band. Developing colonies were scanned and photographed from the growing edge inwards. Micrographs from cultures were assembled to obtain the whole region at which the mCh fluorescence was expressed during the circadian cycle.

2.2.9 Confocal live-cell imaging

Vegetative hyphae at the edge of growing colonies of strains MFNC9, MFNC23 and MFNC30 were scanned every hour under confocal microscopy. Living hyphae were imaged at 25°C (strain MFNC9) and 28°C (strains MFNC23 and MFNC30) on VMM using an inverted Zeiss Laser Scanning Confocal Microscope LSM-510 META (Carl Zeiss, Gttingen, Germany). Cultures were scanned during subjective day and subjective night using the inverted agar block method (Hickey, 2005). Every hour an independent culture was scanned and at least three complete sets of observations were done for each strain. Also, additional observations were done at times at which the peak of fluorescence was detected in order to corroborate results. An oil immersion objective 100X (PH3) 1.3 N.A. plan neofluar was used. While scanning vegetative hyphae, the pinhole was set to 2.3 airy units. A photomultiplier module allowed us to combine fluorescence with phase-contrast channels to provide a simultaneous view of the fluorescently-labeled organelles and the entire cell. Confocal images were captured using LSM-510 software (version 3.2; Carl Zeiss) and evaluated with an LSM-510 Image Examiner (version 3.2). Some of the image series were converted into animation movies using the same software. Fluorescence intensity was measured with Image Pro Plus® and the obtained measurements were exported into Microsoft Excel spreadsheets and analyzed.

2.3 Results

2.3.1 Expression of the RFP mCherry under the control of the *ccg-2* promoter in *N. crassa*

All transformed Pccg-2-mCh strains (MFNC5 to MFNC9) were scanned under fluorescence microscopy and strain MFNC9 (bd, His3::Pccg-2-mCh-tTrpC) was chosen to continue further observations. The strain was first grown in standard Petri plates to monitor the circadian banding pattern (Fig. 2.5A) and then examined using a flu-

orescence lamp optimized for viewing the fluorescence signal from a Petri plate (see methods section 2.2.1). We observed strong production of mCh in bands of conidiation (Fig. 2.5B), while any accumulation of mCh in the vegetative hyphae (inter-band region) was too low to detect using this setup. To further examine fluorescence at the microscopic level, fully-grown cultures in special chambers (Castro-Longoria et al., 2007) were scanned using confocal microscopy. Using this technique we observed a strong accumulation of mCh in the conidiation bands as had been previously seen in culture plates (Fig. 2.5B). For example in Figure 2.5C-E a conidiation band section examined using epifluorescence microscopy illustrates the strong fluorescence found in conidia.

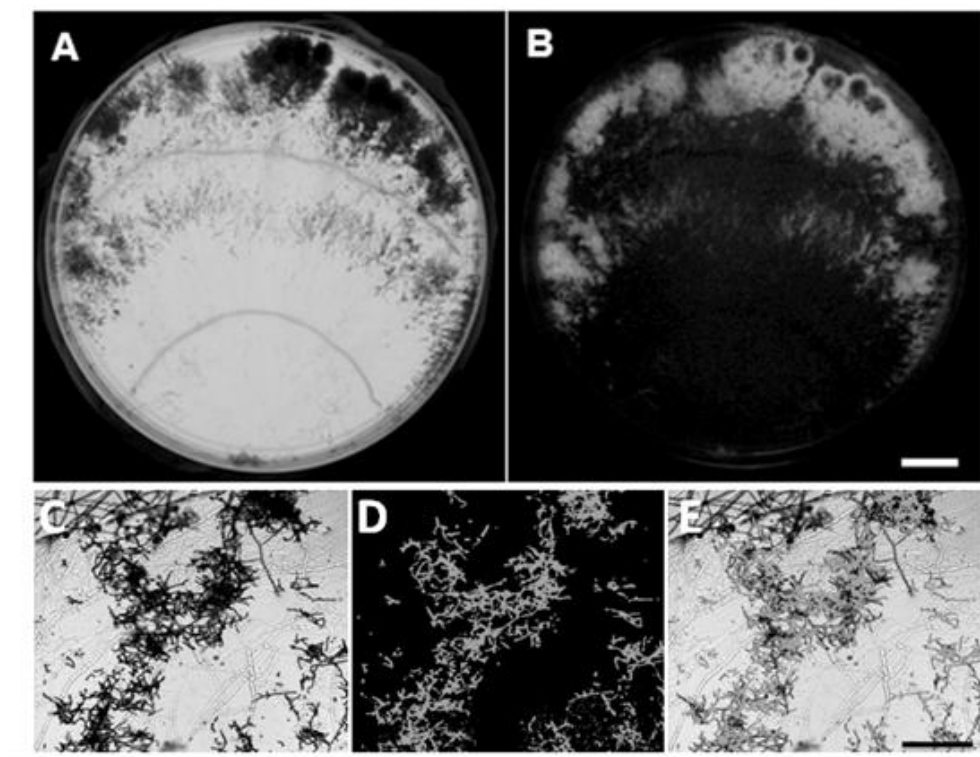


Figure 2.5: Phenotype of strain MFNC9 (Pccg2-mCherryNC) of *N. crassa*. (A) Banding pattern on a culture plate viewed under transmitted light. (B) View of the same culture under a fluorescent lamp (see methods for excitation and emission wavelengths); note the strong expression of mCh on bands of conidiation. (C-E) Close up of a conidiation band from a fully-grown *Neurospora* strain MFNC9 colony grown in a special chamber and scanned under confocal microscopy: (C) Transmitted light channel, (D) mCh fluorescence, (E) Merged images. (A-B) Scale bar = 2 cm; (C-E) Scale bar = 200 μ m.

To trace the dynamics of Pccg-2-mCh in growing MFNC9 colonies and to assess circadian control of the construct, we scanned cultures every hour at low magnification using fluorescence microscopy after an initial 11-hour period of continuous darkness. All observations were carried out in vegetative hyphae growing on an agar surface. Furthermore, to examine Pccg2-mCh's circadian regulation (if any) we adjusted all time units to Circadian time (CT). Circadian time is a formalism used under constant conditions to normalize the rhythm lengths among organisms with different endogenous periods to 24 circadian hours per cycle. This adjustment allows for easier comparisons among different organisms clocks. By convention CT0 corresponds to subjective dawn and CT12 to subjective dusk.

Near subjective dawn (CT1-3) the hyphal fluorescence at the growing edge of the MFNC9 colony was low compared with fluorescence detected in conidia from the previous band (B1) (Fig. 2.6A). A rapid increase in fluorescence was detected from CT4 to CT7 (Figures 2.6B and 2.6 lower panel) and after CT8 fluorescence gradually decreased. After CT11 fluorescence in vegetative hyphae remained at very low, but detectable levels for the following 11 hours (Fig. 2.6C-D). During this time nascent aerial hyphae were monitored in the developing future band (FB2) and a very strong fluorescence signal was observed in aerial hyphae and conidia (Fig. 2.6E).

In addition to fluorescence microscopy, we scanned growing MFNC9 colonies at higher magnification (100x) using confocal microscopy yielding similar results to those previously obtained. The mCh protein was detected in vegetative hyphae at the growing edge of the colony and at CT1 fluorescence was low (Fig. 2.6, lower panel). The level of expression increased gradually and reached a maximum of intensity at CT4 (Fig. 2.6, lower panel, Fig. 2.7). The intensity remained high for the following 5h and then decreased rapidly during the next 3h. During the following 11h, the expression of mCh in vegetative peripheral hyphae was very low. Furthermore the Pccg2 promoter displayed an impressively high dynamic range during the course of the circadian cycle, reaching a maximum expression level at CT3-6 of at least 240 times that during CT11 to CT22 (Fig 2.7). Moreover when the low state cultures (those between CT11-22) where

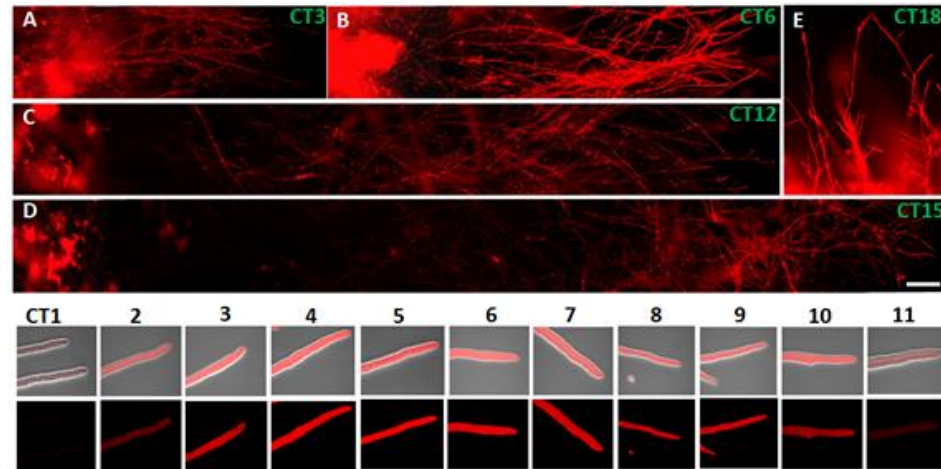


Figure 2.6: Expression of mCh driven by the *ccg-2* promoter during colony development of *N. crassa*, strain MFNC9. (A-E) Colony examined under fluorescence microscopy (10x) after the formation of the first band: (A-D) Vegetative hyphae, (E) aerial hyphae. Lower panel: Rhythmic expression of mCh fluorescence in peripheral vegetative hyphae from CT1 to CT11 examined under confocal microscopy (100x). Upper row of images are the phase contrast and fluorescence channels merged; lower row, fluorescence channel. Scale bar upper panel 1 mm.

exposed to continuous light, we detected a very high production of mCh after one hour (data not shown).

2.3.2 Kinetics of the protein FRQ under the control of the *ccg-2* promoter in *N. crassa*

The use of the mCh reporter proved to be a powerful tool for observing the Pccg2 promoter's dynamics at the cellular level. Moreover this strain served as a control, ensuring that the mCh protein was detectable in *Neurospora*. Our next step was to expand upon this initial strain by having the Pccg2 promoter drive a FRQ-mCh fusion protein instead of the mCh protein alone. We then used this reporter to determine the spatial and temporal distribution of FRQ in living hyphae using the transformant strain MFNC23 (bd, His3:Pccg2-FRQ-mCh). This strain was monitored using confocal microscopy for an entire circadian cycle to follow the expression and intracellular localization of FRQ-

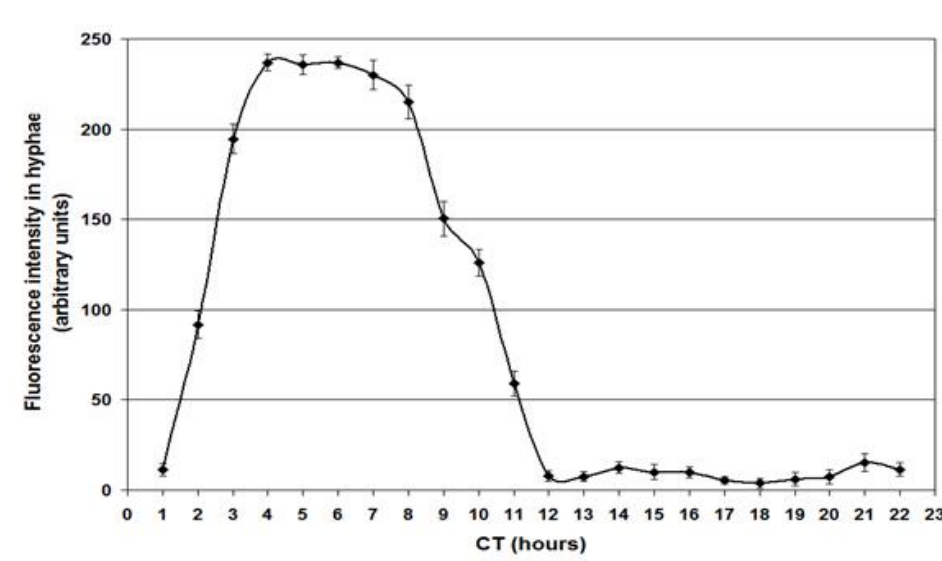


Figure 2.7: Profile of fluorescence intensity of the protein mCh driven by the *ccg-2* promoter during the circadian cycle of *N. crassa*, strain MFNC9. Note that only vegetative hyphae at the edge of the colony were considered. Mean and standard deviation were calculated from measurements on three different hyphae.

mCh driven by the *ccg-2* promoter. The conidiation (banding) pattern of strain MFNC23 was clear with a period length of 16.4 h and hyphal extension rate of 1.0 mm/h.

Fluorescence was detected only in the colony's growth front, for a distance of approximately 150-300 μm from the apices of leading hyphae; beyond that distance only a diffuse signal was detected. Accordingly all observations were carried out in individual hyphae situated at the growth front's edge of the colony. Expression of FRQ-mCh was generally very low during most of the circadian cycle and some hyphae in the same culture did not demonstrate a detectable fluorescence signal. However, using only hyphae expressing detectable levels of fluorescence, a consistent pattern of FRQ-mCh localization was observed.

The nuclear entrance of FRQ-mCh was clear (Fig. 2.8) and during the first hours of subjective day (CT0-CT7) FRQ-mCh was localized inside the nucleus at very low levels (Fig. 2.8A). A gradual increase of fluorescence inside the nucleus was detected from CT8 (Fig. 2.8B) until a strong accumulation was observed at CT11 (Fig. 2.8C).

After the period of strong accumulation, levels of FRQ-mCh decreased and stayed at a low level until another nuclear entry cycle occurred, from CT18-CT21, peaking at CT19. Both of these fluorescence peaks exhibited comparable signal levels. Moreover this nuclear entrance of FRQ-mCh was observed only in nuclei localized subapically; no entry was detected past 150-200 μm from the apices of leading hyphae.

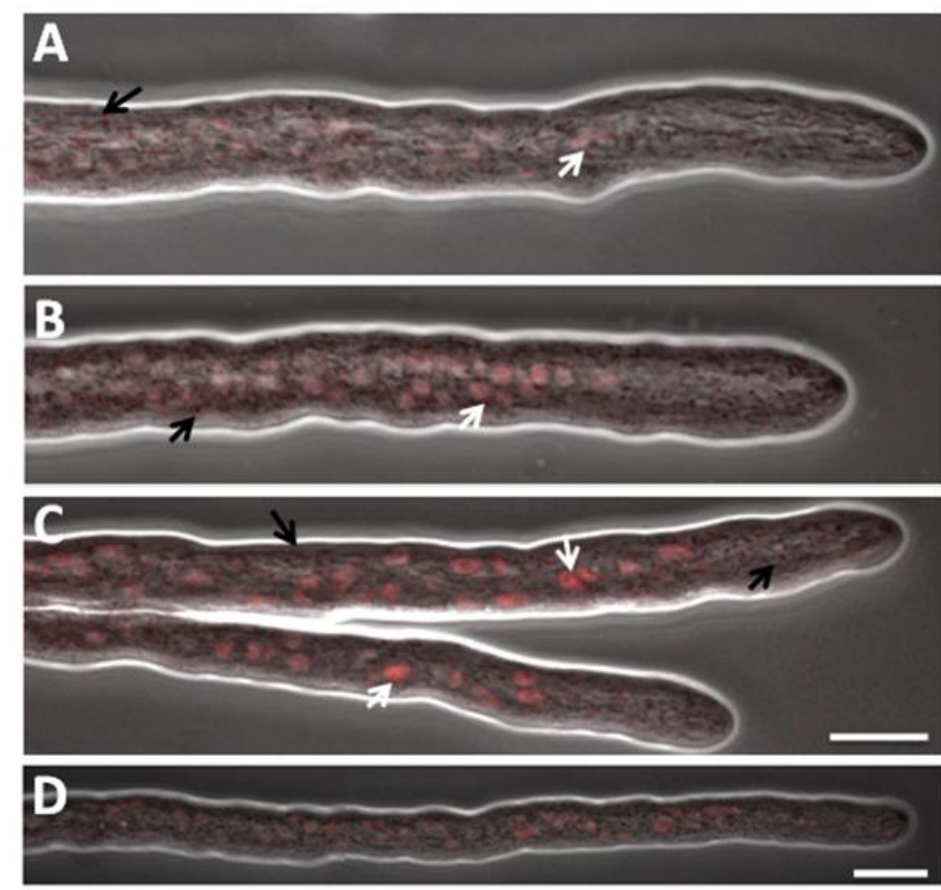


Figure 2.8: Nuclear entrance of FRQ-mCh under the *cgc-2* promoter in vegetative hyphae of *N. crassa*, strain MFNC23. (A) A low accumulation of FRQ-mCh in nuclei was detected during early subjective day and night, image taken at CT2. (B) Gradual accumulation of FRQ-mCh in nuclei, image taken at CT9. (C) Maximum of fluorescence detected in nuclei at CT11 and CT19, image taken at CT11. White arrows point to selected nuclei. Images are the phase contrast and fluorescence channels merged. Scale bar = 10 μm .

2.3.3 Kinetics of the protein FRQ under the control of the *frq* promoter in *N. crassa*

Strain MFNC30 (bd, *bas*^S, FRQ-mCh) contains the mCh gene inserted into the end of the native *frq* gene, enabling the production of the FRQ-mCh fusion by the native *frq* promoter, at the native *frq* locus. Confocal microscopy was again used to follow the production and localization of FRQ-mCh during the circadian cycle. The strain's growth was also monitored in race tubes and the circadian conidiation pattern was even clearer than that seen in MFNC23 with a period length of 24.5 h and hyphal extension rate of 1.06 mm/h.

Fluorescence in the colony was detected only in peripheral hyphae, as in strain MFNC23, therefore only individual leading hyphae in the growing region of the colony were examined. Very low accumulation of FRQ-mCh was detected inside the nucleus at CT1, followed by a period of rapid accumulation, which resulted in a high signal at CT4 (Fig. 2.9A). Following the strong accumulation of FRQ-mCh in nuclei, a gradual decrease in fluorescence intensity inside the nucleus was observed. At CT10 some fluorescence was also present outside the nucleus (Fig. 2.9B) in the subapical region. A strong fluorescence outside the nuclei was more evident after CT10 with almost undetectable levels inside the nucleus (Fig. 2.9C). Behind the subapical region (where FRQ-mCh was localized to the nucleus) an accumulation of fluorescence in the cytoplasm was present (as in Fig. 2.9C) and beyond this area the fluorescence signal was very low and diffuse. Prior to being released into D/D, the fluorescence signal in L/L was relatively strong but was localized completely to the cytoplasm.

After the first nuclear entry, apparently a second entrance of FRQ into the nucleus was detected at CT19 as a low accumulation of nuclear fluorescence, compared with the levels found at CT4-5. This second entrance of FRQ to the nucleus coincided with the higher expression of cytoplasmic FRQ localized near the subapical region of the cell. Also some hyphae did not have much cytoplasmic FRQ in the subapical area and the fluorescence inside the nucleus was clearly observed (Fig. 2.10A-C). Although

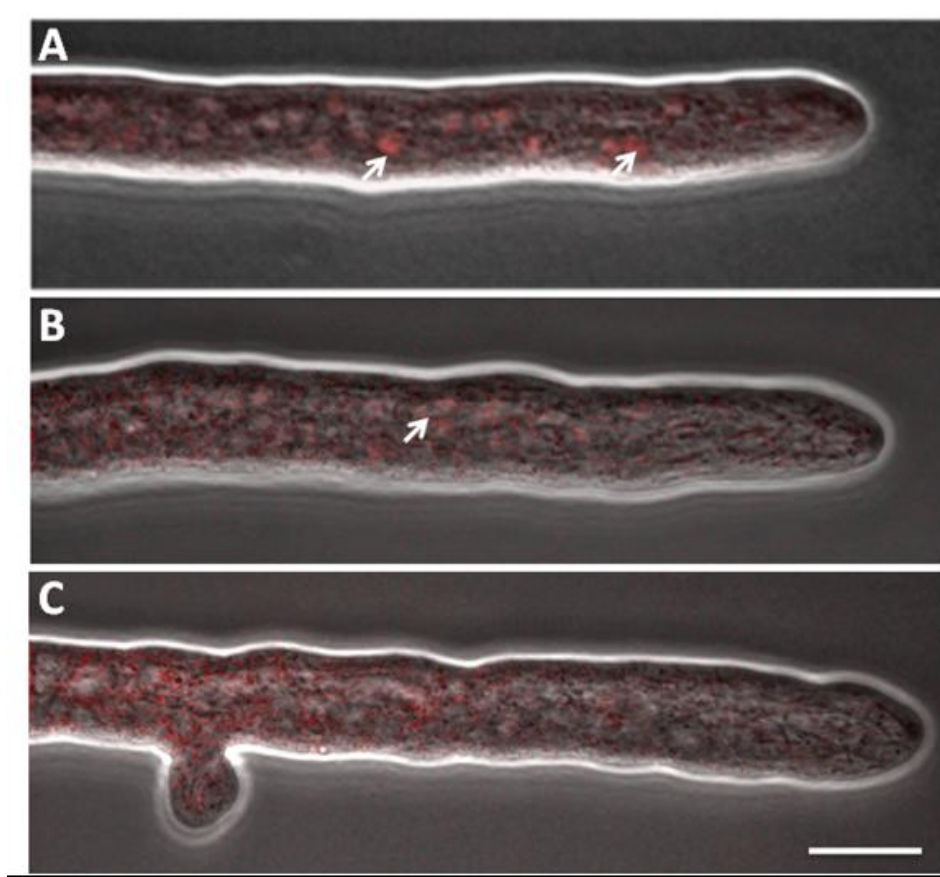


Figure 2.9: Nuclear entrance of FRQ-mCh under the *frq* promoter in vegetative hyphae of *N. crassa*, strain MFNC30. (A) Peak of fluorescence detected in nuclei at CT4. (B) FRQ-mCh detected inside and outside the nucleus, image taken at CT10. (C) Accumulation of FRQ-mCh in cytoplasm at the subapical region of the cell, image taken at CT18. White arrows point to selected nuclei. Images are the phase contrast and fluorescence channels merged. Scale bar = 10 μm .

the fluorescence of FRQ-mCh detected inside the nucleus at CT19 was low, this entrance to the nucleus was also detected by measuring the fluorescence intensity in individual nuclei (Fig. 2.11). The second accumulation of FRQ-mCh can be seen as a smaller peak of fluorescence intensity at CT19 (Fig. 2.11).

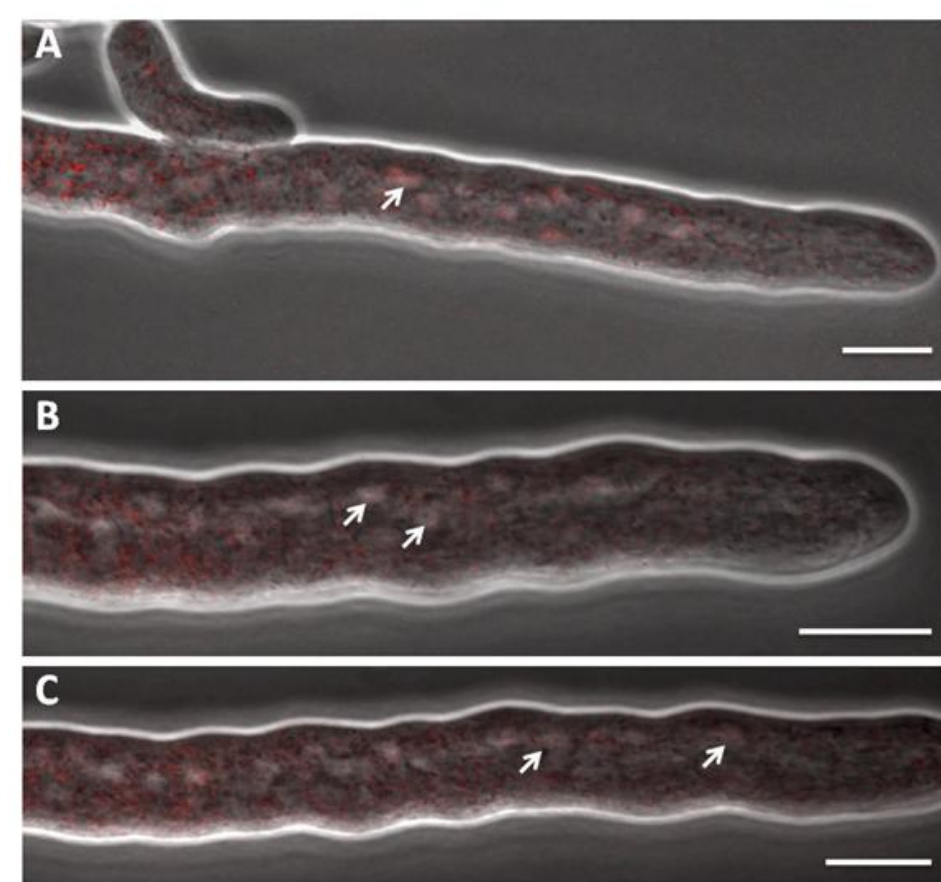


Figure 2.10: Accumulation of FRQ-mCh in cytoplasm and nuclei of *N. crassa*, strain MFNC30. (A-C) Second entrance of FRQ-mCh in the nucleus, images taken at CT19. White arrows point to selected nuclei. Images are the phase contrast and fluorescence channels merged. Scale bar = 10 μm .

To ensure that FRQ-mCh localization was nuclear, we were able to obtain an image of two growing hyphae in which one of them had vacuoles showing no fluorescence. Furthermore both hyphae possess several nuclei with a strong fluorescence signal and in some the nucleolus can be clearly observed (Fig. 2.12A-C). Moreover as a control to ensure that mCh alone does not enter the nucleus of *N. crassa* hyphae during

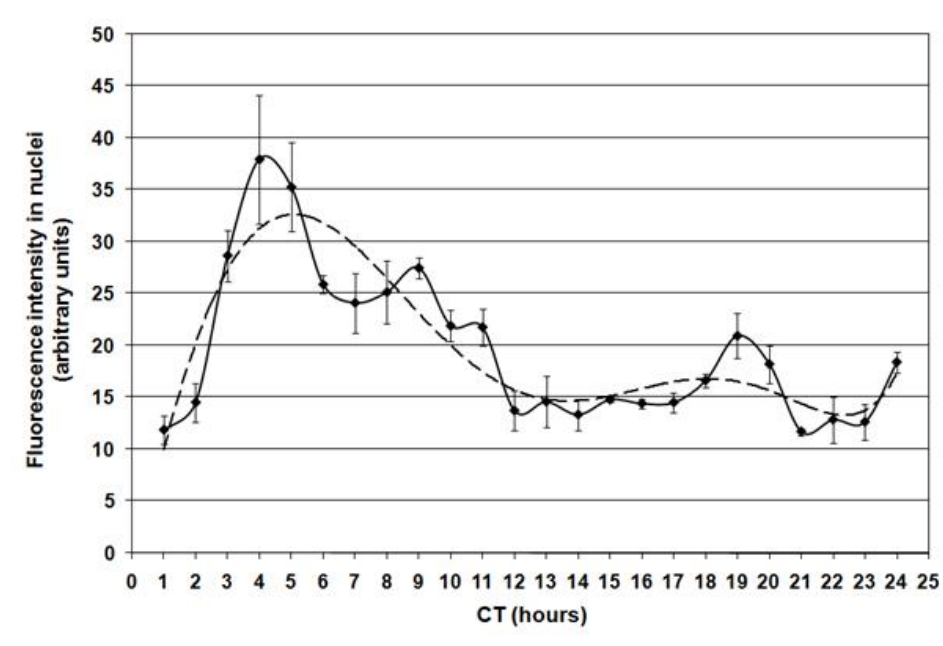


Figure 2.11: Variation of fluorescence intensity in nuclei of the protein mCh driven by the *frq* promoter during the circadian cycle of *N. crassa*, strain MFNC30. Note that only vegetative hyphae at the edge of the colony were considered. Mean and standard error were calculated from measurements on three different cells. Dotted line indicates the general trendline.

the cycle, we used strain MFNC9 expressing mCh alone driven by the *ccg-2* promoter. As demonstrated in Figure 2.13, fluorescence seems to be dispersed in the cytoplasm without any visible nuclear accumulation. At CT4 fluorescence intensity is very high in strain MFNC9 (Fig. 2.7), and therefore we used a lower laser intensity to get a fluorescence signal comparable to that seen in MFNC30. Nuclear size and distribution of strain MFNC30 (data not shown) were similar to those of a strain with nuclei labeled with GFP.

While nuclear localization of the FRQ-mCh protein was clear in MFNC30, fluorescence intensity varied between the examined hyphae, possibly due to the disturbance created while being examined under the microscope. Despite such variability, a general trend in nuclear fluorescence was observed (Fig. 2.11). The first peak of fluorescence was the result of the strong accumulation of FRQ-mCh inside the nuclei and the second peak apparently was caused by a much lower accumulation. Cytoplasmic fluorescence accumulation also showed some variability; it was present during the complete circadian cycle, but followed a differential pattern of expression. At CT1-CT17 the accumulation of cytoplasmic FRQ-mCh was located further from the apices of leading hyphae (150-250 μm) and from CT17-CT23 this accumulation was closest to the subapical region (Fig. 2.9C).

2.3.4 Clock effects in the *N. crassa* constructs

While the fluorescent reporters were useful for measuring the dynamics of the FRQ-mCh protein, we also wanted to ensure that the clock still functioned normally in these strains. Towards this end we measured the period and growth rate for each of the strains used in this study. We find that expressing mCh under the control of the *ccg-2* promoter (strain MFNC9) had little effect on the free-running period of a *bd* culture when grown in constant darkness (Table 2.1). This result was expected since mutations in the *ccg-2* gene do not affect the period of the clock. Secondly, results with strain MFNC23 indicate that overexpressing FRQ-mCh using the *ccg-2* promoter, which is a

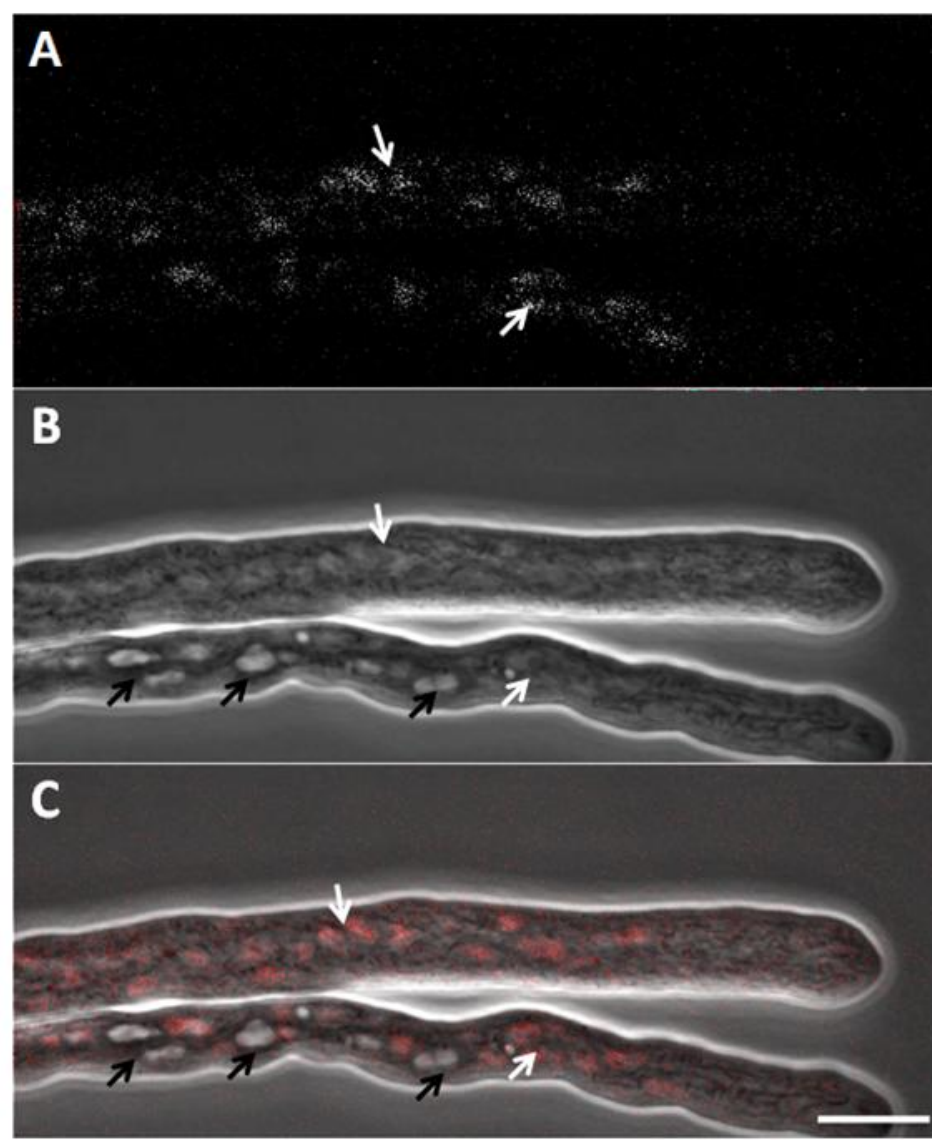


Figure 2.12: Nuclear localization of FRQ-mCh in *N. crassa*, strain MFNC30. A) Fluorescence channel, image taken at CT7. B) Phase contrast channel. C) Merged images. White arrows indicate selected nuclei and black arrows point to selected vacuoles. Scale bar = 10 μm .

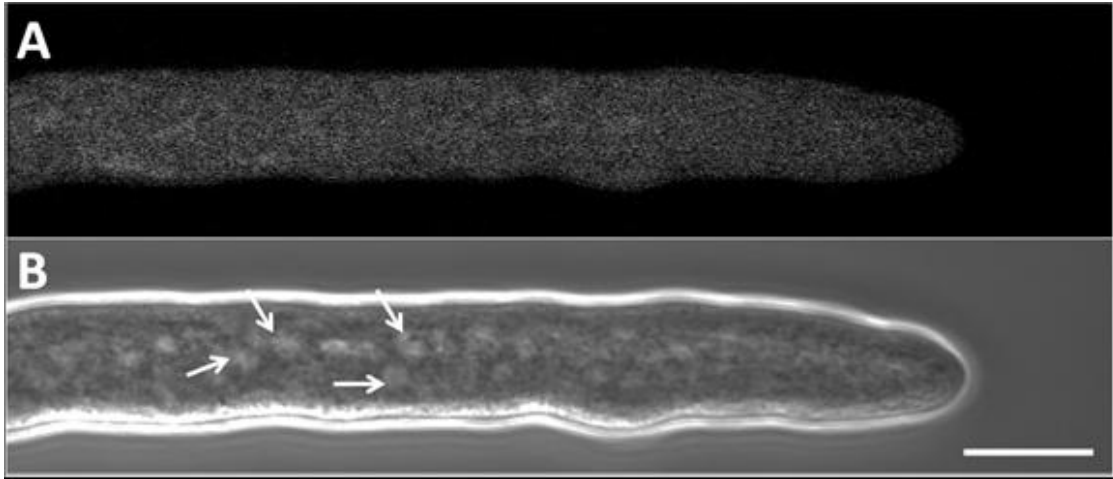


Figure 2.13: Control showing the expression of mCh alone driven by the *ccg-2* promoter in individual hyphae of *N. crassa*, strain MFNC9. A) Fluorescence channel, image taken at CT4. B) Phase contrast channel. Note that fluorescence is evenly distributed throughout the cytoplasm; there is no indication of accumulation in nuclei. Arrows indicate some nuclei. Scale bar = 10 μ m

strong promoter, reduces the *Neurospora* clock period by six hours.

Similar to the period effects observed driving FRQ-mCh with the *ccg-2* promoter, using the native *frq* promoter at an ectopic location to drive production also resulted in a shortening of the clock period. However, when mCh was fused to the resident *frq* promoter in strain MFNC30, one could see a two-hour lengthening of the period. The period difference observed between strains MFNC22 and MFNC30 may be due to the two copies of the *frq* gene present in the former (native and FRQ-mCh integrated ectopically). The similarity in periods between MFNC30 and the *bd* control strain indicates that the FRQ-mCh fusion protein was generally capable of replacing the normal FRQ protein in terms of clock function under these conditions. This can be viewed as a validation of our approach of employing the mCh protein as a useful reporter.

2.4 Discussion

One of the most ancient forms of biological regulation is the circadian rhythmicity found in almost all groups of organisms. The fungus *Neurospora crassa* has been used as a model organism to investigate the components of the circadian clock that regulate molecular, physiological and behavioral activities (Dunlap, 2006). Several properties of *Neurospora*, such as a straightforward handling in the laboratory, an easily-observable macroscopic rhythm (banding pattern) and the availability of the complete genome sequence, make this organism an ideal one for clock research (Bell-Pedersen et al., 2001a). To improve the understanding of how the clock operates in this organism we have created tools that have already proven useful for monitoring the dynamics of the *frq* gene under physiological conditions. The *frq* gene is one of the most important genes involved in the circadian rhythm of *N. crassa*, and consequently it has been intensely studied as one of the central components of the circadian negative feedback loop (Dunlap, 1999). The *frq* gene encodes central components of the circadian oscillator, the *frq* mRNA and two forms of the FRQ protein (Garceau et al., 1997; Liu et al., 1997; Dunlap, 1996; Loros, 1995; Dunlap, 1993). Each form of the FRQ protein enters the nucleus soon after its synthesis in the early subjective day and depresses the levels of its own transcript (Luo et al., 1998).

To elucidate the molecular details of the *frq* gene's dynamics in *Neurospora* a mycelial disk liquid culture has been extensively used (Nakashima, 1981). However some researchers have questioned the relevance this system has to understanding how the rhythm operates in an aerial environment, which is presumably the most similar to natural conditions. Now, by the use of a fluorescent fusion protein, we were able to follow clock gene dynamics while the culture is growing on the surface of agar media. While others have used luminescent proteins to follow the circadian rhythmicity in *N. crassa*, these tools are limited to monitoring the cycle at a macroscopic level (Gooch et al., 2008; Morgan et al., 2003). Our tool, however, facilitates examination of rhythm components at the microscopic level, which allows us to gain insight into the intracellu-

lar transport dynamics of these proteins during the circadian cycle.

Specifically we used our first construct containing the *ccg-2* promoter driving the expression of the mCh protein to gain insight into both the spatial and temporal dynamics of this promoter's activity during the circadian cycle. The *Neurospora ccg-2* (*eas*) gene encodes a fungal hydrophobin (Bell-Pedersen et al., 1992; Lauter et al., 1992) that is transcriptionally regulated by the circadian clock and other developmental pathways (Bell-Pedersen et al., 2001b, 1996a,c). Transcripts of the *ccg-2* gene accumulate during the late night to early morning in liquid cultures (Bell-Pedersen et al., 1996c).

At least two independent pathways are involved in the regulation of *ccg-2*, one from the endogenous clock to control rhythmic expression and another through an asexual development pathway (Bell-Pedersen et al., 1996c). The circadian rhythm and development are therefore major activators of the *ccg-2* promoter, however it is also induced by several additional factors, such as light and carbon source availability (Bell-Pedersen et al., 1996a; Arpaia et al., 1993; Lauter et al., 1992). Previous reports stated that endogenous *ccg-2* message levels increase and reach maximum accumulation after 60 min of continuous light (Bell-Pedersen et al., 1996a). We also detected a high production of mCh from the *ccg-2* promoter after exposing cultures in the subjective night phase of the circadian rhythm (which normally has a low expression of *ccg-2* in vegetative hyphae) for one hour of continuous light (data not shown). Moreover the expression of the mCh protein driven by the *ccg-2* promoter was rhythmic, leading us to conclude that the control of the *ccg-2* gene's expression could be observed using the mCh fluorescence signal. In two developmental stages, aerial hyphae and conidia, there was a high expression of the mCh protein. While we cannot rule out transport of mCh from vegetative hyphae to the aerial hyphae and conidia using our microscopic results, previous reports on the *ccg-2* promoter make it highly likely that the *ccg-2* promoter is active in these regions (Castro-Longoria et al., 2007; Lauter et al., 1992). Since developmental regulation of the Pccg2-mCh construct was so clear we expect this will become a powerful tool to study the dynamics of conidiation and other developmental processes.

Once we determined that the mCh protein reporter functioned well in *N. crassa*,

we tagged the FRQ protein with mCh to follow its intracellular localization during the circadian cycle. The expression of the FRQ-mCh fusion protein under the control of the *ccg-2* promoter was detected in nuclei of vegetative hyphae at very low levels during most of the circadian cycle. However two peaks of fluorescence in the nuclei were observed at CT11 and CT19 indicating that the fusion protein was being translocated into the nucleus. Although the same rhythmic pattern of fluorescence was generally observed, some of the examined hyphae did not express any fluorescence at all. This could have been due to the fact that this strain had two copies of the *frq* gene (the native copy and the ectopic fusion copy), which possibly affected its typical behavior. Moreover since the ectopic copy was driven by the *ccg-2* promoter, which is a much stronger promoter than the native *frq* promoter, we were surprised to see a macroscopic conidiation rhythm at all given previously-published reports on the over expression of *frq* abolishing the circadian rhythm (Aronson et al., 1994). However this may be due to the fact that the *ccg-2* promoter is a clock-controlled promoter while the *qa-2* promoter used by (Aronson et al., 1994) was not.

When we compared the ectopic FRQ-mCh fusion (strain MFNC22) to our native FRQ-mCh fusion strain (MFNC30) we found that the macroscopic rhythm had a period of 24 h, closer to the typical 22 h of a wild-type strain, and that the banding pattern was very clear, at least for the first four days. While the signal was weaker than that observed using the *ccg-2* promoter driving the fusion protein (as expected due to the differences in promoter strengths) the nuclear localization of FRQ during the circadian cycle was similar to results previously obtained (Liu et al., 1997). The FRQ protein reached a maximum inside the nucleus at CT4 followed by a decrease through the rest of the cycle as previously reported (Liu et al., 1997). During the gradual decrease of nuclear FRQ that we observed, apparently another second smaller peak was detected at CT19. It has been suggested that the FRQ protein levels decrease after they are extensively phosphorylated, suggesting that phosphorylation of FRQ may lead to its degradation (He and Liu, 2005; He et al., 2003). Moreover recently the phosphorylation sites of FRQ have been shown influence its interactions with other components of the circadian

oscillator in a phase dependent manner (Baker et al., 2009). Quantitative analysis of the FRQ protein by nuclear extractions during the circadian cycle revealed that the protein FRQ, together with FRH [FREQUENCY (FRQ)-interacting RNA helicase], enters the nucleus soon after its synthesis to repress its own transcript and that nuclear localization is required for its proper function (Cheng et al., 2005; Froehlich et al., 2003; Cheng et al., 2001; Denault et al., 2001; Garceau et al., 1997; Liu et al., 1997; Aronson et al., 1994). The protein FRQ enters the nucleus since a nuclear localization signal (NLS) exists for the small and large forms of FRQ and this signal is necessary and sufficient to direct the FRQ protein into the nucleus (Luo et al., 1998). The apparent second nuclear entrance of FRQ during the subjective night is a novel result and several possible explanations can be listed: a) FRQ has a function outside the circadian feedback loops as previously suggested (Cheng et al., 2005); b) FRQ has a role in the regulation of conidiation, independent of its role in the circadian rhythm; c) FRQ enters in response to a signal from another oscillator, sort of a “cross-talk” with the FRQ-less oscillator; or d) the second entrance of FRQ may be the long form of FRQ, since these experiments were done at 28°C, where the long form of FRQ is at a higher level. Other explanations are possible, and at this time, there are no convincing data to distinguish these alternatives.

In addition to nuclear entrance we observed differential accumulation of FRQ-mCh in the cytoplasm as well. Similar to recently published reports we detected that the subcellular distribution of FRQ shifted from mainly nuclear to mainly cytosolic as recently found (Diernfellner et al., 2009). In our results we generally, detected an accumulation of cytoplasmic FRQ-mCh 150 m from the apices of leading hyphae. This accumulation of FRQ-mCh apparently was nearer the apices for several hours after CT17. By that time the FRQ-mCh expression levels in the subapical area of the cytoplasm were higher, compared with those observed during the first hours of the cycle. A possible explanation for this phenomenon could be that cytosolic FRQ behind the apices is entering the nucleus to inactivate the white collar complex (WCC) transcriptional activator. On the other hand, an accumulation of hyperphosphorylated cytosolic FRQ is required to support the WCC accumulation (Schafmeier et al., 2006). It has been reported that

while low levels of FRQ are required to drive efficient phosphorylation of WCC in the nucleus, a substantially higher concentration of FRQ is required to support accumulation and hyperphosphorylation of WCC in the cytosol (Schafmeier et al., 2008); these findings are consistent with our observations. It has been shown that these conflicting functions are confined to distinct subcellular compartments and coordinated in temporal fashion (Schafmeier et al., 2006) as seen in our experiments.

2.5 Acknowledgements

Chapter 2 contains material originally published as Castro-Longoria, E.*, Ferry, M.*, Bartnicki-Garcia, S., Hasty, J., and Brody, S., 2010: Circadian rhythms in *neurospora crassa*: dynamics of the clock component frequency visualized using a fluorescent reporter. *Fungal Genet Biol*, **47**(4), 332-341.(*equal contribution). Copyright permission to republish here was granted by Elsevier Limited.

Chapter 3

Microfluidics for synthetic biology: from design to execution

3.1 The design of a microfluidic chip

To design a microchemostat chip useful for the type of experiments described in the introduction, one has to know a small amount about fluid mechanics at the microscale. We will briefly describe the physics behind microfluidics here, but the reader is directed to more complete texts if desired (Beebe et al., 2002; Nguyen and Wereley, 2002; Whitesides et al., 2001a; Brody et al., 1996). Those that have not studied fluid mechanics in depth do not have to worry because making a functional microchemostat is not too difficult. The first thing to understand is how fluid flows at the microscale of a microfluidic device. From fluid mechanics we know that there are essentially two major flow regimes: laminar and turbulent flow. Laminar flows contain highly predictable, parallel flow streams resulting in fairly easy to model profiles. In contrast, turbulent flows are unpredictable, difficult to model computationally and contain complicated flow patterns such as eddies and vortices (there is also a transition regime between these two flow types). For microchemostat devices the flow will be exclusively laminar as explained below. However to determine the flow type in a arbitrary system, the most important pa-

parameters are the type of fluid used, the dimensions of the fluid channels and the fluid's velocity in these channels. The relationship between these parameters can be expressed as the Reynolds number (Re), which is a dimensionless quantity useful for determining the dominant profile in a flow system. The Reynolds number is defined by

$$Re = \frac{\rho v D_h}{\mu} \quad (3.1)$$

Where ρ is the density of the fluid, v is the mean fluid velocity, D_h is the hydraulic diameter of the channel (a value which depends on the channels dimensions, see (Nguyen and Wereley, 2002)) and μ is the fluid's viscosity (Beebe et al., 2002). The Reynold's number represents a ratio between the inertial forces and the viscous forces of a fluid's flow. Empirically it has been determined that flows with a high Reynold's number ($Re > 10^3$), indicating the dominance of inertial forces, will be turbulent while low Reynolds number flows ($Re < 1$) will be exclusively laminar (Brody et al., 1996). Typical parameter values for microchemostats with an aqueous fluid are given in Table 3.1. Due to the low Reynolds number in these chips flow is laminar.

Table 3.1: Typical physical parameter values for microchemostat devices used in synthetic biology.

parameter	variable	value	units
density of water	ρ	1×10^3	kg m^{-3}
viscosity of water (dynamic)	μ	1×10^{-3}	$\text{kg m}^{-1}\text{s}^{-1}$
hydraulic diameter	D_h	$1 \times 10^{-4} - 1 \times 10^{-6}$	m
mean fluid velocity	v	$1 \times 10^{-4} - 1 \times 10^{-6}$	m s^{-1}
Reynolds number	Re	$1 \times 10^{-2} - 1 \times 10^{-6}$	N/A

3.1.1 Mixing in microchemostat devices

A major consequence of laminar flow is that mixing will only occur due to diffusion, since bulk mixing relies on some type of turbulent flow. An important way to view the effect of diffusion in a microchemostat is to consider the diffusion length scale,

which describes the one dimensional distance a molecule can be expected to travel in a given amount of time. The relationship is given as (Beebe et al., 2002):

$$d^2 = 2Dt \quad (3.2)$$

where d is the distance a molecule travels, D is the molecule's diffusion coefficient and t is the elapsed time. Since the distance traveled by a molecule is proportional to the square root of the elapsed time, diffusion will become more important at smaller length scales. For a specific example consider the Atto 655 dye, expected to diffuse $10 \mu\text{m}$ in 0.1 seconds, but taking over 1000 seconds to diffuse 1 mm. Diffusion coefficients for representative molecules often encountered in microchemostats are given in Table 3.2.

Table 3.2: Diffusion coefficients for ions and molecules commonly used in microfluidic chemostats.

name	molecular weight (Da)	Diffusion coefficient ($\text{cm}^2 \text{s}^{-1}$)	reference
Sodium ion (Na^+)	22.98	1.3×10^{-5}	(Lide, 2004)
Glucose	180.16	6.7×10^{-6}	(Lide, 2004)
Atto 655 dye	528	4.3×10^{-6}	(Dertinger et al., 2007)
Bovine albumin	67,000	5.9×10^{-7}	(Young et al., 1980)

As expected the diffusion coefficient tends to increase with increasing molecular weight and this is important to compensate for when using a tracer dye to monitor nutrient transport. For example, as can be seen in Table 3.2, one should be careful using Atto 655 dye as a surrogate for bovine albumin transport, or any high molecular weight protein, due to their order of magnitude difference in diffusion coefficients. Another important concept regarding diffusive transport in microchemostats is the Péclet number, which is another dimensionless quantity given by:

$$Pe = \frac{vL}{D} \quad (3.3)$$

Where L is the characteristic length scale, which in a microchemostat corresponds to the channel width. The Péclet number represents a ratio between advection and diffusion of a substance. Conceptually it can be thought of as the ratio of how far “down-

stream” a molecule is carried versus how far it diffuses across the channel in a given unit of time. In microfluidic systems reliant on diffusive mixing, knowledge of the Péclet number is critical for designing functional microchemostats. To determine the length required (Δy_m) for effective diffusive mixing of a substance the following relationship is useful (Stroock et al., 2002):

$$\Delta y_m \approx \frac{vL^2}{D} \quad (3.4)$$

$$\Delta y_m \approx PeL \quad (3.5)$$

Thus, Eq. (3.4) indicates that for two channels with equivalent Péclet numbers, the narrower one will require a shorter length for complete mixing. This statement is important because often in the design of microchemostats one wishes to carefully manage the volumetric flow rate to ensure optimal reagent use. As derived in the next section, there is often a combination of parameter values for the dimensions of a channel which result in the same resistance (and hence the same volumetric flow rate for a given pressure gradient). Often many of these parameter values will result in the same Péclet numbers as well. For example, two channels, one with a two fold greater width and a two fold smaller length will have the same resistance and equivalent Péclet numbers. However the length required for diffusive mixing will differ as described by Eq. (3.4) and this is important to consider in the design.

3.1.2 Calculating flow rates and pressure drops

While there has been some debate as to whether the general Navier-Stokes equation is applicable to the small scale of microfluidic devices, recent work has demonstrated that this is so and suggested that previously observed deviations were due to experimental error (Bao and Harrison, 2006). As a consequence of laminar flow in a microchemostat chip, the Navier-Stokes equations reduce to a simple analog of Ohm’s law. This equation is:

$$\Delta P = QR \quad (3.6)$$

where ΔP is the pressure drop across a channel, Q is the volumetric flow rate and R is the resistance of the channel. This allows the simple calculation of flow rate in a chip as a function of external pressure and channel resistance. To calculate R the dimensions of the channel have to be considered. For cylindrical channels the resistance is given by the Hagen-Poiseuille equation, equal to:

$$R = \frac{8\mu L}{\pi r^4} \quad (3.7)$$

where μ is the fluids viscosity, L is the length of the channel and r is the radius of the channel. For the rectangular channels usually encountered in microchemostats, this equation has to be modified somewhat, taking into consideration the ratio between the width of the channel and the height, known as the aspect ratio. For channels with a low aspect ratio ($w \approx h$) the equation for channel resistance is given by (Beebe et al., 2002):

$$R = \frac{12\mu L}{wh^3} \left[1 - \frac{h}{w} \left(\frac{192}{\pi^5} \sum_{n=1,3,5}^{\infty} \frac{1}{n^5} \tanh\left(\frac{n\pi w}{2h}\right) \right) \right]^{-1} \quad (3.8)$$

while Eq. (3.8) appears complicated, in practice it is not too difficult to work with if desired. Note the $\frac{1}{n^5}$ term in the infinite sum. Since this term quickly approaches zero for increasing n , only the first 5 terms need to be considered to get a reasonable approximation. However, this equation can be further reduced when using a chip with high aspect ratio channels ($w \gg h$). Usually this is the case, as typical channel heights in a yeast or *E. coli* chip will be in the range of 5-10 μm while the width will range from 60-300 μm . In this situation the bracket term in Eq. (3.8) will tend to zero and the resistance simply becomes:

$$R = \frac{12\mu L}{wh^3} \quad (3.9)$$

Using Eqs. (3.6) and (3.9) the flow rates in a microfluidic chip can be solved for in a straightforward manner, using methods similar to nodal analysis for electrical

circuits. First consider a sample microfluidic chip depicted in Figure 3.1A-B, which is shown diagrammatically in stick form to make analysis easier. For each internal node labeled a-d in the figure, the flow entering must equal the flow exiting due to the conservation of mass. This is analogous to Kirchoff's first law for electrical circuits. Thus for all nodes in the device:

$$\sum_{k=1}^n Q_k = 0 \quad (3.10)$$

where n is the number of channels joining at the node. Furthermore, note that the system will be solved once the internal pressures at the nodes are determined, since the flow rates between nodes can be found from Eq. (3.6). We will use the system described in Figure 3.1 as an example to demonstrate how to solve such a problem. The first step would be to come up with a diagram similar to Figure 3.1A, with the external ports and internal nodes clearly labeled.

Next label the current flow directions with arrows between nodes as shown in Figure 3.1B, while making sure to obey the conservation of mass. Note that you may not know the direction of flow beforehand (in fact that may be why you are doing this exercise), however this does not matter initially. As long as the conservation of mass is followed the system can be solved properly. If your initial flow direction guess is incorrect, its solution will be negative, indicating the opposite is the true direction of flow. After this step is complete, develop a system of equations describing the flow in each node. For the example system:

$$Q_1 = Q_5 \quad Q_2 = Q_6 \quad (3.11a)$$

$$Q_7 = Q_5 + Q_6 \quad Q_3 = Q_7 + Q_4 \quad (3.11b)$$

Next use Eq. (3.6) to substitute the pressure and resistance for the current:

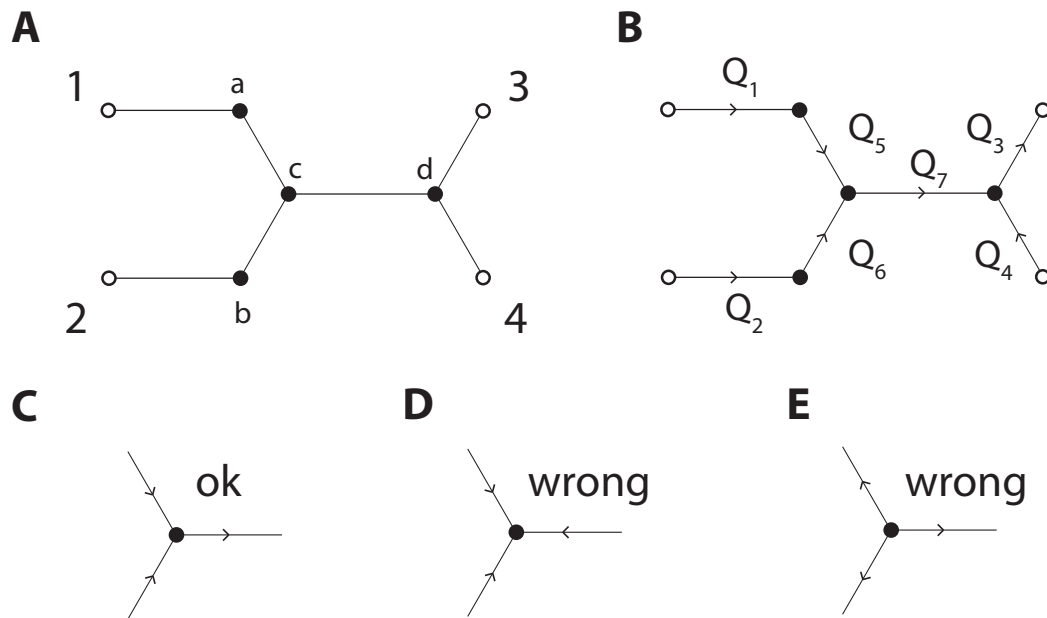


Figure 3.1: Overview of how to conceptually setup microfluidic flow problems. **A.** Stick diagram of a conceptual microfluidic device. External ports with specified pressures (open circles) are labeled 1-4. Internal junctions (whose pressures will be solved for, closed circles) are labeled a-d. **B.** Same diagram as in part A, except the port and junction numbers are removed for clarity. Volumetric flows to be solved for are given by Q_{1-7} . **C-E.** Overview of the correct way to setup flow directions in a microfluidic junction, while obeying the conservation of mass. Part C has the correct setup, containing both inlets and an outlet. Part D is incorrect since there are only inlets. Part E is also incorrect since there are only outlets.

$$\frac{P_1 - P_a}{R_1} = \frac{P_a - P_c}{R_5} \quad \frac{P_2 - P_b}{R_2} = \frac{P_b - P_c}{R_6} \quad (3.12)$$

$$\frac{P_c - P_d}{R_7} = \frac{P_a - P_c}{R_5} + \frac{P_b - P_c}{R_6} \quad \frac{P_d - P_3}{R_3} = \frac{P_c - P_d}{R_7} + \frac{P_4 - P_d}{R_4} \quad (3.13)$$

Since Eqs. (3.12)-(3.13) contain cumbersome fractions, it is useful to define the conductance G as the inverse of the resistance R :

$$G = \frac{1}{R} \quad (3.14)$$

By substituting the conductance for the resistance in Eqs. (3.12)-(3.13) we get the following:

$$G_1(P_1 - P_a) = G_5(P_a - P_c) \quad (3.15)$$

$$G_2(P_2 - P_b) = G_6(P_b - P_c) \quad (3.16)$$

$$G_7(P_c - P_d) = G_5(P_a - P_c) + G_6(P_b - P_c) \quad (3.17)$$

$$G_3(P_d - P_3) = G_7(P_c - P_d) + G_4(P_4 - P_d) \quad (3.18)$$

Expanding and rearranging we get:

$$G_1P_1 = (G_1 + G_5)P_a - G_5P_c \quad (3.19)$$

$$G_2P_2 = (G_2 + G_6)P_b - G_6P_c \quad (3.20)$$

$$0 = G_5P_a + G_6P_b - (G_5 + G_6 + G_7)P_c + G_7P_d \quad (3.21)$$

$$-G_3P_3 - G_4P_4 = G_7P_c - (G_3 + G_4 + G_7)P_d \quad (3.22)$$

Or in matrix form:

$$\begin{bmatrix} G_1P_1 \\ G_2P_2 \\ 0 \\ -G_3P_3 - G_4P_4 \end{bmatrix} = \begin{bmatrix} G_1 + G_5 & 0 & -G_5 & 0 \\ 0 & G_2 + G_6 & -G_6 & 0 \\ G_5 & G_6 & G_5 + G_6 + G_7 & G_7 \\ 0 & 0 & G_7 & G_3 + G_4 + G_7 \end{bmatrix} \begin{bmatrix} P_a \\ P_b \\ P_c \\ P_d \end{bmatrix} \quad (3.23)$$

Where:

$$G_{567} = -G_5 - G_6 - G_7 \quad (3.24)$$

$$G_{347} = -G_3 - G_4 - G_7 \quad (3.25)$$

Equation (3.23) is a linear system which can be either solved manually or with the aid of a computer program such as Excel or Matlab. Of course the above procedure can become tedious, especially for larger microchemostat chips and a method which lends itself to automation would be preferred. To develop such a system first rearrange Eqs. (3.11) to put all currents on the LHS:

$$Q_1 - Q_5 = 0 \quad Q_2 - Q_6 = 0 \quad (3.26a)$$

$$-Q_5 - Q_6 + Q_7 = 0 \quad Q_3 - Q_4 - Q_7 = 0 \quad (3.26b)$$

Now arrange Eqs. (3.26) into matrix form:

$$\begin{bmatrix} 0 \\ 0 \\ 0 \\ 0 \end{bmatrix} = \begin{bmatrix} 1 & 0 & 0 & 0 & -1 & 0 & 0 \\ 0 & 1 & 0 & 0 & 0 & -1 & 0 \\ 0 & 0 & 0 & 0 & -1 & -1 & 1 \\ 0 & 0 & 1 & -1 & 0 & 0 & -1 \end{bmatrix} \begin{bmatrix} Q_1 \\ Q_2 \\ \vdots \\ Q_7 \end{bmatrix} \quad (3.27)$$

which can be expressed as

$$0 = C\vec{q} \quad (3.28)$$

where C is an $i \times j$ matrix called the connectivity matrix for a chip with i nodes and j channels. The C matrix is unique for each chip and should be specified from a graph of the chips architecture. The \vec{q} is a vector of length j representing the flows in the chip. Since \vec{q} is unknown we need to use Eqs. (3.6) and (3.14) to substitute flows for pressures and conductivities:

$$\begin{bmatrix} Q_1 \\ Q_2 \\ Q_3 \\ Q_4 \\ Q_5 \\ Q_6 \\ Q_7 \end{bmatrix} = \begin{bmatrix} G_1(P_1 - P_a) \\ G_2(P_2 - P_b) \\ G_3(P_d - P_3) \\ G_4(P_4 - P_d) \\ G_5(P_a - P_c) \\ G_6(P_b - P_c) \\ G_7(P_c - P_d) \end{bmatrix} = \begin{bmatrix} G_1P_1 \\ G_2P_2 \\ -G_3P_3 \\ G_4P_4 \\ 0 \\ 0 \\ 0 \end{bmatrix} + \begin{bmatrix} -G_1P_a \\ -G_2P_b \\ G_3P_d \\ -G_4P_d \\ G_5P_a - G_5P_c \\ G_6P_b - G_6P_c \\ G_7P_c - G_7P_d \end{bmatrix} \quad (3.29)$$

Thus the flow vector can be split into two vectors as shown in the RHS of Eq. (3.29). The first vector contains only known values, being the external pressures and conductances of the channels connected to these ports. The second vector contains known conductances and the unknown internal node pressures which we are interested in solving for. Separating the conductances from the pressures we get:

$$\vec{q} = \begin{bmatrix} G_1 & 0 & 0 & 0 \\ 0 & G_2 & 0 & 0 \\ 0 & 0 & -G_3 & 0 \\ 0 & 0 & 0 & G_4 \\ 0 & 0 & 0 & 0 \\ 0 & 0 & 0 & 0 \\ 0 & 0 & 0 & 0 \end{bmatrix} \begin{bmatrix} P_1 \\ P_2 \\ P_3 \\ P_4 \end{bmatrix} + \begin{bmatrix} -G_1 & 0 & 0 & 0 \\ 0 & -G_2 & 0 & 0 \\ 0 & 0 & 0 & G_3 \\ 0 & 0 & 0 & -G_4 \\ G_5 & 0 & -G_5 & 0 \\ 0 & G_6 & -G_6 & 0 \\ 0 & 0 & G_7 & -G_7 \end{bmatrix} \begin{bmatrix} P_a \\ P_b \\ P_c \\ P_d \end{bmatrix} \quad (3.30)$$

or:

$$\vec{q} = G\vec{s} + H\vec{p} \quad (3.31)$$

where G is a $j \times k$ matrix of j channels and k external ports containing conductance values, \vec{s} is a k length vector specifying the known external port pressures, H is a $j \times l$ matrix of j channels and l internal nodes containing conductance values and \vec{p} is a l length vector containing the unknown internal port pressures. Combining Eqs. (3.28) and (3.31) we get:

$$0 = C(G\vec{s} + H\vec{p}) \quad (3.32)$$

$$-CG\vec{s} = CH\vec{p} \quad (3.33)$$

$$\vec{t} = I\vec{p} \quad (3.34)$$

where $\vec{t} = -CG\vec{s}$ and $I = CH$. Note that Eq. (3.34) is the same as Eq. (3.23) and can be solved in the same ways. To solve the flow profiles for an arbitrary chip, the C, G and H matrices need to be specified, which can be done once the connectivity and channel geometries are decided upon. To automate this process our lab uses a custom matlab script, written by a former graduate student, called moca. This program has been extended to calculate how the pressure in each external port changes in time as fluid flows from the inlet ports to the outlets.

Alternatives to nodal analysis are commercial software package employing finite element techniques to solve for the flows in a more exact manner. An example of such a software package is the program Comsol, which contains an internal software package explicitly setup to solve microfluidics problems. For the design of microchemostats, this level of computation can be helpful for certain parts of the chip. For example, Comsol, unlike nodal analysis techniques, can model the diffusive transport of nutrients in complicated geometries such as cell traps or junctions. Moreover transient behavior of the chip, including how a cell chamber will respond to pressure surges, can be easily modeled in Comsol but not using nodal analysis techniques. As an additional advantage, Comsol has the ability to create models directly from Autocad files, which can save a considerable amount of time. However software programs such as Comsol are quite expensive and nodal analysis techniques are generally fine for designing basic microchemostats.

3.1.3 Designing a microchemostat chip

To design a microchemostat device one has to know a little about the overall fabrication process. The complete details will be described in the fabrication section, but we will give a brief description here. The general process is known as soft-photolithography, originally developed for the semiconductor industry. When used for microchemostats, soft-photolithography creates reusable master molds with chemicals known as photoresists. Photoresists are viscous chemicals spun on silicon wafers to very precise heights. When exposed to ultraviolet (UV) light, the photoresist crosslinks and becomes resistant to developer solvent, while the uncrosslinked photoresist remains susceptible. To make a microchemostat, a negative image of the device's features is placed between the photoresist and the UV light source. An example of such a mask is shown in Figure 3.2. When exposed, the UV light will pass through the clear sections containing the device's features, while the dark regions will prevent the background from being crosslinked. After the uncrosslinked photoresist is removed with developer, the process is repeated for the next layer. To align multiple layers, an aptly named mask aligner machine is used. This machine contains a microscopy setup so alignment patterns between the previous photoresist layer and the current mask can be viewed. Once all layers have been completed the wafer can be used to produce an almost unlimited amount of microchemostat devices.

When designing a device, the first step is to layout the architecture in a vector graphics software program such as Autocad. While it is possible to use other programs, such as Adobe Illustrator, in general Autocad is superior since it is designed for precision fabrication. Furthermore companies offering extremely high resolution mask printing generally require Autocad files. Student versions of Autocad are reasonably priced and offer more capability than is necessary for designing microchemostats. During the design stage, one needs to decide how many different channel heights will be in the device. For example the cell trap might be $3.5 \mu\text{m}$ while the channel network is $10 \mu\text{m}$, as is often the case for yeast chips. All features with the same height should be on

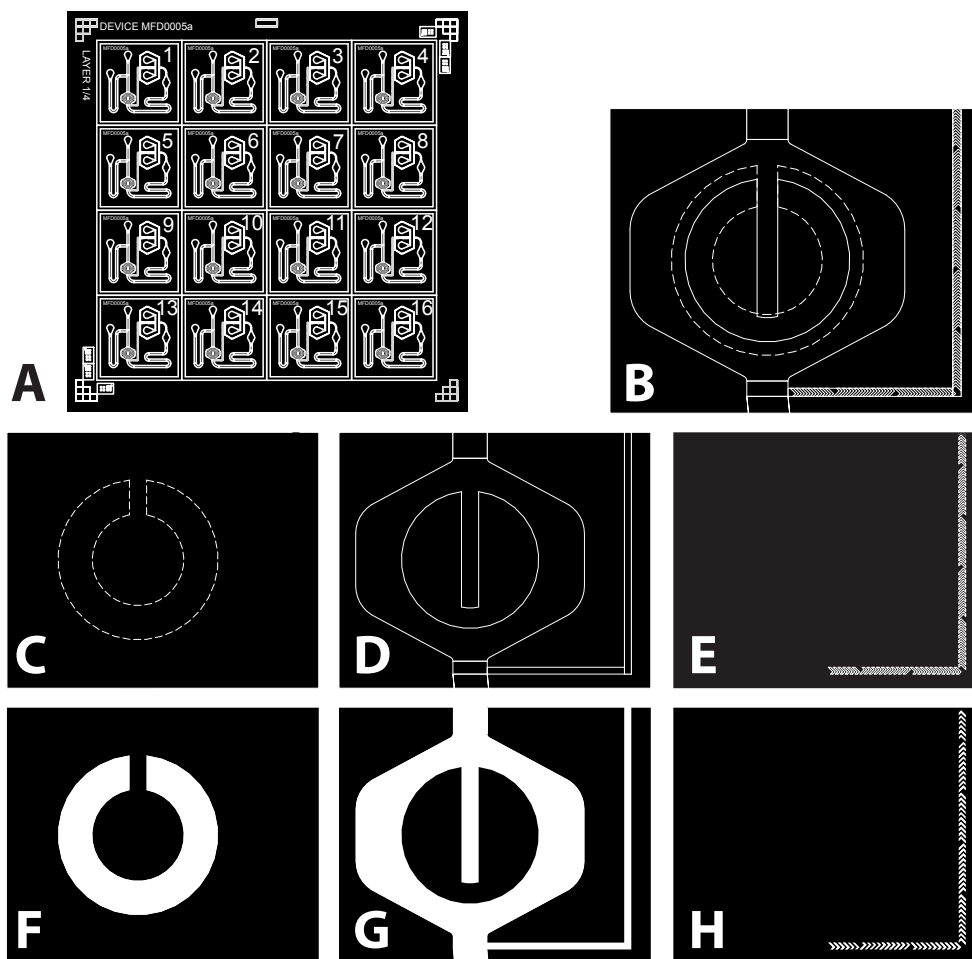


Figure 3.2: Overview of the mask design process for microchemostat devices. **A.** Overview of an Autocad file with the features of the microchemostat shown in white. Note the alignment features in the lower left and upper right corners. Each chip is individually numbered so those defective can be tracked. **B.** Close up of the cell trap region from the Autocad file shown in part A. This region contains features of three different heights, which are in different layers of the Autocad file. The cell trap will be of height $3.5 \mu\text{m}$ and is shown with dashed lines. The central chamber will be $10 \mu\text{m}$ and is shown with solid lines. The staggered herringbone mixers (SHM) will be of height $3 \mu\text{m}$ above the $10 \mu\text{m}$ mixer channel height for a total of $13 \mu\text{m}$. Note the overlap between layers. When layers meet there should always be an overlap to compensate for small errors in mask alignment. **C-E.** Each layer from part B is shown individually, with the cell trap in part C, the cell chamber in part D and the SHM features in part E. When sent for printing the layers should be displayed individually as is shown here. **F-H.** Depiction of what the mask will look like after printing. The features of the device will be clear (white in the figure) to allow UV light to pass, while the background is black.

the same layer in the Autocad file to make work easier (see Figure 3.2).

When designing a chip with multiple layers, care must be taken to provide an accurate method for alignment during fabrication. During the alignment process one will need to look through the mask at the pattern from a previous layer and adjust the controls so the current mask will perfectly overlap. As shown in Figure 3.3 there are three degrees of freedom which need to be manipulated during the alignment process: xy translation and rotation. To make sure the wafer and mask are in perfect alignment, two locations must be viewed on the wafer to compensate for small errors in rotation. The center of the mask essentially determines the axis of rotation. The further away the two locations are from the center (and each other), the easier small errors in rotation will be to see.

In Figure 3.2A the alignment locations are in the lower left corner and upper right corner of the mask, the furthest possible from the center. The alignment features shown in Figure 3.3 are designed to have coarse and fine features to speed the alignment process and work quite well in practice. To align the patterns, one adjusts the mask aligner controls until the points of the squares meet in all locations. Note that a separate alignment pattern will be necessary for each layer other than the first, since the mask's viewing window will cross link the photoresist (and therefore remove the wafer's alignment pattern for the layer) after each alignment and exposure.

When considering a device design and alignment pattern, it is critical that the thinner layers are fabricated before the thicker ones. For example a $3.5\ \mu\text{m}$ layer should always be fabricated before a $10\ \mu\text{m}$ layer. We have found that if thicker layers are fabricated first, the later layers will spin unevenly, since the larger features from the previous layer prevent an even coating of the wafer. Furthermore, it is important not to increase the height too greatly between consecutive layers, since this limits the contrast in the mask alignment process. Recall that mask alignment occurs after spinning the current (uncrosslinked) photoresist layer, which covers all previous (crosslinked) photoresist layers. Fortunately, the wafer's alignment pattern on the previously crosslinked photoresist layer can usually be seen through the current layer. However if the height

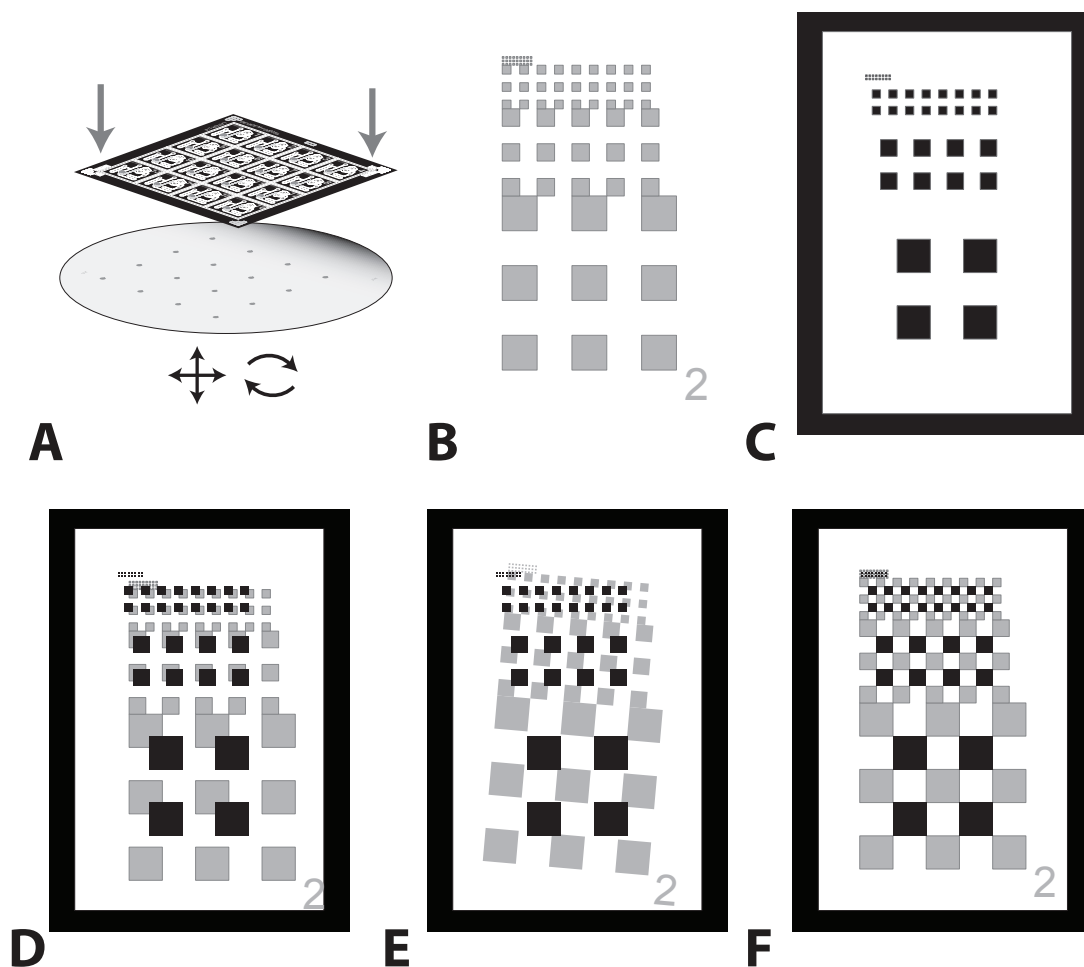


Figure 3.3: Overview of the an alignment pattern for microchemostat devices. **A.** Overview of the alignment process, with a mask shown above a wafer containing a previously deposited photoresist layer with alignment patterns. The mask aligner will have controls to compensate for both translation and rotation (bottom arrows). The arrows pointing down on the mask show the alignment pattern location. **B.** Alignment pattern present on the wafer from the previous photoresist deposition. Each layer will require a separate alignment pattern; the layer number is shown in the lower right. The pattern is composed of sets of squares whose sides are reduced by half in each iteration. **C.** Alignment pattern present on the mask. The clear window surrounding the squares allows the fabricator to view the pattern from the previous layer. The objective is to make the points of the squares from the mask and the previous layer touch. **D** Mask and wafer out of alignment by xy translation only. **E** Mask and wafer out of alignment by rotation only. **F.** Mask and wafer in perfect alignment.

ratio between the two layers is greater than about 5:1, the contrast becomes so poor that it is difficult to see the wafer's alignment pattern. In general we try and limit the height ratio to 3:1, since mask alignment is generally the most difficult and frustrating part of fabrication.

Once the alignment strategy is settled upon, the device features can be laid out in Autocad. For this purpose simple rectangles are usually sufficient, but arc segments can be used if more complex shapes are desired. We have found that curved sections are superior for cell containing channels, since they prevent clogging. For areas of the chip not expected to contain cells, rectangular segments meeting at sharp corners are fine. When designing channels, all features should be closed objects in Autocad, there should be no open segments. While resulting in lines across channels, these will not be printed since lines are considered to be of infinitesimal thickness by the printer and only closed regions are recognized (compare Figure 3.2D and G). Ensuring that all regions are closed in Autocad will not only make printing easier, but also facilitates importing into Comsol and Illustrator.

In general when laying out features, one must consider the tradeoff between compacting the device into as small a space as possible and maintaining usability. For example, placing two ports closer than 2 mm is not advisable since it makes it extremely difficult to plug in the port lines upon setup. Furthermore having a channel pass closer than a 1 mm to a port should also be avoided since it can be damaged if the port hole is punched incorrectly. Along these same lines, there should be at least 1 mm between a feature and the edge of the chip, so when the PDMS slab is diced into individual units no features are damaged.

In addition, when two layers are contiguous there should be some overlap between them to compensate for the small errors in alignment that inevitably occur. For example, in Figure 3.2B the cell trap layer overlaps the cell chamber layer. If the layers were designed with no overlap a small alignment error could create a gap between them resulting in a non-functional chip. Even with the alignment patterns described in Figure 3.3 and a meticulous alignment procedure, small errors will occur and can be compen-

sated for with layer overlap. When layers overlap the total height is usually a smooth transition between the height of the thicker layer alone and the sum of the heights of the overlapping layers. As shown in Figure 3.2B the cell chamber wall starts out at $10\ \mu\text{m}$ and gradually increases to $\sim 14\ \mu\text{m}$ in the overlapping area. This phenomenon should be remembered when modeling the flow profile of a device in Comsol for example, since a $\sim 40\%$ change in height due to overlap will have a large effect on the channel's resistance.

Another common mistake results from layers unintentionally intersecting due to small alignment errors. This can create fluidic “short circuits” and non-functional chips. The solution here is to again make sure an adequate margin is present between non-intersecting layers to compensate for fabrication problems. Most importantly, keep in mind the concept of tolerances. While the feeling for this comes from experience, always assume that some fabrication error is inevitable rather than trying to come up with the most beautiful design in Autocad. The best design will be one that can tolerate some fabrication error and still work properly, even if it is not the most “compact” design. The size of the channels is also affected by these same concepts. We have found that channel widths smaller than $60\ \mu\text{m}$ should be avoided since they are prone to clogging with debris that can enter the chip (often residual PDMS). Moreover long channels should generally be $10\ \mu\text{m}$ or more in height, also to prevent clogging.

Of course the ultimate limitation for microfluidic design is the resolution of the printer making your masks. This limit usually comes into play before that imposed by the UV light source or the photoresist. We use a company named CAD/Art for mask printing which has a 20,000 dpi printer. While this is normally adequate for microchemostats, higher resolution options used in the semiconductor industry are available at far greater expense. Using this process, we have been able to make features separated by as little as $13\ \mu\text{m}$ *as long as they are on the same layer*. However even this is dependent on the type of photoresist used. For example the spatial resolution of a thinner photoresist, like that used to make a $10\ \mu\text{m}$ layer, is generally greater than that of a thicker resist, used for making a $35\ \mu\text{m}$ layer. General guidelines for recommended

channel dimensions are given in Table 3.3. Note it is certainly fine to make channels having dimensions other than those given in the table and for specialized features (like high resistance cell feeding channels) this may be necessary. For the normal fluidic “backbone” of the chip, the channel dimensions listed in Table 3.3 should be fine.

Table 3.3: General guidelines for channel dimensions in microchemostat chips.

Channel type	organism	width range	height range
General flow network (no cells)	any	60-100 μm	10-15 μm
High flow channel (no cells)	any	300-400 μm	20-45 μm
General cell channels	<i>E. coli</i>	150-300 μm	6-15 μm
	yeast	200-300 μm	10-15 μm
	mammalian	200-300 μm	25-35 μm
Cell trap	<i>E. coli</i>	varies	1 μm
	yeast	varies	3.55 μm
	mammalian	varies	25 μm

While the general guidelines listed so far should be useful for creating a microchemostat device, as a case study we will describe our design process for an updated dial-a-wave chip. The device, called MFD005_a, was designed as an improved version of the chip described in (Bennett et al., 2008). The chip is designed to grow cells reliably in a monolayer and cope with high growth by flushing excess cells into a waste port. The chip is also designed to generate arbitrary, time varying inducer concentrations, so the cell’s response to a dynamic environment can be recorded. Often we use the chip to generate arbitrary waveforms, such as sine waves, square waves, or waves having a random period component. The waves generated by the device have high temporal accuracy and the chip is easy to use. An overview of the device is shown in Figure 3.4. The chip has five external ports, which is a reduction from eight in the Bennett chip. Reducing ports saves on consumables and eases setup, so finding the minimum number necessary to produce a working chip should always be a design goal. The chip is designed to use hydrostatic pressure and therefore no pumps are required of any kind for operation. We have found that hydrostatic pressure gives the most reliable, steady and cost effective means of controlling the pressures in a microchemostat device. In a later

section we will describe our use of linear actuators to alter the inlet hydrostatic pressure of our device and why this is advantageous compared to other means such as syringe pumps.

The role of each port of the MFD005_a chip is given in Figure 3.4. When an experiment is running, fluid will enter from ports 1 and 2 which meet at the dial-a-wave junction (Figure 3.4B). The DAW junction has two inlets and three outlets. As described in a later section the ratio of the inputs from port 1 and 2 leaving the junction to the cell chamber is determined by each ports pressure. Excess fluid is diverted through a shunt network to port 3, which is a waste port. Fluid leaving the central fork of the junction for the cell chamber travels through a long channel where it is mixed into a uniform concentration by staggered herringbone mixers (SHM). The ingenious SHM mixers (as shown in Figure 3.4C) are designed to induce a corkscrew effect in the fluid stream and increases the surface area available for mixing (Williams et al., 2008; Stroock et al., 2002). Since mixing only occurs due to diffusion in a microchemostat, as mentioned in section 3.1.1, this increase in surface area will logarithmically reduce the length of a channel necessary for uniform mixing.

Table 3.4: Role and pressures for each port in the MFD005_a device. All pressures are given in inH₂O above the height of the microscope stage

Port	Description	Contents	Run inH ₂ O	Load inH ₂ O
1	Inlet 1 for DAW	Media + inducer + tracking dye	25	25
2	Inlet 2 for DAW	Media	25	25
3	Cell and shunt waste	dH ₂ O	5.5	5.5
4	Alternate outlet	dH ₂ O	6	17
5	Cell port	Media + cells	6	18

Even with the help of SHM features, mixing still requires a length which depends on the log of the Péclet number (Stroock et al., 2002). Thus a central question when designing our device was how long to make the mixing channel from the DAW junction to the cell port. If the channel were too short, the two inputs would not be completely mixed, resulting in a non-uniform and uneven concentration profile over the cell culture. However making the channel too long is also disadvantageous since it increases the

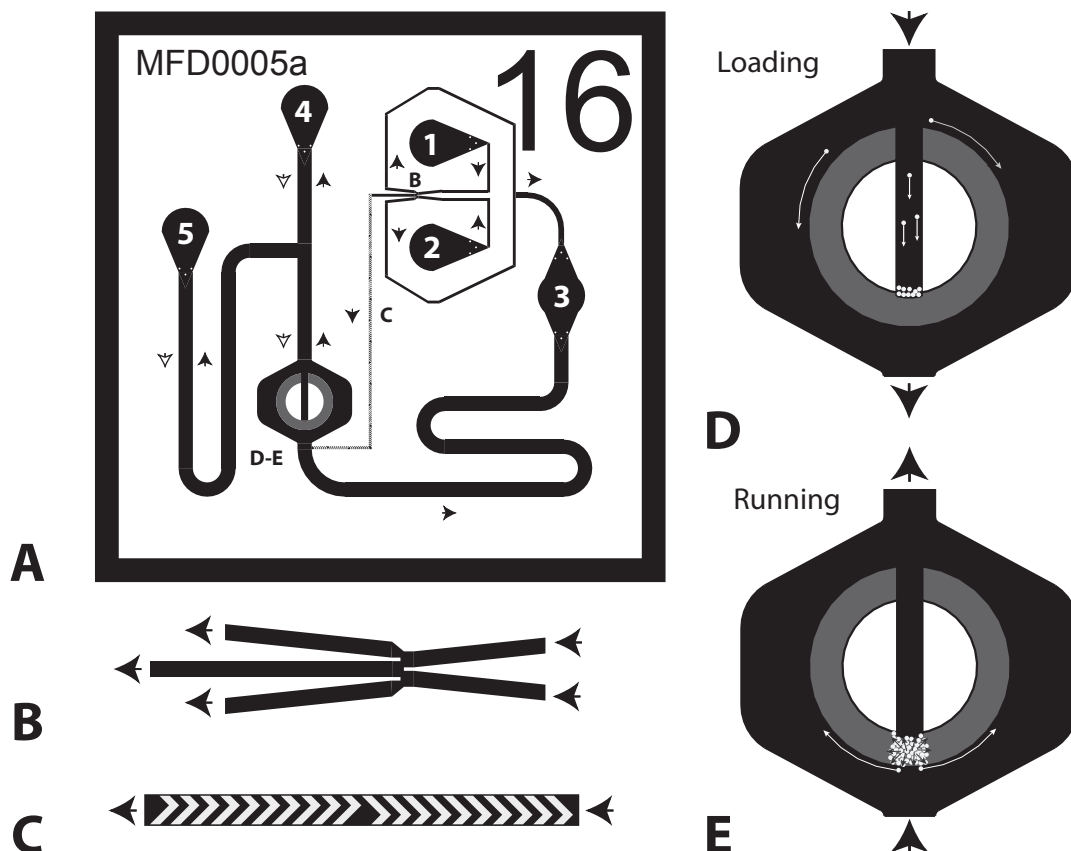


Figure 3.4: Overview of the MFD005_a chip and components. **A.** MFD005_a architecture. Flow directions in each segment during running conditions are given by black arrows, during loading conditions by white arrows. Note that only flow from ports 4, 5 and across the cell chamber changes direction during loading. Letters represent locations of the features described in other parts of the figure. External ports are numbered 1-5. Each port is described in Table 3.4. **B.** Depiction of the DAW junction. Flow direction is indicated by the black arrows. The two inlets on the right come from ports 1 and 2. The flow from the inlets converges in a ratio dependent on the inlet pressures of each. The middle fork of the junction leads to the cell chamber while the two outer forks lead to port 3, the cell and shunt waste port. **C.** Depiction of the staggered herringbone mixers (SHM), which reduce the channel length required for mixing. These mixers immediately follow the DAW junction and continue until just before the cell chamber. **D.** Overview of trap region of the MFD005_a chip under loading conditions. Black region represents the cell chamber with a height of 10 μm . Gray region is the actual cell trap, with a height of 3.525 μm . White circles represent cells entering from the cell port and either passing around the trap to the cell and shunt waste (port 3), or entering the central channel and moving to the trap entry barrier. **E.** Cell trap upon running of an experiment. Cells begin to grow in the trap and the colony expands (black arrows). Eventually the colony fills up the gray region near where they were loaded. The growth of the cells will force some out of the trap into the outer channel where they will be efficiently carried away to the waste port (white arrows).

delay time for a signal to propagate the length of the channel. To find the optimum channel length we require knowledge of the flow velocities as a function of the external port pressures. This is a good example of the usefulness of the modeling techniques mentioned in section 3.1.2. Using nodal analysis or Comsol it is easy to determine the flow rates and hence the Péclet number for various substances and flow regimes. We performed just such an analysis when designing the MFD005_a device to determine the necessary channel length for efficient mixing, shown in Figure 3.5.

After mixing, fluid from ports 1 and 2 enters the cell chamber and proceeds to the outlet ports 4 and 5. Fluid also enters a diversion channel and exits at port 3. By controlling the height of port 3 relative to ports 4 and 5, one can set the ratio of fluid passing through the chamber versus exiting through the diversion channel. Modulation of this diversion ratio is important for controlling the flow velocity across the cell chamber. For example, say you wanted to minimize the flow velocity in the cell chamber while still retaining functionality of the DAW junction. Without a diversion channel you could lower the height of the input ports 1 and 2 relative to 4 and 5 and reduce the flow velocity in the cell chamber. However this would also reduce the flow velocity in the mixing channel between the DAW junction and the cell chamber. This reduction in mixing channel velocity would increase the delay time for fluid transit and negatively impact the chips function. With a diversion channel, an alternative is to maintain the height difference between ports 1-2 and 4-5 and instead lower port 3. This would increase the ratio of fluid entering the diversion channel and hence lower the fluid velocity in the cell chamber. This is another example of flow modeling's usefulness, since the diversion channel's length is critical for determining the amount of fluid diverted for a given height change.

Modeling also allowed us to solve a problem with flow reversal (backflow) in the diversion channel, which would sometimes occur over the course of an experiment in a previous version of this device. The plot in Figure 3.5C represents a time dependent solution for the flow profile in the device's diversion channel, compensating for pressure changes due to fluid movement over the course of an experiment. The solid blue line

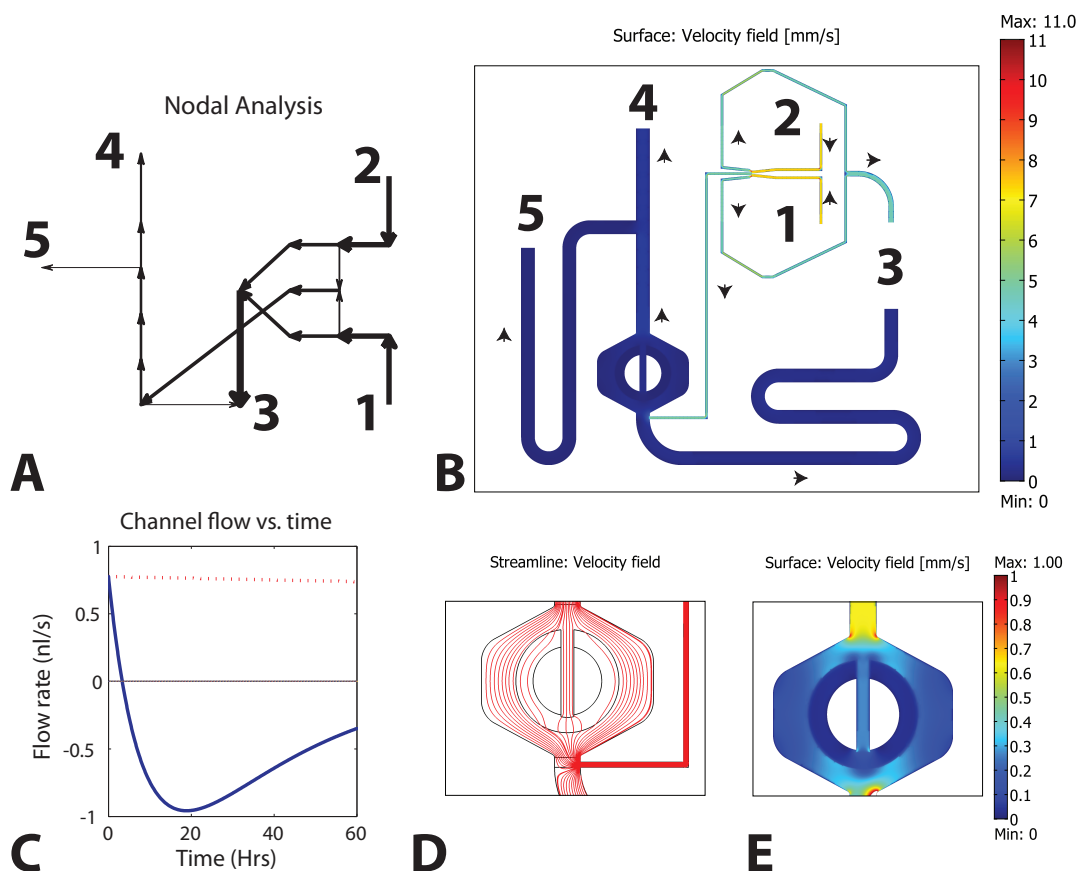


Figure 3.5: Comparison of a nodal analysis tool (moca) and Comsol (finite element analysis package). **A.** Graph from the moca Matlab script depicting flow in the Figure 3.4A device. Arrow size and direction represent the volumetric flow in the device's channels. Numbers are the device's external ports. **B.** Flow velocity through the device modeled using Comsol. The velocity's magnitude is given by the channel's color, while the black arrows indicate direction. Numbers are the external ports. The MFD005_a geometry was loaded directly from Autocad, simplifying setup. **C.** Flow direction in a channel section over the course of an experiment modeled using nodal analysis. This process helped solve backflow problems, resulting in a redesign of the diversion channel's dimensions. Blue line: fluid flow using 1 ml syringes. Red dashed line: 60 ml syringes. **D.** Streamlines showing the path of fluid particles in the cell trap. While this plot was generated for running conditions, the plot is very similar for loading conditions (although the flow direction is reversed). Note that only about one fourth of the flow enters the central channel, most flow is directed around the trap. Hence, when loading, most cells will not enter the trapping region. **E.** Plot of the velocity field inside the trap region. Note that the velocity is lowest inside the trap itself and considerably higher in the outer channel region. This allows nutrients to be continually replenished from the outer channel into the cell trap and helps remove cells once they outgrow the trap.

represents the flow rate when small diameter syringes are used for the outlets. The fluid level in these syringes increases in height rapidly for a given volumetric flow. Under certain conditions this height increase can be large enough to change the flow velocity in the chip. When the blue line crosses the zero point of the y axis, flow reversal has occurred. The red dashed line represents the same initial setup using larger diameter 60 ml syringes. These syringes undergo far less increase in height for a given volumetric flow than the smaller syringes and therefore it takes far longer (much longer than an experiment would last) to reach a flow reversal condition. The solution was reached by redesigning the diversion channel to have a greater resistance and by using larger syringes. While this model was created using nodal analysis, it could also be done in Comsol.

3.1.4 Design of an improved DAW junction

Another opportunity for flow modeling came from designing the DAW junction. As mentioned previously, this junction is designed to combine the inputs from ports 1 and 2 of the MFD005_a device in a precise ratio depending on the input pressures. By controlling the input pressures as a function of time, one can generate precise waves of inducer concentration and hence expose cells to a fluctuating environment. To set the mixing ratio, the pressure of one input is increased and the other decreased by the *same* amount. By changing the input pressures in an opposing manner, the flow rate out of the junction remains constant and hence the downstream flow rates are not altered (this can be easily demonstrated using nodal analysis). Of course, by the conservation of mass, if the total outlet flow does not change, then the total inlet flow must not change either. Instead the ratio between the two inlet flows changes.

Initially one might think that a simple T-junction would suffice to reliably mix the two inputs streams. Indeed, when the output is derived nearly equally from both inputs (near a 50% mixing ratio), a T-junction works fine. However, as depicted in Figure 3.6, a T-junction does not work well for skewed output ratios, when most of the

output is coming from only one of the inputs. As an example of a skewed ratio, consider when 95% of the output is coming from input 1 and the other 5% is coming from input 2, with a total flow rate of 1 nanoliter / sec (nl/s). Under these conditions the input 1 flow rate will be 0.95 nl/s, while the input 2 flow rate will be only 0.05 nl/s. Going further, for a mixing ratio of 100%, the input 1 flow rate will be 1 nl/s and the input 2 flow rate will be 0 nl/s. Of course in practice, even with the most accurate system, an entirely stagnant flow is impossible to achieve. In reality this situation represents an unstable equilibrium, prone to backflow. If attempting this with a real device, either a true 100% ratio will not be achieved, or (more likely) fluid from input 1 will begin to flow into input 2. This backflow situation will result in improper mixing of the input 2 source, preventing the system from functioning properly if later switched. For example, consider if backflow had occurred for one hour and then the system was switched, from a mixing ratio of 100% to 0%. In this situation, the residual flow from input 1 would have to flow back again before fresh input 2 media could again enter the junction. Depending on the residual flow rate from input 1 to 2, this could take a considerable amount of time.

To overcome this difficulty the chip in (Bennett et al., 2008) contained a shunt network designed to direct some fluid from each input to a waste port at all mixing ratios, in addition to the junction outlet. This system prevents backflow because the inlet flow rates never approach zero, even for skewed outlet ratios. A comparison of a T-junction to the DAW junction used in the MFD005_a device is shown in Figure 3.6. While the shunt network solved the backflow problem, the response of the junction to input pressures was somewhat different than expected. Ideally the output response of the DAW junction should be linear, but we had found significant deviations from linearity with the Bennett device. These deviations made experimental setups sometimes difficult. To investigate the cause of these deviations we turned to modeling in Comsol.

We determined that diffusive transport between the input streams could cause significant deviations from an ideal response. Diffusion *at the junction* leads to transport of nutrients destined for the output into the shunts, altering the expected response. This deviation was especially pronounced at skewed mixing ratios similar to what we had

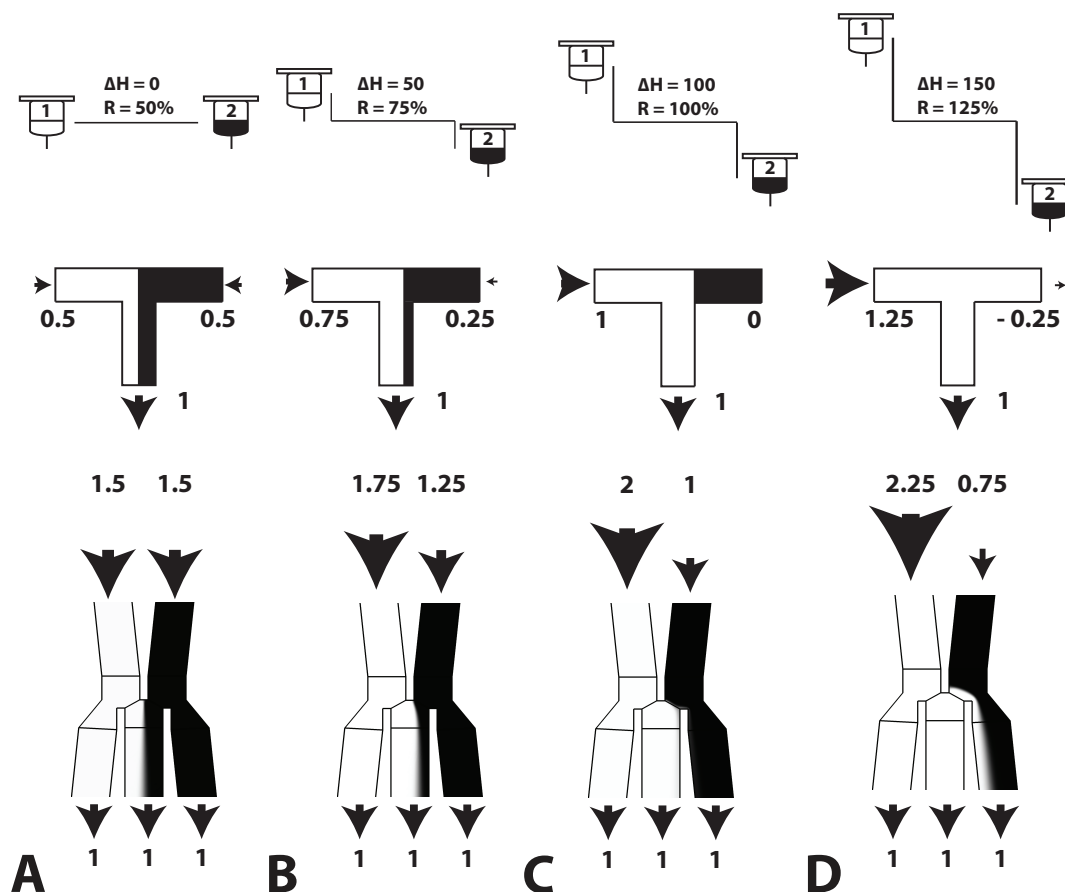


Figure 3.6: Comparison of a T-junction to the improved DAW junction. Top portion of the figure shows the relative heights of the input reservoirs for each mixing ratio. Middle and bottom portions of the figure depict the performance of a T-junction and the DAW junction respectively. Four mixing ratios, from 50% to 125%, are shown. Due to symmetry, mixing ratios from -25% to 50% will be the reverse of those shown here. Numbers given at inlets and outlets are volumetric flow rates, (nl/s). Inlet's colored white represent an added fluorescent dye. **A.** Mixing ratio of 50% ($R=50\%$), with equal flows from both input reservoirs ($\Delta H=0$). Note the sharp interface between fluid streams, as diffusion has not yet caused appreciable mixing. **B.** Mixing ratio of 75%, both junctions continue to perform well. Note that the flow rate in inlet 1 has increased in the exact amount it has decreased in inlet 2. **C.** Mixing ratio of 100%. The T-junction fails here as the flow rate in input 2 has dropped to zero, likely leading to a backflow situation. Note the DAW junction continues to perform well, since all flow from input 2 is directed into a shunt. **D** Mixing ratio of 125%. At this point backflow has occurred in the T-junction. In the DAW junction, excess flow from input 1 is directed into a shunt and flow continues from input 2. Note that the DAW junction's output to the cell chamber (center channel of the junction) will be the same in both C and D. This is why the output measured near the cell chamber seems to plateau after increasing ΔH beyond the 100% level.

observed. To correct these problems we designed a new DAW junction (depicted in Figure 3.4B) to minimize the contact distance between the two fluid streams and increase the flow velocity. These changes essentially increased the flow's Péclet number in the junction to limit diffusive mixing. Moreover we altered the shunt network compared with the Bennett design so the shunt entrances would be nearly parallel to the outlet. The idea was to minimize any changes in flow direction occurring at the junction. The performance of this new junction is shown in Figure 3.7.

3.1.5 Calibration of the DAW junction

The junction is designed to be used in conjunction with linear actuators to physically move the input reservoirs up and down thereby altering their hydrostatic pressures. To map the height of the input 1 and 2 reservoirs to a mixing ratio of the DAW junction, we have come up with a simple calibration scheme. First we find two sets of reservoir heights corresponding to mixing ratios beyond 0% and 100%. Each set represents flow from one of the inputs being completely diverted into a shunt. Since the heights do not have to be exact at this step, it is relatively quick and easy to setup (unlike trying to find the exact 0% and 100% heights). Next we program the linear actuator controllers to generate a triangle input wave and begin to move the reservoirs. Generally we use an input wave with a 5 minute period. We then monitor the fluorescence near the cell chamber to record the output signal. The two signals are overlaid and any delay is removed, as shown in Figure 3.7A. In this figure the input is shown in red and the output in green. We expect the output to closely track the input signal until a plateau is reached, indicating complete diversion of an inlet into a shunt. As can be seen in the figure, this is essentially what we see, with a slight rounding at skewed mixing ratios.

Once this mapping is complete we compress the data into a single curve, as shown in Figure 3.7B. This figure depicts one of the external port pressures mapped to a mixing ratio of the DAW junction. An ideal response would be a plateau at 0% leading to a linear ramp until another plateau is reached at 100%. The output of our junction

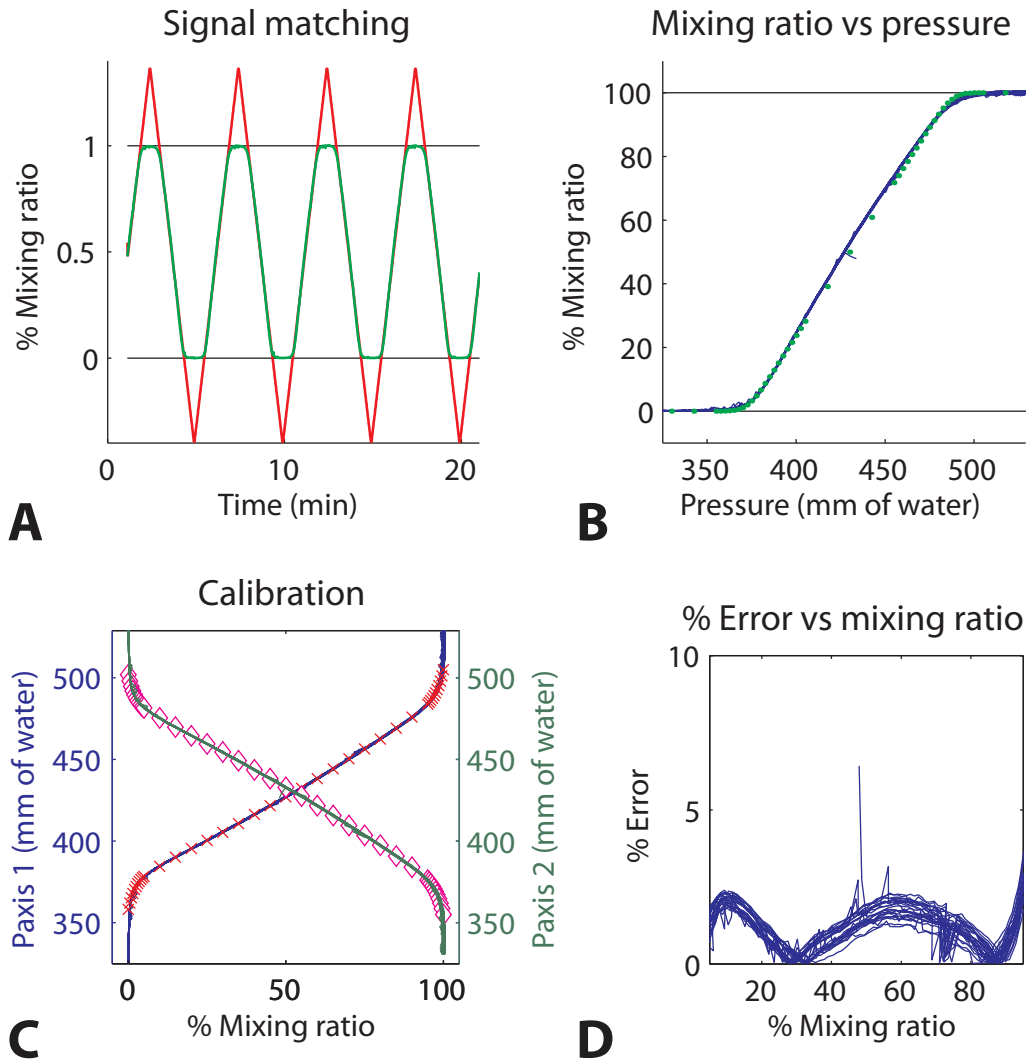


Figure 3.7: Performance of the DAW junction. **A.** Calibration signal (red) overlaid with output signal (green) after correction for the delay in acquisition. During calibration the system is designed to intentionally overshoot the bounds of the DAW junction. Since the starting and ending points for calibration are not critical, this eases setup. The ideal response would closely track the input signal and plateau beyond mixing ratios of 0% and 100%. As can be seen in the figure, this is what we observe, except for a slight rounding near the beginnings of the plateaus. **B.** Compression of the data in part A into a single curve by mapping the input pressure directly to the output mixing ratio. Blue curve is the compressed data, while the green dots are the expected results from Comsol modeling. As can be seen in the figure, the modeling and experimental results are in excellent agreement. **C.** Completed calibration for both inputs. Red crosses and pink diamonds represent polynomial fits of inputs 1 and 2 respectively to the output mixing ratio. These fits can be used to program a linear actuator controller to generate precise inducer waves. **D.** Measure of the percent error of the *uncalibrated* output signal, which general is less than 3%.

(blue curve) closely approximates this, again with slight rounding near 0% and 100% mixing ratios. As an additional example of Comsol's utility, the green dots represent modeling results generated of the junction's response. As can be seen in the figure, the modeling and experimental results are in excellent agreement. In Figure 3.7C the calibration results for each input are shown. A high order polynomial fit is used for each input, which can then be programmed into the linear actuator controller. Figure 3.7D represents the percent error of the output signal as a function of mixing ratio for the *uncalibrated* system. Even without calibration the system is highly accurate, usually having an error of less than 3%.

3.1.6 Design of an improved yeast cell trap

Beyond the flow network or DAW junction, the most important part of a microchemostat chip is the cell trap. Often a successful design will hinge on a properly functioning trap. A microchemostat's cell trap should ideally be easy to load, force the cells to grow in a monolayer so they are all in the same focal plane, allow nutrients to enter the trap even when packed with cells, force cells to grow in well defined directions to assist with cell tracking and allow cells to exit the trap without clogging the device. For some cell types, specifically mammalian cells, controlling the flow rate in the trap is also extremely important. We have found that even hearty mammalian cell lines, such as 3T3 cells, can be killed by extremely low flow rates (less than 1-5 $\mu\text{m/s}$). This requires the design of highly specialized traps to prevent any flow from reaching the cells after loading. We have never encountered an issue where yeast or *E. coli* cells seem adversely affected by flow, however the flow rate can be important for intercellular communication by diffusible substances (Danino et al., 2010).

Often the goals mentioned above are difficult to achieve completely, for example a trap with high cell retention is often very difficult to load. This is the case with the $T\mu\text{C}$ chip described in (Cookson et al., 2005). To overcome these problems an improved yeast cell trap, known as the doughnut trap, was designed. Figure 3.4D and E contain

an overview of this trap. The salient feature is improved loading while retaining the ability to image cells in a monolayer. Another major issue in the trapping region is clogging of cells from excess growth. Yeast cells grown in glucose can clog a device in several hours if the microchemostat is not properly designed. As shown in Figure 3.4 the outer channel is designed with a height of $10\ \mu\text{m}$. This height is large enough that no cells will be able to clog it under normal circumstances. The height of the trap is kept at $3.525\ \mu\text{m}$ for yeast cells of the W303 background. Note that the height of the trap is the most critical parameter of the entire chip as will be stressed in the fabrication section. Even height differences as little as $0.1\ \mu\text{m}$ can make a difference in terms of the effectiveness of the trap. If the trap is too high, yeast cells will flow right through and not be trapped at all. Even those that are trapped may not grow in a monolayer and hence a uniform focal plane will be impossible to achieve. However, if the trap is too low, then it will be impossible to get the cells into the trap. Thus, the height of the trap depends intimately on the cell type and even the cell strain. We have noticed that some larger backgrounds of yeast actually require a slightly higher trap than other common laboratory yeast strains.

Upon loading, when cells flow into the chamber containing the trap, most will actually flow around the trap to the cell and shunt waste (port 3), since this region's flow mostly goes around the trap. This is actually beneficial to the design since it allows growing cells to be quickly whisked away when they overgrow the trap, while minimizing any movements of the cells in the trap due to flow (which can make cell tracking difficult). Furthermore this difference in flow rates is primarily a consequence of the difference in the heights between the two regions. Recall Eq. (3.9) which states that resistance of a channel scales with the cube of the height. Thus while the height difference between the trap and the outer channel is only ~ 3 fold, the resistance difference will be ~ 27 fold.

Those cells entering the central channel will move to the base and become stuck at the entrance barrier. Since the trap height is slightly smaller than the diameter of a yeast cell, the cells cannot enter the trap without some assistance from the experimenter.

Once enough cells have accumulated behind the entrance barrier, the experimenter will flick the microfluidic line attached to the cell port with his index finger. This perturbation will cause a momentary pressure disturbance which will force some cells under the barrier into the trap. Once in the trap they will be efficiently held between the roof of the trap and the glass cover slip.

During the course of the experiment, cells will divide and enter exponential growth. They will quickly fill up the trap and the colony will come into contact with its walls. The pressure exerted on the trap's walls by the growing colony will generate a flow of cells, which can be modeled as a particulate flow (Mather et al., 2010). This flow will expel some cells from the trap into the outer channel, to be carried away into ports 4 and 5 (note port 5, originally the cell port now functions as a waste port). The design of the cell trap should take cell flow into account so it can be directed in appropriate ways. For example, to track cells often it is useful to direct their movement in a regular direction to limit the difficulty of tracking. With the doughnut trap, cell flow is directed in radial directions which works fairly well. However we have been considering designing a new trap with internal baffles to limit lateral movements of the cells.

The MFD005_a device has been used successfully to generate many types of input concentration waves for numerous yeast strains and genotypes. In general the chip takes 1-2 hours to setup and can run for several days depending on the conditions. The chip is highly useful for all types of small scale experiments involving dynamic environments. However, upon building this chip we realized that most of the time during an experiment our microscope sat idle between imaging frames. To make better use of our time and resources we decided to build a parallel version of the MFD005_a device which we have named the MDAW device.

3.2 A parallel DAW device

The parallel version of our MFD005_a device was designed to have eight copies of the smaller device on a single larger device. This parallel architecture greatly increases

the throughput of a run by allowing eight independent subexperiments to be conducted at a time. The utility of this design can be seen by comparing the number of ports required to carry out equivalent experiments for the progression of chip designs. With the Bennett chip, 64 ports are required to conduct eight experiments, for the MFD005_a device, 40 ports are required, while the MDAW device requires only 26 ports. Since setup time is directly proportional to the number of ports a chip contains, this reduction represents a significant savings of both time and consumables. Of course designing such a device presents its own challenges, a major one being space. Since we wanted all features to fit entirely on a single 24x40 mm coverslip, space was at even more of a premium than with the MFD005_a device.

To conserve space we compressed the features of the MFD005_a device as much as possible while retaining functionality and maintaining a margin for fabrication errors. We made the device radially symmetric in order to provide equal resistance paths to the ports shared among the subexperiments. To divide the space we separated the chip into eight circular sectors of equal area, similar to slices of a pizza. While a rectangularly shaped device would have been a better fit for the coverslip, it would have been more difficult to ensure the resistances were equal to the outlets for all subexperiments. Moreover excessive stage movement between locations during acquisition can generate bubbles in the microscopy oil. These bubbles sometimes show up after several hours into an experiment and can cause a severe loss of focus or degradation of image quality. To prevent these problems the cell chambers were placed as close to each other as possible, which essentially requires radial symmetry. As an added bonus, this lowers the amount of time for stage movement between positions.

An overview of a MDAW subexperiment is shown in Figure 3.8A. Compare this to the MFD005_a device in Figure 3.4A. Both contain a DAW junction, SHM features and a cell trap that are essentially identical, although the length of the channel between the DAW junction and the cell chamber has been reduced slightly in order to conserve space. In fact ports 1, 2, and 5 and the channels linking them are essentially equivalent to ports A, B and C respectively in the MDAW device. The major difference is that ports 3

and 4 on MFD005_a have been consolidated in the MDAW device. In the MDAW device we call the port 3 analog the consolidated shunt port and the port 4 analog, the consolidated alternative outlet. The consolidated shunt port is connected to each subexperiment by an extensive collection network. This collection network can be seen in Figure 3.9. To create this collection network Comsol modeling was essential to ensure that the flows would be equal to their equivalents in the MFD005_a device. This modeling indicated that the height of the collection network would have to be increased to 35 μm to sufficiently lower the resistance (shown in dark blue in Figure 3.9). Moreover the shunt channels from the DAW junction now connect to the diversion channel before it reaches the consolidated shunt port, whereas in MFD005_a they both reach port 3 independently. Comsol modeling indicated that back flow from the shunt into the diversion channel could be a problem if the diversion channel was not long enough. The connection point was extended to ensure this would not happen.

It was easier to consolidate port 4 into the alternate outlet port on the MDAW device since it was in the center of the chip and each subexperiment had an independent path to the port. Thus the height of these channels could remain 10 μm . However the channel length between cell chamber and the alternate outlet port had to be reduced, which altered the resistance somewhat. Comsol modeling allowed us to determine the port pressures which led to equivalent flow. One might wonder how many ports could be shared among a device of this size. Of course if a multilayer microfluidic device were used then there would be no restriction, however we believe the time required to manufacture multilayer devices does not justify their added benefits and therefore we avoid their use if possible. For a single layer device, at most two ports can be shared among *all* subexperiments due to geometric constraints. It is possible to share additional ports between adjacent subexperiments, however, with the MDAW device this would have meant sharing the cell ports (port C) and we wished them to remain independent. It is also possible to add y-junctions or manifolds to connect multiple outlet ports to a single reservoir. However if this is done, extra care must be taken to ensure no bubbles are introduced in the lines. This is especially a problem with small diameter y-junctions.

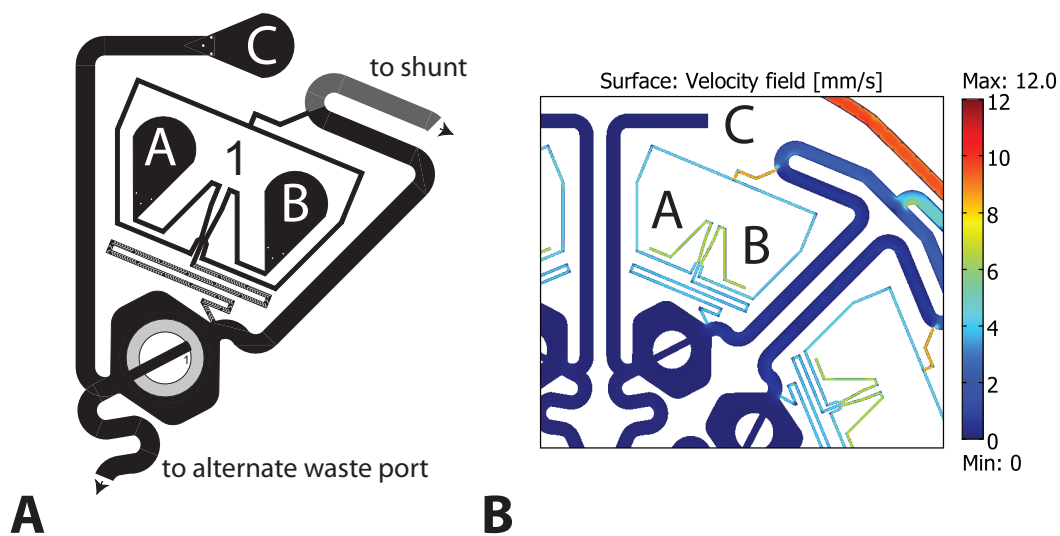


Figure 3.8: Graphic of the individual subexperiments in the MDAW microfluidic device. **A.** This is a subexperiment from the MDAW device. It is essentially a compressed version of the MFD005_a device shown in Figure 3.4A. The ports labeled A, B and C are equivalent to ports 1, 2 and 5 respectively in Figure 3.4A. The equivalents to port port 3, the cell and shunt waste and port 4 the alternate outlet port, in the MFD005_a device are shared among all eight subexperiments in this device. The arrows point to these shared ports. This port sharing reduces the number of outlets and eases the setup of such a large device. To make identification easier under the microscope, we have placed the subexperiment number above the DAW junction and near the cell trap. **B.** Closeup of a Comsol model of the MDAW device. Comsol modeling was crucial for designing the combined collection network so each subexperiment's shunt would function similar to the MFD005_a device. Since the collection network combines the output of eight subexperiments, the resistance had to be lowered so it would carry the combined flow as efficiently as that in the MFD005_a device.

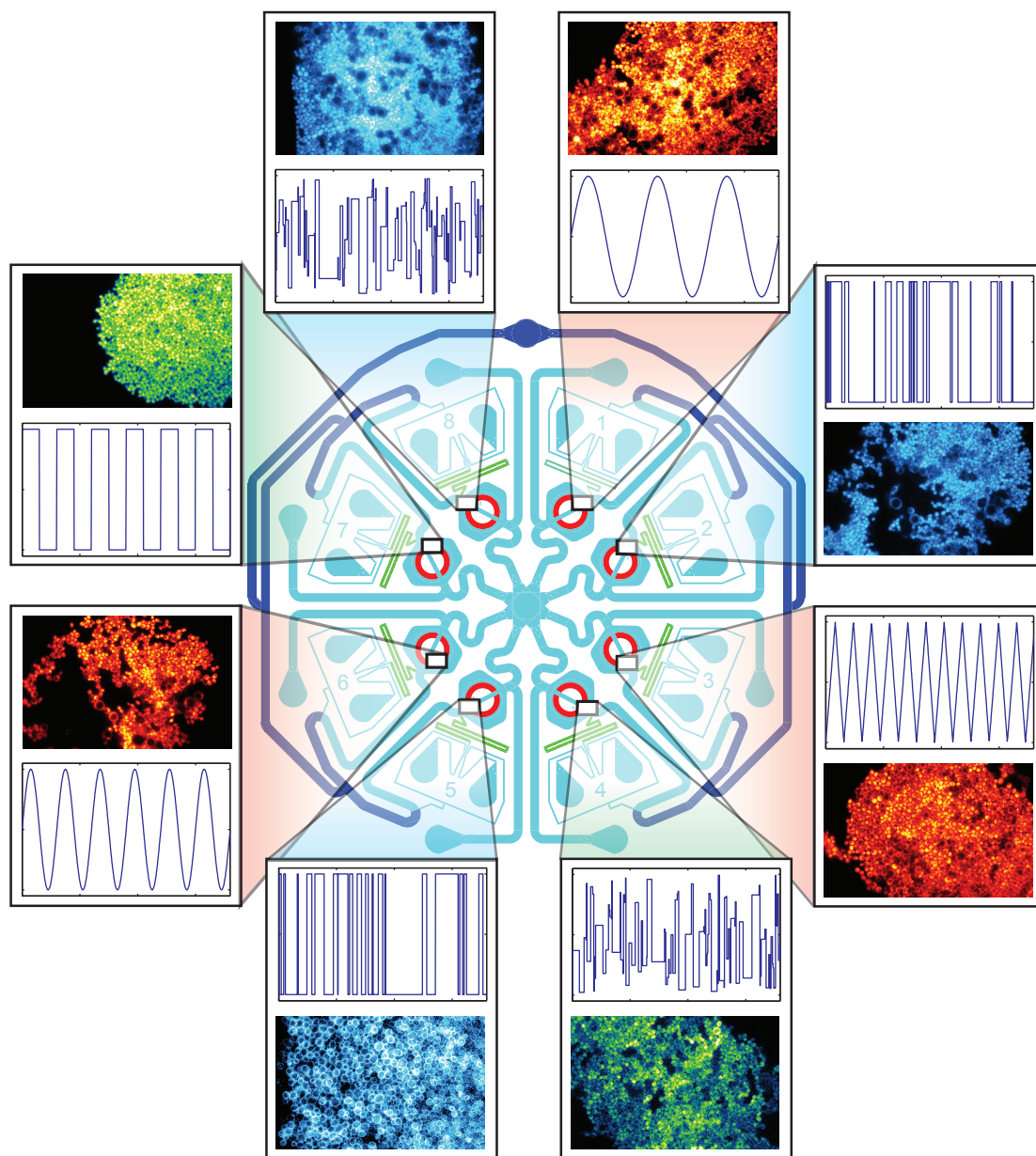


Figure 3.9: Graphic of the MDAW microchemostat device. The MDAW device has eight independent subexperiments. Each subexperiment can generate a separate inducer signal for an independent yeast strain. Examples of each are given in the breakout boxes. The system is capable of generating both periodic and pseudo random waves. The symmetry of the chip is important to ensure that all subexperiments have equal resistance outlet paths to the shared ports: the combined alternate outlet port (center) and the combined cell and shunt waste (top).

Even at eight subexperiments you begin to push the limit of what modern microscopes can accomplish. For example, on our current setup using the Nikon TI, the amount of time it takes to autofocus, change filter cubes, acquire a phase contrast image and 2-4 fluorescence channels and move stage positions for eight subexperiments is nearly one minute. Since phase contrast images must be taken approximately every minute for adequate cell tracking, the microscopy setup becomes limiting before the microfluidics. While laser based focus systems would offer an increase in speed, many, like the Nikon Perfect Focus System, do not work well with PDMS devices. Thus while other microfluidic devices have been produced which offer a far greater number of independent experiments, often they cannot track *individual* cells due to excessive movement between frames (Taylor et al., 2009). This prevents the acquisition of cell trajectories and the device essentially functions similar to a highly parallel flow cytometer. Thus the device chosen should reflect the type of study and data required. For generating large numbers of cell trajectories in a dynamic environment with relative ease of setup, our device works well. For generating population level data using a extremely large set of conditions the device described in (Taylor et al., 2009) would be superior.

3.3 Cell tracking

For microchemostat experiments cell tracking is essential for capturing high quality data. In fact, one could argue that effective cell tracking is as important as the design of a microfluidic device itself. Like a high powered computer running an early version of DOS, even the best device is not much use if the cells cannot be tracked. Thus most articles making use of microchemostats make a reference to “custom Matlab code” used for cell tracking (Taylor et al., 2009; Bennett et al., 2008; Kurth et al., 2008; Hersen et al., 2008; Lee et al., 2008). Our lab is no different and we have spent much time and effort generating a software package which works quite well but has room for improvement. There is also a program called CellTracer available free online (<http://www.stat.duke.edu/research/software/west/celltracer/>). It should be stressed that

a microchemostat should be designed with cell tracking in mind from the beginning, rather than designing software to track how the cells happen to grow in the device. For example, by making the cell culture expand in defined, regular directions the cell tracking routine becomes less complex and hence works better. An excellent example of this concept is the trap described in (Rowat et al., 2009) which constrains yeast cells in essentially one dimension and makes lineage tracking quite robust.

The essential problem for tracking all types of cells, and yeast cells are no exception, is that they simply are not unique, at least as viewed under phase contrast microscopy. This can be seen in Figure 3.10 which compares different parameter values for a population of cells. Ideally each cell would occupy a unique position in some high dimensional space, corresponding to a combination of parameters, such as cell area, eccentricity and fluorescence, specific for that cell and invariant in time. This would be similar to a bar code or serial number for cells. However as seen in Figure 3.10 there is simply no combination of inherent characteristics visible under this type of imaging which can uniquely identify *all* members of the population at once. If there were, there would be no clusters of high density in the histogram. Moreover, since cells grow and divide, there is often a high amount of variability in the geometric properties between frames for the *same* cell. Unfortunately the only parameter which is unique for all cells confined to a monolayer is position. Thus it is of critical importance to keep track of cellular position during a microchemostat experiment and this explains why phase contrast images must be taken frequently. For fast growing cell types such as yeast or *E. coli*, frequent sampling is a necessity. If the cellular movement is greater than one cell diameter between frames, cell tracking becomes next to impossible.

Cell tracking software can be divided into two basic types, segmentation based methods and non-segmentation based methods (Mosig et al., 2009; Miura, 2005). Segmentation methods are the more common type and will be the focus of this discussion. In a segmentation method, a transmitted light image of the cell population is converted to a binary image containing only the outlines of cells. This is repeated for each image of the experiment and trajectories are formed by linking cellular objects between

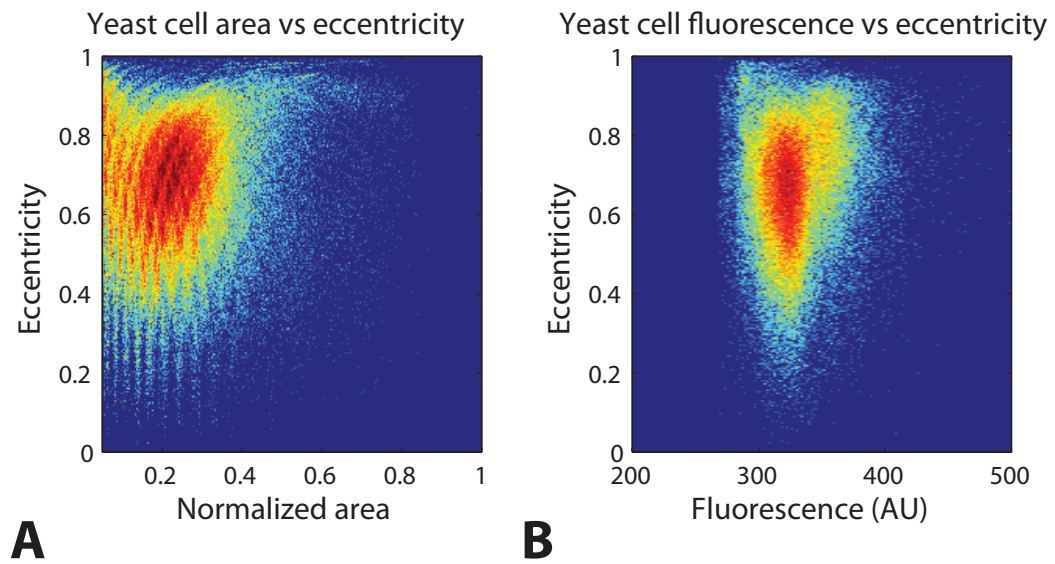


Figure 3.10: Comparison of different cell parameters for a population of yeast cells. **A.** Two dimensional histogram of yeast cell eccentricity versus area. Striations in the data are a remnant of the ellipse filter used to segment the cellular boundaries. Notice that most cells have similar values for eccentricity and area. **B.** Similar plot as part A, except here eccentricity and mean fluorescence are plotted.

frames based on shared characteristics. Binary images are preferred since there are a large number of mathematical functions available for processing them. To convert a transmitted light image to a binary image the simplest method to use is a threshold. Essentially anything below the threshold is converted to black and anything above to white. Phase contrast images typically have a light halo around the boundary of cells, which provides high contrast, and thus are perfect for thresholding. A comparison of phase contrast imaging to differential interference contrast imaging, which is less suitable for thresholding, is shown in Figure 3.11.

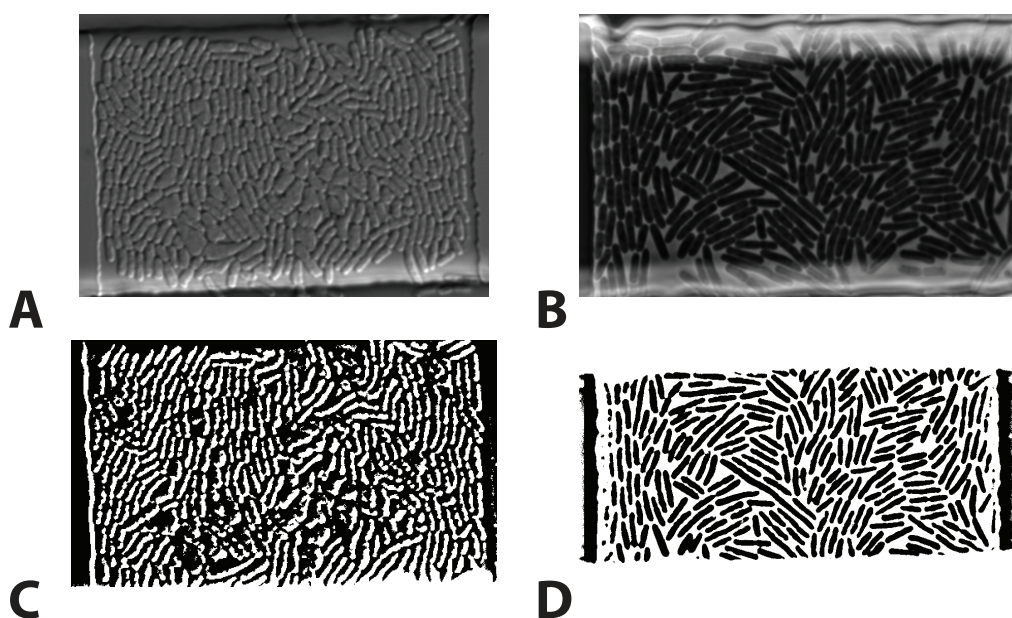


Figure 3.11: Comparison of phase contrast and differential interference contrast (DIC) imaging with regards to cell tracking. **A.** DIC image of an *E. coli* colony growing in a microchemostat device. **B.** Phase contrast imaging of a similarly grown *E. coli* colony. **C.** Binary image created by thresholding the DIC image shown in part A. Notice how difficult it is to distinguish the cellular boundaries. **D.** Thresholded version of the phase contrast image in part B. Notice how much more clear the cellular boundaries are compared to C.

Typically a threshold value will be chosen to retain the boundary halo while discarding all other features, thus preserving only the boundary of cells. This procedure works fairly well assuming there are no other “phase objects” present in the cell. Unfor-

tunately, yeast vacuoles are quite prominent under phase contrast microscopy and often are difficult to remove by thresholding alone. This necessitates later post-processing steps to remove the vacuolar artifacts to prevent errors in segmentation. Some yeast backgrounds or mutants can have especially prominent vacuoles which can be problematic. Moreover, environmental conditions, stress and aging can increase vacuole prominence. Thresholding based segmentation routines will need to cope with vacuoles and this is a downside of the technique for yeast. In spite of these issues, thresholding usually works well enough to be a reliable first step of the tracking procedure when chosen appropriately.

After thresholding the cellular boundaries are generally prominent but incomplete. Due to the aforementioned vacuole problems, often an aggressive threshold value is chosen leaving only the most prominent features of the image. While more successful in removing vacuolar artifacts, this will also remove some the cell's boundaries. For efficient processing of binary images, the image must be composed of only completely closed objects. Thus any cells lacking completely closed boundaries will not be found by the algorithm. Even if vacuoles are not a problem, a morphological closing operation is performed to repair inevitable boundary defects. This closing operation is done using either a structuring element or the watershed algorithm. Structuring elements are small geometrical objects which can reinforce common motifs of the image. We have found them to be very useful for processing *E. coli* cells.

Implemented in ImageJ and Matlab, the watershed algorithm is good at repairing small defects in cellular boundaries. However, if even a small vacuolar remnant remains, the watershed algorithm will bisect the cell through it, causing improper segmentation. An example of how the watershed algorithm performs in segmentation is given in Figure 3.12. Note that another thresholding tradeoff comes from deciding how much to emphasize cells at the edge versus those in the interior of a microchemostat's colony. Multiple cells in close contact reinforce their boundary halo's, causing the signal from these areas to be greater than from isolated cells at the edge of the colony. When choosing a threshold value that maximizes boundaries and minimizes vacuoles, often

the boundaries of cells on the colony edges are removed. This can be seen in Figure 3.12. These boundary cells are consequently often dropped from the segmented image.

After segmentation the binary image is processed to extract useful data from the contained objects. To assist in this processing we fit each object to an ellipse since we have found that it generates a good approximation to a yeast cell's shape. After processing each image in a run we link cells between images to form trajectories. To accomplish this we have a scoring function which compares two cells and generates a score based on how likely they are to be the same cell. We compare the position, area, eccentricity, and orientation of each pair of cells to be scored. While we could also use the fluorescence values of the cell, we have found that this usually does not improve the score's power and often isn't possible since we take phase contrast more often than fluorescence images. The scoring of cells between frames is usually the most computationally intensive part of the entire process. To aid in the computation we only compute scores for cells in the same general location of the two images, since if the cells have moved more than one cell diameter between frames they become virtually impossible to track anyways. This greatly reduces the computational time. Images of the MFD005_a and MDAW traps generally contain ~ 1000 cells when fully packed; runs sampled every minute for 2-3 days will have thousands of phase contrast images to process. Clearly, any savings in time are important.

After scoring we remove cells which are below a threshold empirically determined to result in a poor match. To match a cell from the current frame to one from a previous frame there are several cases which need to be dealt with. These cases are depicted in Figure 3.13 The first is the easiest which is a unique match between a cell from frame n and a cell from frame $n-1$. In this case the cell from frame n is assigned to the $n-1$ cell's trajectory. An example of our algorithm's scoring output for the single match case is given in Table 3.5. The next case is when two cells match to the same trajectory. This often happens due to excessive cell movement and the cellular position becomes a less powerful discriminant. In this case the cell with the highest score will be retained as the trajectory's match and the other cell will be moved to its next highest

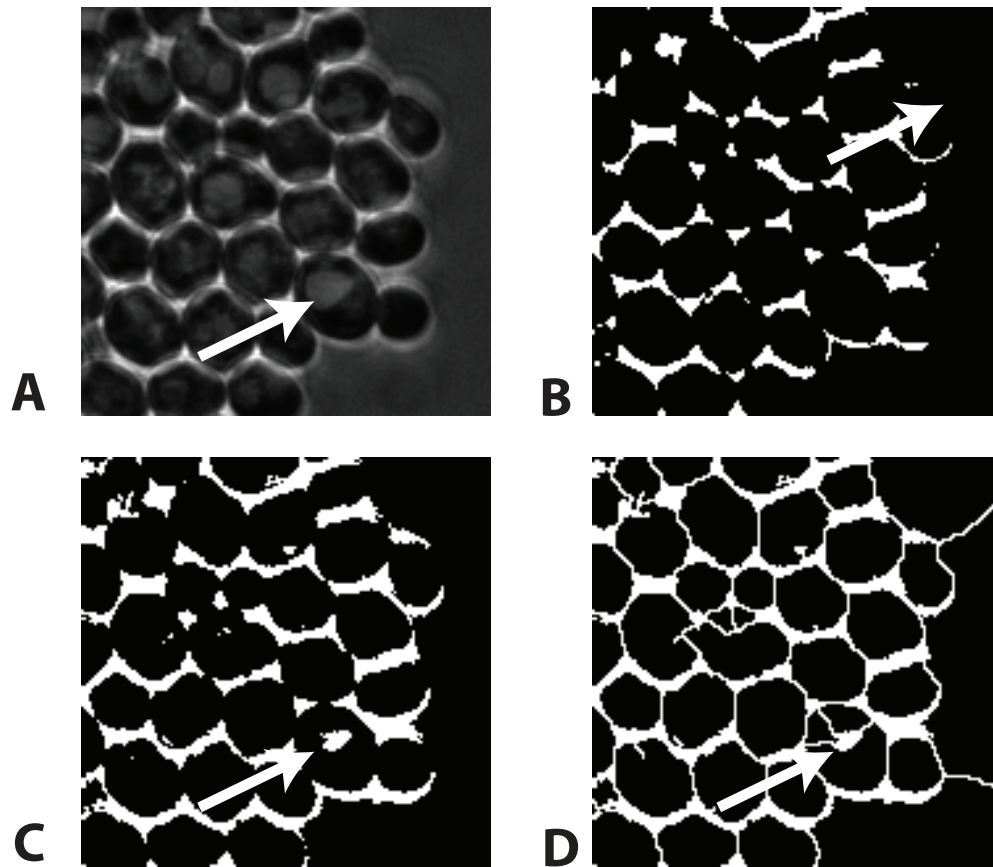


Figure 3.12: Segmentation of yeast phase contrast imagery. **A.** Phase contrast image of a tightly packed yeast cell colony. The white arrow points to a cell with a prominent vacuole. **B.** Binary image created by thresholding the image from part A. The thresholding value was chosen to minimize vacuolar artifacts, but also has the effect of removing boundaries of cells on the colonies edge. The white arrow points to a cell with a deficient boundary. This cell will not be closed by the watershed algorithm and therefore will not be present in the segmented image. **C.** Binary image created by thresholding A with a less stringent cutoff value. Notice that the boundaries are thicker and well defined, but that the vacuoles are more prominent than B. White arrow points to a vacuolar artifact. **D.** Segmented image made from performing the watershed algorithm on the thresholded image from part C. Note that the vacuolar artifact has caused the segmented cell to be split into three regions. In later processing steps each of these regions will be considered cells, thus potentially causing errors in tracking.

scoring trajectory. The third case is a skip, where a trajectory was present in frame n-2 but for whatever reason a match was not found in frame n-1. This often happens due to a segmentation error in frame n-1.

Table 3.5: Sample yeast cell tracking output. Comparison of a cell from a given trajectory and the nearest cells in the next frame. The data for the trajectory is taken from its matched cell in the previous frame. This is called the base cell. The predicted column refers to the algorithm’s prediction of how the cell’s properties should have changed in the current frame based on its previous behavior. This prediction is usually generated from MatPIV data of the colonies movement. While not shown here, it is also possible to predict a change in area from previous growth data. Note that a lower score is better and all scores above 1 are considered to be below the scoring threshold and thusly discarded.

Trajectory 36	Base	Predicted	Cells			
Score			0.1	2.1	2.5	2.5
Area	871.0	871.0	856.0	615.0	608.0	560.0
CentroidX	592.4	591.1	591.3	605.1	575.3	572.2
CentroidY	596.2	602.6	599.1	630.9	566.9	631.0
Eccentricity	0.5	0.5	0.5	0.5	0.8	0.5
Orientation	63.0°	63.0°	50.8°	71.7°	51.2°	-53.3°
Object	610	NaN	621	640	603	601
Fluor mean	NaN	NaN	392.6	331.2	390.3	326.4
Fluor std	NaN	NaN	603.4	316.3	538.5	277.2

If vacuoles are prominent, this type of skipping may happen often and should be corrected for. By keeping trajectories for an extra frame you can match a cell from frame n to a cell from frame n-2. The next case is the start of a trajectory. Here a new cell is formed. The last case is the removal of a trajectory, here the cell either left the field of view or died. One has to be careful that the algorithm is not too “greedy” by always finding a match for a cell in the previous frame. Cells are born and cells die, these events will happen and if an algorithm is too greedy it will end up making improper trajectories. For example, often a greedy algorithm will cause a trajectory, which should have ended due to a cell leaving the trap, to jump to an adjacent trajectory. This is sometimes worse than ending a trajectory prematurely because it can be difficult to detect unless one goes through the data very carefully. Thus to obtain long, reliable trajectories one needs

above all else good data and an algorithm which is balanced among all cases.

To reliably link cells into trajectories the number of cells uniquely matching a trajectory should be maximized. As stated earlier, the largest impediment to unique matching is movement of cells as the colony expands. This can be severe for *E. coli* or even yeast grown in rich media. In fact, sometimes it is possible to see movement of the colony due to growth in real time under high magnification. To correct for bulk movements of cells a particle image velocity (PIV) program can be invaluable. PIV programs are imaging analysis routines which are able to detect particulate flows in a sequence of images by comparing how the field of view changes in time. This is very useful for tracking bulk movements of cells and can often significantly improve the fidelity of tracking. We use a program called MatPIV, which has been conveniently implemented in Matlab, to track cell flow in our images (Sveen, 2004). Using this data we come up with a predicted position for each trajectory present in frame $n-1$ for frame n . An example of how this is useful is shown in Figure 3.14. The MatPIV generated velocity field has been used to adjust the position of the cells resulting in more robust tracking.

In principle, the change in a cell's area and eccentricity could also be predicted from previous data. These changes would be most pronounced for newer, smaller cells. However, we have not done this and it is unlikely to improve tracking appreciably. An overview of the entire procedure is given in Figure 3.14. The overall sequence of events is presented in the figure. We have done much work to improve the visualization of the trajectory data to ensure high quality. While the linking of trajectories works very well, the biggest improvements can be made in the segmentation steps of the process. Indeed, some cell tracking methods have no segmentation step at all, relying on comparison based methods for identifying cells in an image field (Miura, 2005). These methods generally rely on comparing a reference library of known cells to the current image using a cross correlation function. The cross correlation function will be maximized when the reference image matches a cell in the target image. Indeed, MatPIV works in a very similar way for tracking cell flows.

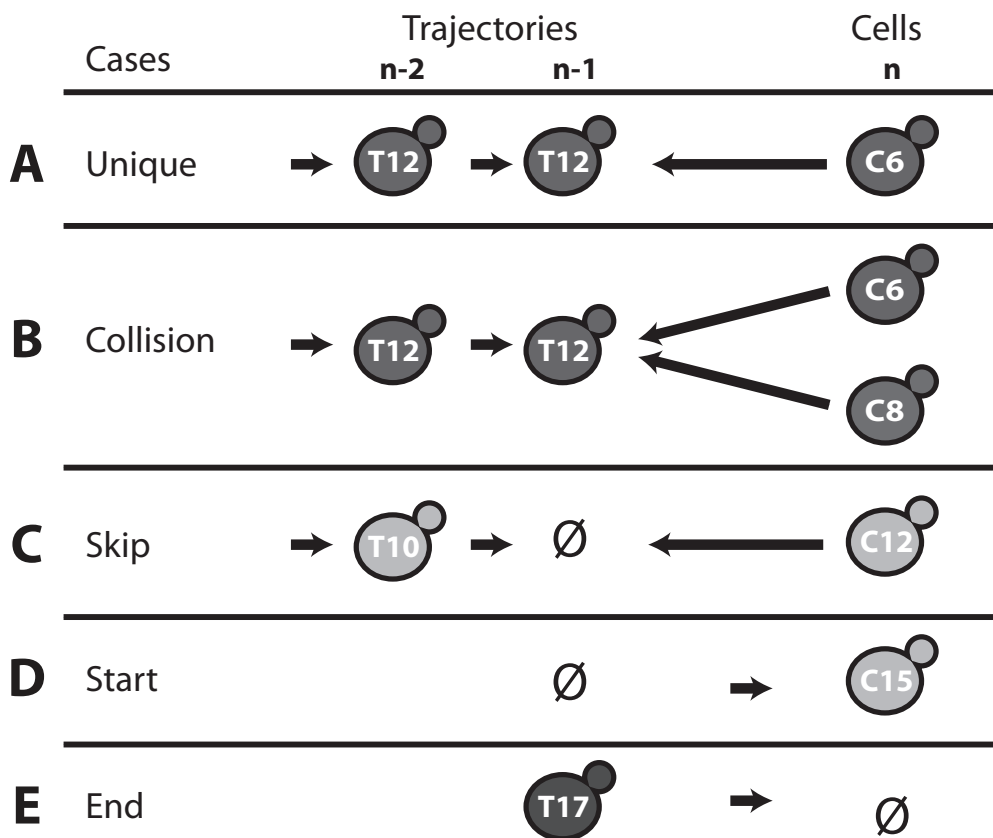


Figure 3.13: Different cases which need to be handled in cell tracking. Each case is given on the left hand side of the figure. The cells' representing trajectories present in frames $n-2$ and $n-1$ are given in the middle portion of the figure. These cells are labeled with their trajectory number (e.g. T12). Cells in the current frame (n) are shown on the right hand side of the figure. They are labeled with their cell number (e.g. C6). **A.** Unique match. A trajectory present in the previous two frames matches a single cell in the current frame. **B.** Collision. Two cells have the same trajectory as their best match. Normally the highest scoring cell is chosen as the match, however this is a symptom of poorly acquired data (cells have moved too much between frames) and will likely lead to mistakes. **C.** Frame skipping. A trajectory present in frame $n-2$ did not find a match in frame $n-1$ but does find a match in frame n . This often is caused by segmentation errors in the $n-1$ frame, especially vacuolar splitting of cells (see Figure 3.12D). If this case is handled, longer trajectories can be generated, however there is a potential for the algorithm to become overly greedy. **D.** Start of a trajectory. A cell is either born or moves into the frame. **E.** End of a trajectory. A cell either dies or moves out of the frame.

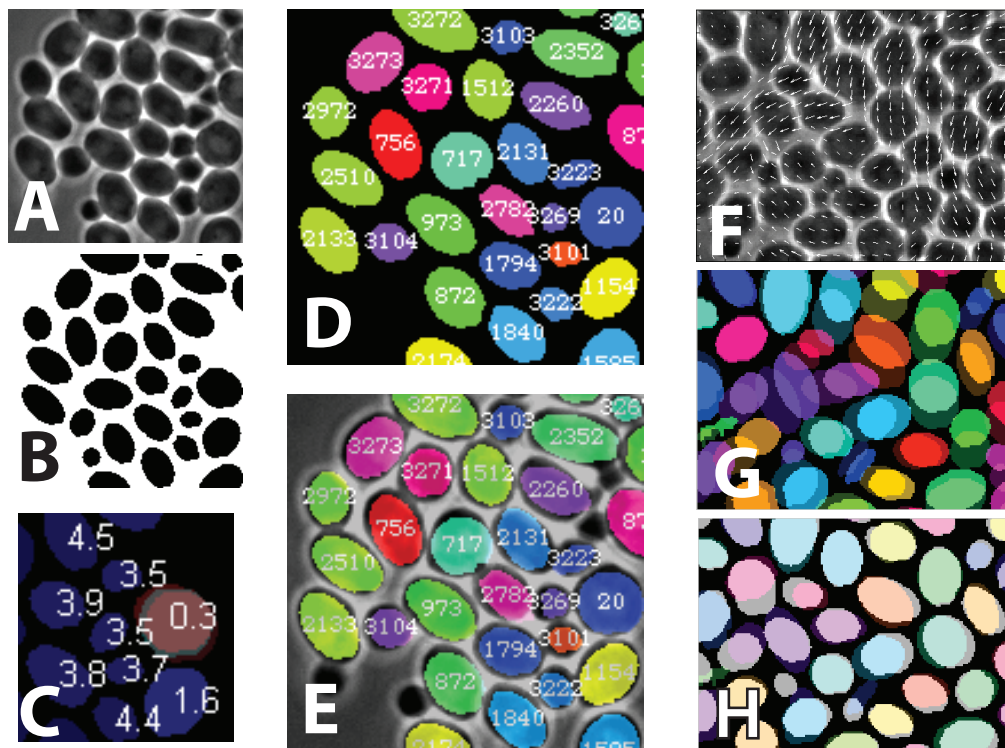


Figure 3.14: Overview of the cell tracking process. **A.** Raw data: phase contrast image of yeast cells. Note the high contrast between the boundary of the cell and the exterior. **B.** Segmented image after thresholding, application of the watershed algorithm and fitting the resultant objects to ellipses. **C.** Scoring of a cell from frame n (shown in red) to trajectories present in frame $n-1$. Lower score is better. Notice that the red cell has closely overlapped with a previous trajectory and generates a better score. All other scored cells are above the scoring threshold (which is set at 1). Note that the scoring system here has generated good contrast between the ideal match and the neighbors. This is indicative of a good match. **D.** Colored image of the masks after trajectory finding is complete. Colored regions represent trajectories which are numbered. **E.** Overlay of the trajectory image from part **D** with the phase contrast image of part **A**. Note most cells were assigned trajectories except for smaller cells and cells near the exterior. **F.** Example of MatPIV processing for cell flow. White arrows indicating the cell flow velocity are overlaid with a phase contrast image of the colony. **G.** Image of cells from frame $n-1$ (opaquely colored objects) overlaid with cells from frame n (translucent objects). Notice there is an overall movement of cells towards the lower left corner of the image due to cell flow. Also note that the distance traveled here is almost one half cell diameter between frames for some cells. One can see how this movement could generate ambiguous situations for similarly shaped cells without prior knowledge of the cell flow. **H.** Same cell field as in part **G** except MatPIV velocity information has been applied to correct for cell flow. Notice the much better overlap compared to part **G**. This will lead to more reliable matches since cell position is crucial for reliable matching.

In principle, comparison methods could get around the vacuole problems mentioned above which are the bane of the segmentation approach for yeast. However, comparison methods can have problems if the cells change markedly between frames, which will happen due to growth, division and rotation. While there are ways to correct for this, in general they are computationally intensive. In fact, the whole process is much more computationally intensive than the segmentation method. We are currently working on a hybrid method which employs an initial segmentation step that is corrected using a comparison step. Since segmentation works quite well, running it initially will reduce the space to be searched by direct comparison. The subsequent comparison step will correct for any initial errors in segmentation. Fortunately, cross correlation methods lend themselves to parallel processing, and modern graphics cards can be programmed to greatly speed up computation (Owens et al., 2008). In the future we expect more use of parallel processing and comparison based methods for cell tracking. However, it should be emphasized that no matter how well designed an algorithm is, the most crucial determinants for success are the quality of the initial data and the regularity of a cell colonies movements.

3.4 Acknowledgements

Chapter 3 contains material originally published as Ferry, M.*, Razinkov, I.*, and Hasty, J., 2010: Microfluidics for synthetic biology: From design to execution. *Methods in Enzymology*, accepted (*equal contribution). Copyright permission to republish here was granted by Elsevier Limited.

Chapter 4

Reconstructing the galactose network: the role of feedback induction

4.1 Introduction

Before the synthetic biology concepts mentioned in the introduction can be fully realized, the basic principles governing genetic interactions need to be elucidated in a natural genetic circuit. One such circuit is the galactose utilization pathway of the bakers yeast, *Saccharomyces cerevisiae*. The organism *S. cerevisiae* is well suited for synthetic biology since it is quick and easy to grow, has been well characterized genetically, has extensive molecular tools available, has a vast scientific infrastructure devoted to its study and is of great industrial importance (it is estimated that 4.3×10^5 tons of *S. cerevisiae* are grown each year for commercial purposes (Vincent et al., 1999). Furthermore the galactose utilization pathway of yeast is ideal for the modeling of genetic circuits since it is composed of a relatively small number of genes (on the order of 10^1), is subject to fascinating types of regulation including positive and negative feedback control and has been qualitatively well characterized by decades of research (Gancedo, 1998; Lohr et al., 1995; Johnston, 1987; Klar and Halvorson, 1974; Douglas and Hawthorne, 1966; Mundkur, 1952; Wilkinson, 1949; Sohngen and Coolhaas, 1924). While the preferred

carbon and energy source for *S. cerevisiae* is glucose (Rubio-Teixeira, 2005; Gancedo, 1998) growth on galactose is possible if glucose is not present in the environment.

4.2 The *S. cerevisiae* galactose utilization pathway

The purpose of the galactose pathway in yeast is to convert the monosaccharide galactose into glucose-1-phosphate through the enzymes of the Leloir pathway, the reactions of which have been heavily conserved throughout evolution (Rubio-Teixeira, 2005; Johnston, 1987). The enzymatic reactions of the Leloir pathway consist of a kinase (Gal1), a transferase (Gal7), an epimerase (Gal10), and a mutase (Gal5) (Rubio-Teixeira, 2005; Johnston, 1987). These four genes are generally considered to be the structural elements of the galactose pathway, while the Gal3, Gal4 and Gal80 genes are considered to be the regulatory elements, although these definitions are not rigid and there is some overlap between the two groups (Rubio-Teixeira, 2005; Lohr et al., 1995; Johnston, 1987).

Galactose can be found in the environment of yeast as a free monosaccharide, as part of the disaccharide melibiose or as the more complex carbohydrate raffinose, which is found in beet and cane molasses (Vincent et al., 1999). The utilization of melibiose requires the activity of a secreted α -galactosidase encoded by the MEL1 gene which is also regulated in response to galactose and is thus considered part of the galactose pathway (Rubio-Teixeira, 2005; Vincent et al., 1999). Utilization of raffinose requires the action of invertase to cleave raffinose into its constituent parts, fructose and melibiose and the above mentioned MEL1 gene (Vincent et al., 1999). Once galactose is liberated from melibiose by α -galactosidase it is imported into the yeast cell through the action of galactose permease, the product of the Gal2 gene (Rubio-Teixeira, 2005; Lohr et al., 1995; Johnston, 1987).

4.2.1 Structural elements of the galactose utilization pathway

When galactose enters the yeast cell the first step of its catabolism is carried out by the Gal1 gene product, galactokinase, which catalyzes the ATP dependent phosphorylation of galactose into galactose-1-phosphate (Rubio-Teixeira, 2005; Lohr et al., 1995; Johnston, 1987). The second step involves the reversible transfer of uridine-monophosphate (UMP) to galactose-1-phosphate from uridine-diphosphate (UDP) glucose by the enzyme galactose-1-phosphate uridylyltransferase, encoded by the Gal7 gene product (Rubio-Teixeira, 2005; Holden et al., 2003). Note that in this process a single molecule of glucose-1-phosphate is also released. The third step regenerates UDP-glucose from UDP-galactose by altering the stereochemistry of the galactose C4 carbon to that of glucose (Rubio-Teixeira, 2005; Holden et al., 2003). This step is catalyzed by the Gal10 product, uridine diphosphoglucose 4-epimerase (Rubio-Teixeira, 2005). The end result of this pathway is the conversion of one molecule of galactose into one molecule of glucose-1-phosphate (Rubio-Teixeira, 2005; Lohr et al., 1995; Johnston, 1987). The glucose-1-phosphate can then be converted to glucose-6-phosphate by phosphoglucomutase (the Gal5 gene product) which can then enter the Embden-Meyerhof glycolytic pathway (Rubio-Teixeira, 2005; Lohr et al., 1995; Johnston, 1987). Since Gal5 is not specific to galactose metabolism, its gene product is not regulated as tightly as the other galactose utilization genes, Gal1, 7 or 10 (Rubio-Teixeira, 2005; Johnston, 1987). Please see Figure 4.1 for an overview of this pathway.

4.2.2 Regulation of the galactose utilization pathway

The regulation of this pathway has been traditionally examined on three carbon sources: an inducing carbon source - galactose, a non-inducing carbon source such as glycerol-ethanol or raffinose, and a repressing carbon source - glucose (Rubio-Teixeira, 2005; Lohr et al., 1995; Johnston, 1987). Under inducing conditions the structural genes of the Leloir pathway, the Gal1, 7 and 10 genes, can each represent between 0.3 to 1.5% of total protein and between 0.25 to 1% of total mRNA in the yeast cell (Johnston,

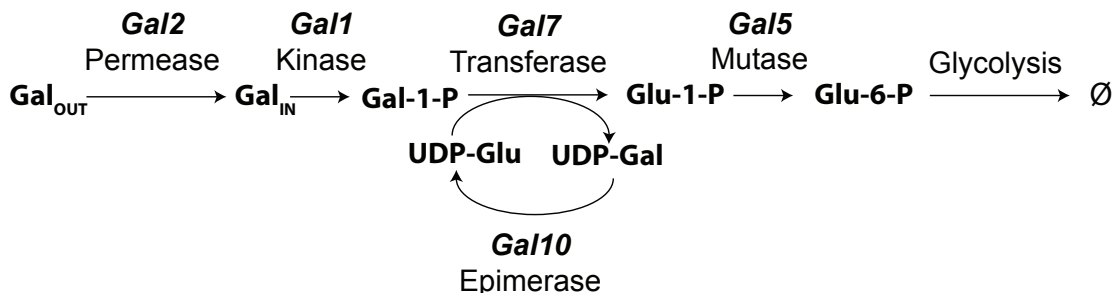


Figure 4.1: Overview of the Leloir pathway which converts galactose into a form suitable for central metabolism. Gene products are listed in italics while chemical species are listed in roman font. Abbreviations are Gal: Galactose, Gal-1-P: Galactose-1-phosphate, UDP-Gal: Uridine diphospho galactose, UDP-Glu: Uridine diphospho glucose, Glu-1-P: Glucose-1-phosphate, Glu-6-P: Glucose-6-phosphate. Adapted from: (Johnston, 1987)

1987; St John and Davis, 1981). Along with Gal2, these genes are induced 1000 fold over repressing conditions (Rubio-Teixeira, 2005; Lohr et al., 1995). Clearly genes with expression levels of this magnitude must be regulated carefully to prevent an unnecessary metabolic burden being placed on the cell. The regulation of the structural genes has traditionally been viewed as the role of the Gal3, Gal4 and Gal80 genes. Please see Figure 4.2 for an overview of the regulation of this pathway.

The Gal4 gene is a DNA binding transcription factor which is responsible for the only known transcriptional activation of the Gal structural genes (Johnston, 1987). Gal4p binds to upstream activation sequences, known as UASgal sites, in the promoters of genes it regulates (Rubio-Teixeira, 2005; Lohr et al., 1995; Johnston, 1987). Genes that are strongly expressed in response to galactose, such as Gal1, 7 and 10 have two UASgal sites in their promoters, while genes with lower levels of expression in response to galactose such as Gal80, have only a single site (Rubio-Teixeira, 2005; Lohr et al., 1995; Johnston, 1987). Under non-inducing and repressing conditions the Gal80 protein is able to block Gal4p's activity by binding to its transcriptional activation AR2 domain (Lohr et al., 1995). This binding is thought to block the interaction of Gal4 with general transcription factors necessary to initiate transcription of its target genes (Rubio-Teixeira, 2005; Lohr et al., 1995).

4.2.3 Growth under inducing conditions

Under inducing conditions galactose is sensed by Gal3, which relieves Gal80's repression of Gal4 through a still unclear mechanism (Rubio-Teixeira, 2005; Bhat and Murthy, 2001; Lohr et al., 1995; Johnston, 1987). Gal3 is believed to sequester Gal80 in the cytoplasm and prevent its transport into the nucleus. With Gal80 in the cytoplasm, it is unable to interact with Gal4 and Gal4 is able to activate the transcription of its downstream targets. These genes include both Gal3 and Gal80 as well as Gal1,2,7 and 10 (Rubio-Teixeira, 2005; Bhat and Murthy, 2001; Lohr et al., 1995; Johnston, 1987). Although both structural and regulatory target genes are upregulated, their levels of induction differ. The regulatory genes are only induced 3-10 fold over their repressed levels, far less than the 1000 fold induction of the structural genes. This difference in expression has been traditionally explained on the differing promoter regions between these genes (Rubio-Teixeira, 2005; Lohr et al., 1995). It is of interest to note again that both Gal3 and Gal80 are upregulated in response to galactose, indicating that one response to the inducer is to express a component responsible for the network's repression.

4.2.4 Growth under repressing conditions

When glucose is present it overrides the signal of the inducer (if also present) through a general mechanism known as carbon catabolite repression which affects the expression of many genes including those of the Gal network (Rubio-Teixeira, 2005; Bhat and Murthy, 2001; Gancedo, 1998; Lohr et al., 1995). Since catabolite repression has numerous targets, some have suggested that the glucose regulatory network is separate from and superimposed onto the galactose network (Johnston, 1987). There are three basic mechanisms responsible for the down regulation of the Gal network in response to glucose: by removing the ability of Gal4 to bind to the UASgal sites of target promoters, by reducing the level of the positive feedback elements like Gal2 and Gal3 more than the negative element Gal80 and by direct repression of the Gal promoters through Mig1 binding (Rubio-Teixeira, 2005; Bhat and Murthy, 2001; Lohr et al.,

1995; Johnston, 1987). Upon glucose exposure the Gal4 gene is down regulated which is thought to reduce Gal4p's already low concentration in the cell to the point where it is no longer able to bind to the UASgal sites of its target promoters (Johnston, 1987). Moreover the Gal2 protein is ubiquitinated and targeted for degradation in the vacuoles which decreases the amount of galactose entering the cell (Horak and Wolf, 1997). Finally the Mig1 repressor protein levels increase rapidly and are responsible for blocking the expression of genes positively acting on Gal4, like Gal1 and Gal3 (Johnston, 1987).

4.2.5 Growth under non-inducing conditions

Under non-inducing conditions such as a glycerol-ethanol carbon source the Gal system is in a fundamentally different state than it is under repressing conditions. This difference can be demonstrated by the kinetics of induction of the Gal structural genes after a transfer from a non-inducing to an inducing carbon source compared to transfer from repressing to an inducing carbon source (Johnston, 1987; Adams, 1972). For example when yeast is grown on glycerol-ethanol and then switched to galactose the activity of galactokinase (encoded by Gal1) can be detected after twenty minutes compared to 3 to 5 hours after a transition from glucose to galactose (Johnston, 1987; Adams, 1972). One explanation for this phenomenon is that the galactose system is poised for induction under poor, non-inducing carbon sources like glycerol-ethanol (Rubio-Teixeira, 2005; Johnston, 1987). For example in non-inducing conditions, Gal4 still binds to the promoters of Gal regulated genes like Gal2, it is just kept transcriptionally inactive by Gal80 (Rubio-Teixeira, 2005; Johnston, 1987). This is in direct contrast to the depletion of Gal4 from its regulated promoters seen under repression conditions. It is thought that the presence of Gal4 on its regulated promoters allows a more rapid response to galactose since it does not need to be resynthesized like it does under a switch from repressing to inducing conditions (Rubio-Teixeira, 2005; Johnston, 1987).

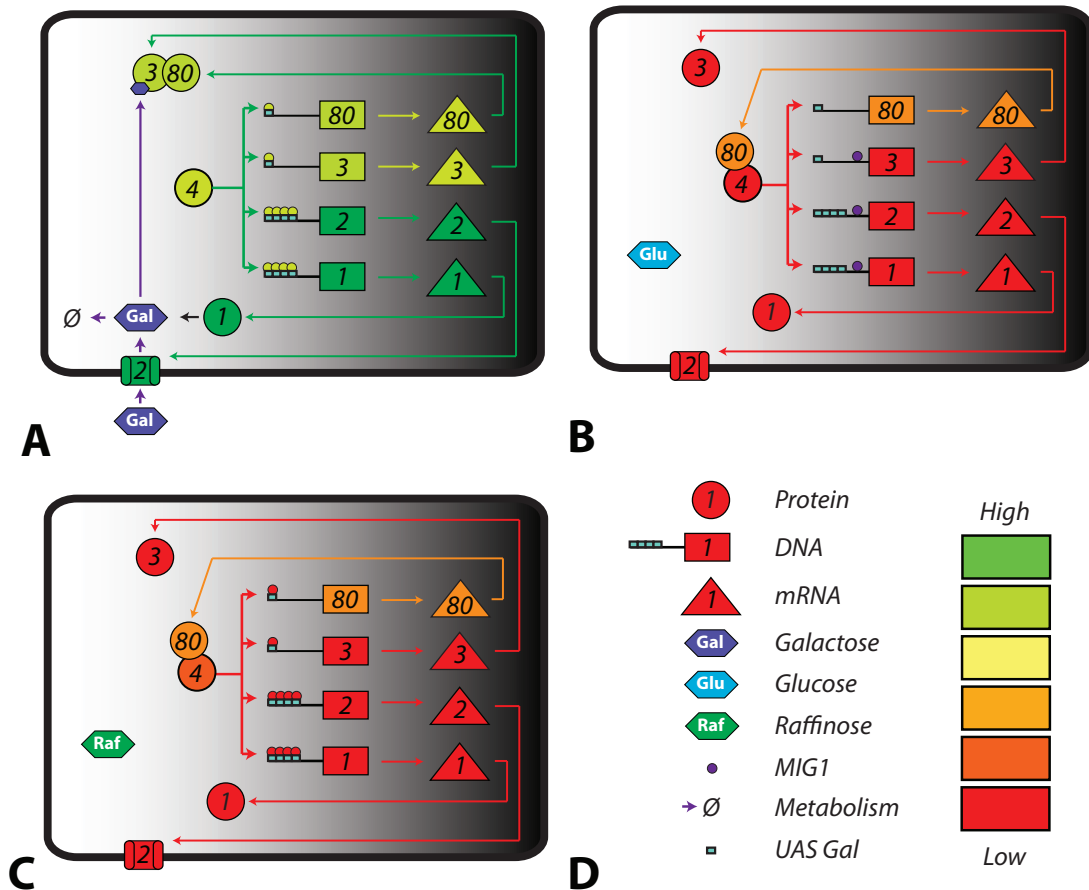


Figure 4.2: Depiction of the conceptual galactose regulation model outlined in the text. **A.** Growth under galactose as the sole carbon source. Note the induction of both Gal3 and Gal80 (compare this with the levels in parts B and C). Gal3 binds Gal80, relieving the repression of Gal4. **B.** Growth under glucose as the carbon source. Note the repression of Gal4 compared to part A and the binding of the repressor MIG1 to the promoters of the Gal1, Gal2 and Gal3 genes. Also note the large reduction of Gal3 compared to the only moderate reduction of Gal80. Additionally, Gal4 has been blocked from its binding sites on the Gal gene promoters (red arrows). Gal80 binds Gal4 to further repress its activity. **C.** Growth under raffinose (non-inducing) as the sole carbon source. Note the main difference from part B is that Gal4 still binds to (red circles) but does not activate the transcription of the Gal gene promoters. Gal80 is free to bind Gal4 and repress transcription of the targeted promoters. **D.** Legend for the symbols described in the text. Protein, DNA and mRNA are depicted by circles, squares and triangles respectively. Carbon sources are shown as hexagons. The transcriptional repressor MIG1 is shown as a purple circle which binds upstream of the UAS Gal sites present in the promoters of targeted yeast genes.

4.3 Project overview

4.3.1 Primary question and general motivation

The motivating question for this project concerns the induction of both positive and negative feedback mechanisms in response to stimulus. In the *S. cerevisiae* galactose network, cells respond to an input of galactose by upregulating the repressor Gal80 (resulting in negative feedback), the transporter Gal2 and the galactose sensor Gal3 (both resulting in positive feedback). *A priori* this seems counterintuitive, what advantage does a cell obtain by repressing the very network necessary to metabolize the input signal? However this regulatory motif is not unique to the yeast galactose network and therefore it may have broad importance for understanding how organisms cope with their environment. Indeed the canonical *Lac* operon of *E. coli* is a network with a similar topology in some ways and is also involved in carbon source selection. However, while the topology of the network is qualitatively similar, there are important regulatory differences. For example, in the *Lac* operon, the repressor LacI is expressed constitutively and unlike its analog in yeast (Gal80), it is not upregulated in response to lactose (Chang et al., 2010; Robert et al., 2010; Ozbudak et al., 2004).

4.3.2 Additional examples of networks containing positive and negative feedback

There are of course many gene networks, both synthetic and natural, which contain positive feedback components (Danino et al., 2010; Stricker et al., 2008; Dunlap, 2006; Ozbudak et al., 2004). These networks generally fall into one of two types: switches, like the Gal network and the *Lac* operon, or oscillators, like circadian or synthetic oscillators. A good example of an oscillator composed of both positive and negative feedback components is the circadian network in the filamentous fungus *Neurospora crassa*, discussed in Chapter 2. In the *N. crassa* circadian oscillator an inducing signal (light) leads to the expression of both positive and negative regulatory elements.

Upon exposure to light, both the positively acting white collar genes and the negatively acting frequency gene are upregulated. This induction is thought to lead to a robust, yet controlled light response (Heintzen et al., 2001; Dunlap, 1999). Another example of an input signal activating both positive and negative regulatory elements is the NF- κ B network of mammalian cells, important for activating responses to immune challenge (Nelson et al., 2004). In this system an input signal causes the positive regulator NF- κ B to translocate from the cytoplasm to the nucleus and activate gene transcription. One of the targets of NF- κ B is its own repressor I κ B α , which then negatively regulates the activity of NF- κ B (Nelson et al., 2004). In this system the interplay between the positive and negative regulatory elements can lead to oscillations in the localization of NF- κ B, which is thought to be important for the fidelity of the input signal transmission (Nelson et al., 2004).

4.3.3 The importance of activating positive and negative feedback in response to stimulus

In both circadian systems and the NF- κ B network, oscillations may occur in the levels or locations of the genetic components (Nelson et al., 2004; Heintzen et al., 2001; Dunlap, 1999). Although, unlike circadian systems, in the NF- κ B network oscillations are heavily damped. In these systems, as well as synthetic oscillators, the activation of both positive and negative feedback elements is important for generating and/or sustaining oscillations. Much depends on the actual parameters of the system, such as induction, delay and decay kinetics, to determine whether or not oscillations will occur (Stricker et al., 2008). In contrast no known natural oscillations exist in the yeast galactose regulatory system, so the role of inducing both components is less clear. Importantly, the *Lac* operon does not make use of induced negative feedback as mentioned above, although the qualitative requirements of this network are similar to the Gal network. Both are strongly repressed by glucose through catabolite repression and both sense their inducers through regulatory systems which lead to gene activation.

Since both architectures function as switches, leading to steady state on/off behavior for a given inducer concentration, I speculated that the network architecture may contribute to a dynamic stimulus response. In fact, by considering that the natural environment is continually in flux, I postulated that this architecture helps tune the genetic response to the current conditions, while retaining the ability to respond rapidly to changes in carbon source availability.

A balance exists between specialization for the current environment and the ability to quickly adapt to environmental change. An organism's overspecialization for its current environment would be disadvantageous if this meant reacting to environmental change became prohibitively expensive or impossible. This idea, that there is a trade off between specialization to a static environment and adaptability to environmental changes, may explain some evolution experiments demonstrating the emergence of yeast strains with high growth rates on specialized carbon sources after many generations (Ferea et al., 1999). These emergent strains, while well suited to the environment selected for, are likely less fit compared to wild type strains in an environment with an altered carbon source. This reduced fitness could be due to alterations in the gene regulatory network of the yeast, the appearance of which was documented in (Ferea et al., 1999), perhaps making switching from one state to another more difficult compared with the wild type strain.

Consider the problem of when a cell should switch from one carbon source to another if both are present and changing in its environment. The existence of sophisticated gene regulatory networks for carbon source metabolism indicates that sensing and responding to environmental fluctuations must represent a crucial evolutionary advantage to the cell. Consider the converse: if the environment never changed, there would be no need for metabolic gene regulation, since some constant level of expression would be optimal for an eternally static environment. Of course an eternally static environment is a ridiculous concept, even a carefully controlled chemostat is not completely static if one considers the internal cellular environment. Since cells are continually growing and dividing their internal state is in constant flux due to the cell cycle. Thus, even if the

external environment remains relatively constant, a cell's internal environment will not.

Of course yeast cells did not evolve in the constant environment of a chemostat and thus we should view the cell's genetic architecture in the context of how it's structured to cope with change. One such example of an environmental change problem is a poor quality carbon source present in abundance and a high quality carbon source present in low, perhaps fluctuating amounts; at what point does it become advantageous to invest in the metabolic machinery to metabolize the high quality source? The answer to this question would have to do with the likely future availability of the carbon source which could only be estimated by the past information present to the cell. This information must be stored in the regulatory state of a carbon source utilization network, like the galactose network, with the positive and negative elements playing a role in the storing and processing of this information. Indeed memory effects have been documented in the Gal network (Acar et al., 2005), however the extent to which changing environments could be generated for probing cellular gene networks in a tightly controlled experimental platform has been limited. Now with the microfluidic technology I developed and described in Chapter 3, it is possible to generate tightly controlled, dynamic environments while tracking the fate of hundreds to thousands of cells for relatively long time periods. This technology has enabled the capture of high quality data sets which shed light on the regulatory dynamics of the Gal network.

4.3.4 Primary hypothesis

The explored hypothesis comes from the question stated in section 4.3.1, concerning the role of induced negative feedback in signal detection. I speculated that induced negative feedback prevents the cell from synthesizing expensive metabolic machinery in response to transient spikes in galactose availability. In this sense, negative feedback would filter high frequency input, which probably has a high likelihood of disappearing from the environment. These concepts were explored in a previous set of experiments by our lab (Bennett et al., 2008). While transients should be filtered, it would

be advantageous for the cell to detect low levels of a steadily increasing, high quality carbon source. In this case, mobilizing the metabolic machinery necessary to utilize this resource before competitors do would be crucial. Here the presence of positive feedback would lead to a more sensitive system, able to detect small concentrations of the inducer molecule. The positive feedback component would act as an amplifier, generating a fast, robust response to positive changes in inducer availability. However, strong positive feedback loops have the disadvantage of potentially causing the system to over respond to either transient increases in galactose availability or stochastic fluctuations in the regulatory components. In both cases, strong positive feedback would lead to unnecessary activation of the Gal network, representing an expensive waste of metabolic resources. **I hypothesized that inducing both positive and negative feedback enables a rapid, robust Gal network response, tuned to the galactose concentration, while preventing unnecessary activation by inducer transients and stochastic fluctuations.** These ideas are depicted in Figure 4.3

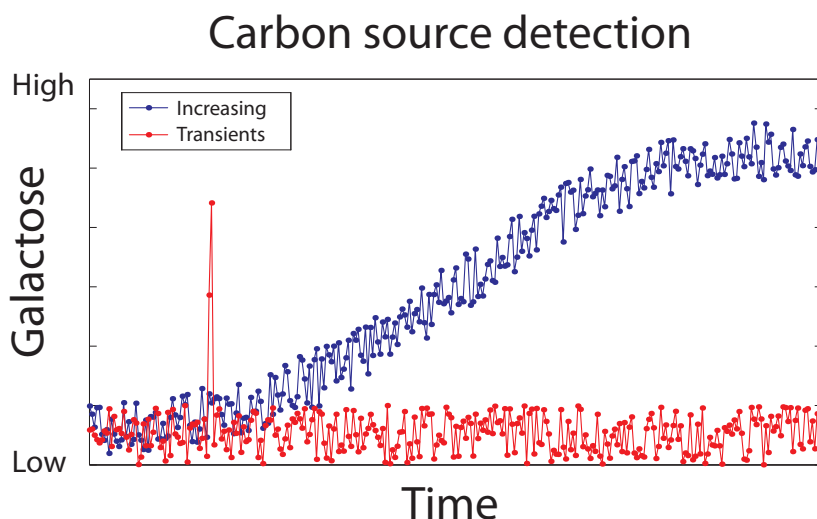


Figure 4.3: General carbon source detection problem as described in the text. The system must be able to tune the metabolic, structural components of the Gal network to the appropriate level based on the carbon source level in the environment. The system must respond optimally to steadily increasing carbon source levels, while filtering transient fluctuations. Furthermore, stochastic fluctuations of the regulatory components must not lead to inappropriate network activation.

4.3.5 Approaches taking to test the primary hypothesis

To test this hypothesis I used a synthetic biology approach, combining modeling of the galactose network with molecular biology and long duration fluorescence microscopy. The idea was to break apart the native *transcriptional* regulation of the Gal network, replace it with artificial regulation and probe the system under various parameter regimes. Towards these goals I created various yeast strains with the positive and negative feedback elements of the network altered. I have compared how these strains respond to galactose induction to the wildtype strain and have developed a better understanding for the role of dual feedback induction in response to stimulus. Moreover I have tagged the genes in the native Gal network with fluorescent fusion proteins so that their dynamics can be followed using flow cytometry and fluorescence microscopy. I have developed a high throughput microfluidic platform for experimentation described in Chapter 3 which has allowed me to probe both the wildtype and altered strains under a variety of dynamic environments.

4.4 Strain construction and promoter testing

As stated in section 4.3.5, I essentially wished to break the Gal network apart and reconstruct it using artificial promoters. This concept is shown in Figure 4.4. The yeast base strain used for all experiments was the K699 strain, a W303 derivative, with genotype *ura3, his3, trp1, leu2* (Jansen et al., 1996; Nasmyth et al., 1990). This strain was chosen because it has wildtype copies of the ADE2 and ADE3 genes, which decreases autofluorescence. Also, unlike the commonly used S288C strain, it contains a wildtype copy of the Gal2 gene (Rohde et al., 2000). The first step of construction was to match the most highly expressed component of the Gal network to the fluorescent protein with the weakest signal. This would ensure that components having a low abundance would still be detectable, within the limits of our technique. From literature studies it was clear that Gal1 would be expressed much more highly than Gal3 or Gal80 and thus it

would be matched with the weakest fluorescent protein. We obtained the yCCFP and yVYFP fluorescent proteins from the O'Shea lab, which are yeast enhanced versions of the popular CFP and YFP proteins respectively (Raser and O'Shea, 2004). I also tested the mCherry (mCh) gene obtained from (Shaner et al., 2004) along with a variety of fluorescent proteins described in (Janke et al., 2004) including a blue fluorescent protein, EBFP and an additional red fluorescent protein, RedStar2.

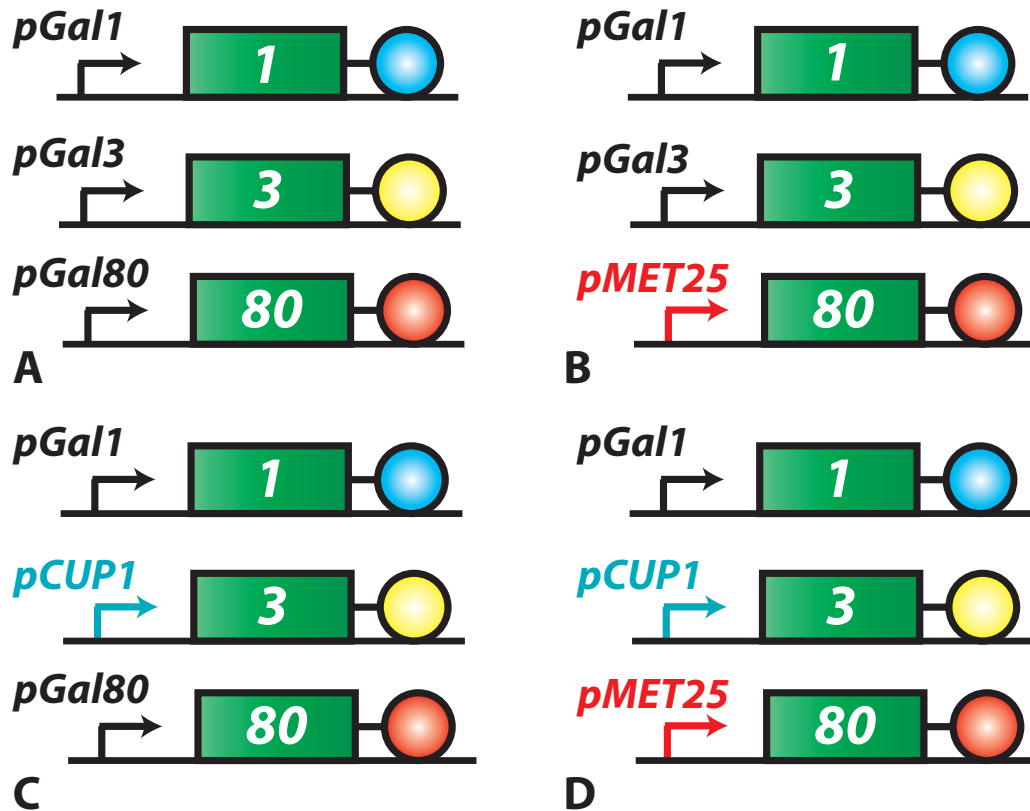


Figure 4.4: General strategy for strain construction to test the hypothesis given in the text. **A.** Modified version of the wildtype yeast strain with each of the Gal genes tagged with separate fluorescent reporter genes. Gal1 is tagged with yCCFP, Gal3 tagged with yVYFP and Gal80 tagged with mCh. **B.** Negative feedback removed strain. The Gal80 promoter was replaced with the pMET25 promoter, the level of which can be set by the methionine concentration in the media. All components are again tagged with the same fluorescent proteins as in part A. **C.** Positive feedback component removed, the Gal3 promoter was replaced with the pCUP1 promoter. **D.** All feedback removed strain: both the Gal3 and Gal80 promoters were removed and replaced with the pCUP1 and pMET25 promoters.

To determine which fluorescent protein was best matched to each Gal gene, fusions were made of every fluorescent protein at our disposal with each of the Gal genes of interest: Gal1, Gal3 and Gal80. Moreover, I also made a fluorescent fusion to the Gal2 gene. To make these fusions a standard technique, known as double fusion PCR, was used. This process allows the combination of three PCR fragments through a series of PCR reactions (Wach, 1996). Generally the fluorescent fusion PCR product was combined with two fragments of ~ 500 bp in length specific for the targeted gene. By adding longer flanking homology regions, the transformation efficiency can be greatly increased (Wach, 1996). Through this process 24 yeast strains were produced, listed MFSC26 to MFSC49 in Table A.1. Each was tested for the strength of the fluorescence signal and the relative signal intensity of the fluorescent proteins. For the final constructs I was limited to one protein in the cyan region, one in the yfp region and one the red region due to spectral overlap. I quickly determined that the yCCFP and yVYFP fluorescent proteins were superior to the alternatives provided by (Janke et al., 2004). Furthermore the mCh protein was determined to give a superior signal to the RedStar2 protein. As described in Chapter 2 this protein is also optimized to tolerate fusions well, something that many red fluorescent proteins are not suited for. I was able to get a superior signal from mCh compared to yCCFP and thus I ranked the available fluorescent proteins yCCFP, mCh and yVYFP from lowest to highest quality. Based on expression data from the library of fusions, I paired Gal1 with yCCFP, Gal3 with yVYFP and Gal80 with mCh in order to optimize the resultant signal from strains with all three gene fusions.

4.4.1 Promoter testing

In order to replace the native Gal promoters with artificial, inducible promoters, a platform was needed to test the strength of each alternative. There were numerous promoters provided by (Janke et al., 2004), some of which were inducible. Unfortunately one of the current limits for synthetic biology is the low availability of controllable promoters, which limits the control one can exert over a genetic network. In yeast there are

few commonly available promoters having a high dynamic range of induction and which can be efficiently repressed. Unfortunately the most commonly used inducible promoter is the Gal1 promoter since it is highly expressed in galactose and can be tightly repressed by glucose (Johnston, 1987). Clearly this promoter would be unacceptable for our purposes, so the alternatives were the pCUP1, pMET25, pADH1-LacI, pADH1-TetR and the pTetO7 promoter. The pCUP1 promoter is inducible over a wide range by copper, while promoters of the pMet family are repressible by methionine (Janke et al., 2004). The pADH1-LacI and TetR are synthetic derivatives of the alcohol dehydrogenase 1 promoter, which are controllable with Isopropyl β -D-1-thiogalactopyranoside (IPTG) and anhydrous tetracycline (ATc) respectively.

The pTetO7 promoter is also controllable with ATc and is the only synthetic promoter in yeast with an expression level comparable to the structural Gal promoters (Belli et al., 1998; Gari et al., 1997). While other yeast inducible promoters exist of course, many are involved in basic metabolism or nutrient assimilation (such as the Pho gene promoters) and thus may be coupled to the Gal network in an indirect manner. To test promoter strengths we again made use of double fusion PCR, targeting the inducible promoters mentioned above to a neutral locus, the His3 locus, which is already non-functional in the K699 strain. Each promoter was fused to the yeGFP gene and integrated at this locus. Additionally we produced strains containing the pGal1, pGal2, pGal3 and pGal80 promoters also fused to yeGFP and targeted to this locus. This procedure allowed comparisons between the promoters we were interested in and the artificial alternatives. Moreover we integrated the constitutive promoters available from Janke at this locus: pGPD, pTEF, pADH1 and pCYC1. The resultant yeast strains were named MFSC1-5,13-22 and 65 (see Table A.1 for exact genotypes). To test these constructs we made use of a BD FACScanTM flow cytometer for comparison of the fluorescent protein signal level in each strain. While other techniques could have been used, flow cytometry would be used for later experiments with these constructs so we wanted to ensure they would be detectable by this technique.

4.4.2 Calibration of the flow cytometer

When using flow cytometry one must select two primary parameters when acquiring data: the voltage and amp gain of the instrument. Ideally a combination of these parameters will be found which uses the instrument's complete dynamic range. For the BD FACScanTM flow cytometer, the dynamic range is 2^{10} . Unfortunately the promoters we tested varied in strength over several orders of magnitude, preventing the same voltage and amp gain settings for use with each sample. Often experimentalists will acquire data in a log binning mode to overcome this issue. This mode uses bins of exponentially increasing size to expand the effective dynamic range of the instrument. However data acquired using log binning is more difficult to analyze since each bin's counts must be normalized by the effective bin size which is often unknown. To address this issue we investigated how the fluorescence signal of our constructs varied as a function of the voltage and amp gain parameters using linear binning. The results of these investigations are given in Figure 4.5. We found that the fluorescence mean of a sample increases as a function of the cytometer voltage by a power-law relationship. A power law is specified by two parameters, an exponent and a scaling factor as shown in Eq.4.1a.

$$y = Ax^b \quad (4.1a)$$

$$Fluor_{mean} = A_{vat}(Voltage)^{7.5} \quad (4.1b)$$

We determined that the exponent is specific for the machine and not the sample. An exponent value of 7.5 fit well for all data collected at various voltage settings, at least with the BD FACScanTM flow cytometer. We note that this flow cytometer was the only one tested and others may be better fit by another exponent value. We also found that there was a machine dependent background value that appeared to vary slightly between experiments. To compensate for this we processed a sample of wildtype yeast as a negative control in each experiment for all voltage values tested. This gave background value which could be used to normalize the mean of the experimental samples for that voltage. The background value was usually at least 2 to 20 times less than the experimental

mean and importantly *did not change appreciably over the instrument's entire range of voltages*. Furthermore this background signal did not appear to be caused by the yeast's autofluorescence, which is not detectable until an extremely high voltage setting is used with this instrument (see Figure 4.6). We speculate that this machine background is caused by a dark current in the instrument's photomultiplier tube, setting its minimum detectable signal. After normalization the data was fit to a power law using an exponent of 7.5 and the scaling factor determined using the curve fitting toolbox of Matlab. The data shown in Figure 4.5 was taken with the MFSC5 strain, containing His3::pADH1-yVYFP. As is shown in the figure, the data is well fit to a power law with an exponent of 7.5. The R^2 value is 0.999 indicating an excellent fit.

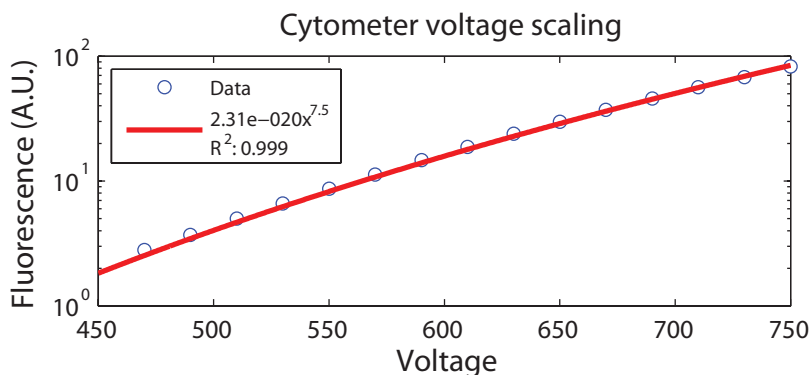


Figure 4.5: Power law relationship between a sample's fluorescence mean and cytometer voltage. This is a semi-log plot with the fluorescence mean of strain MFSC5 His3::pADH1-yVYFP plotted as a function of voltage. The data was fit to a power law with an exponent of 7.5 as described in the text. The fitted curve, with scaling factor and R^2 value are shown in the legend. The R^2 value of close to one indicates an excellent fit to the data.

The scaling factor, or A_{val} as its given in Eq.4.1b, is specific for each promoter and proportional to its strength assuming the power law relationship holds. To confirm that the power law relationship was a valid method to compare promoter strengths, we looked at how the data was transformed by a change of variables as follows: consider two samples, one a reference called x and the other an experimental sample called y . Suppose that the two samples fluorescence mean's follow the power law relationship

with scaling factors of A_x and A_y respectively. Then there must be a voltage gain setting for each (V_x and V_y) where the mean fluorescent values are equal, or:

$$A_x(V_x)^{7.5} = A_y(V_y)^{7.5} \quad (4.2)$$

Solving for V_x in terms of V_y we get:

$$V_x = \sqrt[7.5]{\frac{A_y}{A_x}} V_y \quad (4.3)$$

Consequently, once the scaling factors are determined, we can scale the voltage of an experimental sample using Eq. 4.3 to obtain the voltage producing the same fluorescence mean of a reference sample. If the power law relationship held, all samples should collapse onto a single curve on a semi-log plot once this voltage scaling was applied. We performed this analysis for each of the promoters of interest and the results are given in Figure 4.6. In this figure the mean of each promoter was recorded for several voltage settings and the scaling factors determined. Each promoter was determined to follow the power law relationship as shown in Figure 4.6 part A. After applying the scaling factor, the data collapsed onto a single curve as shown in Figure 4.6 part B, indicating that these data were well described by this family of curves.

In addition to the voltage gain parameter, we also investigated how the fluorescence mean signal scales as a function of the amp gain. The amp gain increases the fluorescence mean in a linear way that is proportional to the signal at an amp gain of 1.0. It is therefore important to realize that the fluorescence increase as a function of amp gain will be different for samples of differing intensity. For example a sample having a mean of 5 with an amp gain of 1.0 will have a mean of 10 at an amp gain of 2.0 assuming the same voltage gain is used. However a sample with a mean of 12 for an amp gain of 1.0 will have a mean of 24 at an amp gain of 2.0. The overall relationship becomes:

$$Fluor_{mean} = A_{val}(Amp_{gain})(Voltage_{gain})^{7.5} \quad (4.4)$$

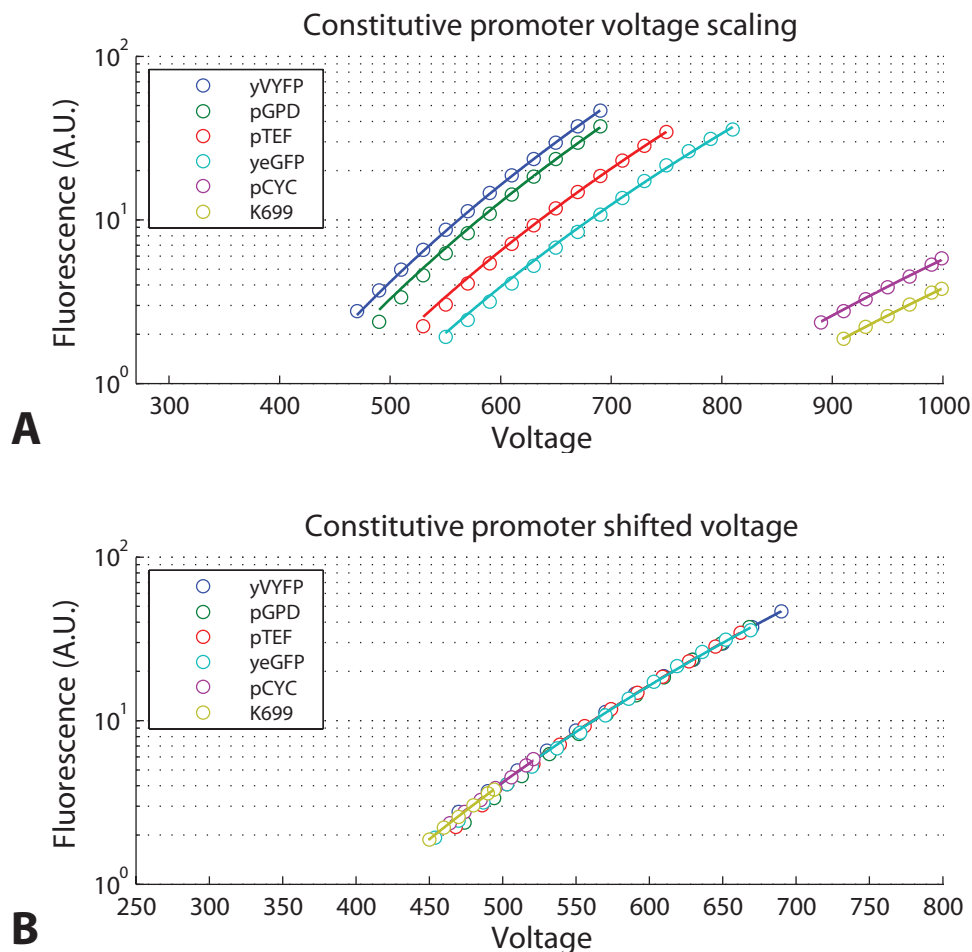


Figure 4.6: Power law scaling for a variety of tested promoters. **A.** Fluorescence mean data taken for the listed promoters as a function of voltage and plotted on a semi-log axis. The power law relationship, with an exponent of 7.5 of each, is well followed. Note that the background auto-fluorescence of yeast is detectable starting at a voltage of near 900. Furthermore this background is separate from the machine background which does not scale with voltage as described in the text. Note that the amp gain was set at 1 for all samples. The tested samples are given in the legend of the figure. **B.** Collapse of all tested samples onto a single curve using the voltage scaling relationship given in the text. This collapsing indicates that the data is well fit by a power law relationship with an exponent of 7.5 for all voltage settings.

This relationship can be used to compare fluorescence means acquired using different parameters on a flow cytometer. This is useful if linear binning is used to acquire the data and the dynamic range of the instrument is insufficient to record each sample with the same settings. For the promoter investigations in this project, we acquired all samples with an amp gain of 1.0 and a range of voltage gain settings to reliably measure the scaling factor (A_{val}) of each promoter.

4.4.3 Results of the promoter strength experiments

Using the techniques described in section 4.4.2 we measured the strengths of the promoters described in section 4.4.1. The results are shown in Figure 4.7 for the constitutive promoters tested. In this figure a typical scatter plot of forward scatter versus fluorescence for the GPD promoter is given in part A. In general there is a strong correlation between forward scatter and fluorescence as expected, and this is true for all promoters except the pADH1 promoter. The pADH1 promoter showed evidence of being bimodal in this type of scatter plot, indicating it may not be the best choice for a constitutive promoter.

The GPD and TEF promoters are the strongest constitutive promoters tested and showed far less variability than the lower strength pADH1 promoter when cells were grown in glucose. This may explain why they are often selected for the promoters of antibiotic resistance genes in yeast. The CYC1 promoter was extremely weak, just barely above the background detection level. Since it is so weak and coupled to the cell cycle, it was not considered useful for this study. We also determined the relative fluorescence of the yVYFP protein compared to the yeGFP protein used for most of the promoter testing constructs. Although the blue light laser of the BD FACScanTM machine is optimized for yeGFP, the signal from the yVYFP protein was considerably stronger. This indicates that yVYFP is a superior alternative to yeGFP for most purposes.

Next the inducible promoter strengths were tested and the results are given in Figure 4.8. As expected no artificial promoter could compare to the Gal1 or 2 promoters

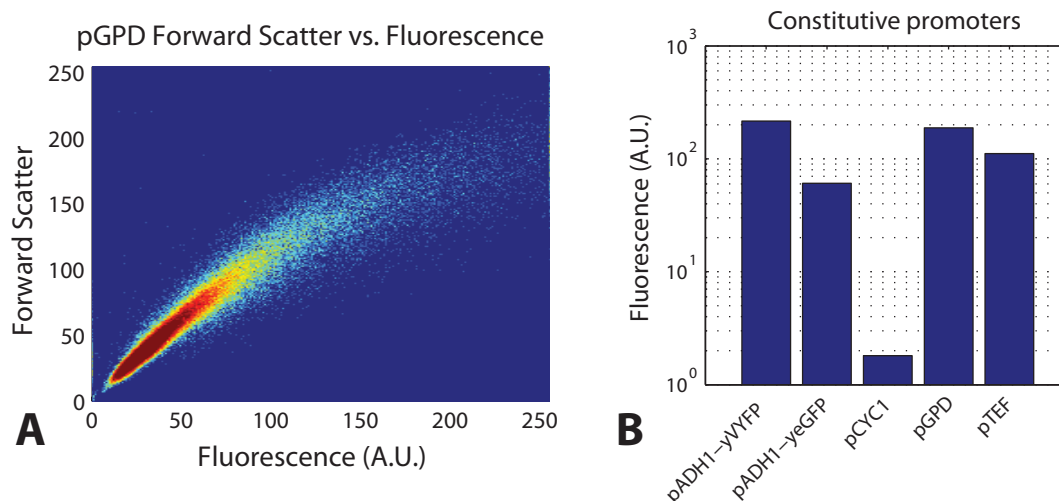


Figure 4.7: Flow cytometry analysis of constitutive promoters. **A.** A typical scatter plot of forward scatter versus fluorescence for GPD promoter. **B.** Bar graph of the fluorescence mean of various constitutive promoters tested, shown on a log scale.

in terms of strength or dynamic range. The Gal3 and Gal80 promoters were close in strength to the pADH-LacI and pADH-TetR promoters. These pADH derivatives seem to have decreased strength compared to the unmodified version (compare Figures 4.7 and 4.8). The pCUP1 and pMET25 promoters were both far stronger than the pGal3 and pGal80 promoters, but weaker than the pGal1 and pGal2 promoters. Additionally the pMET25 promoter, which is repressed by methionine, had a high basal activity level.

The artificial promoters tested in Figure 4.8 were all tested in synthetic complete (SC) media plus glucose and whatever relevant chemical was necessary for induction. However the pGal promoters were tested in SC media plus galactose for induction and glucose for repression. To ensure the artificial promoters would work well in galactose media, additional flow cytometry experiments were conducted. The results of these are shown in Figure 4.9. Unfortunately we determined that the pADH1 promoter has very low activity in galactose, although it is generally thought of as constitutive (Grilly et al., 2007). This promoter drives the production of alcohol dehydrogenase, an enzyme important for fermentative growth. Since yeast grows primarily fermentatively on glucose but not on galactose (Lagunas, 1979) we speculate that less of this enzyme is

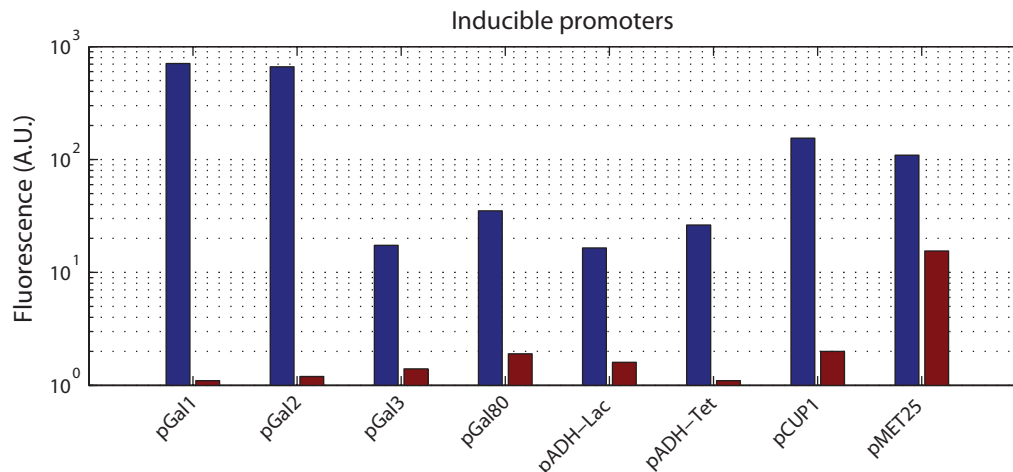


Figure 4.8: Flow cytometry analysis for tested inducible promoters. Bar graph on a log scale is shown for each tested promoter. Blue bar is induced fluorescence mean, red bar is uninduced fluorescence mean. Note that the pMET25 promoter has a high basal activity even in uninducing media.

required in galactose. This low expression would obviously prevent the use of pADH1-Tet and pADH1-Lac promoters for this study, which is unfortunate since their induction levels in glucose media are near that of galactose induced Gal3 and Gal80. This left two choices for the Gal3 and Gal80 replacement promoters: the pCUP1 and pMET25 promoters. Testing of these promoter's activity indicated that both function well in galactose media, although the expression of each was reduced somewhat compared to glucose media (see Figure 4.9 part A). We developed induction curves for each promoter in both glucose and galactose, shown in Figure 4.9 part B.

4.4.4 Cloning work for necessary strains

The results of the promoter strength experiments indicated that pMET25 and pCUP1 would have to be paired to Gal3 and Gal80. However pMET25 was not an ideal promoter due to its high basal activity. Yet pGal80 is also expected to have a higher residual activity than pGal3 under both non-inducing and repressing conditions (Bhat and Murthy, 2001) and slightly elevated concentrations of the repressor would be

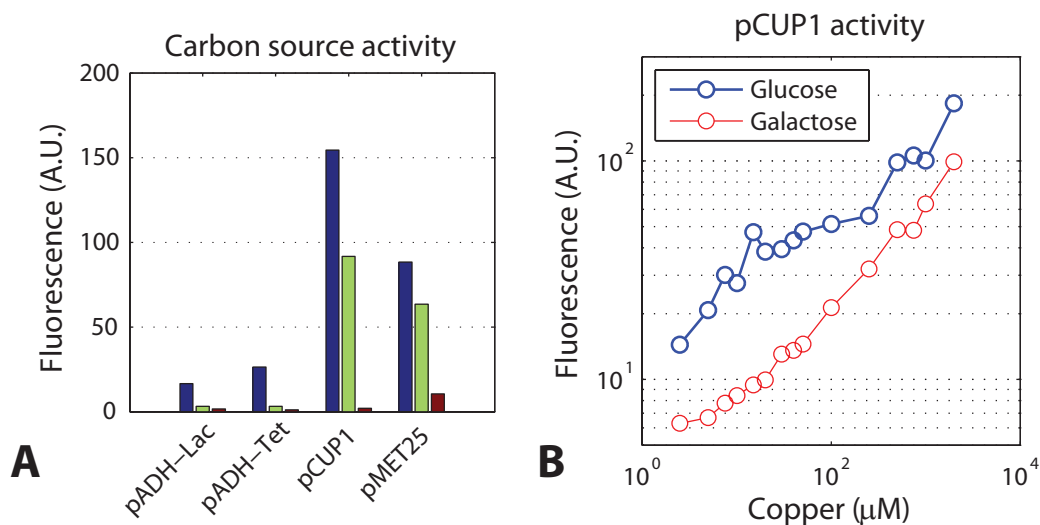


Figure 4.9: Flow cytometry analysis for inducible promoters grown in glucose and galactose media. **A.** Bar graph on a linear scale depicting the expression level for each tested promoter in the different media types. Blue bar is induced fluorescence mean in glucose, green bar represents galactose and red bar is uninducing conditions in galactose. Note that pCUP1 and pMET25 retain activity in both media types but the pADH1 derivatives do not. **B** Induction curve for the pCUP25 promoter in both glucose and galactose media

expected to be less destabilizing than that of the positive feedback component. For these reasons the pMET25 promoter was matched with Gal80 and the pCUP1 promoter was matched to Gal3. The double fusion PCR method was used to generate constructs for tagging the Gal1, Gal3 and Gal80 strains with yCCFP, yVYFP and mCh respectively. Yeast cells were transformed with a standard protocol (Amberg et al., 2005). Whenever possible antibiotic resistance cassettes were used instead of auxotrophic markers due to limit the potential for growth issues (Baganz et al., 1997). Once the triple fusion strain was made it was used as a base for later strain construction. We also produced every possible single and double fusion strain along with numerous deletions (all of these strains are listed in Table A.1). The pCUP1 and pMET25 promoters were used to replace the native pGal3 and pGal80 promoters again using the yeast double fusion PCR procedure; although the pCUP1 promoter proved extremely difficult to fuse to Gal3, possibly due to the GC rich content of the CloneNat resistance marker, to which it was attached. The strains which proved to be most relevant for the current study are listed in Table 4.1.

Table 4.1: Relevant strains produced in this study for which extensive experimental data was collected. HygR refers to Hygromycin resistance, NatR: CloneNat resistance and G418R: Geneticin resistance

Name	Genotype	Parent
MFSC73	Gal1-yCCFP (HygR), Gal3-yVYFP (NatR), Gal80-mCh (G418R)	MFSC70
MFSC101	Gal1-yCCFP (HygR), Gal3-yVYFP (NatR), pMET25-Gal80-mCh (G418R)	MFSC97
MFSC123	Gal1-yCCFP (HygR), pCUP1-Gal3-yVYFP-(NatR), Gal80-mCh (G418)	MFSC71
MFSC124	Gal1-yCCFP (HygR), pCUP1-Gal3-yVYFP-(NatR), pMET25-Gal80-mCh (G418)	MFSC121

4.5 Experimental results for the engineered strains

4.5.1 Flow cytometry results

After producing the triple fusion strain known as MFSC73 (also referred to as wildtype since its Gal gene regulation is intact) the strain was examined by flow cytometry. A BD LSRII™ flow cytometer, capable of detecting the signal from each of

the three fluorescent proteins, was used for the analysis. The results from this strain were compared to the controllable Gal80 strain, MFSC101, for various concentrations of methionine. Recall that the pMET25 promoter used in this strain is *repressible* by methionine and hence higher concentrations of methionine indicate lower levels of Gal80. Each of these strains was grown in various concentrations of galactose to create Gal gene induction curves. To ensure that the Gal network would be fully induced, the cells were grown for 8 hours at 30°C in synthetic complete media. Furthermore raffinose was included at 2 %w/v to ensure that the cells would be able to grow, even at low levels of galactose. To ensure that the growth of the cells would not appreciably alter the level of the carbon source in the media, the cells were passed to an extremely low density ($OD_{600} = 0.01$) before growth. The results of this experiment are given in Figure 4.10.

From these experiments we confirmed that, as expected, Gal80 is a potent inhibitor of the Gal regulatory network, capable of complete repression if expressed at high enough, constitutive levels. The wildtype stain was responsive to a large range of galactose values, from 1×10^{-3} %w/v to 0.1 %w/v, at which point the promoter began to saturate. The dynamic range of the Gal1 promoter in the wildtype strain was close to 30 fold over the background auto-fluorescence level. While this is less than previously reported values (Rubio-Teixeira, 2005; Bhat and Murthy, 2001; Johnston, 1987), the discrepancy is likely due to the background auto-fluorescence of yeast in the yCCFP excitation wavelengths obscuring the true Gal1 level at low concentrations of galactose. Furthermore we found that a Hill function fit the data well, as shown in Figure 4.10, indicating that this class of functions would well describe the induction of this promoter. The fit to a Hill function also indicates cooperativity in the induction of the promoter.

In contrast to the wildtype stain, the Gal80 controllable stain (MFSC101) contained a range of induction behaviors depending on the level of constitutive Gal80 production. As mentioned previously, at extremely high levels of Gal80 (corresponding to 0 μ M methionine), the system was incapable of induction for any level of galactose. We interpret this as indicating that Gal3 is incapable of fully deactivating the high levels of Gal80 in this strain, preventing the activation of the positive feedback loop. In contrast,

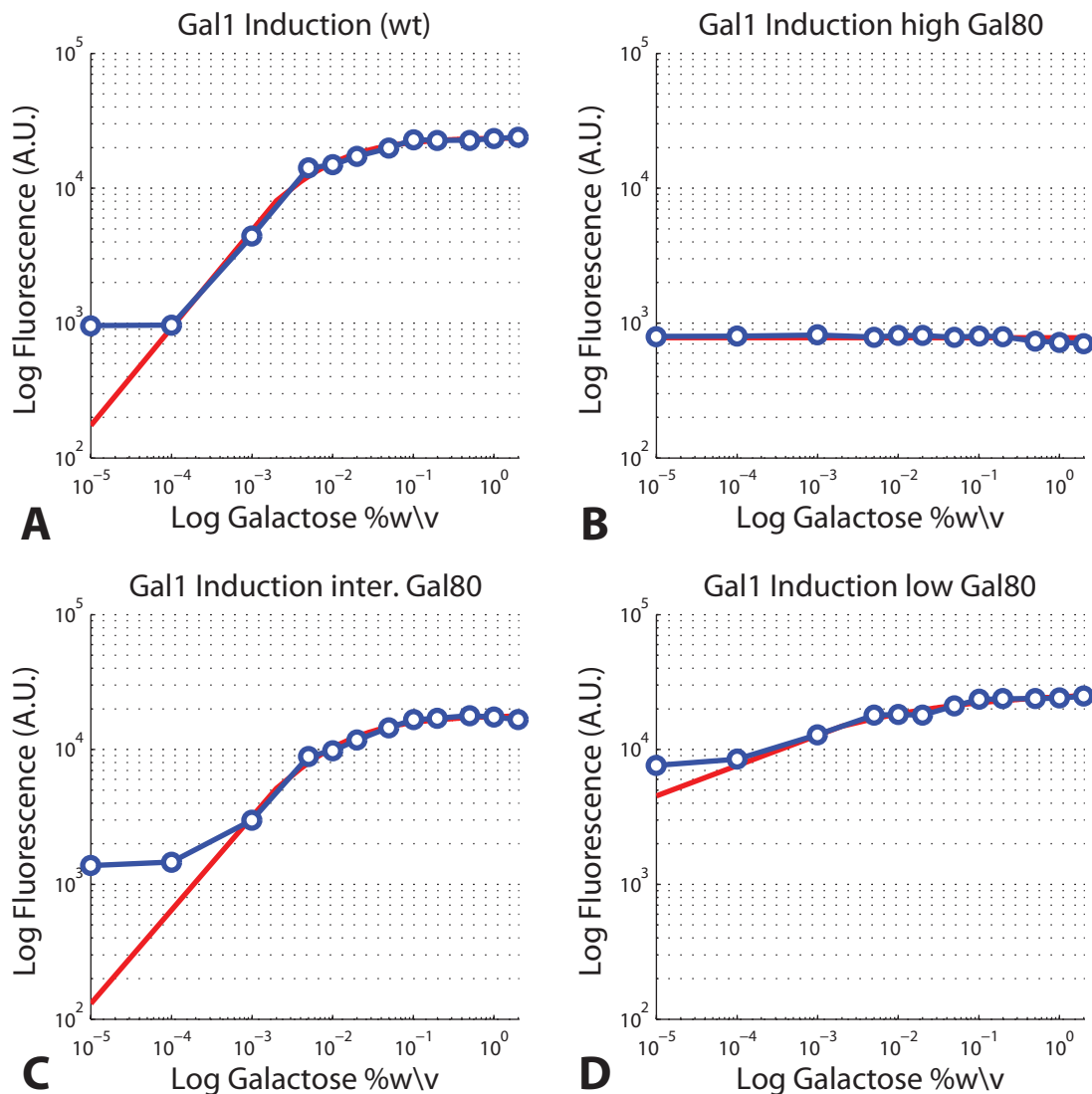


Figure 4.10: Gal1 induction for the wildtype and controllable Gal80 strain at several concentrations of galactose and Gal80. Mean Gal1-yCCFP fluorescence versus galactose is plotted on a log-log axis for each strain. The red line represents a fit of the data to a Hill function. **A.** Wildtype strain's induction for galactose concentrations of 1×10^{-5} to 2 %w/v. The Gal1 promoter saturates at 0.1 %w/v galactose, while below 1×10^{-3} %w/v the activity is below the technique's detectable limit. **B-D.** Induction curves for the Gal80 controllable strain at a high ($0 \mu\text{M}$ methionine, part B), intermediate ($500 \mu\text{M}$ methionine, part C) and low ($5000 \mu\text{M}$ methionine, part D) level of Gal80. High levels of Gal80 leads to a complete repression of the network at all galactose levels. At intermediate levels of Gal80 the network responds well to the inducer, although the maximum Gal1 level is slightly less than the wildtype. At low levels of Gal80 the systems's dynamic range is highly reduced. Unlike the wildtype, or even the same strain at intermediate levels of Gal80, this strain cannot be completely shut off, even at zero to low levels of galactose.

at intermediate levels of Gal80, corresponding to a methionine level of 500 μM , the system was inducible over a similar range compared to the wildtype strain. However, there were differences in the induction profile. First, the promoter required a higher galactose concentration to fully activate (compare the induction levels at 1×10^{-3} %w/v galactose in Figure 4.10 parts A and C), and the maximum induction level was slightly less in the controllable strain versus the wildtype under these conditions. Furthermore at even lower levels of Gal80, corresponding to a 5000 μM methionine concentration, the system was largely on, even at very low levels of galactose. This premature induction results in a severe degradation of the systems dynamic range, as can be seen in Figure 4.10 part D.

In addition to the mean fluorescence levels for galactose induction, we also examined the distribution of fluorescence values in the cellular population at each data point. The results of this analysis for the Gal1 gene for both the wildtype and Gal80 controllable strain at 500 μM methionine are given in Figure 4.11. To accomplish this analysis a custom software program was developed in Matlab to assist in the data processing. This program is called FlowMSF. The FlowMSF software routine was optimized to detect multiple fluorescence modes in a cellular population, something we found lacking in other software alternatives. In part A of this figure it can be seen that at full induction the wildtype strain has a single narrow peak of fluorescence, indicating a uniform response by these cells. In contrast the controllable Gal80 strain behaves differently, as can be seen in Figure 4.11 part B. In both parts A and B of this figure the fluorescence values were plotted on a log axis, so values differing by orders of magnitude could be visualized.

Note that in section 4.4.2 we mentioned that data should be acquired using linear binning, a practice which we continue to follow here. However after acquisition the data was *displayed* on a log axis (which is functionally equivalent to log binning) to enhance visualization. *All statistics were calculated from the linear binned data.* Furthermore due to the 2^{18} dynamic range of the BD LSRIITM instrument, much greater than the BD FACScan, all data could be acquired with the same voltage settings without saturation

problems. To assist in visualizing the data, the cells were gated so only those with forward scatter values within 20% of the mode would be analyzed. Gating by the forward scatter in this way ensures that the population is composed of younger, healthier cells. The controllable strain was found to exhibit bimodal fluorescence, as can be seen in Figure 4.11 part B. The lower mode, with a value of 392 A.U. in this figure, represents the auto-fluorescence of background yeast cells as determined by comparing to the K699 control. The cells in this mode represent members of the population who do not respond to the galactose signal, at least within the detection limits of the technique.

In contrast to the non-responders, the upper mode, with a value of 10886 A.U., represents cells that have activated the Gal system. While these cells are active, the Gal1 level is slightly less than the wildtype cells at full induction, as mentioned previously. This indicates that constitutive Gal80, even at levels permitting some cells to respond in a manner similar to the wildtype, limits the full induction of the Gal system. The population is well separated between the modes, indicating that at least after eight hours of induction the system has approached a stable distribution. However, multiple factors are responsible for generating the fluorescence distributions seen in Figure 4.11. Of course one is the switching frequency of the Gal system under these conditions, which will lead to some cells activating while others will not. Another factor though, is the growth of the cells. While the difference in growth rates between galactose and raffinose media is not extremely large (110 minute doubling time in galactose, 120 minutes in raffinose) over the course of eight hours this difference may skew the population towards responding cells, since non-responders grow more slowly. Thus the population's behavior needs to be viewed from the context of both genetics and growth kinetics.

Due to the bimodality depicted in Figure 4.11, the mean fluorescence of the population was not adequate to describe the true behavior of the system over the range of induction values tested. Instead the FlowMSF program was modified to plot the distribution of fluorescence values for each induction point in a format similar to a scatter plot. Values between induction points were interpolated. This type of analysis depicts how the population as a whole changes with inducer concentration, rather than focus-

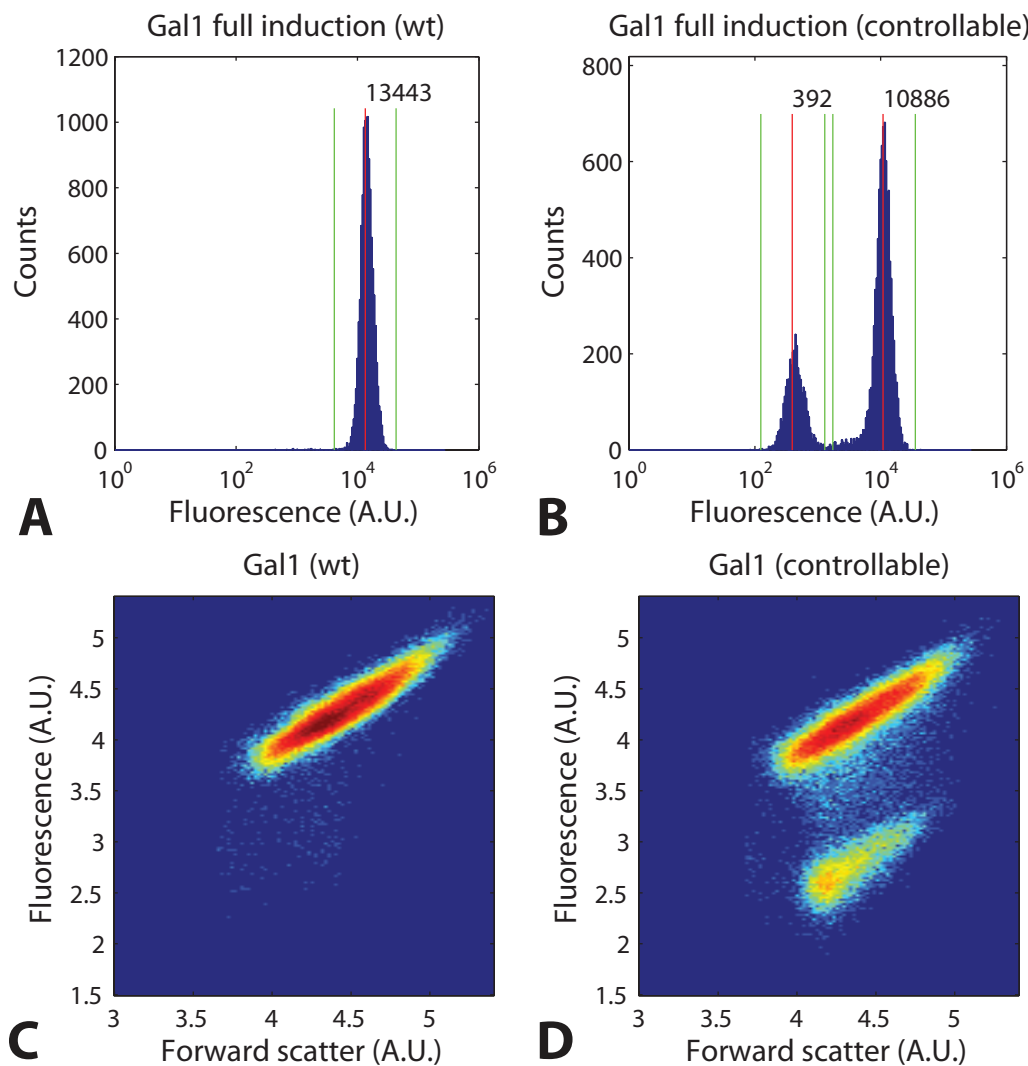


Figure 4.11: Histograms and scatter plots which demonstrate bimodality in the Gal80 controllable strain, but not the wildtype strain, at full induction. Red lines indicate mode locations, with the fluorescence value of the mode given above the line in arbitrary units. Green lines indicate the boundaries of the modes as calculated by the custom Matlab program described in the text. Fluorescence axes for the histograms and scatter plots are log scale. For these histograms the populations were binned to be within 20% of the forward scatter mode. For the scatter plots the population was not binned. **A.** Histogram for the wildtype strain, demonstrating a unimodal distribution at full induction (2% w/v galactose). **B.** Histogram for the Gal80 controllable strain, grown at an intermediate level of Gal80 (500 μ M methionine) and the same galactose concentration as A. Note the appearance of two modes, representing cells which have responded and failed to respond to the inducer. **C.** Scatter plot for the wildtype strain under the same conditions as part A. Note the appearance of a single mode. **D.** Scatter plot for the controllable strain under the same conditions as part B, note the bimodal distribution.

ing on a single statistic such as the mean. Plots for Gal1 induction in the wildtype and controllable strain are given in Figure 4.12. In this figure both galactose and the cell's fluorescence values are plotted on log axes. As shown in part A of this figure, the wildtype strain responds uniformly for all induction values, with the exception of $1 \times 10^{-3}\%$ w/v galactose. At this concentration the wildtype strain has a greater variance in the distribution of fluorescence values, but remains unimodal. In contrast the controllable Gal80 strain exhibits a much different fluorescence profile depending on the level of Gal80.

For high levels of Gal80 ($0 \mu\text{M}$ methionine) the system is uniformly in the non-responding state, and the mean value of the population does an adequate job of representing its behavior. However, for intermediate levels of Gal80, the system is bimodal for virtually all levels of galactose. Notice first the distribution at low levels of galactose ($1 \times 10^{-5}\%$ w/v). Unlike the wildtype strain, this strain displays a wide distribution of fluorescence values, although the majority are concentrated in the non-responding state. This expanded distribution of fluorescence indicates that, at low levels of galactose, intermediate amounts of Gal80 are able to effectively limit most, but not all, cells to the non-responding state. Some cells are able to activate under these conditions, although the level of activation is variable. As the level of galactose increases, the upper mode representing responding cells, becomes increasingly populated. At the critical level of $1 \times 10^{-3} - 5 \times 10^{-3}\%$ w/v galactose, the upper mode becomes the more heavily populated, indicating most cells are responding at this point. Compare, however, the distribution at these galactose concentrations to the wildtype. While the wildtype displays a graded response, with a level of Gal1 evenly spread between the non-responding and fully responded states, the controllable strain displays an all or none response, with fewer intermediate cells. This type of bimodal behavior, with a sharp distinction between the on and the off state, is a hallmark of unconstrained positive feedback and can indicate bistability of the genetic network (Ozbudak et al., 2004). In fact the *Lac* operon, which also contains constitutive levels of the repressor, can exhibit similar behavior for certain inducer concentrations (Ozbudak et al., 2004).

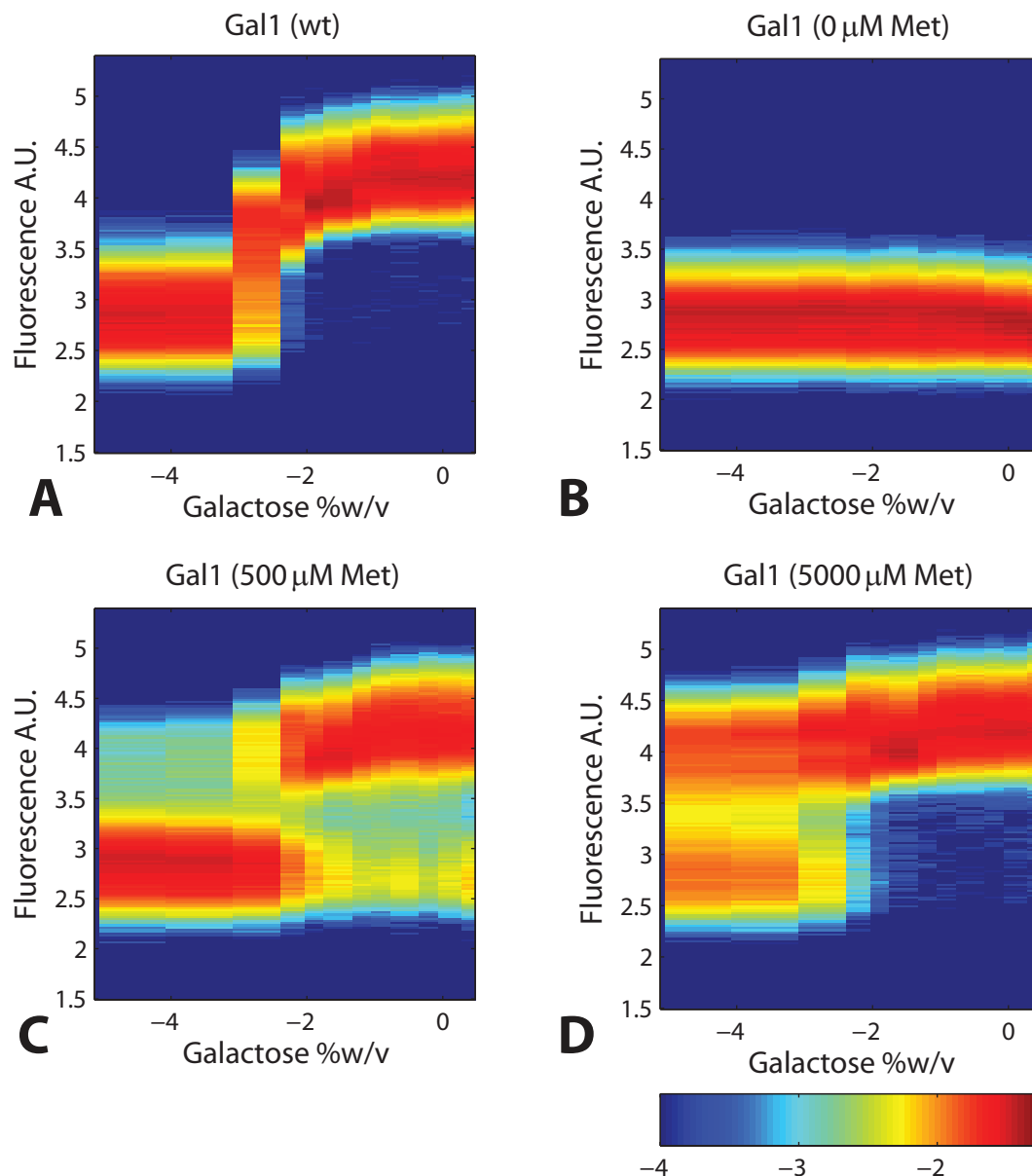


Figure 4.12: Gal1 induction profiles, representing the distribution of cellular fluorescence, for the Gal80 controllable and wildtype strains. All plots are on a log-log axes. The data have been normalized so the total counts for each induction level are equal. The colorbar, also on a log scale, represents number of counts (A.U.). **A.** Wildtype strain: notice the distribution's uniformity at all galactose levels, with the exception of 1×10^{-3} % w/v galactose, when the variance of the population increases. **B-D.** Results for the controllable strain at high, intermediate and low ($0 \mu\text{M}$, $500 \mu\text{M}$ and $5000 \mu\text{M}$ methionine) levels of Gal80. For high Gal80 levels the system is exclusively in the non-responding state, while for intermediate levels, bimodality is evident, with few cells present between the modes. For low levels of Gal80, the system has shifted even further to the responding state compared with intermediate levels.

For intermediate levels of Gal80, the upper mode continues to increase in fluorescence values, even after the major transition point, in a manner similar to the wildtype. As galactose increases, the lower mode becomes less populated, although a significant fraction of non-responding cells remain, even at full induction. In contrast, for low levels of Gal80, the system is almost evenly distributed between the responding and non-responding states for extremely low levels of galactose. This indicates that low levels of Gal80 are incapable of fully repressing the Gal network, even when the inducer is at levels below that which the system should respond to. After the 1×10^{-3} - 5×10^{-3} % w/v galactose transition point, the population is almost exclusively in the responding mode and unlike the intermediate state, few non-responding cells remain (compare Figure 4.12 parts C and D). Note that in the low Gal80 induction curve, the responding cells are able to increase the output of the Gal network slightly as galactose increases. The Gal1 level at full induction is slightly increased over the wildtype for the low Gal80 strain.

To confirm if the other components of the Gal network behave in a similar manner to Gal1, analogous induction curves were generated for Gal3 and Gal80 in both the wildtype and Gal80 controllable strain. The results for the wildtype strain are given in Figure 4.13. As expected, the Gal3 and Gal80 promoters respond in a qualitatively similar manner to the Gal1 gene for the wildtype strain, with a lower dynamic range compared to the structural component. These results were expected, since the promoter structures for the Gal genes are known to be similar (Bhat and Murthy, 2001; Johnston, 1987). The induction curves comprised of mean fluorescent levels are well fit to Hill functions, although not as well as the Gal1 promoter. This may be due to the lower signal to noise ratio for the Gal3 and Gal80 outputs compared to Gal1, which will reduce the curve fitting effectiveness at low induction values. The population plots also show that the Gal3 and Gal80 populations are unimodal and distributed over a fairly narrow range of values for each level of induction.

The Gal3 and Gal80 induction results for the Gal80 controllable strain are shown in Figure 4.14. As can be seen in the figure, the Gal3 gene behaves in a similar fashion

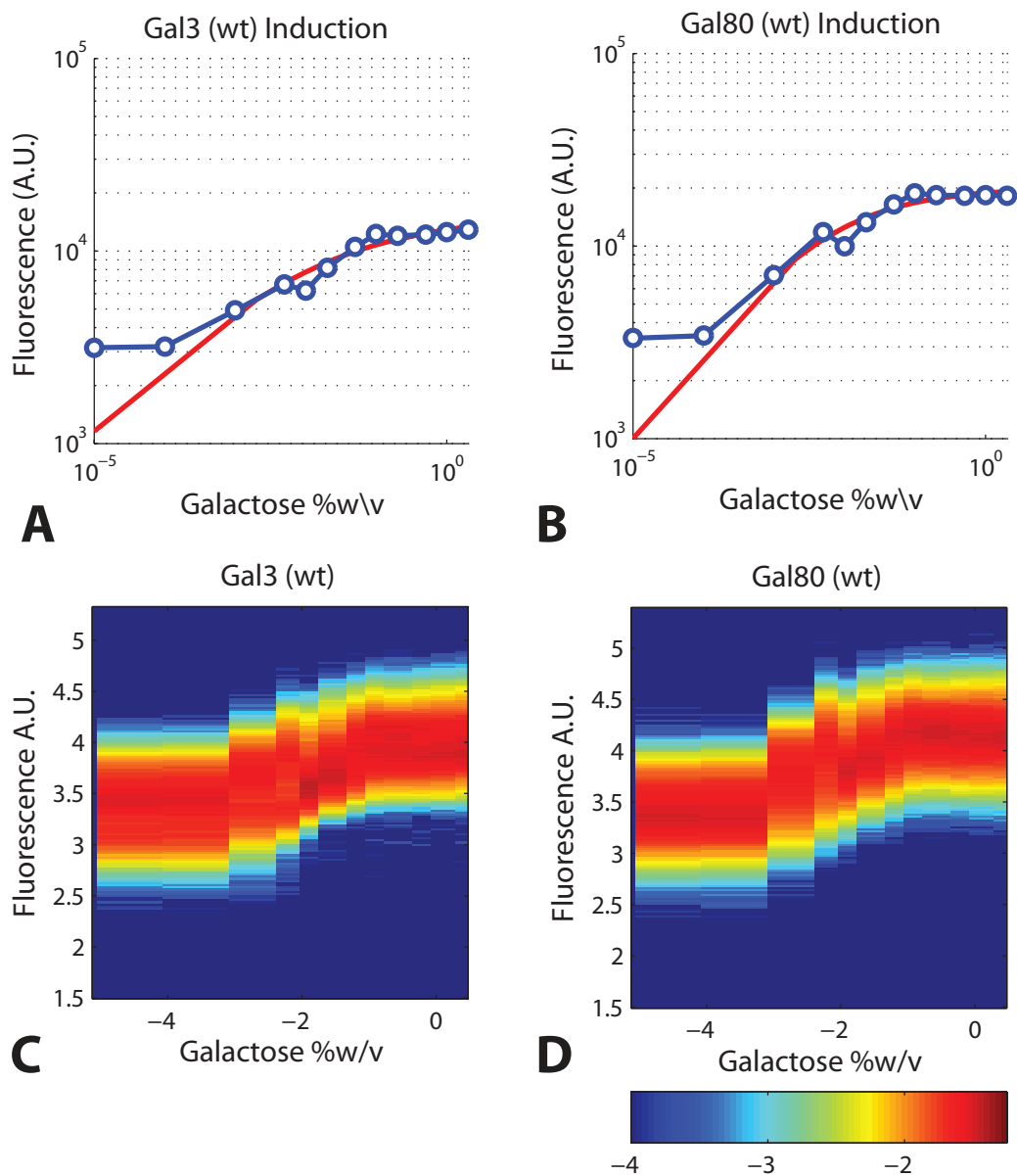


Figure 4.13: Galactose induction curves for Gal3 and Gal80 in the wildtype strain. **A-B.** Gal3 and Gal80 induction curves generated and plotted in same manner as those of Figure 4.10 part A. **C-D.** Scatter plots of Gal3 and Gal80 induction plotted in the same manner as Figure 4.12.

to Gal1 for this strain as well. For high levels of Gal80, Gal3 remains low regardless of the galactose concentration, although it does increase slightly at high levels of galactose. Gal80 remains high for all levels of galactose, as expected. The slight increase in Gal80 at high galactose levels could be due to the pMET25 promoter having a slightly higher expression level in galactose compared to raffinose. For intermediate levels of Gal80, Gal3 is bimodal, although the transition between the two modes occurs over a slightly wider range of galactose concentrations compared to Gal1 (compare Figures 4.12 part C and 4.14 part E). The upper mode clearly shows an increase in intensity with increasing galactose concentration, while the lower mode remains prominent. Gal80 is relatively constant for all levels of induction and has a lower value compared to the 0 μ M methionine level. For low levels of Gal80, Gal3 is again bimodal, although the population is more uniformly distributed between the two modes compared to Gal1. Like the intermediate Gal80 condition, the level of Gal3 increases even in the upper mode for high levels of galactose. Again the Gal80 level is constant and low compared to the other conditions for this strain.

The Gal1 and Gal3 data is summarized in Figure 4.15 for the fold induction in both the wildtype and controllable strains. This figure summarizes the data presented in the induction curves by comparing the difference between induced and uninduced conditions for high, intermediate and low levels of Gal80. As can be seen in the Figure, the wildtype strain has the highest dynamic range of any tested strain or condition, while the intermediate level of Gal80 in the controllable strain comes closest. While the controllable Gal80 strain with a low level of Gal80 is close to or slightly above the activation level of the wildtype when induced, the uninduced level is much greater than in the wildtype. Thus the intermediate level of constitutive Gal80 comes closest to replicating the behavior of the wildtype in terms of dynamic range, although no amount of *constitutive* Gal80 can completely replicate the wildtype Gal network's response.

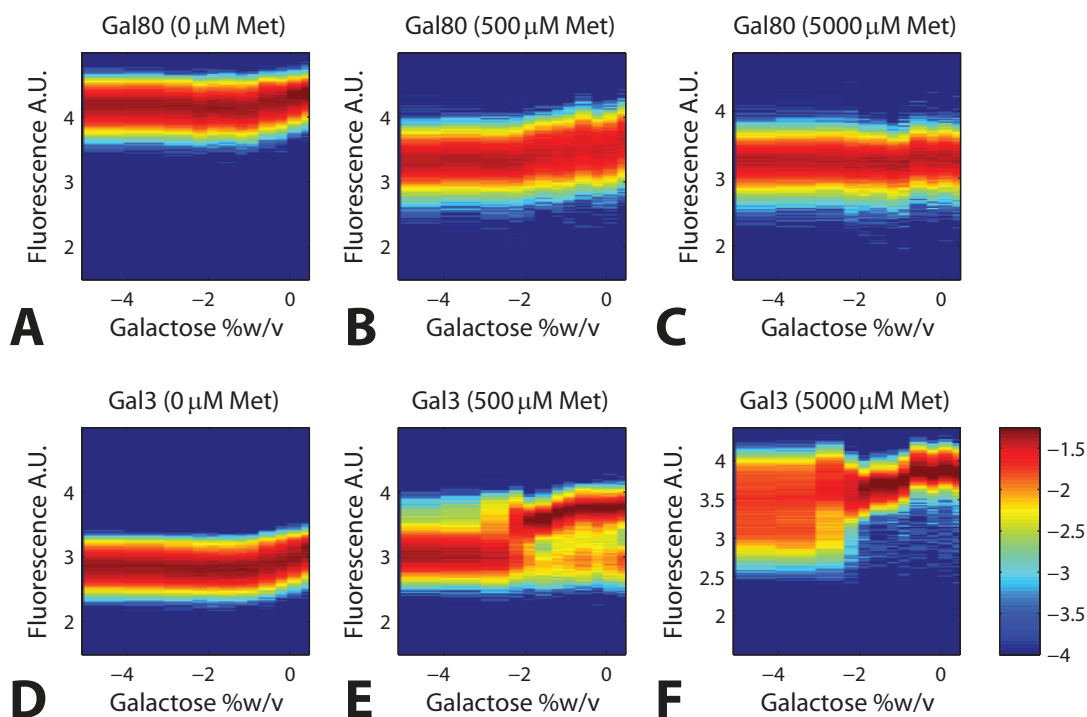


Figure 4.14: Galactose induction curves for Gal3 and Gal80 in the Gal80 controllable strain. All plots were generated using similar procedures to Figure 4.12, except that the cells were gated by 20% of the forward scatter mode. **A-C.** Gal80 levels for methionine concentrations of 0 μM , 500 μM and 5000 μM , corresponding to high, intermediate and low levels of Gal80. **C-E.** Gal3 levels for the same concentrations of methionine in parts A-C. Note similarity to Figure 4.10, although the transition point between the upper and lower modes occurs over a larger range of galactose for intermediate levels of Gal80.

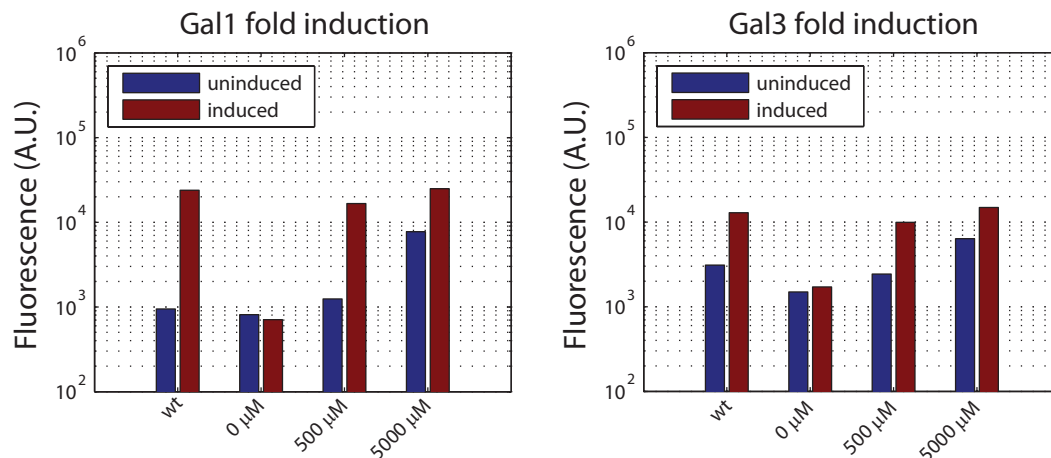


Figure 4.15: Fold change of the Gal1 and Gal3 proteins between inducing and uninducing conditions for the wildtype and controllable Gal80 strains. These data were compiled from mean fluorescence values given in Figures 4.10 and 4.13 **A**. Gal1. Note the wildtype has the largest difference between induced and uninduced conditions, while the intermediate level of Gal80 (500 μ M of methionine) in the controllable strain comes closest of any of the three Gal80 levels. **B**. Gal3 plot similar to part A. The intermediate level condition is again the closest to the wildtype.

4.5.2 The ratio of Gal3 to Gal80

Since Gal3 and Gal80 are the critical players in the regulation of the Gal network, it was of interest to see how each of these components varied in relation to each other over the range of galactose induction. For example, did the bistability of the controllable Gal80 strain result from runaway positive feedback? If so then one might expect to see a higher level of Gal3 in these responding cells compared to Gal80. Conversely, Gal80 might be expected to dominate in the non-responsive cells. In fact, one might expect to see the levels of Gal3 and Gal80 anti-correlated in the controllable strain or even the wildtype strain under some circumstances. To investigate this we used a scatter plot to display the Gal3 versus Gal80 values for the wildtype and controllable Gal80 strains at an intermediate level of Gal80. The results are depicted in Figure 4.16. This figure represents the wildtype and controllable Gal80 strain induced with 0.001% w/v galactose. By examining Figure 4.12 one can see that at this level of galactose, the variance of the wildtype and controllable populations is maximal in terms of Gal1 output. From Figure

4.16 we can see that the behavior of Gal3 and Gal80 in these two strains is quantitatively different.

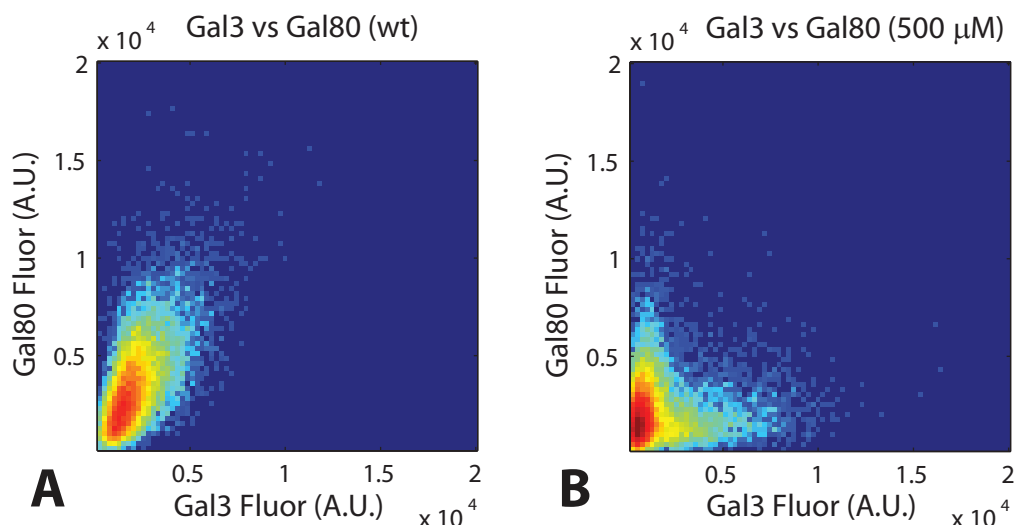


Figure 4.16: Comparison of Gal3 and Gal80 in the wildtype strain and the controllable strain with an intermediate level of Gal80. These are scatter plots with linear axes. All cells were gated to be within 20% of the forward scatter mode, to limit correlations due to size alone. Both plots are from induction with 0.001% w/v galactose. **A.** Wildtype strain. Gal3 and Gal80 are positively correlated as might be expected given that they are both induced in response to galactose. **B** Controllable strain with an intermediate level of Gal80. Note that the levels of Gal3 and Gal80 are biased towards unbalanced ratios. The space occupied by the wildtype strain, a space expected to have similar levels of Gal3 and Gal80, is under represented in the controllable strain.

In the controllable strain, the cells are clustered in two areas: one with a high level of Gal3 versus Gal80 and another with the converse relationship. There is relatively little density between these two clusters, an area which would represent relatively equal levels of the two components. The exception is at extremely low levels of each, which is due to cellular autofluorescence. In contrast the wildtype primarily occupies the space unoccupied by the controllable strain. This is perhaps not too surprising given that both Gal3 and Gal80 are upregulated in response to galactose and would therefore might be expected to have a positive correlation. However the functional consequences of this behavior should be emphasized. In the controllable strain, Gal3 and Gal80 are essentially unbalanced for this level of constitutive Gal80 and galactose. Some cells

have a skewed level of Gal3 compared to Gal80 and some have the reverse. Yet, the levels of these two proteins are much closer in the wildtype and indeed few wildtype cells approach the areas of high density for the controllable strain.

To investigate if the *ratio* of Gal3 to Gal80 is important for the activation of the Gal network, we first examined how this ratio changes as a function of galactose in both the wildtype and the Gal80 controllable strain. To calculate this ratio, the FlowMSF program had to be modified slightly. Since the ratio removes all information about the level of the proteins, we had to carefully exclude the background autofluorescence of yeast to ensure this would not confound the analysis. To accomplish this we gated the cells by the magnitude of their yVYFP and mCh signals. Only cells that were greater than either the yVYFP *or* the mCh threshold were analyzed. Also, since there is a strong positive correlation between fluorescence and size that would be potentially confounding, we gated the cells to retain only those with forward scatter values within 20% of the mode. To ensure that this analysis would not yield data from autofluorescence alone, we examined the K699 negative control. We found that barely any signal from the negative control using the gates and thresholds developed; all fluorescent strains had far more counts for all levels of galactose.

Note that in this analysis, the log of the Gal3/Gal80 ratio is used to compensate for its small values when Gal80 is much greater than Gal3. The results from the Gal3/Gal80 data are shown in Figure 4.17. This figure shows results for the wildtype strain (part A) and the controllable Gal80 strain with two levels of Gal80: intermediate (part B) and low (part C). The wildtype Gal3/Gal80 ratio has a unimodal distribution for all levels of galactose examined. In contrast, the controllable Gal80 strain, with an intermediate level of Gal80, has a bimodal distribution for all levels of galactose examined. Finally the same strain with a low level of Gal80 has a bimodal distribution at low levels of galactose and transitions to a unimodal distribution at high levels of galactose. We also found that the controllable Gal80 strain with a high value of Gal80 had a relatively constant ratio of Gal3/Gal80 at all galactose concentrations. This ratio demonstrated a strong bias of Gal80 to Gal3 in this strain, not surprising giving the other induction

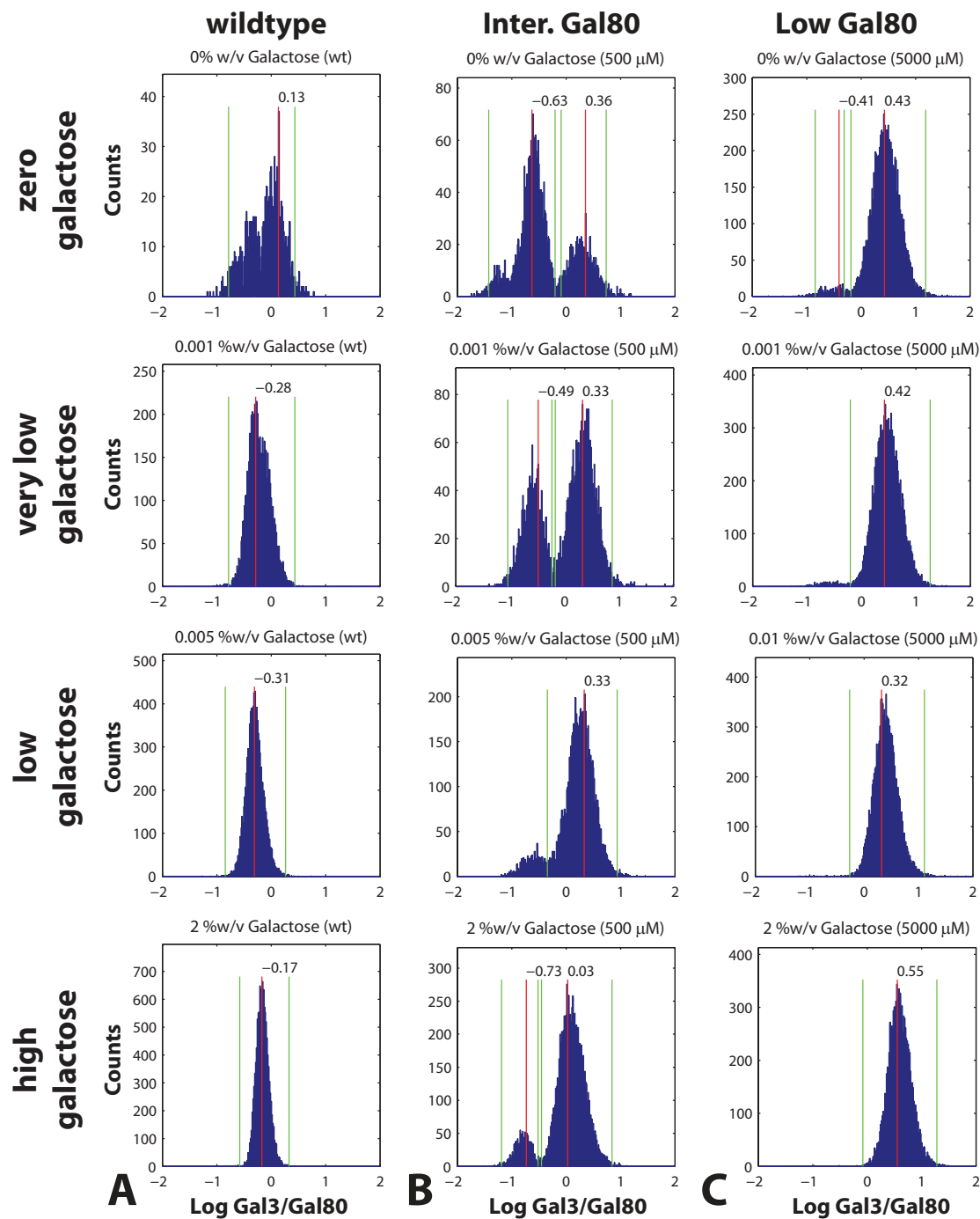


Figure 4.17: Histograms of the Gal3/Gal80 ratio for the wildtype and controllable Gal80 strains at several levels of galactose. For all plots, the x axis is the log of the Gal3/Gal80 ratio and the y axis is counts. Red lines are mode locations, while green lines are mode boundaries. **A-C.** Gal3/Gal80 ratio in the wildtype and the controllable Gal80 strain, with intermediate Gal80 and low Gal80 levels, for four concentrations of galactose.

results. To gain greater insight into the behavior of the Gal3/Gal80 ratio in these strains, we plotted the mode locations and the boundary between the modes for the wildtype and controllable Gal80 strain for all three levels of Gal80. The results of this analysis are shown in Figure 4.18

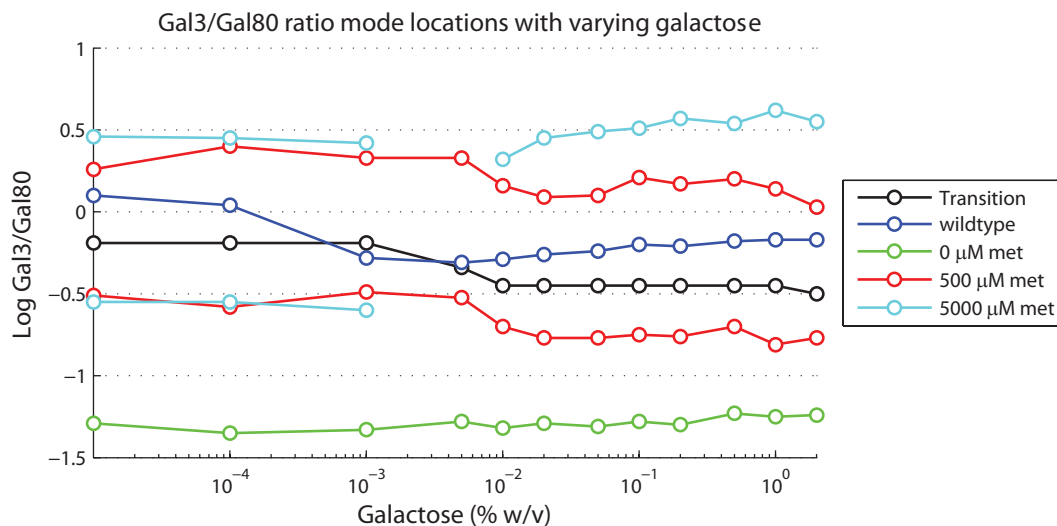


Figure 4.18: Plot of the Gal3/Gal80 mode locations as a function of galactose in the wildtype and controllable Gal80 strain. Black line indicates the boundary between the Gal3 skewed mode and the Gal80 skewed mode in the controllable strain with intermediate levels of Gal80 (500 μM methionine). Green line indicates the mode locations for the Gal80 controllable strain for high levels of Gal80. Note it is heavily skewed towards Gal80 as expected. Red lines indicate the two modes of the controllable strain for intermediate levels of Gal80. The lower line is the Gal80 skewed mode, while the upper line is the Gal3 skewed mode. Cyan lines indicate the two modes for the Gal80 controllable strain at low levels of Gal80. The upper and lower lines represent Gal3 versus Gal80 skewed modes respectively. Note that the Gal80 skewed mode no longer exists for galactose concentrations greater than 0.001% w/v. Blue line is the wildtype mode location. Note that it stays relatively constant after an initial transient for low levels of galactose. Also note that the mode location stays near the boundary between the skewed modes for the controllable strain with an intermediate Gal80 level.

As stated earlier, the Gal80 controllable strain with a high level of Gal80, had a ratio skewed in the Gal80 direction which remained relatively constant for all levels of galactose. The controllable strain with an intermediate level of Gal80 had two modes which shifted in the Gal80 direction between 0.001% w/v and 0.01% w/v galactose.

As seen in Figure 4.12, these galactose levels correspond to the transition point where the majority of cells move from the non-responding state to the responding state in this strain. The boundary point between the two modes is also plotted in Figure 4.18 as a black line. As can be seen in the figure, this boundary location also shifts in the Gal80 direction as the galactose concentration increases. Furthermore, the mode locations for the Gal80 controllable strain with a low level of Gal80 are near that of this strain with an intermediate level of Gal80, for low concentrations of galactose.

While the mode locations are similar, the number of cells contained in each mode differs between the strains, as can be seen in Figure 4.17 parts B and C. Above galactose concentrations of 0.01% w/v, the Gal80 biased mode is no longer present in the controllable strain with low Gal80; only the Gal3 biased mode remains. Note that as galactose levels increase, the Gal3 bias of this mode also increases. For the wildtype strain, the Gal3/Gal80 ratio has a relatively large variance at low levels of galactose, as can be seen in Figure 4.17. At galactose concentrations where Gal network induction becomes detectable (0.001%w/v to 0.01%w/v galactose), the Gal3/Gal80 mode moves near the location of the boundary point between the modes in the controllable-intermediate Gal80 strain. Above 0.01% w/v galactose, the mode locations for the wildtype strain stay above the boundary point and increase slightly in the Gal3 direction with increasing galactose.

To determine how the production of Gal1 is related to the Gal3/Gal80 ratio, we altered the FlowMSF program to generate a scatter plot of these variables. The data was processed the same way as the histogram data in Figure 4.17. The results of this analysis are given in Figures 4.19 and 4.20. In these figures results for the wildtype and controllable Gal80 strain for low and intermediate levels of Gal80 are given. In these figures a white line is drawn representing the mode boundaries determined from the Gal80 controllable strain with an intermediate level of Gal80 (the black curve in Figure 4.18). The white text in the figures gives the Gal3/Gal80 ratio represented by the white line.

For the wildtype strain, the Gal1 level is low as expected for 0.0001% w/v galactose, with a relatively large variance in the Gal3/Gal80 ratio. As galactose increases to

0.001-0.005% w/v, a positive correlation between the value of the Gal3/Gal80 ratio and the Gal1 fluorescence can be seen. Note that the mode value for these two induction levels is almost exactly on the boundary point derived from the controllable strain. Further note that these levels of galactose correspond to the points in the induction curve having the greatest variability for the wildtype strain (see Figure 4.12). As the level of galactose is increased to 0.01% w/v the Gal3/Gal80 ratio in the wildtype strain begins to acquire a Gal3 bias, and when 0.1% w/v galactose is reached, the distribution of fluorescence values is completely off the transition line. Note for the 0.01% w/v induction level there is a slight correlation between the variables for cells near the transition line, but this appears to end for Gal3 skewed ratios. Upon further induction, the mode of the Gal3/Gal80 ratio moves up slightly, indicating increasing Gal1 levels, but stays at the same ratio value.

In contrast, the Gal80 controllable strain at intermediate Gal80 is separated by the transition line into cells which are non-responding (those with a Gal80 skewed ratio) and cells which respond (those with a Gal3 skewed ratio). There is a positive correlation between the Gal3/Gal80 ratio and the Gal1 production level for low levels of galactose. For cells at the 0.0001% w/v induction level, there are no cells with a Gal80 skewed ratio which strongly express Gal1. However there are some cells with a Gal3 skewed ratio which are not fully induced. As the galactose level is increased to 0.001% w/v the number of these cells decreases and two well separated modes are apparent. Again a positive correlation between the Gal3/Gal80 ratio and the Gal1 fluorescence is apparent. When 0.005% w/v galactose is reached, the Gal3 skewed mode is at full induction and a correlation between the Gal3/Gal80 ratio and the induction level no longer is present. The population remains relatively static for higher levels of galactose, although the number of cells in the non-responding mode appears to fluctuate somewhat. The variance of the Gal3/Gal80 ratio is also greater in the controllable strain than in the wildtype for higher levels of galactose (see Figure 4.20 parts A and B).

For low levels of Gal80 in the controllable strain, the system is largely induced even for low levels of galactose. Note that in Figure 4.19 part C the upper panel is

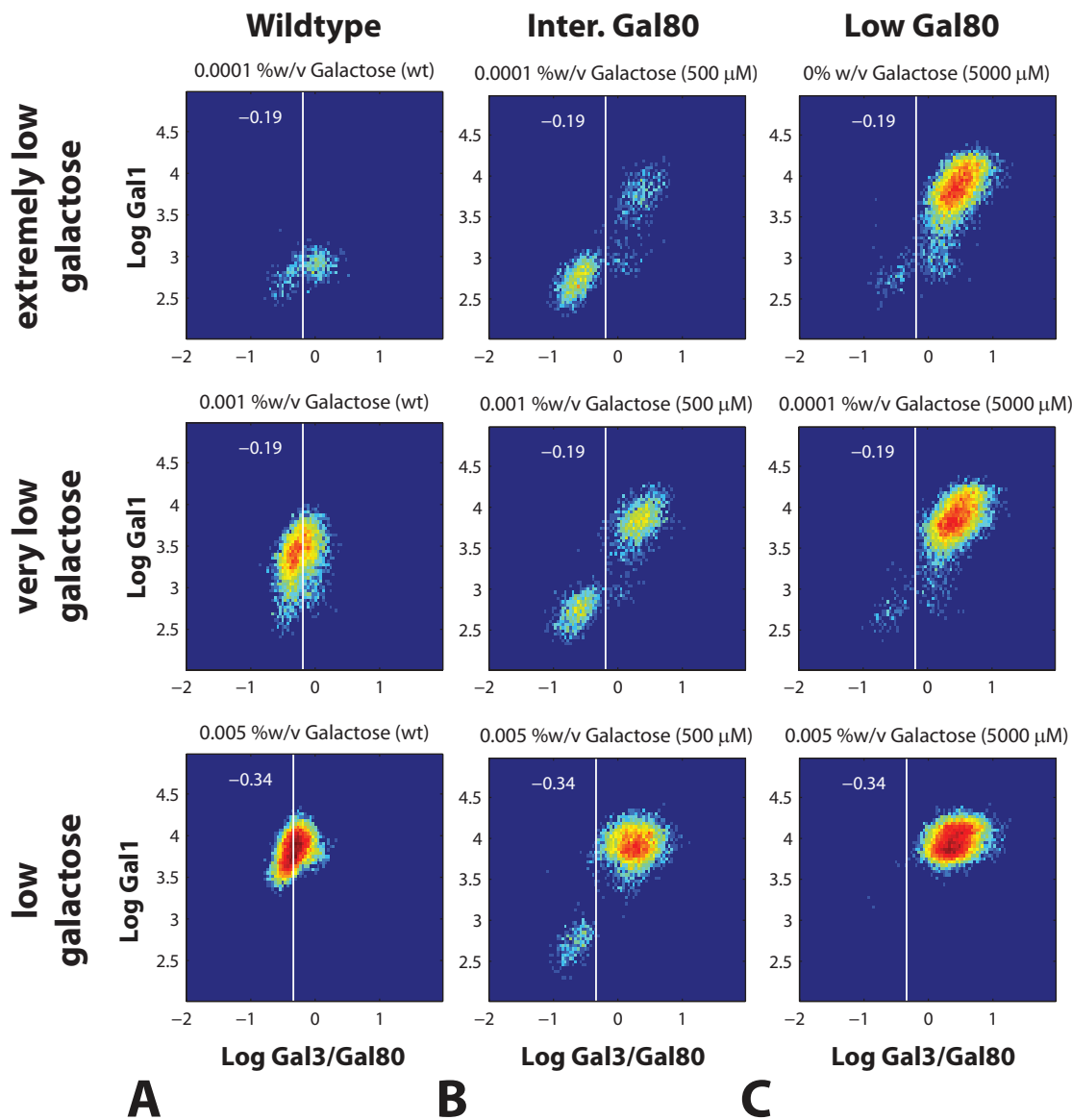


Figure 4.19: Scatter plot of Gal1 fluorescence versus the log of the Gal3/Gal80 ratio for the wildtype and controllable strain: low galactose concentrations. For all plots, the x axis is the log of the Gal3/Gal80 ratio and the y axis is the log of the Gal1 fluorescence. The white line is the location of the boundary between the modes of the controllable strain at intermediate Gal80 levels. **A-C.** Gal3/Gal80 ratio in the wildtype and the controllable Gal80 strain, with intermediate Gal80 and low Gal80 levels, for three concentrations of galactose.

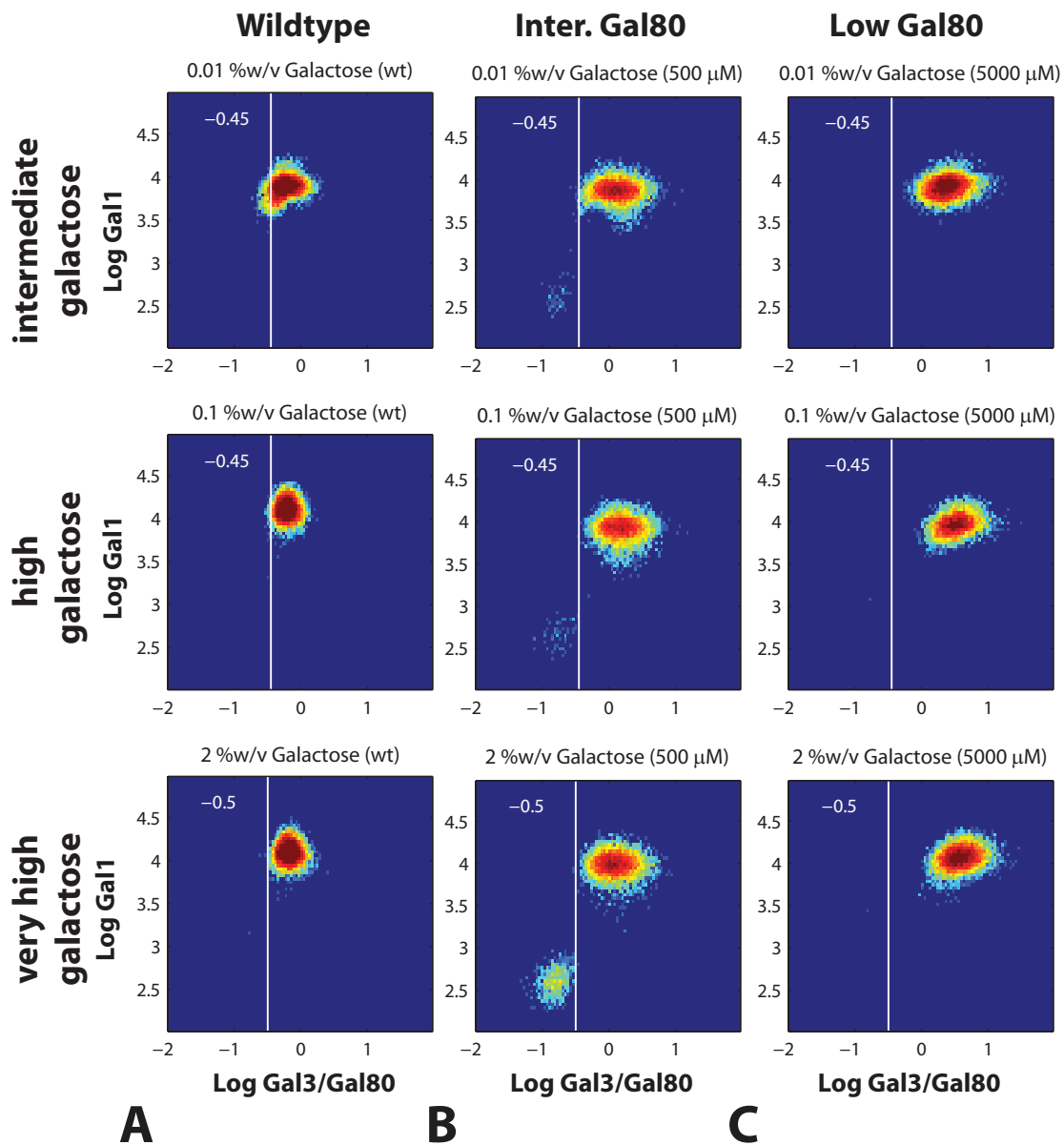


Figure 4.20: Scatter plot of Gal1 fluorescence versus the log of the Gal3/Gal80 ratio for the wildtype and controllable strain: high galactose concentrations. A continuation of the previous figure with results from higher levels of galactose

at 0% w/v galactose, a lower value than any in parts B and C. While there are some non-responding cells with Gal80 skewed ratio, they are fewer in number than in the intermediate Gal80 strain at low values of galactose. Furthermore, the positive correlation between induction level and the Gal3/Gal80 ratio is even more apparent in this strain compared to the intermediate Gal80 level. Moreover, there are also a number of cells with a Gal3 skewed ratio not having a high level of Gal1 production, although these cells are in the minority. At a galactose level of 0.0001% w/v the number of Gal3 skewed cells with low levels of Gal1 has been reduced, while the correlation between the Gal3/Gal80 ratio and Gal1 levels is still strong. At 0.005% w/v galactose non-responding cells are virtually absent and only a slight positive correlation between the variables remains. By 0.01% w/v galactose the correlation has been vastly reduced although the mode value continues to acquire a further Gal3 bias as the galactose level increases to 2% w/v.

4.6 Probing the Gal network with a dynamic environment

While flow cytometry can be useful for studying cells in steady state conditions, to probe the dynamics of the Gal system we turned to the microfluidic devices developed in Chapter 3. We first used the MFD005_a chip for probing the wildtype and the controllable strain with a dynamic environment. An example of the differences between cell types visible by fluorescence microscopy is shown in Figure 4.21. The initial microfluidics experiments confirmed the results from flow cytometry; chiefly that the Gal network exhibited bistability in the Gal80 controllable strain for intermediate and low levels of Gal80. Moreover the cellular state was spatially correlated between neighboring cells, indicating that cells were more likely to be similar to their neighbors than to a randomly chosen cell. All three fluorescent fusion proteins were detectable using the microscopy setup described in Chapter 3, although it was necessary to optimize the exposure times to limit the cytotoxicity of the fluorescence excitation light. The cells

grew well in the chip, although cells in the field of view exposed to the excitation light sometimes appeared to be more heavily vacuolated than cells in regions which were not imaged.

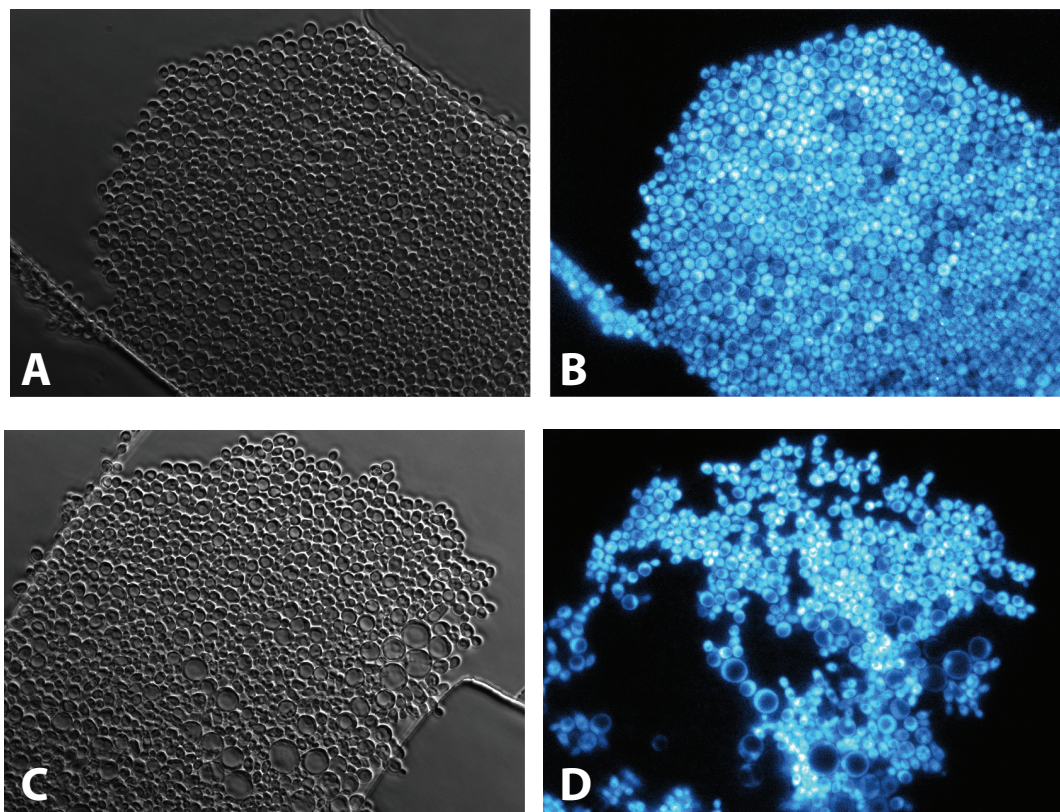


Figure 4.21: A comparison of the cell fields of the wildtype and Gal80 inducible strains grown in the MFD005_a microfluidics chip. **A.** Phase image of the wildtype strain grown in the device. **B.** yCCFP fluorescence from the cell field of part A. Note the uniformity in the fluorescence signal. **C.** Phase image of the inducible Gal80 strain grown in the same device with an intermediate level of Gal80. **D.** yCCFP fluorescence from the cell field of part C. Note areas of responding and non-responding cells, confirming the results of flow cytometry

After confirming the suitability of the MFD005_a device for growth of our engineered strains, we proceeded to measure their response to a dynamic environment. The results of two such experiments are given in Figure 4.22. This figure compares experiments utilizing a sine wave versus a square wave of galactose input. In both experiments

shown in the figure, the wildtype strain was used. The black line in the figure represents the concentration of glucose in part A and galactose in part B. In both experiments the cells were initially grown overnight in 2% w/v raffinose, passed in the morning to an $OD_{600} = 0.25$ in fresh 2% w/v raffinose media and allowed to grow for 3-4 hours. Synthetic complete media was used as the base for each of the input medias (the media in ports 1 and 2 of the MFD005_a device, see Chapter 3). For the inducing media, galactose was included at 0.2% w/v, while for the repressing media glucose was included at 2% w/v. Unlike (Bennett et al., 2008), we did not include galactose in the repressing media since we found it to be unnecessary and sometimes counterproductive. Furthermore, to ensure optimal growth of the yeast cells, the pH of the media was rigorously adjusted to 5.6 before use (Amberg et al., 2005).

From these experiments it was clear that the cells strongly responded to the input drive signal and that the response was detectable in all three channels. Unlike (Bennett et al., 2008), we did not use Sulfarhodamine 101 dye since it interfered with the mCh signal. Instead we used the Atto 655 dye (Sigma Aldrich), since its excitation wavelength of 663nm is far outside the area of mCh emission. As seen in Figure 4.22, the cell's response to the drive proceeds on multiple time scales. The fast component leads to production and degradation of the Gal proteins in close tune with the drive, while an increase in their overall mean's occurs on a longer time scale. The increase in the Gal80-mCh mean appears to take longer to reach a steady state than either that of Gal1 or Gal3. This indicates an unbalance between positive and negative feedback, at least at early time points of induction and may indicate that Gal80 has a role in the attenuation of the network's response. While these response characteristics could be extracted from either drive, we found that the data generated from a square wave drive was simpler to analyze than the sinusoidal drive. Additionally, the system seemed to be perturbed to a greater extent by the sharp transitions in the square wave drive, compared to the less informative tracking behavior evident in the sine wave drive. Consequently all later experiments were performed using a square wave drive.

We were able to track the progress of individual cells in this and later experi-

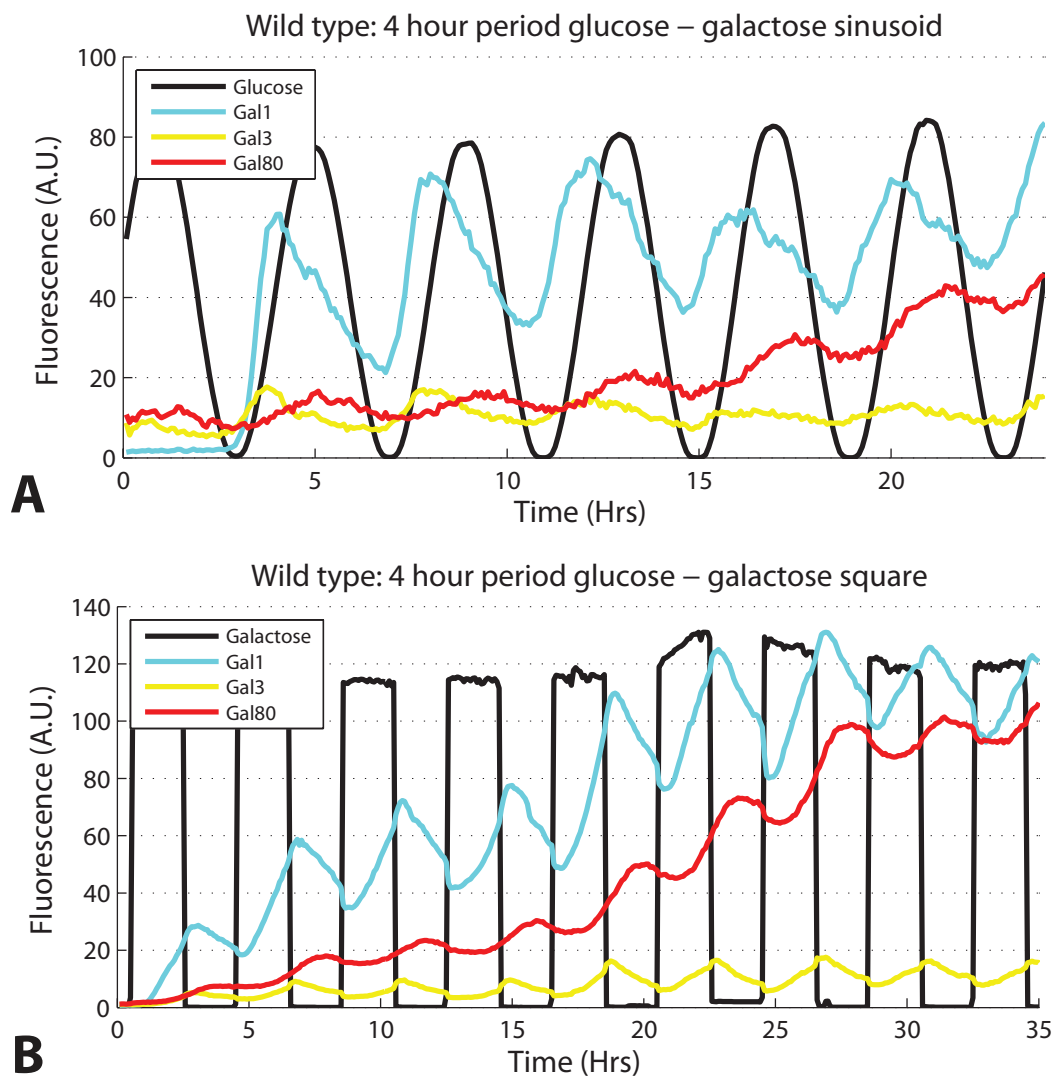


Figure 4.22: A comparison of two induction signals using the MFD005_a microfluidics chip. **A.** Sine wave input to the wildtype strain grown in the MFD005_a device with a period of 4 hours. Components are given in the legend. Note the cells respond well to the drive with a peak that slightly leads the peak of glucose repressor. Also note that Gal1 and Gal3 respond to the drive in a similar manner, while the Gal80 signal has a longer timescale of induction. **B.** Same strain as in part A exposed to a square wave drive. Notice that in this plot the black line indicates galactose (unlike part A where it indicates glucose). The cells also respond well to this drive which is more clear than the sinusoidal drive of part A.

ments using the techniques given in Chapter 3. An example of single cell tracking using the controllable Gal80 strain with an intermediate level of Gal80 is given in Figure 4.23. In part A of this figure, single cell trajectories from this strain are recorded and plotted with the input galactose drive shown in black. Blue trajectories are from cells which initially respond and continue responding over the course of the experiment. Yellow trajectories are from cells which do not respond at any time to the input drive. Red trajectories represent cells which switch between the non-responding and the responding states. While these cells are in the minority, by measuring their appearance, information can be gained on the Gal network's switching frequency under these conditions. In part D of this figure, a return map is depicted which shows how the population changes over the course of one drive cycle. As can be seen in the figure, the cells fall into the same three classes, non-responding, responding and switching with the same associated colors. The return map helps summarize the data from one drive period, making it easier to identify the number and behavior of cells in the population.

While periodic driving can be useful for probing cellular behavior in dynamic environments, eventually the cells reach a pseudo steady state as mentioned previously. At this point in the experiment, information gained is essentially redundant and hence of steadily decreasing value. To expand the power of each microscope experiment, we altered the drive and started using a more powerful device. This device, known as the MDAW device and described in Chapter 3, contains eight subexperiments equivalent to the MFD005_a device on a single chip. This larger device captures far more data at a time, greatly increasing an experiment's throughput. In addition to using this larger device, we began using modified square waves to gain more information from each subexperiment. The square waves were modified by varying the times between the on and off states in the drives. For a periodic drive, the time between states remains constant and defines the drive. In contrast, in this new signal the time between states varied randomly between each cycle. This leads to a signal with much higher frequency content than a periodic drive. In these signals the periods between cycles varied from 15 minutes to 8 hours and we named them random drives.

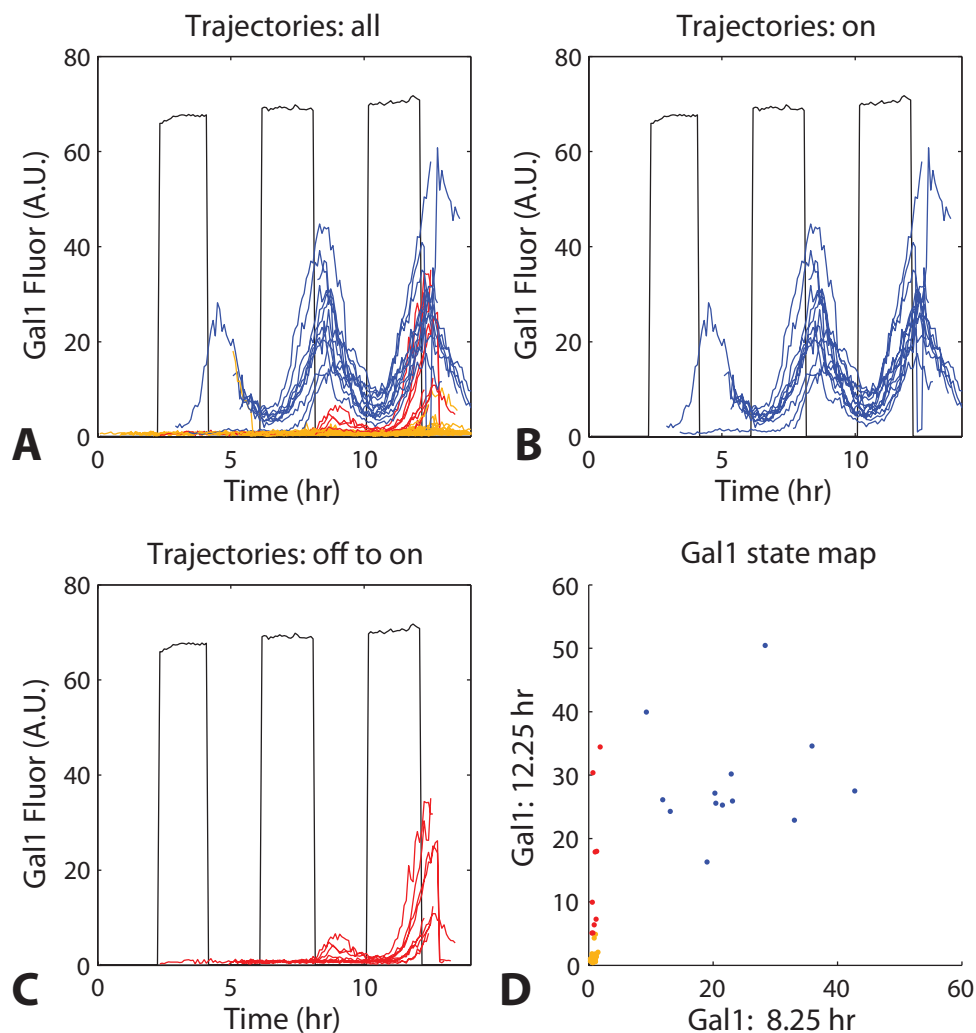


Figure 4.23: Single cell trajectories generated from the controllable Gal80 strain subjected to a square wave drive with a four hour period. Blue trajectories are from cells responding to the input drive, yellow trajectories are from cells which do not respond. Red trajectories are from cells which switch from the non-responding to responding state over the course of the experiment. **A.** All trajectories from the experiment. **B.** Only trajectories from responding cells. **C.** Only trajectories from cells which switch from the non-responding to the responding state. **D.** Return map indicating the state of selected cells over one drive period. Blue cells are responding cells which cluster at high fluorescence values for both time points. Yellow cells cluster at low fluorescence values for both time points. Red cells are those that have switched, which cluster at low fluorescence levels for the first time point and high for the second.

An example of the data captured by a random drive experiment is given in Figure 4.24. In this figure results from three subexperiments are displayed, all from the same MDAW experiment (there are five more for this experiment which are not shown). Fluorescence is plotted on a log scale since the expression of the Gal components varies over orders of magnitude. To demonstrate the device's technical refinement, note that it continued to generate data for over 40 hours. In fact we have run other experiments where nearly 72 hours of data was acquired. In part A of the figure, a periodic square wave drive is displayed and the cells can be seen approaching a pseudo steady state as the experiment progresses. In parts B and C random drive signals are displayed, with the higher frequency content of these signals apparent. Since more frequencies are present, the cellular response to a larger array of environments can be captured. Some of these additional frequencies are ones which might be neglected when choosing a strictly periodic drive, since they might be considered to be of less duration than the cells could respond to *a priori*. When high frequency components are included in the random drive signal, a response can be seen for a pulse of as little as 15 minutes. While the response is not large, it is consistent, indicating that while the system may not respond to high frequency input with a strong amplitude, the signal is still detected.

To demonstrate the superiority of the random drive signal more clearly, Figure 4.25 shows a phase space plot of Gal3 versus Gal80 for both the periodic signal from Figure 4.24 part A and the random drive signals from parts B and C. The mean fluorescence values of the population are plotted in this figure. As can be seen in the figure, the random drive signals explore a far larger space than the periodic signal, confirming what the visual inspection of the response curves suggested. Thus, the random drive represents a more effective use of experimental time and has proven to be a powerful method to generate large quantities of data from a single experiment. Note in this figure galactose exposure times are shown in blue, while raffinose exposure times are shown in red. Transition times between the two carbon sources are shown in green. The beginning and ending of the experiments are shown with green and red dots respectively. Also note that since results from multiple subexperiments are shown, there are multiple

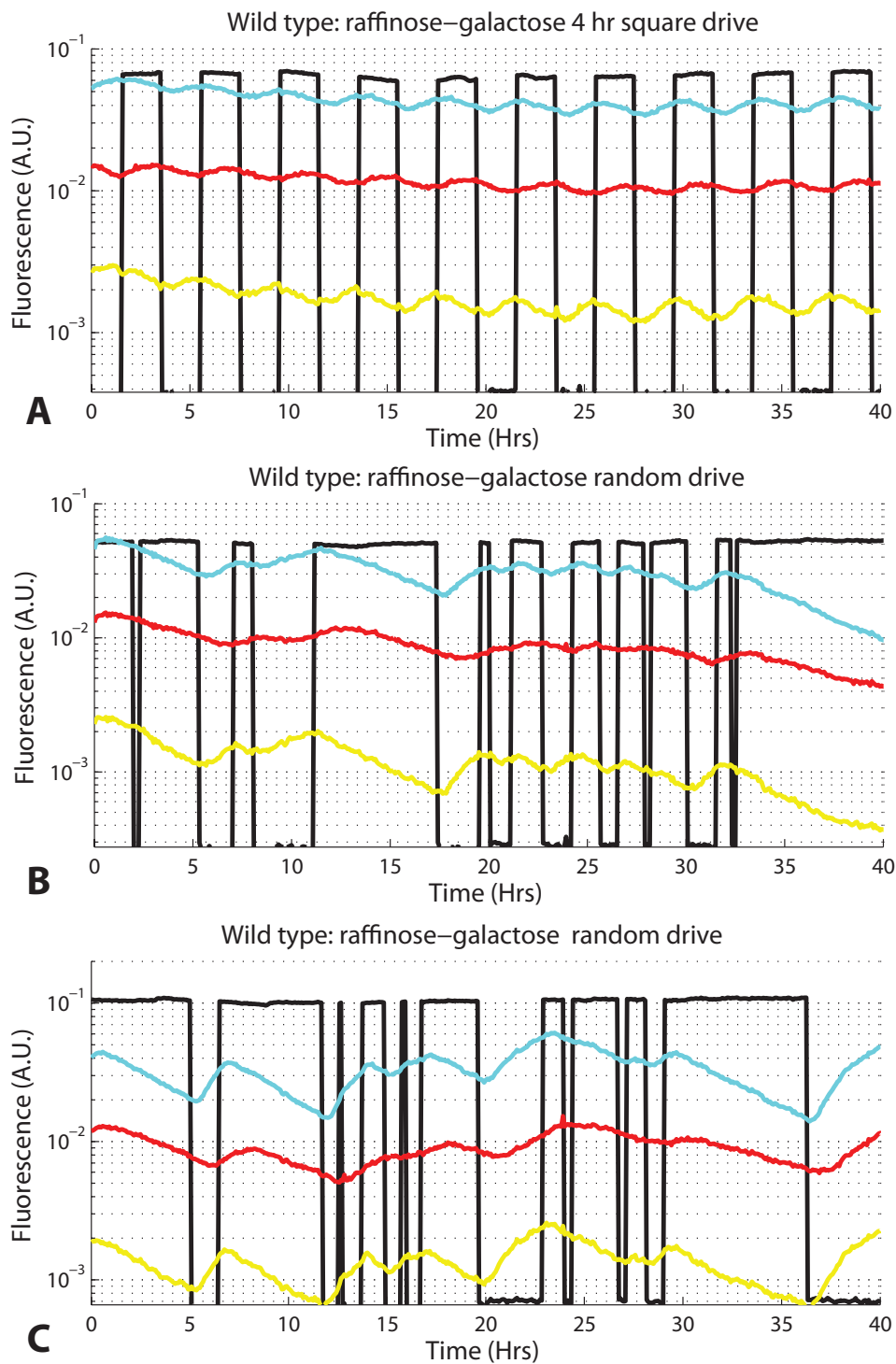


Figure 4.24: Comparison of periodic to random drive signals. Fluorescence axis is log scale. Black line represents galactose, cyan: Gal1-yCCFP, yellow: Gal3-yVYFP and red: Gal80-mCh. **A.** 4 hour periodic square wave. **B-C** Aperiodic, random drive signals.

green and red dots. As can be seen in the figure, when galactose is present in the media the level of Gal3 begins to rapidly increase, while the Gal80 level increases at a lower rate initially. This behavior is in agreement to that shown in Figure ???. Furthermore when raffinose is the sole carbon source the level of Gal3 and Gal80 decrease in a fairly uniform way, likely due to dilution from the cell's growth.

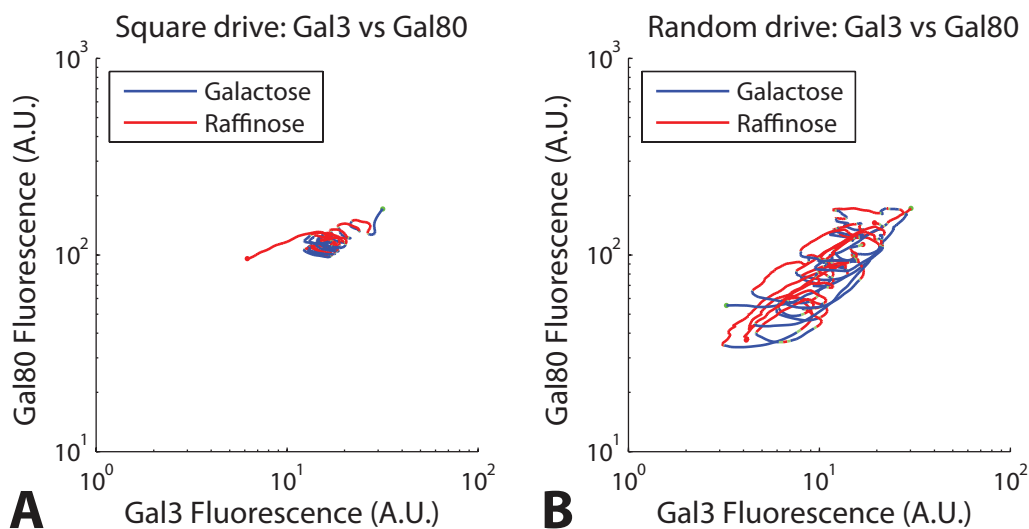


Figure 4.25: Comparison of the phase space explored by a periodic signal compared to the random drive signal. The Gal3 versus Gal80 fluorescence values are plotted in log space for each plot **A**. 4 hour periodic square wave. **B**. Random drive signals from three regions of the MDAW chip.

Next the behavior of a population of single cells was examined over the course of a microfluidics experiment and compared to the steady state data gathered from flow cytometry (described in section 4.5.2). The results are given in Figure 4.26 for Gal1 and Figure 4.27 for Gal3. Both figures contain data collected from the same experiment using the MDAW microfluidic device. The data for each time point (sampled every five minutes) was plotted on a log scale, so widely differing fluorescence values would be visible. Consequently the y-axis of each plot is on a log scale while the x axes are on a linear scale. The data has been normalized to ensure each time point contains the same number of cells. Thus, increases in the number of responding cells indicates that the population has begun to shift states as the experiment progresses and is not simply due

to more cells being present at later times.

Results for the controllable Gal80 strain are given in parts A, B and D for each figure, while the wildtype is shown in part C. The Gal80 controllable strain was cultured at an intermediate level of Gal80. In parts A and B the cells were cycled between glucose and galactose with 4 and 6 hour square wave drives respectively. As can be seen in the figures, the population contains both responding and non-responding cells, although the amount of responding cells increases as the experiment progresses. Compared to raffinose conditions, the Gal network is efficiently repressed when the glucose cycle begins, likely due to the catabolite repression machinery active under these conditions. The behavior of the wildtype strain in a raffinose - galactose drive is shown in part C of the figures. As can be seen in the figures, the wildtype population has a narrower distribution compared to the controllable strain, even though raffinose is a far less effective repressor of the Gal network compared to glucose. Also note the linear increase and decrease in Gal1 and Gal3 production, since the data is plotted on a log axis, this indicates exponential production and decay of these proteins.

Finally compare the response of the controllable Gal80 strain in a galactose - raffinose drive (part D) to the wildtype strain in the same conditions. Clearly there is a large difference between the two responses, indicating that inducible Gal80 is quite important under raffinose conditions. In Figure 4.26 part D note the rapid disappearance of the non-responding cells after only one drive period. Compare this to parts A and B, which contain a persistent non-responding mode for the duration of the experiment. These data indicate that the carbon catabolite repression machinery, which is also a form of inducible negative feedback, is able to prevent transitioning of cells between states quite effectively. Also note the low numbers of cells between the responding and non-responding states (the 5 hour time point in part D of this figure is illustrative of this effect). This is consistent with the flow cytometry data, which indicated an all or none response for the Gal80 controllable cells. Similar to these results, the flow cytometry results also had little density between the states. The lack of cells between states in the driving results is also consistent with the Gal network being rapidly induced upon

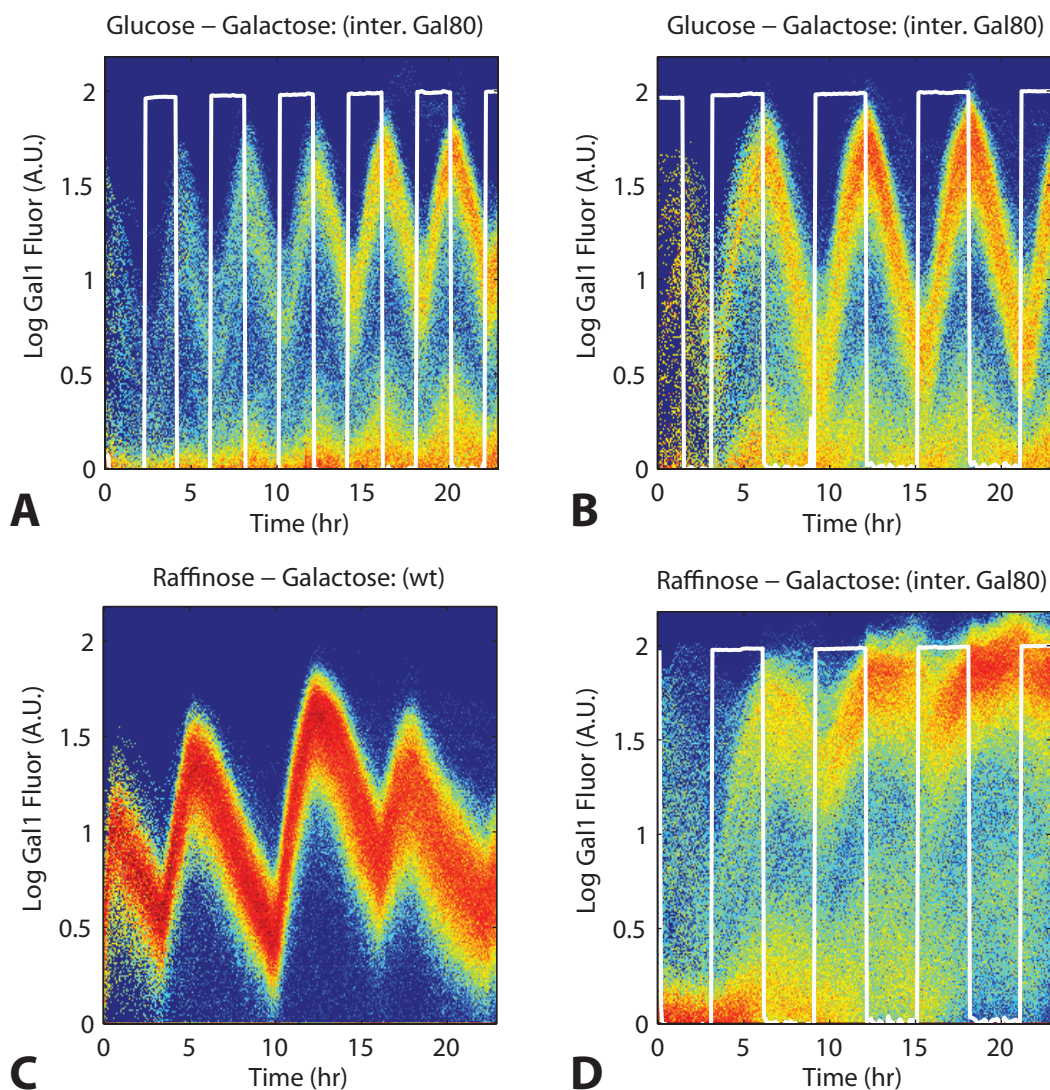


Figure 4.26: Scatter plot of single cell Gal1-yCCFP fluorescence means versus time for the wildtype and Gal80 controllable strain. Drive is shown with a white line and represents galactose in these plots. **A.** 4 hour periodic square wave drive between glucose and galactose for the Gal80 controllable strain at an intermediate level of Gal80. **B** Same conditions as part A except the drive period has been increased to 6 hours. **C.** Wildtype strain cycled between galactose and raffinose with a six hour drive period. **D** controllable Gal80 strain cycled between galactose and raffinose with a six hour drive period.

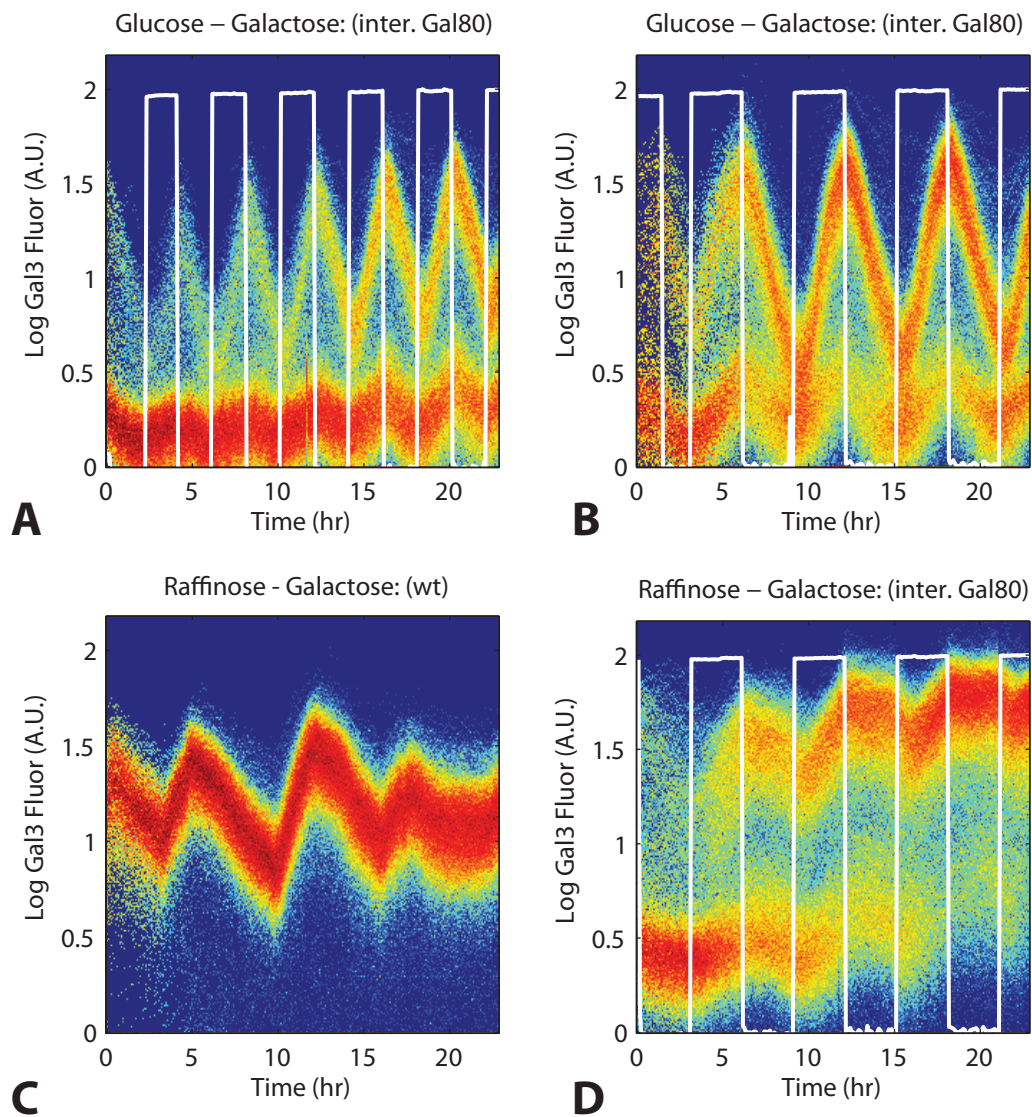


Figure 4.27: Scatter plot of single cell Gal3-yCCFP fluorescence means versus time for the wildtype and Gal80 controllable strain. Same experiment and conditions as Figure 4.26 **A**. 4 hour periodic square wave drive between glucose and galactose for the Gal80 controllable strain at an intermediate level of Gal80. **B** Same conditions as part **A** except the drive period has been increased to 6 hours. **C**. Wildtype strain cycled between galactose and raffinose with a six hour drive period. **D** controllable Gal80 strain cycled between galactose and raffinose with a six hour drive period.

switching to the responding state. In this model, once the threshold for unrestrained positive feedback has been reached, induction is unencumbered by negative feedback and therefore rapid. In contrast to inducing conditions, the negative consequences of unrestrained positive feedback are clearly demonstrated upon the removal of galactose. Note how poorly the Gal network is repressed in a raffinose drive (no induced negative feedback) compared to the glucose drive (induced carbon catabolite repression, compare parts B and D). This indicates that Gal80 has a far larger role to play in repression of the Gal system under raffinose compared to glucose conditions.

The Gal3 results, shown in Figure 4.27 largely mirror those of Gal1, although there are some differences. Compare Figure 4.26 part D to Figure 4.27 part D. In the Gal3 results, the lower mode, representing non-responding cells, persists for a longer period of time compared to Gal1. This may indicate that the Gal1 and Gal3 promoters, often thought to be nearly identical except for their absolute levels of induction, may have slightly different behavior under dynamic conditions. Furthermore, note that in the Gal3 results, like the results for Gal1, there are few cells between the two states, most cells are concentrated near the mean of each state. This behavior again indicates that the Gal system's induction kinetics are likely to be rapid, reflecting the potency of unconstrained positive feedback in these conditions. Moreover, note that the lower state is weakly responding to the input signal, albeit with a far lower amplitude than the upper state. This may indicate that labeling the lower state as non-responders is not entirely correct. In fact these cells do weakly respond, even in a glucose drive. Compare the lower states in Figure 4.27 parts A and B. The lower mode amplitude is greater in the 6 hour drive than it is in the 4 hour drive, likely because the longer drive period allows more time for the Gal system to activate. While this lower state response was not clearly visible for the Gal1 results, this does not necessarily preclude a weak response in the lower state for Gal1. The fluorescence exposure time may have been too low to detect this response, something which can only be rectified by increasing exposure times and comparing to a K699 control.

Finally the Gal3/Gal80 ratio in the driven system was also investigated, using

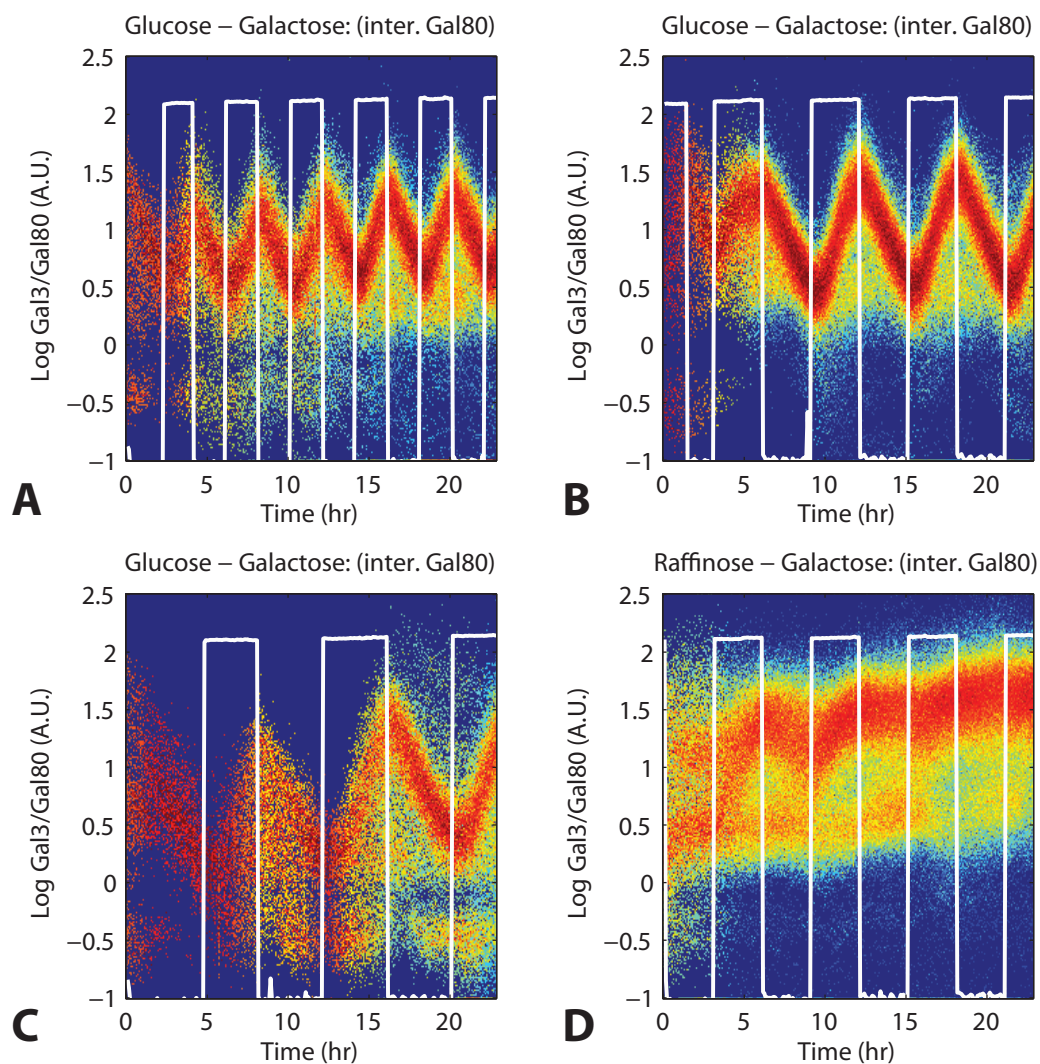


Figure 4.28: Gal3/Gal80 ratio under driven conditions. These data were taken from the same experiment as Figures 4.26 and 4.27. **A.** 4 hour periodic square wave drive between glucose and galactose for the Gal80 controllable strain at an intermediate level of Gal80. **B-C** Same conditions as part A except the drive period has been increased to 6 and 8 hours respectively. **D.** Controllable Gal80 strain cycled between galactose and raffinose with a six hour drive period.

similar techniques to that described in section 4.5.2. Specifically, threshold values for the yVYFP and mCh channels were chosen to limit the contribution of background autofluorescence to the ratio measurements. In contrast to the flow cytometry measurements, the cells did not have to be gated by size (proportional to forward scatter in flow cytometry), since mean, instead of total, fluorescence was extracted for each cell. The results of this analysis are given in Figure 4.28 which shows how the ratio of Gal3 to Gal80 changes in time as a function of the drive signal for the Gal80 controllable strain. All conditions shown in this figure are for intermediate levels of Gal80 (500 μ M methionine). In parts A-C results for glucose-galactose drives of periods 4, 6 and 8 hours are given. In each the ratio fluctuates over a fairly narrow range as a function of the drive period. This indicates that the ratio of the feedback components is sensitive to the drive signal over a range of periods. The amplitude of the Gal3/Gal80 ratio is also larger in the 6 and 8 hour drives compared to the 4 hour drive.

In contrast to the glucose drive results, the raffinose drive leads to fundamentally different behavior. Supporting the results from flow cytometry, a raffinose drive results in a bimodal distribution of the Gal3/Gal80 ratio. It should be noted that the mode values measured here will be different than those measured by flow cytometry in section 4.5.2. This difference is due to the fluorescence values being instrument specific and the readings have not yet been calibrated to provide absolute protein levels. Also note that transitions between the lower and upper modes can be seen at the beginning of each drive period. By the end of each drive cycle, few cells occupy the space between the two modes (referred to as the boundary region). This lack of cells in the boundary region is also consistent with the flow cytometry results, indicating Gal3/Gal80 ratios falling here are unstable and therefore transient. These data indicate a qualitative difference between carbon sources with regards to the Gal3/Gal80 ratio in a dynamic environment. When induced negative feedback is present in the controllable strain, through the induction of carbon catabolite repression by glucose, the Gal3/Gal80 ratio can be maintained in a fairly narrow range and closely tracks the drive. Conversely, when absent due to constitutive Gal80 expression in raffinose, the ratio can no longer track the drive or

even approach a value enabling efficient repression. Thus induced negative feedback is critical for both preventing inappropriate activation and enabling efficient repression; behavior critically important for adapting to a dynamic environment.

4.7 The significance of induced negative feedback

The Gal3/Gal80 ratio represents a balance between positive and negative feedback components in the Gal network. This balance fundamentally differs between the wildtype and controllable Gal80 strains. When Gal80 is produced at an intermediate constitutive level, two modes in the Gal3/Gal80 distribution are present. The Gal3 biased mode represents cells with a dominance of positive over negative feedback; these cells are uniformly responding. Conversely, the Gal80 biased mode represents dominant negative feedback, with uniformly non-responding cells. The region between these modes is unstable in the controllable Gal80 strain, populated by few cells compared to the wildtype strain. This boundary region represents the point where the positive feedback components of the Gal network overwhelm the negative component and the system is pushed into the responding state. Indeed, this type of behavior is common in systems characterized by strong positive feedback and suggests that **one role of inducible negative feedback is to prevent the emergence of bistability in the native network**. While extremely high or low levels of constitutive Gal80 also prevent bistability, they do so at the expense of the system's dynamic range.

Interestingly, the boundary point changes as galactose increases, shifting to a lower Gal3/Gal80 ratio. This indicates that one of galactose's effects is to increase the potency of the positive feedback component. The shift in the Gal3/Gal80 ratio begins at 0.001% w/v and continues until 0.005% w/v galactose. This change is likely related to Gal3's binding to and activation by galactose, known to be required for optimal inactivation of Gal80 (Bhat and Venkatesh, 2005). Thus, the increase in galactose will lead to an increase in the total pool of *active* Gal3 due to the law of mass action. Eventually the amount of galactose will become saturating, resulting in all of the available Gal3 being

converted to the active form. Since the Gal3/Gal80 boundary point does not shift above 0.005% w/v galactose, this appears to be the saturation point. Moreover, since Gal3 and Gal80 are known to *bind* each other in a 1:1 ratio (Acar et al., 2010; Timson et al., 2002), this boundary point likely represents equimolar concentrations of Gal3 and Gal80 in the cell. Intriguingly, the boundary point shift occurs at galactose concentrations leading to maximal Gal1 variability in both the wildtype and controllable strains. This indicates that the Gal network is extremely sensitive at these galactose concentrations, with small changes in galactose or the feedback components causing a large change in output.

In stark contrast to the controllable Gal80 strain, wildtype cells maintain a ratio of Gal3 to Gal80 near the boundary point (determined from the Gal80 controllable strain) at low levels of galactose. Indeed for galactose levels of 0.001% w/v to 0.005% w/v, the mode of the wildtype Gal3/Gal80 ratio lies almost exactly on the boundary point. Interestingly, while the system is located on the unstable boundary point, it does not demonstrate bistability. This would again indicate that inducible negative feedback stabilizes the network against inappropriate activation by the positive feedback component. Even at higher levels of galactose, when the system might be expected to fully commit to the responding state, the Gal3/Gal80 ratio mode remains near the boundary point, although it acquires a Gal3 bias. The wildtype strain therefore maintains a tighter balance between positive and negative feedback than the controllable strain is capable of. Even at high levels of galactose, the Gal3/Gal80 ratio exhibits far lower variability in the wildtype than the controllable strain, an indication of its tight control. The wildtype strain's Gal3/Gal80 ratio appears to quickly achieve an optimal balance between positive and negative feedback which is nearly invariant as the inducer level increases. Negative feedback induction thus allows the Gal network to contain the advantages of positive feedback, in terms of induction speed and strength, without the disadvantage of inappropriate activation. While at first appearing counterintuitive, induced negative feedback is critical for maintaining tunability and optimizing the cell's Gal network mobilization to a level appropriate for the conditions.

While differences were apparent between the controllable Gal80 strain with an

intermediate level of Gal80 and the wildtype strain under static conditions, they were most evident under dynamic conditions. Probing using high-throughput microchemostat devices illustrates the strong advantages of tight feedback balancing in dynamic environments. This balancing allows the wildtype network to occupy a regime where the ratio can be quickly adjusted for changes in carbon source availability, an area unstable in the controllable strain. The consequences of each strain's ability to balance feedback are most apparent in a galactose - raffinose drive, since the induced negative feedback mechanisms from carbon catabolite repression (such as MIG1) are not active. In these conditions, the controllable Gal80 strain's Gal3/Gal80 ratio is again bimodal, mirroring the flow cytometry results. Since the controllable Gal80 strain cannot maintain a Gal3/Gal80 ratio near the boundary point, it is incapable of shutting off the Gal network when galactose is removed, in contrast to the wildtype strain. The wildtype strain is able to quickly respond to the removal of galactose, allowing it to optimally adjust to its new environment.

Thus while examining static conditions allowed us to uncover the existence of bistability in the controllable Gal80 strain, the fitness consequences of this behavior were not immediately apparent. For example, the dynamic range between the controllable strain and the wildtype was similar, at least for the responding cells. However, the negative consequences of unrestrained positive feedback became immediately clear in a dynamic environment. In this case the lack of uniformity and its inability to turn off the Gal network would put the controllable strain at a clear disadvantage compared to wildtype under dynamic conditions. Furthermore, while control of the Gal3/Gal80 ratio was clearly important in static conditions, some of the results were confounding. For example, some controllable Gal80 cells had a Gal3/Gal80 ratio biased for Gal3, but were not induced for low levels of galactose. We speculated that these cells may represent transients, or those transitioning between a uninduced and induced state. This idea was reinforced by the microfluidic experiments, indicating the likelihood of cells moving between a non-responding and responding state, at some points in the drive cycle. Overall our results emphasize the utility and necessity of studying gene regulatory

networks in a dynamic context, the context most applicable to the natural environment.

Chapter 5

Summary

The field of synthetic biology has the potential to revolutionize knowledge of biological networks and function. Much is hoped for from the field; the applications could greatly alter the way food, fuel and medicine are produced and consumed. However there are also those who object to foundations of synthetic biology, those who think altering life poses inherent risks that can never be adequately mitigated or even known beforehand. Thus the field is one which provokes both hope and fear. This dichotomy in the public's response to our field needs to be addressed through education and thoughtful engagement. While those in the scientific community may disagree with the points of some detractors, it is important that these voices are not ignored or trivialized. Otherwise the field may run into the same problems which have plagued genetically modified foods, where the great promise of technology to expand and protect food supplies are rejected simply because of the techniques used to create them.

In Chapter 2, we investigated the dynamics of the frequency (*frq*) gene of *Neurospora crassa* in Castro-Longoria, E.*, Ferry, M.*, Bartnicki-Garcia, S., Hasty, J. and Brody, S., 2010 (*equal contribution). This gene has long been considered essential to the function of the circadian rhythm in this organism. Moreover, deciphering the coupling of core oscillator genes such as *frq* to the output pathways of the circadian rhythm has become a major focus of circadian research. To address this coupling it is critical to

have a reporter of circadian activity that can deliver high resolution spatial and temporal information about the dynamics of core oscillatory proteins such as FRQ. However, due to the difficulty of studying the expression of circadian rhythm genes in aerobic *N. crassa* cultures, little is known about the dynamics of this gene under physiologically realistic conditions. To address these issues we created a fluorescent fusion to the *frq* gene using a codon optimized version of the mCherry gene. To trace the expression and accumulation of FRQ-mCherryNC (FRQ-mCh) during the circadian cycle, growing vegetative hyphae were scanned every hour under confocal microscopy (100x). Fluorescence of FRQ-mCh was detected only at the growing edge of the colony, and located in the cytoplasm and nuclei of vegetative hyphae for a distance of approximately 150-200 μm from the apices of leading hyphae. When driven by the *frq* promoter, we discovered a second FRQ entrance into the nucleus during the circadian cycle; however the second entrance had a lower accumulation level than the first entrance. Thus this fluorescent fusion protein has proven useful in tracking the spatial dynamics of the FRQ protein and has indicated that the dynamics of the FRQ protein's nuclear trafficking may be more complex than previously realized.

In Chapter 3 we investigated novel microfluidic “microchemostat” devices suitable for culturing cells exposed to dynamic environments in Ferry, M.*, Razinkov, I.*, and Hasty, J., 2010 (*equal contribution). We detailed the exact process of making microchemostat devices, from describing the relevant physics governing flow at the microscale, to the cell trap design considerations crucial for a successful device. We mentioned the software programs and techniques relevant to analyzing microchemostat devices, a process that is critical for a well optimized, efficient design. As a case study we explored the steps taken to create two yeast microchemostats, a single chamber design, MFD005_a and its parallel version, the MDAW device. We explored how the fluidic junction of the device was improved from a previous design to optimize its performance for generating dynamic environments. The importance of a shunt network was stressed and the calibration of the system was discussed. We further documented the difficulties in making the MDAW device, mostly concerning how to fit all the nec-

essary features into a compact design. Furthermore the necessity of flow modeling to predict the dimensions of the combined shunt network in this device was emphasized. Next we described the necessary algorithms and techniques for successful cell tracking in microchemostat devices. The importance of properly sampled data, couple with an appropriately designed cell trap was emphasized. We discussed each individual case which is encountered over the course of cell tracking and how improperly sampled data can severely restrict the ability to generate long cell trajectories. Finally we discussed methods and procedures for setting up microchemostat experiments, with an emphasis on practical tips for success. We included comprehensive tables describing the necessary parts for both microchemostat devices and the accessory equipment necessary for their manufacture.

In Chapter 4 we used the tools described in Chapter 3 to investigate the response of the Gal network in *S. cerevisiae* to dynamic stimulus. To accomplish this task we altered the native regulation of the network to remove the transcriptional feedback of the Gal3 and Gal80 genes. By replacing the native promoters with artificial, inducible promoters we were able to see how the system behaved when inducible feedback was no longer available. To achieve these goals we investigated several artificial promoters obtained from a *S. cerevisiae* strain repository using flow cytometry. Over the course of these experiments we developed a method to calibrate the flow cytometer for comparing various sample's fluorescence means measured using different acquisition parameters. Through these experiments we determined that certain promoters derived from the *adh1* gene were not suitable for use in galactose media due to their limited expression. In contrast, other promoters, including the pCUP1 and pMET25 promoters, were capable of high, albeit slightly reduced, expression in media containing either glucose or galactose. After these investigations were complete, we constructed several novel strains using standard molecular biology techniques. The resulting strains were then investigated for their galactose response using flow cytometry and microfluidics. We determined that removal of *inducible* Gal80 expression leads to bistability in the Gal network. Moreover, these cells have largely lost the ability to tune the induction level of

the Gal network to the level appropriate for the inducer. We found that each of the states in the Gal80 controllable strain were well characterized by their the ratio of the positive component, Gal3, to the negative component, Gal80. The wildtype strain was shown closely tracking a Gal3/Gal80 ratio which was unstable in the Gal80 controllable strain. This tracking indicates that inducible negative feedback in the wildtype strain allows the system to be highly responsive to changes in galactose concentration, without risking the potentially negative effects of unrestrained positive feedback. The microfluidic experiments demonstrated that maintaining the Gal3/Gal80 ratio was important for the cellular response to a dynamic environment. However, the ratio could also be controlled by glucose, a strongly repressive carbon source, indicating that multiple pathways interact to control the Gal network's state.

The results of my work indicate that much still needs to be done to understand how organisms cope with *dynamic* environments, the type of environments they encounter every day in the natural setting. Understanding dynamics and the ability to cope with change will be crucial for biological solutions to fundamental problems which affect our society. Algae based approaches to biofuel production are a perfect example of this; the dynamics of an algae pond's environment are not well understood and hence how one strain out-competes another is difficult to understand (Benemann and Oswald, 1996). Often strain optimization is crude and unguided, with only vague notions of "tolerance" to environmental conditions used to select candidates. My research suggests tools and analytical techniques which could be useful for studying competitive advantages in dynamic environments. These tools could be applied to determine the fitness advantages of certain species under conditions simulating those of the natural world. With the knowledge gained from such experiments, rational design of genetic circuits to help a commercially important organism remain stably cultivated in exposed setting will become closer to reality.

Appendix A

Yeast Strains

A.1 Complete strain list

Table A.1: Table of *S. cerevisiae* strains made for this project.

Name	Genotype	Parent	Marker
MFSC1	Gal1::pGAL1-yeGFP	K699	
MFSC2	Gal1::pGAL1-yeGFP	K699	
MFSC3	Gal3::pGAL3-yeGFP	K699	
MFSC4	Gal3::pGAL3-yeGFP	K699	
MFSC5	His3::pADH1-yVYFP	K699	G418R
MFSC6	HO::pGal1-yeGFP	K699	
MFSC7	His3::pADH1-ECFP	K699	G418R
MFSC8	His3::pADH1-EBFP	K699	G418R
MFSC9	His3::pADH1-EYFP	K699	G418R
MFSC10	His3::pADH1-RedStar2	K699	G418R
MFSC11	His3::pADH1-mCh	K699	G418R
MFSC12	His3::pADH1-yVYFP	K699	G418R
MFSC13	His3::pCUP1-yeGFP	K699	NatR
MFSC14	His3::pADH-yeGFP	K699	NatR
MFSC15	His3::pCYC1-yeGFP	K699	NatR
MFSC16	His3::pGPD-yeGFP	K699	NatR
MFSC17	His3::pTEF-yeGFP	K699	NatR
MFSC18	His3::pGAL1-yeGFP	K699	NatR
MFSC19	His3::pGALL-yeGFP	K699	NatR
MFSC20	His3::pGALS-yeGFP	K699	NatR
MFSC21	His3::pMET25-yeGFP	K699	NatR
MFSC22	His3::pADH1-LacI sites -yeGFP	K699	NatR

Table A.1 – Continued

Name	Genotype	Parent	Marker
MFSC23	His3::pADH1-yCCFP	K699	G418R
MFSC24	HO::pCLN2-TetR-PEST-tCLN2	NAO osc.	HygR
MFSC25	HO::pCLN2-TetR-PEST-tCLN2	NAO osc.	HygR
MFSC26	Gal1-yVYFP	K699	HygR
MFSC27	Gal1-RedStar2	K699	HygR
MFSC28	Gal1-mCh	K699	HygR
MFSC29	Gal1-yCCFP	K699	HygR
MFSC30	Gal1-yeGFP	K699	HygR
MFSC31	Gal2-yVYFP	K699	HygR
MFSC32	Gal2-RedStar2	K699	HygR
MFSC33	Gal2-mCh	K699	HygR
MFSC34	Gal2-yCCFP	K699	HygR
MFSC35	Gal2-yeGFP	K699	HygR
MFSC36	Gal3-yVYFP	K699	HygR
MFSC37	Gal3-RedStar2	K699	HygR
MFSC38	Gal3-RedStar2	K699	HygR
MFSC39	Gal3-mCh	K699	HygR
MFSC40	Gal3-yCCFP	K699	HygR
MFSC41	Gal3-yCCFP	K699	HygR
MFSC42	Gal3-yeGFP	K699	HygR
MFSC43	Gal80-yVYFP	K699	HygR
MFSC44	Gal80-RedStar2	K699	HygR
MFSC45	Gal80-RedStar2	K699	HygR
MFSC46	Gal80-mCh	K699	HygR
MFSC47	Gal80-yCCFP	K699	HygR
MFSC48	Gal80-yCCFP	K699	HygR
MFSC49	Gal80-yeGFP	K699	HygR
MFSC50	His3::pGal1-yeGFP	K699	NatR
MFSC51	His3::pGal1-yeGFP	K699	NatR
MFSC52	His3::pGal2-yeGFP	K699	NatR
MFSC53	His3::pGal2-yeGFP	K699	NatR
MFSC54	His3::pGal3-yeGFP	K699	NatR
MFSC55	His3::pGal3-yeGFP	K699	NatR
MFSC56	His3::pGal80-yeGFP	K699	NatR
MFSC57	His3::pGal80-yeGFP	K699	NatR
MFSC58	HO::pCLN2-Gal4-tCLN2	NAO osc.	HygR
MFSC59	HO::pCLN2-Gal4-tCLN2	NAO osc.	HygR
MFSC60	HO::pCLB2-TetR-tCLB2	NAO osc.	HygR
MFSC61	HO::pCLB2-TetR-tCLB2	NAO osc.	HygR
MFSC62	HO::pTEF-TetR	K699	G418R
MFSC63	HO::pGPD-LacI	K699	G418R

Table A.1 – Continued

Name	Genotype	Parent	Marker
MFSC64	HO::pGPD-LacI, His3::pADH1-LacI-yeGFP	MFSC22	G418R, NatR
MFSC65	His3::pADH1-TetR-yeGFP	K699	NatR
MFSC66	HO::pTEF-TetR, His3::pADH1-TetR-yeGFP	MFSC62	G418R, NatR
MFSC67	Gal1-yCCFP	K699	HygR
MFSC68	Gal3-yVYFP	K699	NatR
MFSC69	Gal80-mCh	K699	G418R
MFSC70	Gal1-yCCFP, Gal3-yVYFP	MFSC67	HygR, NatR
MFSC71	Gal1-yCCFP, Gal80-mCh	MFSC67	HygR, G418R
MFSC72	Gal3-yVYFP, Gal80-mCh	MFSC68	NatR, G418R
MFSC73	Gal1-yCCFP, Gal3-yVYFP, Gal80-mCh	MFSC70	HygR, NatR, G418R
MFSC74	Δ Gal2::pUG73	K699	Leu
MFSC75	Δ Gal3::pUG73	K699	Leu
MFSC76	Δ Gal80::pUG73	K699	Leu
MFSC77	Δ Gal2::pUG73, Gal1-yCCFP	MFSC67	HygR, Leu
MFSC78	Δ Gal2::pUG73, Gal1-yCCFP, Gal80-mCh	MFSC71	HygR, G418R, Leu
MFSC79	His3::pGal1-yeGFP	K699	NatR
MFSC80	His3::pGal2-yeGFP	K699	NatR
MFSC81	His3::pGal3-yeGFP	K699	NatR
MFSC82	His3::pGal80-yeGFP	K699	NatR
MFSC83	Δ Gal2	MFSC74	N/A
MFSC84	Δ Gal3	MFSC75	N/A
MFSC85	Δ Gal80	MFSC76	N/A
MFSC86	Gal1-yCCFP, Δ Gal2	MFSC77	HygR
MFSC87	Gal1-yCCFP, Δ Gal2, Gal80-mCh	MFSC78	HygR, G418R
MFSC88	Gal1-yCCFP, Gal3-yVYFP, Δ Gal2	MFSC70	HygR, NatR
MFSC89	Δ Gal2, Δ Gal80	MFSC83	N/A
MFSC90	Δ Gal3, Δ Gal80	MFSC84	N/A
MFSC91	Gal1-yCCFP, Δ Gal2, Δ Gal3	MFSC86	HygR
MFSC92	Gal1-yCCFP, Δ Gal2, Δ Gal3, Gal80-mCh	MFSC87	HygR, G418R
MFSC93	Gal1-yCCFP, Gal2 ?, Gal3 ?, Δ Gal80	MFSC91	HygR
MFSC94	Gal1-yCCFP, Δ Gal2, Gal3-yVYFP, Δ Gal80	MFSC88	HygR, NatR
MFSC95	Δ Gal2, Δ Gal3	MFSC90	N/A
MFSC96	Δ Gal2, Δ Gal3, Δ Gal80	MFSC91	N/A
MFSC97	Gal1-yCCFP, Gal3-yVYFP, Δ Gal80	MFSC70	HygR, NatR
MFSC98	Gal1-yCCFP, Δ Gal2, Δ Gal3, Δ Gal80	MFSC96	HygR
MFSC99	pMET25-Gal80-mCh	K699	G418R
MFSC100	Gal1-yCCFP, Δ Gal2, Gal3-yVYFP, pMET25-Gal80-mCh	MFSC94	HygR, NatR, G418R
MFSC101	Gal1-yCCFP, Gal3-yVYFP, pMET25-Gal80-mCh	MFSC97	HygR, NatR, G418R
MFSC102	Gal1-yCCFP, Δ Gal2, Δ Gal3, pMET25-Gal80-mCh	MFSC98	HygR, G418R
MFSC103	pTetO7-Gal2-yVYFP	K699	HygR
MFSC104	pTetO7-Gal2-yVYFP	K699	HygR

Table A.1 – Continued

Name	Genotype	Parent	Marker
MFSC105	pTetO7-Gal2-yVYFP	K699	HygR
MFSC106	pTetO7-Gal2-yVYFP	K699	HygR
MFSC107	Gal2-yVYFP	K699	HygR
MFSC108	Gal2-yVYFP	K699	HygR
MFSC109	His3::pCMV-rtTA - His5 - pCMV-tetR-ssn6	K699	His
MFSC110	His3::pCMV-rtTA - His5 - pCMV-tetR-ssn6	K699	His
MFSC111	Gal2-yVYFP, His3::pCMV-rtTA - His5 - pCMV-tetR-ssn6	MFSC103	HygR, His
MFSC112	Gal2-yVYFP, His3::pCMV-rtTA - His5 - pCMV-tetR-ssn6	MFSC103	HygR, His
MFSC113	Gal2-yVYFP, His3::pCMV-rtTA - His5 - pCMV-tetR-ssn6	MFSC103	HygR, His
MFSC114	Gal2-yVYFP, His3::pCMV-rtTA - His5 - pCMV-tetR-ssn6	MFSC103	HygR, His
MFSC115	Gal1-yVYFP	K699	HygR
MFSC116	Gal1-mCh	K699	HygR
MFSC117	Gal2-yCCFP	K699	HygR
MFSC118	Gal80-yCCFP	K699	HygR
MFSC119	Gal3-yVYFP, Gal80-yCCFP	MFSC68	HygR, NatR
MFSC120	Gal2-yCCFP, Gal3-yVFP, Gal80-mCh	MFSC72	HygR, NatR, G418R
MFSC121	Gal1-yCCFP, pMET25-Gal80-mCh	MFSC99	HygR, G418R
MFSC122	Gal1-yCCFP, Δ Gal80	MFSC85	HygR
MFSC123	Gal1-yCCFP, pCUP1-Gal3-yVYFP, Gal80::Gal80-mCh	MFSC71	HygR, NatR, G418R
MFSC124	Gal1-yCCFP, pCUP1-Gal3-yVYFP, pMET25-Gal80-mCh	MFSC121	HygR, NatR, G418R
MFSC125	Gal1-yCCFP, pCUP1-Gal3-yVYFP, Δ Gal80	MFSC122	HygR, NatR

Appendix B

Microfluidics for synthetic biology

B.1 DAW Hardware and software

B.1.1 Hardware

As mentioned in section 3.1.4, the DAW junction works by changing the relative pressures at DAW ports, while keeping the total pressure the same. Physically this can be achieved in a number of ways: by pneumatically pressurizing the syringes, using a syringe pump, or changing the hydrostatic pressures of the syringes. Our initial design relied on pneumatically pressurized syringes, but due to problems with flow control we switched to a hydrostatic system. We use two vertically mounted linear actuators to change heights of liquid filled syringes that feed into the DAW junction, Figure B.1A. The smooth motion of the linear actuators allows for smooth changes in mixing ratios. Linear actuators are also a better solution in case of a hardware malfunction. If the actuators break down or cannot move to a new position, they will still allow the experiment to continue, since the flow depends only on the position of the syringe. The inability to move the syringes will only result in a constant inducer level, while maintaining a steady flow. In case of a malfunction with syringe pump or pneumatically driven system the flows will change over time and might even result in flow reversal, which would most likely ruin the experiment.

The first version of DAW system had two linear actuators, which could be controlled independently, Figure B.1A. By attaching a syringe with media to each actuator and moving them equal distances in opposite directions we were able to change the ratio of pressures at the DAW ports while keeping the total pressure constant. Since we have constrained our total pressure to be constant, the movement of one actuator has to be mirrored by the movement of other actuator in opposite direction. In essence, the second linear actuator could be replaced with a linear guide and a pulley system, as seen in Figure B.1B. The linear guide consists of a rail and a guide block that slides along the rail. We found that the guide block does not have enough mass to keep a taught line through the pulley system. A steel block was used to weigh down the guide. Also, the length of the line between the linear actuator cart and the guide block needs to be adjustable. This can be achieved by attaching the line to guide block with a pinch mechanism operated by a screw.

The elimination of the second linear actuator proved to have a major benefit of reduced setup cost per DAW unit. However, when considering the additional parts and labor required to fabricate a pulley system the value of this benefit diminishes. Unless you intend on running a full 8 trap MDAW chip, we recommend on installing a dual linear actuator system. During installation the actuators should be securely attached to some sort of a support system. In our case we attached them to metal struts that are directly connected to the wall studs.

From Table B.1, which lists all the required parts for a dual linear actuator system, we can see that there are 2 linear actuator controllers(RPCON) and a single communication gateway module(SIO). The SIO module is used for communication to a computer, while the RPCON's connect the actuators to the SIO. This setup seems redundant, but it allows for easy expansion. The SIO module can operate up to 16 individual linear actuators, while maintaining only a single connection to the computer. Using this system from the start will allow one to easily expand from 2 to 8 axis DAW system. Also the SIO can be wired to communicate with a computer via USB interface.

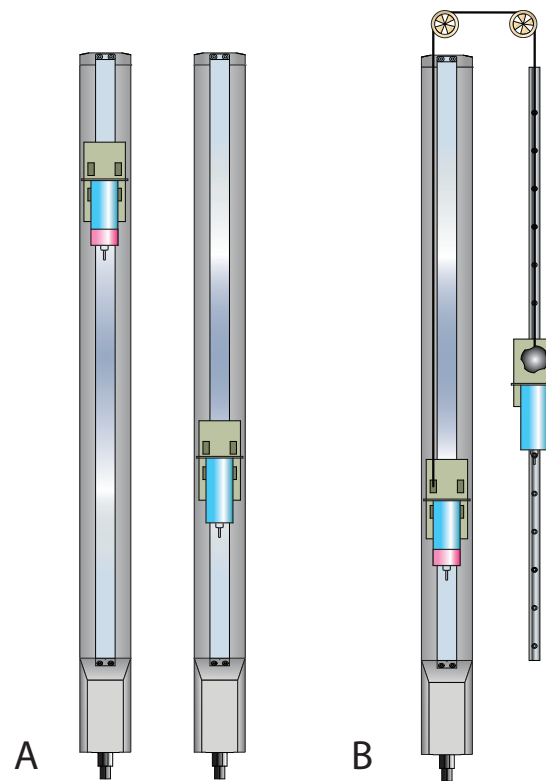


Figure B.1: Linear actuator setup for DAW. **A.** Dual linear actuator setup. Each actuator can be move individually. One of the actuators(left) moves a media syringe with added dye. **B.** Alternate design of the DAW system using only a single linear actuator. The actuator controls the position of both syringes simultaneously. To eliminate friction in the system the following components need to be in a single plane in space: both pulleys, line attachment to actuator, and line attachment to linear guide block.

Table B.1: Hardware required for DAW actuator setup

Equipment	Qty	Part No.	Vendor
Linear actuator: fast speed, 800mm travel length	2	RCP2-SA7C-I-56P-16-800-P1-M-BE	Valin Corp.
Controller	2	RPCON-56P	Valin Corp.
Communication gateway module	1	RGW-SIO	Valin Corp.
Serial communication cable	1	CB-RCA-SIO-050	Valin Corp.
USB adapter	1	RCB-CV-USB	Valin Corp.
USB cable	1	CB-SEL-USB010	Valin Corp.
24V DC power supply	1	OMRON-S8VS-06024	Valin Corp.
AC power cable	1	70355K34	McMaster-Carr

B.1.2 Software - *iDAW*

To control the linear actuators we have created a custom software, nicknamed *iDAW*, using the National Instruments LabVIEW environment. Currently there are two major versions of the software, for the 2 and 8 actuator systems. Both versions, manuals and installation guides are freely available by request.

The graphical user interface presents the user with three main areas: actuator controls, calibration and experiment setup as seen in Figure B.2. During a typical experiment, the actuators first have to be calibrated to the specific chip. This calibration establishes a relationship between relative positions of each actuator and the respective mixing ratios. There are two ways to calibrate the system: manually and automatically. The automatic calibration was already discussed in an earlier section. During manual calibration the actuator positions are changed to create different mixing ratios. Once all the calibration points have been acquired the software creates a calibration function. The software allows up to 11 calibration points, but we have found that a two point calibration performs very well. Also, depending on the number of points, the order of the calibration function can be increased for improved data fit.

To start the manual calibration procedure the actuators are moved together to a height that provides the desired flow to the cell trap. Since the pressures at both syringes are the same, this becomes the 50% value for the calibration. Next, the actuators are linked to move equal distances in opposite directions. The positions are adjusted until there is only media with the inducer going through the mixer, this becomes the 100%

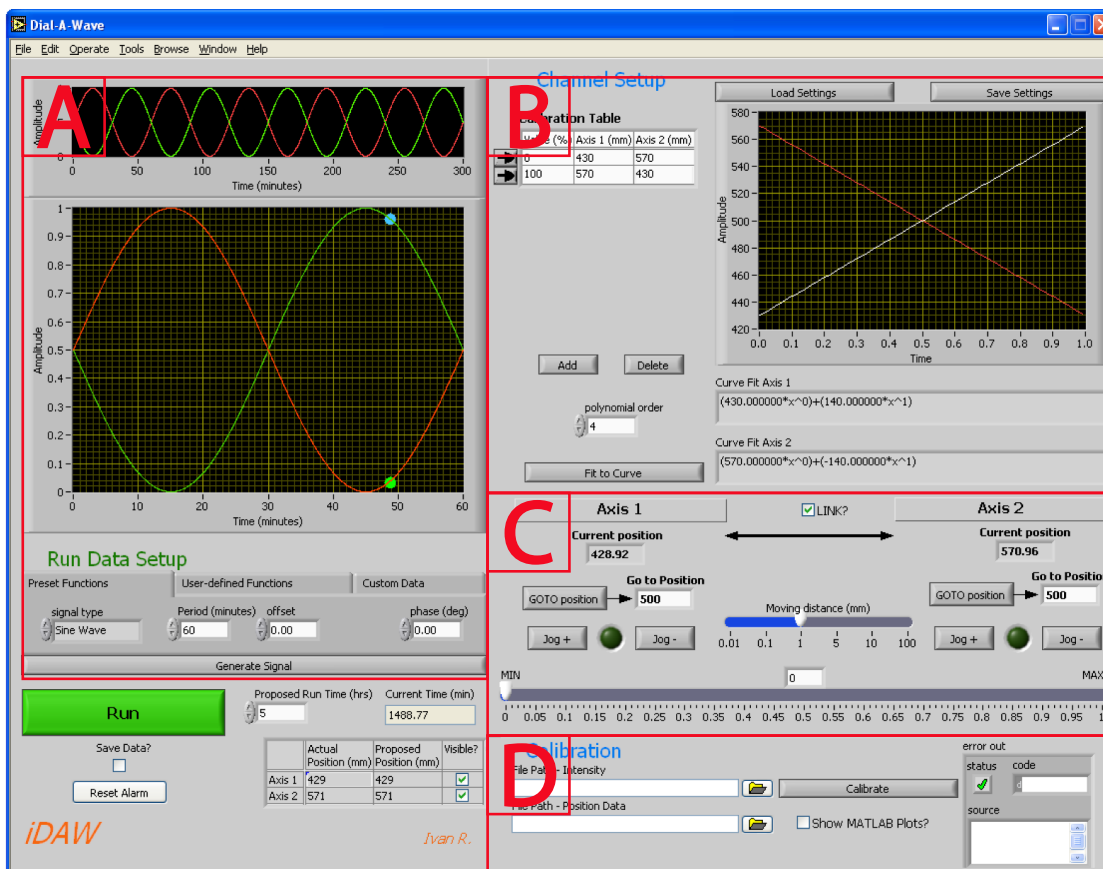


Figure B.2: Screenshot of *iDAW* software. **A.** Experimental parameter setup allows user to setup up mixing ratios as a function of time. Most mathematical functions or an arbitrary dataset can be used as templates. **B.** Manual calibration. The table records the calibration points and the graph shows the calibration functions. In this example a two point calibration was used to create a linear calibration profile. **C.** Actuator controls allow the actuators to be moved independently or together when in “Linked” mode. **D.** Automatic calibration functions take position data from the actuators and fluorescence data from the microscope to determine the calibration profiles.

point. Similarly, the 0% point is recorded. The 0% and the 100% points are used to make a linear calibration function as can be seen on the graph in Figure B.2B.

The experimental setup area of *iDAW* allows the user to create a profile of induction vs time. The user can choose from a number of built-in functions, such as square or sine waves, or load an arbitrary function. The software automatically adjusts the inducer values to fit between 0% and 100%. The proposed induction profile is plotted for the duration of the whole run and the individual linear actuator positions are constantly updated, Figure B.2A. These displays eliminate errors during experimental setup and actual run-time.

With the design of the chip drafted and thoroughly analyzed we begin the fabrication process. An overview of fabrication is shown in Figure B.3. The complete fabrication of a microfluidic chip can be broken down into three main phases. In the first phase we create a patterned wafer by photolithography. Next, we use this wafer to create a silicon rubber mold by a process of soft lithography. And finally the silicon is prepped and bonded to a glass coverslip to make a functional microfluidic device.

B.2 Photolithography

Photolithography was initially developed for the semiconductor industry and later applied to a variety of fields, including microfluidics (Xia and Whitesides, 1998). The process relies on transfer of a geometrical pattern from a mask onto a photosensitive layer via light radiation. The first step involves thorough cleaning of the wafer, which will act as the foundation for all the features. It is very important to remove all debris and any chemicals from the surface of the wafer, as they will get incorporated into the final wafer design and will highly affect the adhesion properties of photoresist to the wafer. Next, we deposit a small amount of photoresist onto the wafer and spin the wafer at predetermined speed to create a photoresist film of precise height, this step is called spin-coating. The wafer is then soft-baked by gradual heating on a level hot plate, which removes solvent and enhances photoresist adhesion to the wafer. At this point the wafer

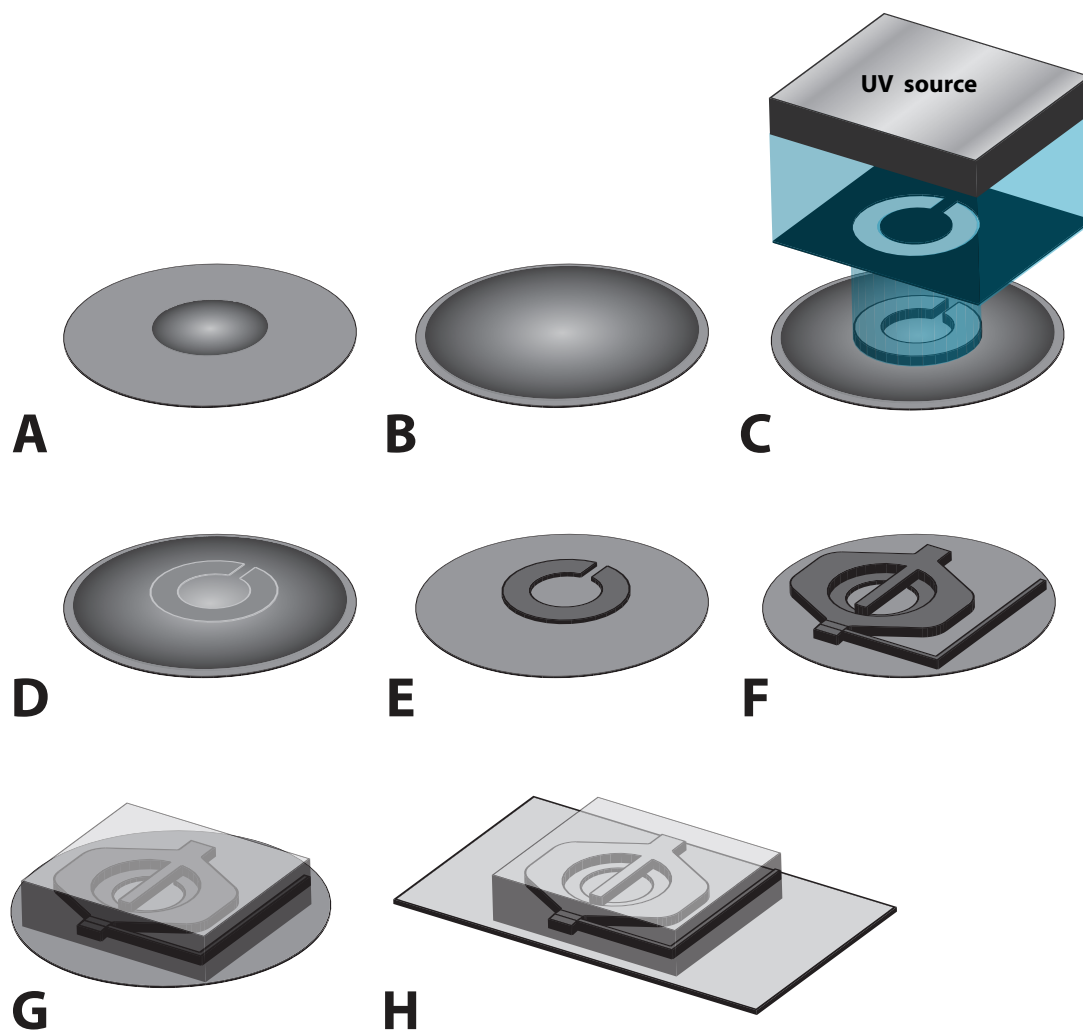


Figure B.3: Overview of the fabrication process. Photolithography(A-F), soft lithography(G), and PDMS processing(H). **A.** Photoresist deposition. **B.** Spin coating: the deposited photoresist is spun at a specific speed to create a uniformly thick layer. **C.** UV exposure cross-links the photoresist creating a pattern identical to the photomask. **D.** Post-exposure baking joins the silicon wafer and the cross-linked photoresist. **E.** Developing removes the uncross-linked photoresist, revealing the features. **F.** Repeating steps A-E creates additional features. **G.** Pouring and curing PDMS over the patterned wafer creates a mold. **H.** Bonding the PDMS mold to a glass coverslip finishes a microfluidic chip.

is exposed to UV light through a photomask, this transfers the pattern from the mask onto the photoresist layer. We use the SU-8 2000 line of photoresist from MicroChem Corporation. SU-8 is a negative photoresist, which means that areas of the film exposed to UV radiation will form solid structures, while unexposed areas will be washed away during the developing step. The wafer is then baked again, in the post-exposure bake, to increase the level of cross-linking. And finally to complete a single photolithographic cycle, the wafer is developed by immersion in solvent which removes uncross-linked photoresist leaving only the desired pattern on the wafer. Since all of the chip designs we use require wafers with multiple heights this cycle is repeated a number of times.

Photoresist

Manufacturers, such as MicroChem, make a variety of photoresist formulations. The SU-8 line of resists alone has 3 sub-categories with a total of 18 different formulations, specific for heights ranging from 1.5 μm to 550 μm (MicroChem, 2010). We use the SU-8 2000 photoresists which have great adhesion to silicon wafers and are able to make high aspect ratio structures (del Campo and Greiner, 2007). The “negative” denomination of a photoresist means that areas of the film exposed to UV radiation will form solid structures, while unexposed areas will be washed away during the developing step. Specifically, exposure to UV radiation changes the chemistry of the resist by generating very strong acid within the film, which starts the cross-linking reaction of the SU-8 epoxy. The main difference between the various SU-8 2000 formulations is the epoxy solids content that directly relates to the viscosity of the liquid as can be seen in Table B.2.

Commonly there is a need for a non-standard formulation. It is possible to make new, less viscous, formulations by adding SU-8 thinner to the initial, more viscous, stock of photoresist. It should be noted that the manufacturer’s naming scheme loosely relates to the height of the photoresist film when it is spun at 3000 rpm. Thus, for 2002 and 2005 photoresists, spin-coating at 3000 rpm would in theory produce 2 μm and

Table B.2: SU-8 2000 photoresists formulations

SU-8 2000	%Solids	Viscosity (cSt)
2000.5	14.3	2.49
2002	29.00	7.5
2005	45.00	45
2007	52.50	140
2010	58.00	380
2015	63.45	1250
2025	68.55	4500
2035	69.95	7000
2050	71.65	12900
2075	73.45	22000
2100	75.00	45000
2150	76.75	80000

5 μm film heights, respectively. Using this information we can plot these theoretical heights against the percentage of solids for each formulation, as seen in Figure B.4. By making a curve fit function of percent solids(s) as a function of height(h), as written in Eq. (B.1), we are able to estimate the required solids for any new formulation. For example, to make a new formulation, which would produce 3 μm height at 3000 rpm, we use Eq. (B.1) to determine that it requires 35% solids.

$$s = 0.0235h^3 - 0.834h^2 + 10.807h + 9.5781 \quad (\text{B.1})$$

Next, the amount of thinner required for the new formulation can be calculated using the relationship described in Eqs. (B.2), where $mass_{total}$ is the desired mass of the new formulation, $mass_{thinner}$ is the required mass of thinner, $mass_{initial}$ is the required mass of original photoresist, $s_{initial}$ is the percentage of solids in the original photoresist, and s_{final} is the percentage of solids in the desired photoresist formulation.

To make the formulation measure out and deposit the predetermined amounts of photoresist and thinner into a clean dark glass bottle, make sure to do this in a fume hood. Drop a clean stir bar into the bottle and place on a magnetic stirrer, until it is thoroughly mixed. Due to the viscosity of photoresists removing the stir bar could be

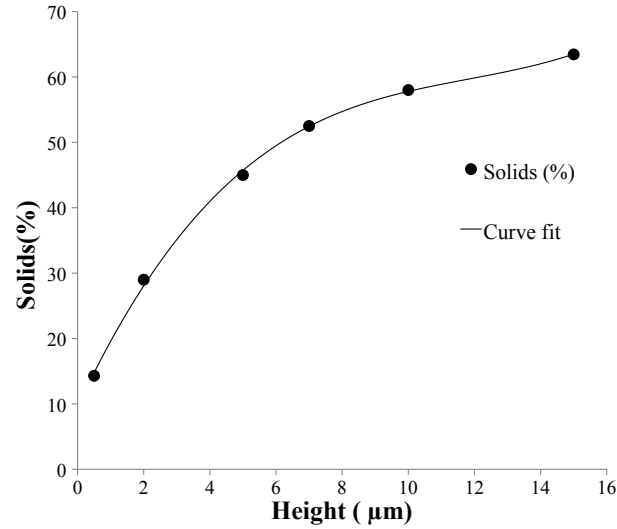


Figure B.4: Graph of SU-8 formulation vs percent solids. Relationship between estimated height of SU-8 formulations when spun at 3000rpm and their solids content.

difficult, so we leave it in the bottle until the photoresist runs out.

$$mass_{thinner} = mass_{total} \left(1 - \frac{S_{final}}{S_{initial}}\right) \quad (\text{B.2a})$$

$$mass_{initial} = mass_{total} - mass_{thinner} \quad (\text{B.2b})$$

Finally, to complete the process it is necessary to characterize the new photoresist formulation by making a spin speed curve. This step should also be performed for any standard formulations that have not been previously characterized by your lab. To create a spin speed curve for a particular photoresist the photolithographic cycle, described later on, should be repeated 3-6 times with various spin-coating speeds. For each speed measure and record the feature heights using a surface profilometer. Plotting and curve fitting the data will produce enough data to reliably estimate spin speeds for specific heights. As mentioned earlier, the functionality of a cell trap is dependent on its height. Thus, it is critical to manufacture the exact height required by the design. The spin-curves allow us to estimate only a rough range of speeds required to achieve a height. Using this range as a starting point, we perform as many spin test as necessary

to get the desired height. An example of an actual spin curve for 2003 formulation can be seen in Figure B.5. Examining the figure it becomes evident, that our 2003 formulation produces $2.6 \mu\text{m}$ and not $3 \mu\text{m}$ height at 3000 rpm, this fact reinforces the need for photoresist characterization.

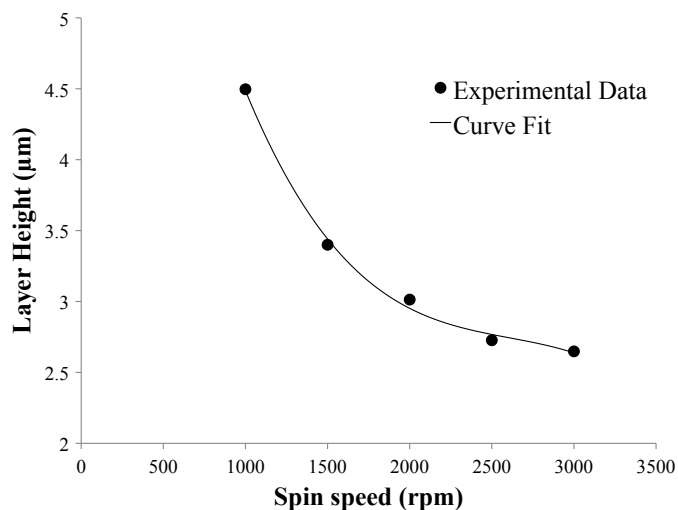


Figure B.5: Graph of SU-8 formulation vs percent solids. Relationship between estimated height of SU-8 formulations when spun at 3000 rpm and their solids content.

Equipment and environment

Due to sensitivity of photolithography to contamination it is usually performed in a cleanroom environment. A number of universities and research centers have shared facilities that house equipment necessary for photolithography and other dust-sensitive processes. We have made wafers in various environments from a Class 100 cleanroom to a basic HEPA filtered room with no rating. The latter type of non-cleanroom manufacturing environment is achieved by creating a dedicated fabrication space, installing HEPA filters over the air ducts and changing the ceiling panels to non-particulate releasing tiles. Also to prevent uncontrolled photoresist cross-linking, the lights should be fitted with UV absorbing filters. This can be easily done by placing thin filter sleeves over the fluorescent lights bulbs. Although it is beneficial to carry out the whole manufactur-

ing process in the cleanest possible environment, in our case only photolithography is performed in the cleanroom. While soft lithography and PDMS processing are carried out in regular lab space.

It is important to point out that the chemical safety precautions are more important than the cleanliness of the facility. Some of the chemicals used in photolithography are potentially carcinogenic, labs should use a properly functioning fume hood when working with photoresists and developers at all times. A standard fume hood convects air from the environment past the user, into the hood and out a ventilation shaft. Since users are generally the largest source of particulates in a clean environment, use of a standard fume hood can increase the local concentration of particulates over the work surface in the hood, even if the surrounding environment is clean. In contrast, biosafety cabinets contain a laminar air stream between the interior and the user, preventing the transfer of particulates into the hood. However, unless specially made and calibrated, biosafety cabinets can potentially allow chemical fumes to escape into the work area. Purpose built hoods, protecting both the user from chemical fumes and the interior from particulates, do exist but are expensive. For microchemostat fabrication we have found that a standard chemical fume hood is sufficient, however electrical engineering facilities will often contain specialty hoods. Since hot plates and spin processors are used with uncured photoresists, it is essential that they be placed in the fume hood. However, the process of soft-baking removes the solvent from photoresist, allowing one to work with a mask aligner outside of the fume hood.

Photomasks

Conventional photolithography requires expensive chrome photomasks, we use the cheaper photomasks printed on a transparency-like material as described in (Whitesides et al., 2001b). As mentioned earlier, all of our masks are made by CAD/Art Services, Inc(Bandon, Oregon). They use a photographic process to print the design on a 0.007” polyester mylar sheet coated with photographic silver. Since our masks are

designed in AutoCAD software, we just provide them with a *.dxf file. However, they do accept a variety of other CAD files, listed in order of preference: *.dwg, *.gds, *.cif, *.gerber and *.eps. Due to the limits of their photoplotting process, the minimum feature size is defined by a circle with 10 μm diameter. Although, it is possible to print various size masks, we usually order an 8 by 10 inch sheet. This gives us enough room to fit up to 6 individual layer masks and since most of our design require less than 6 layers we can have a whole chip printed on a single sheet. When ordering the mask, it is important to specify the polarity of the mask, considering that we are working with a negative photoresist, our masks need to have clear features on a black background. Once the masks have been printed, they are cut out and individually glued at the corners to a 3 by 3 inch glass square using clear instant adhesive. It is important to have the emulsion side of the mask facing away from the glass, since it needs to be in contact with the photoresist later on. Also, when gluing the photomask to the glass make sure to keep the glue away from any transparent parts of the mask. For storage and transport we keep the masks in individual plastic bags, this prevents them from getting dirty and scratched.

Sample fabrication parameters

For each individual wafer we create a table with fabrication parameters, this is an effective way of condensing all of the necessary information for manufacturing the wafer. Most of the parameters, such as layer heights and number of layers, will be dictated by your design, however some of them have to be calculated after the design is done. For example, the exposure time will depend on the exposure dose required for the photoresist and on the UV lamp power. MicroChem's datasheets provide exposure energy ranges for different heights. For example, 0.4 μm layer requires 60-80 $\text{mJ}\cdot\text{cm}^{-2}$ and 3 μm layer requires 90-105 $\text{mJ}\cdot\text{cm}^{-2}$. Given that our mask aligner UV lamp has an effective power of 1.4 $\text{mJ}\cdot\text{cm}^{-2}$, we can calculate the exposure times using Eq. (B.3),

see Table B.3.

$$Exposure\ Time = \frac{Exposure\ Dose}{Effective\ Power} = \frac{\frac{mJ}{cm^2}}{\frac{mW}{cm^2}} = \frac{mW \cdot s}{cm^2} = seconds \quad (B.3)$$

Table B.3: Calculated and experimental exposure times.

Layer height(μm)	Exposure energy($\frac{mJ}{cm^2}$)	Calculated exposure time (s)	Experimental exposure time (s)
0.4	60-80	43-57	60
3	90-105	64-75	80

With additional information from photoresist spin curves we can finalize the fabrication parameters into a table, as seen in Table B.4 and proceed to fabrication.

Table B.4: Sample table of wafer fabrication parameters.

Layer number	1	2	3	4
Layer height (μm)	0.4	1	3	10
SU-8 formulation	2000.5	2000.5	2002	2005
Spin speed (rpm)	3750	700	1000	660
Soft-bake at 95°C (s)	120	120	150	240
Exposure time (s)	60	60	80	100
Post-exposure bake at 95°C (s)	160	160	180	240

Photolithography: Protocol

All of the necessary equipment, supplies and chemicals for this protocols are listed in Table B.6 at the end of this section.

B.2.1 Cleaning the wafer

Place the wafer inside the spin processor (spinner) with reflective surface facing up, this is your working surface. Try to align the center of the wafer with the center of the vacuum chuck of the spinner, this eliminates uneven rotation. If you have cleanroom paper, line the inside of the spinner with it to help with cleaning up process. Set the

rotational speed to 3000 rpm and start the spinner. At this point it is recommended to turn on the mask aligner and UV source, as the lamp needs time to warm up.

B.2.2 Applying the cleaning agents

Thoroughly clean the wafer by applying chemicals in the following order: acetone, isopropanol, methanol and DI water, during the application of gentle pressure with a polyester swab. Make sure not to press too hard, but rather smoothly move the tip across the spinning surface of the wafer.

B.2.3 Drying the wafer

Place the clean wafer on a hot plate set at 200°C and let dry for 5 minutes. Once done with the drying cycle set the temperature to 95°C, as it will take some time to cool down. By the time your are done with step 6 your hot plate should be at the right temperature.

B.2.4 Centering the wafer on the spinner

Pick up the wafer from the hot plate with wafer tweezers and let it cool prior to positioning on the spinner chuck. Once cool, position the wafer on the chuck, making sure it is centered with respect to the chuck. To check if the wafer is centered, spin it at 500 rpm, if the wafer is centered correctly when spinning it will look like a circle. However, when off center, it will spin creating an oval shape. For best results it is recommended to center the wafer as much as possible. It is helpful to use a wafer alignment tool, although we have made a custom one, there are plenty of commercially available options.

B.2.5 Dispensing photoresist

Dispense 5-10 ml of photoresist in the center of the wafer. The total amount of photoresist depends highly on its viscosity, with higher volumes needed for more viscous formulations. When working with photoresists make sure to never dispense directly from the main source. Constantly opening the bottle will cause solvent evaporation and build-up of dry photoresist on the mouth of the bottle. This leads to change in the viscosity of the resist and to contamination with solid particles. The best practice is to have a working 30ml amber glass bottle, which you refill from the main stock. The dark glass will limit the amount of UV entering and reacting with the photoresist. Make sure to label the bottles as all photoresist look the same.

B.2.6 Spin coating

Depending on desired layer thickness the spin speed during the second step will vary. Program the spinner for a two step cycle. Step 1: 500 rpm for 15 seconds, acceleration of 100 rpm/second; Step 2: desired spin speed for 30 seconds, acceleration of 300 rpm/second. For example, to achieve a layer thickness of 0.4 μm with SU-8 2000.5 we spin for 30 seconds at 3750 rpm; 3 μm with SU-8 2002 we spin for 30 seconds at 1000 rpm. These numbers are true for our formulations but might not be correct for your formulations, since the age of photoresist will have an effect. As mentioned earlier it is absolutely crucial to create spin-curves for each photoresist prior to final wafer fabrication.

B.2.7 Soft-baking at 95°C

Previously it was recommended to have a pre-bake step at 65°C prior to soft-baking 95°C. According to MicroChem and our own experience pre-baking step is not really necessary. We have eliminated it from our protocols and have not noticed any significant effects.

Using an infrared thermometer check the temperature of the hot plate, it should be 95°C. Place the wafer on the center of the hot plate and be careful as the wafer may sometimes slide off the hot plate. Keep the wafer on the hot plate for 1-3 minutes, depending on the layer thickness. MicroChem's material datasheets can act as a guide in selecting the baking time, however the exact time can only be determined empirically. A good way of optimizing baking time is to remove the wafer from the hot plate and let it cool. Once cool, place the wafer back on the hot plate. If the photoresist film "wrinkles" keep it on the hot plate for another 30 seconds. Repeat this process until the film no longer "wrinkles" (MicroChem, 2010).

For example for 0.4 μm layer the softbake time is 120 seconds and for 3 μm layer it is 150 seconds.

B.2.8 Alignment of photomask and UV exposure

Turn on the mask aligner UV source, if this has not been done in Step 1. Place the wafer on top of the vacuum chuck in the mask aligner. Turn on the vacuum, to secure the wafer on the chuck. Position the photomask in the mask holder on the aligner, with the transparency side facing the wafer, turn on the vacuum to secure the mask. During exposure the light path should be as follows: glass, printed mask, photoresist film, wafer. Make sure the z-axis of the wafer is all the way down, then move the mask into horizontal position. If the wafer is too high it can come in contact with the mask and smear the photoresist film. Move the wafer up slowly until it makes contact with the mask. Usually this creates a number of light diffraction patterns on the mask, which can be observed by looking at the mask at an angle. For alignment the best distance is usually right after the diffraction patterns appear. This distance allows for independent movement of the wafer and the mask, while keeping them close enough to each other to see the features on the wafer through the mask. For an alignment methodology see the "Special notes on alignment" section at the end of the protocol.

Once the wafer and the mask have been aligned, bring the wafer in complete

contact with the mask without forcing or overextending the z-axis. Expose the wafer for a predetermined time. Move the z-axis down, lift the mask, turn off the vacuum to the wafer chuck and remove the wafer.

B.2.9 Post exposure baking (PEB) at 95°C

Bake the wafer on the 95°C hot plate for a specified time. Once again this time will depend on the thickness of the layer, with some rough estimates present by MicroChem's datasheets. For example for 0.4 μm layer our PEB is 160 second and for 3 μm layer it is 180 seconds. If the exposure times are correct you should be able to see the pattern within the photoresist film within 15 seconds of baking.

B.2.10 Developing

Fill up a crystallizing dish with enough SU-8 Developer to cover the wafer. Make sure the wafer has cooled down to room temperature, before immersing it in the developer. Next, while keeping the bottom of the dish on the surface of the fume hood, move the dish in a circular fashion. This technique improves removal of uncross-linked photoresist. Continue this process for 1-2 minutes. MicroChem suggests other methods, such as ultrasonic or megasonic baths, but we have not needed them in the past.

B.2.11 Cleaning

Pick up the wafer from the dish using tweezers and rinse it with fresh SU-8 Developer, you can let the developer collect in the dish. Follow by a rinse with fresh Isopropanol and air dry using filtered air or nitrogen. At this point you should clearly see the features on the wafer. Sometimes the wafer will have white streaks, this is due to photoresist that has not been removed by development. Clean the wafer with fresh developer, rinse with fresh Isopropanol and dry.

B.2.12 Examining the wafer

Cleaning completes a single photolithographic cycle. At this point it is necessary to examine the wafer under a microscope, if the process was successful then the features will have uniform color and straight, smooth edges.

B.2.13 Measuring feature height

Using a surface profilometer measure a number of height points for each important feature. Since the height of cell traps is absolutely crucial for microfluidic chips, it is necessary to measure the height of the trap in different locations on the wafer and see that it conforms to your design specification.

B.2.14 Hard-baking at 200°C

If there are no more layers to deposit, place the wafer on 200°C hot plate for 5 minutes. If there are any cracks on the surface of the features, this step should remove them. It is beneficial to ramp up the wafer temperature to 200°C.

Special notes on alignment

As mentioned in the chip design section, the wafer is made layer-by-layer from the ground up. It is recommended to deposit the smallest height features first and gradually move in increasing order. Although the design of the chip should account for small alignment errors, this sequential approach to wafer manufacturing can result in propagation of errors from one layer to the next. Since the compounded effect of these errors can be significant, it is crucial to have the best possible alignment at each layer. Due to lack of a consistent protocol for alignment, it can be most time consuming and very frustrating step of wafer manufacturing. Here we propose a simple methodology that should let a minimally experienced person successfully align layers.

Most of the manual mask aligners use micrometers for x , y , z and θ stage movements. The micrometers are primarily used for very fine axis adjustments, but they also can be used to precisely record the position of the wafer. Also, it is easy to see that if two different alignment elements on the wafer are individually aligned to their respective alignment elements on the photomask, then the whole wafer is completely aligned to the mask. Thus, the positional data should be identical at both alignment elements. By systematically adjusting and recording the x , y , and θ positions we can find a set of values that is identical for both alignment elements.

Protocol

Photomasks presented in Figure B.6 will be used as an example. For correct scale it should be noted that alignment elements presented in Figure B.6A and C, are located in the center of the mask and are 80% of the width of the mask.

Using the x , y and θ micrometers on the mask aligner, find the alignment features from layer #1 and roughly position them under alignment elements of photomask for layer #2, Figure B.6D. Adjust the magnification of the mask aligner, so that most of your field of view is covered by a single alignment element, Figure B.6E.

Next, adjusting only the y -direction, align the top of the features to the top of the photomask alignment box. Record the position of y -direction micrometer, this is the y_1 point. Repeat this step for the bottom side of the features and record the micrometer position, this is the y_2 point. In a similar fashion obtain micrometer readings for alignment of left and right sides of the features to the alignment box, x_1 and x_2 , Figure B.6F. Although it would seem that if the edges are aligned then position y_1 would be equal to y_2 , and x_1 equal to x_2 , however, this is rarely the case. In reality, the new photoresist layer makes the features seem somewhat distorted when viewed through the microscope. Though, assuming that the distortion is equal in all directions we can take the average of the two positions to get the actual aligned position, as seen by values in brackets in Table B.5. Repeat the four measurements for the right side alignment element. Record all the data points into a table, as seen in Table B.5.

In the first row of the table, the average positions for x and y are different for left

and right sides. This would indicate that wafer is not aligned. Change the θ micrometer position by a small amount, in the example case we moved from 17 to 15. Repeating all the measurements it becomes evident that the left side and right sides are diverging from each other. This is probably not the right direction for θ movement. Move the θ from the initial position by the same amount in the opposite direction and repeat the measurements. In our example the θ position changed from 15 to 19. It is clear that the x-y positions are converging, but are not exactly equal yet. In the same direction, change θ position by the smallest possible step, and repeat measurements. If the positions are identical the wafer is aligned, if not, repeat θ movement and measurements. In our example, θ movement from 19 to 20 resulted in identical x-y positions for both sides, successfully terminating alignment procedure.

We have determined through experience that developing a systematic way of placing the wafer and the photomask into the mask aligner greatly reduces the time for alignment. The wafers we use have two flat edges, so when placing the wafer into mask aligner we find a surface on the mask aligner and roughly align the edge to that surface. Same trick is applied for the photomask. This results in relatively consistent placement of wafer and photomask, thus lowering the final alignment adjustments.

For the UV exposure step, set the x and y micrometer positions to the averaged values of x and y, respectively.

Table B.5: Sample alignment datasheet.

θ	Left		Right	
	$X_1, X_2, (\bar{X})$	$Y_1, Y_2, (\bar{Y})$	$X_1, X_2, (\bar{X})$	$Y_1, Y_2, (\bar{Y})$
17	15, 14 (14.5)	13, 13.5 (13.25)	16, 17 (16.5)	11,10 (10.5)
15	14, 13 (13.5)	14, 15 (14.5)	17, 19 (18.0)	9,10 (9.5)
19	15, 15 (15.0)	12, 12.5 (12.25)	16, 15 (15.5)	14,12 (13)
20	15, 16 (15.5)	12, 12 (12)	16, 15 (15.5)	12,12 (12)

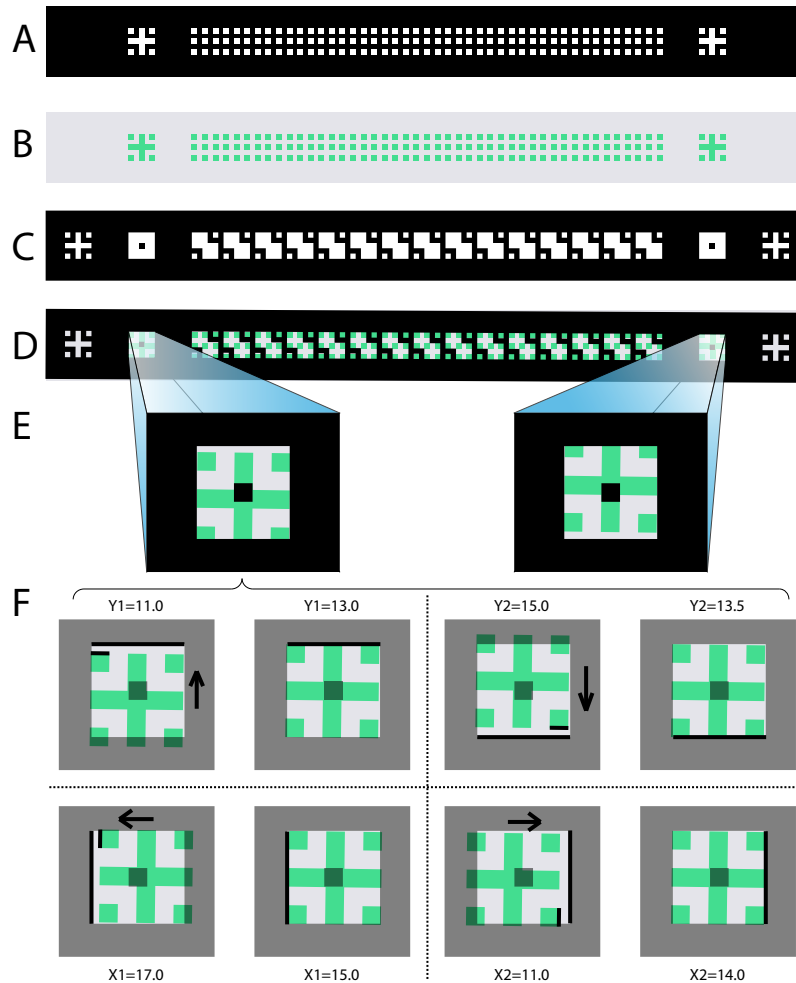


Figure B.6: Sample layer alignment technique. **A.** Photomask of layer #1, features are created by the transparent areas of the mask. **B.** Features(green) on wafer(gray) for layer #1. **C.** Photomask of layer #2. **D.** Alignment of wafer with features from layer #1 to photomask for layer #2, as seen through the microscope of mask aligner. **E.** Close up view of alignment of the outermost left and right features. **F.** For each side (left and right), the features on the wafer are aligned to the 4 four sides of the alignment box. The mask aligner micrometer position is averaged for x (15, 14) and y (13,13.5) directions, to provide a single xy (14.5, 13.25) position. Note that it would seem that y1 and y2 positions should be identical if the feature sides are aligned to the alignment box. In reality, due to the new photoresist layer the features from previous layer become distorted, resulting in the difference. If the xy positions from the left and the right side are identical the alignment is good, otherwise the θ position needs to be changed and the whole process repeated. The transparency of the photomask has been adjusted for demonstration purposes.

Table B.6: Photolithography Equipment, chemicals and supplies

Equipment	Model No.	Manufacturer
Mask aligner	Model 200	OAI
Spin processor	WS-400BZ-NPP-Lite	Laurell Technologies Corporation
Surface profilometer	Dektak 150	Veeco
Infrared thermometer	62	Fluke
Hot plate		
Fume hood		
Chemicals and Supplies	Part No.	Supplier
SU-8 Photoresists 2000.5-2050 (500ml)	varies	MicroChem
SU-8 Developer (4L)	Y020100-4000L1PE	MicroChem
SU-8 2000 Thinner (4L)	G010100-4000L1PE	MicroChem
AlphaLite Polyester swab	18-375	Fisher Scientific
Glass bottle (amber)	41265T31	McMaster-Carr
Instant Adhesive	495045	Loctite
Borosilicate glass square, 3' X 3', 1/8" thick	8476K131	McMaster-Carr
Silicon Wafer	100MM/CZ/1-0-0/Boron/ P Type/ Resis-10-20/ Thick 500-550/Oxy 9-21/ SLBACK: ETCH ACID	WaferNet, Inc.
Wafer tray	H20-3000-01-1415	Entegris, Inc.
Wafer cover	H20-3000-02-1216	Entegris, Inc.
Wafer tweezers (125mm)	S3WF	SPI Supplies
Crystallizing Dish (740ml)	08-741E	Fisher Scientific
Wash bottles (500ml)	08-647-707	Fisher Scientific
Acetone		
DI Water	Milli-Q or better	
Isopropanol	HPLC grade	
Methanol	HPLC grade	

B.3 Soft Lithography

Soft lithography is a microfabrication technique that relies on the use of a patterned elastomer to create structures, in our case, by cast molding. Although a number of different elastomers can be used, PDMS (polydimethylsiloxane) has become the standard choice for microfluidics. PDMS is optically transparent, permeable to biologically important gases, chemically and thermally stable, the surface can be chemically modified and it does not absorb water. The PDMS we use comes as a two part kit: silicone monomer and curing agent. Mixing the components in specific ratio creates PDMS prepolymer that remains liquid for a few hours. The PDMS mold is prepared by pouring liquid pre-polymer over a patterned wafer, curing it at elevated temperature and removing from the wafer. Since PDMS is initially in liquid phase, it easily conforms to the

geometry of the wafer. Once cured, it remains flexible and allows for easy peel-off from the wafer. Furthermore, treating the wafer with a release agent improves the peel-off process (Xia and Whitesides, 1998; Whitesides et al., 2001b; Duffy et al., 1998; Sia and Whitesides, 2003). All the tools, chemicals and equipment required for soft lithography are listed in Table B.7

Soft Lithography: Protocol

B.3.1 Aluminum holder

Cut out a 20 cm circle from aluminum foil. Place the wafer, features up, in the center of the foil. Next, carefully holding the wafer down, start to fold the foil up all the way around the perimeter. This will create 5 cm high walls around the wafer that will hold PDMS in. Make sure that the foil is really tight against the edge of the wafer, this prevents significant leaks of PDMS under the wafer.

B.3.2 Applying release agent (for new wafers only)

It is necessary to perform this step in a fume hood following all safety precautions, as most release agents are toxic. Place the wafer into a dedicated silanizing desiccator. Using a syringe with a needle, draw up the release agent, we use (TRIDECAFLUORO-1,1,2,2-TETRAHYDROOCTYL)-1-TRICHLOROSILANE. Deposit only a single drop ($\sim 30 \mu\text{l}$) of the release agent into an open top small container inside the desiccator, see Figure B.7. Close the lid of the desiccator and turn on the vacuum. The release agent will vaporize and evenly deposit onto the wafer. Let this reaction happen for about 15 minutes. Using too much release agent will inhibit PDMS binding to glass coverslip.

B.3.3 Preparing PDMS

In a clean weighing tray measure out, in 10:1 ratio, and mix 40 grams of silicone elastomer base with 4 grams of silicon curing agent. Continue vigorously mixing with a clean spatula. The consistency of the mixture should start to change from clear to foamy. Mix the components thoroughly for 3 minutes.

B.3.4 Degassing PDMS

Mixing introduces a lot of air bubbles into the PDMS. To degas, place the weighing tray into the dedicated desiccator and turn on the vacuum. As pressure within the desiccator drops, the trapped air bubbles will expand and PDMS might spill out of the tray. Quickly releasing the vacuum should pop a significant portion of the bubbles. Turn on the vacuum again and repeat this cycle until there are no more bubbles. Depending on the vacuum pressure this should take 10-20 minutes. Also, it is possible to degas by pouring mixed PDMS into a 50 ml Falcon tube and centrifuging it at $\sim 2700g$ for 10 minutes.

B.3.5 Pouring PDMS

Place the wafer into the degassing desiccator and pour the PDMS over it. Since PDMS is very viscous, you might have to use a spatula to get all of it onto the wafer. This process will introduce new air bubbles into the PDMS. Repeat step 4 until there are no visible bubbles in the PDMS. Sometimes the PDMS will leak under the wafer and you will see bubbles forming around the perimeter of the wafer. You can ignore them when considering to stop degassing.

B.3.6 Curing

Place wafer in 80°C oven for 1 hour.

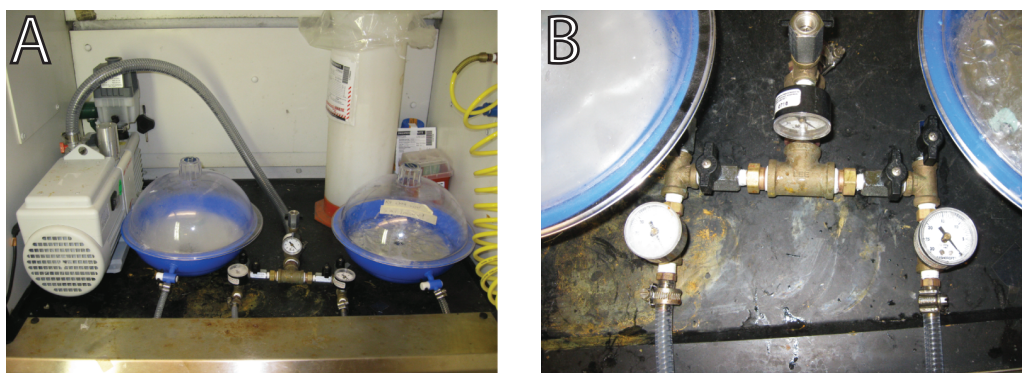


Figure B.7: Vacuum pump and desiccators. **A.** Vacuum pump and desiccators located in the fume hood. Each desiccators for a single purpose: 1) wafer silanizing (left) and 2) PDMS degassing (right). Note the opaqueness of the silanizing desiccator, this is due to silanizing agent vapor deposition over the years. **B.** Vacuum manifold connecting the vacuum pump to the desiccators. The manifold allows for individual control of vacuum or atmospheric pressures to each desiccator. See Table B.7 for parts list.

B.4 PDMS processing

During the final phase of manufacturing the individual chips are cut out, cleaned and bonded to coverslips. Although the processing is performed in regular lab environment it is critical to get the chips and coverslips as clean as possible. This eliminates debris from the chip and improves the overall quality of the devices. To improve the final bond between PDMS and glass coverslip, it is recommended to complete soft lithography and PDMS processing in the same day. All the required materials and tools for this phase of manufacturing are listed in Table B.8.

PDMS processing - Protocol

B.4.1 Removing PDMS layer

Take the wafer out of the oven and let it cool down to room temperature. Carefully peel of the foil from PDMS. Some PDMS may have gotten under the wafer. You

Table B.7: Soft lithography equipment, chemicals and supplies.

Equipment	Qty	Part No.	Vendor
Vacuum pump RV8	1	A65401906	Edwards
Vacuum pump EMF 10 exhaust mist filter	1	A46226000	Edwards
Vacuum pump oil return kit	1	A50523000	Edwards
Vacuum pump inlet connection (NW25 to 3/4" hose barb)	1	NGT908000	Edwards
Vacuum pump NW25 clamping ring	1	C10514401	Edwards
Desiccators	2	08-642-5	Fisher Scientific
Ceramic desiccator plate	2	08-642-10	Fisher Scientific
Isotemp Oven	1	506G	Fisher Scientific
Vacuum manifold parts	Qty	Part No.	Vendor
1/2" stainless steel hose clamps	5	6151K51	McMaster-Carr
1" stainless steel hose clamps	5	6151K53	McMaster-Carr
1' 3/4" ID, 1" OD wire-reinforced tubing	5	5393K45	McMaster-Carr
1' 1/4" ID, 1/2" OD wire-reinforced tubing	10	5393K31	McMaster-Carr
3/4" MPT to 3/4" barb adapter	1	5365K23	McMaster-Carr
3/4" FPT to 3/4" FPT to 1/4" FPT tee	1	4429K229	McMaster-Carr
1/4" MPT to 1/4" MPT nipple	3	9171K122	McMaster-Carr
1/4" FPT to 1/4" FPT to 1/8" FPT tee	3	4429K223	McMaster-Carr
1/4" MPT to 1/4" FPT T-handle valve	5	4912K87	McMaster-Carr
-30 in Hg vacuum gauge with 1/8" MPT at back	3	3935K21	McMaster-Carr
3/4" MPT to 1/2" MPT reducing nipple	1	9171K223	McMaster-Carr
1/2" FPT to 1/2" FPT to 1/2" FPT tee	1	4429K253	McMaster-Carr
1/2" MPT to 1/4" MPT reducing nipple	2	9171K219	McMaster-Carr
1/4" FPT to 1/4" FPT to 1/4" FPT tee	2	4429K251	McMaster-Carr
1/4" MPT to 1/4" barb adapter	2	53505K64	McMaster-Carr
PTFE thread seal tap	1	4591K12	McMaster-Carr
Chemicals and supplies	Qty	Part No.	Manufacturer
Silicone elastomer kit (TRIDECAFLUORO-1,1,2,2-TETRAHYDROOCTYL)-1-TRICHLOROSILANE Aluminum foil		Sylgard 184 T2492	Dow Corning UCT

need to remove this layer prior to peeling off the top layer of PDMS. Using a razor blade, cut the bottom layer as close to the edge of the wafer as possible. It is also possible to rub the edge of the wafer with your gloved finger. This will break the PDMS on the edge, disconnecting the bottom and top layers of PDMS. Very slowly lift up the top layer of PDMS. Allow the PDMS to lift off from the wafer by itself, this is best done by raising a part of PDMS to a small height, stopping and letting the PDMS catch up. Lift up the PDMS in 3-4 places around the perimeter of the wafer, before peeling it off completely. Wafers are very brittle, so make sure not to twist or apply excessive pressure on it, as it will easily break. For safe storage place the wafer into a labeled wafer holder.

B.4.2 Cutting PDMS

Using the dissecting scope, examine the features on the PDMS. Sometimes the angle of the light source needs to be adjusted to get enough contrast to see the microscopic features. Placing the PDMS on a dark background also improves contrast. Next, using a razor blade carefully cut out individual chips, leaving extra room around the perimeter of the chip. Try to leave at least 3mm of extra PDMS around each port, it will improve the chip's bonding and prevent port leaks.

B.4.3 Punching ports

Place the chip with feature side up and, using the dissecting scope, locate the outline of the port. Place the tip of 25 gauge leuc stub within the outline and, making sure it is as vertical as possible, apply downward pressure. The PDMS should first deform and then break; sometimes a final push is required to completely break through the PDMS on the exit. Next, carefully pick up the PDMS chip and remove the PDMS core using tweezers. Slowly pull out the puncher from the hole, while rotating it back and forth. Continue this for all ports on the chip. Sometimes the punching will tear the PDMS around the port, this is most likely due to a dull punching tip. Simply, swipe the punching tip against an abrasive surface 2-3 times and retry the punching. It is also possible to use a biopsy punch, which combines the leuc stub and tweezers in a single tool, to make the holes.

B.4.4 Cleaning ports

Attach a 23 gauge leuc stub to a syringe and fill it with DI water. Hold the tip of the leuc stub against a port and apply pressure. A stream of water should exit from the other side of the chip. Keep the pressure for 3-5 seconds. Repeat this process of all ports on both sides of the chip.

B.4.5 Cleaning chips

Spray each chip with 70% Ethanol and gently rub using your gloved finger. Thoroughly rinse the chip with MilliQ quality water and blow dry using clean dry air. Make sure to dry both sides of the chip and all the ports. Place the dry chips in a clean Petri dish. Apply scotch tape to both sides of the chip. The next step is crucial for clean chips. Careful not to tear the PDMS, run your fingernail over the features a few times, covering the are of the whole chip. Repeat the scotch tape cleaning 3-5 times. Once done, use a fresh piece of tape to cover the chip and put the chip in the Petri dish.

B.4.6 Cleaning coverslips

Spray both sides of the coverslips with n-Heptane and gently rub the surface using your finger. To prevent the coverslip from breaking, apply pressure using your finger on both surfaces at the same time. Wipe the coverslip completely dry with a Kimwipe. Repeat the process using Methanol. Finally, wash the coverslips with DI water and dry using clean air. Make sure the coverslips are completely free of dust, spot or streaks. If you notice something, redo the DI water wash step. Once done, place the clean coverslips into a Petri dish and cover.

B.4.7 Bonding chips to coverslips

Open the compressed O₂ valve on your tank and make sure the flow through the UVO cleaner is 0.4-0.6 scfm. Warm up the UVO cleaner, by running it for 5 minutes. Once the warm up is done, open the loading tray, there should be a faint smell of ozone. Place the chips with feature side up and coverslips onto the tray. Close the tray and run the bonder for 3 minutes. When done, open the tray and place the chip onto the coverslip using tweezers. To improve the bond, using tweezers, gently apply pressure around the perimeter of the chip. Make sure that chip and coverslip come in contact as soon as possible, as the chemistry allowing for bonding changes with time. Place bonded chips

in 80°C oven overnight. If you have a lot of chips, it might be beneficial to break up the bonding step in 2 or more batches.

B.4.8 Troubleshooting

Poor chip bonding - this can be caused by a number of issues.

- 1) Too much release agent used during wafer preparation. Try lowering the amount of release agent or shortening the coating time.
- 2) Check O₂ supply to UVO bonder.
- 3) Expose the chips and coverslips exactly for 3 minutes. Make sure to bond chips and coverslips immediately after exposure to ozone.
- 4) Place a weight on top of the chips during overnight baking. Make sure not to break the coverslip.

Collapsed features:

- 1) Usually only the lowest features will collapse, but if enough pressure is applied from the top of the chip even taller features are susceptible. Lower the amount of pressure applied on the top of the chip during bonding.
- 2) Try placing the coverslip on top of the chip during bonding. This should prevent features lower than 0.5 μm from collapsing.

B.5 Experimental setup for *E. coli*

Although it is possible to perform microfluidic experiments without a lot of specialized equipment, we have found that purpose-built tools, such our DAW and syringe towers, greatly increase productivity and experiment control. As mentioned in earlier sections, we use linear actuators to control the hydrostatic pressure of syringes, Figure

Table B.8: PDMS processing equipment, chemicals and supplies.

Equipment	Qty	Part No.	Vendor
Dissecting scope	1		
Fiber optic light source	1	Dynalite 150	A.G. Heinze, Inc.
UVO Cleaner	1	Model No. 42	Jelight Company Inc.
Flowmeter	1	FR4A37	Key Instruments
1/8 Male pipe adapter	2	5454K65	McMaster-Carr
Polyurethane tubing			
Chemicals and supplies	Qty	Part No.	Manufacturer
Leur stub (25 gauge)		75165A686	McMaster-Carr
Biopsy punch Harris Uni-Core 0.5 mm		15071	Ted Pella, Inc.
Razor blades		12-640	Fisher Scientific
10ml Disposable syringe		14-823-2A	Fisher Scientific
Cover slips No. 1 1/2, size: 24x40 mm, thickness: 0.16-0.19 mm		12-530F	Fisher Scientific
Magic Tape		810	Scotch
Kimwipes, Kimberly-Clark No. 34155		06-666A	Fisher Scientific
Compressed O ₂		Medical grade	
n-Heptane		HPLC grade	
Methanol		HPLC grade	
DI Water		Milli-Q or better	

B.9B. However, we use special syringe towers, as shown in Figure B.8, for controlling the height of our static syringes used for waste, cell and shunt ports. The towers are equipped with rulers, allowing us to record the position of syringes for an experiment. This data is used in subsequent experiments to reliably reproduce flows within the chip. Image data acquisition is performed by a Nikon fluorescence microscope, see Table B.11 for component list. Our complete experimental setup can be seen in Figure B.9A, and functional mDAW chip with attached lines in Figure B.9C.

For experiments, we modify our standard LB media, by adding 0.075% Tween 80 and filtering it through 0.22 μm filter. Addition of Tween 80 prevents the cells from sticking to chip walls without any noticeable harm to the cells. Depending on your experiment, make sure to add antibiotics and any inducers to the media.

B.5.1 Overnight culture

Grow up an overnight culture of cells from -80°C stock or from a plate. Grow the cells in 3 ml of LB media with appropriate antibiotics in 37°C shaker incubator.



Figure B.8: Syringe towers. Made from commercially available erector set, the towers provide support for static syringes. We use a three pillar design with six adjustable platforms, which hold 2-9 syringes each. The ticked lines in the drawing represent rulers that are used for consistent syringe placement. All the parts necessary for constructing the tower are listed in Table B.9.

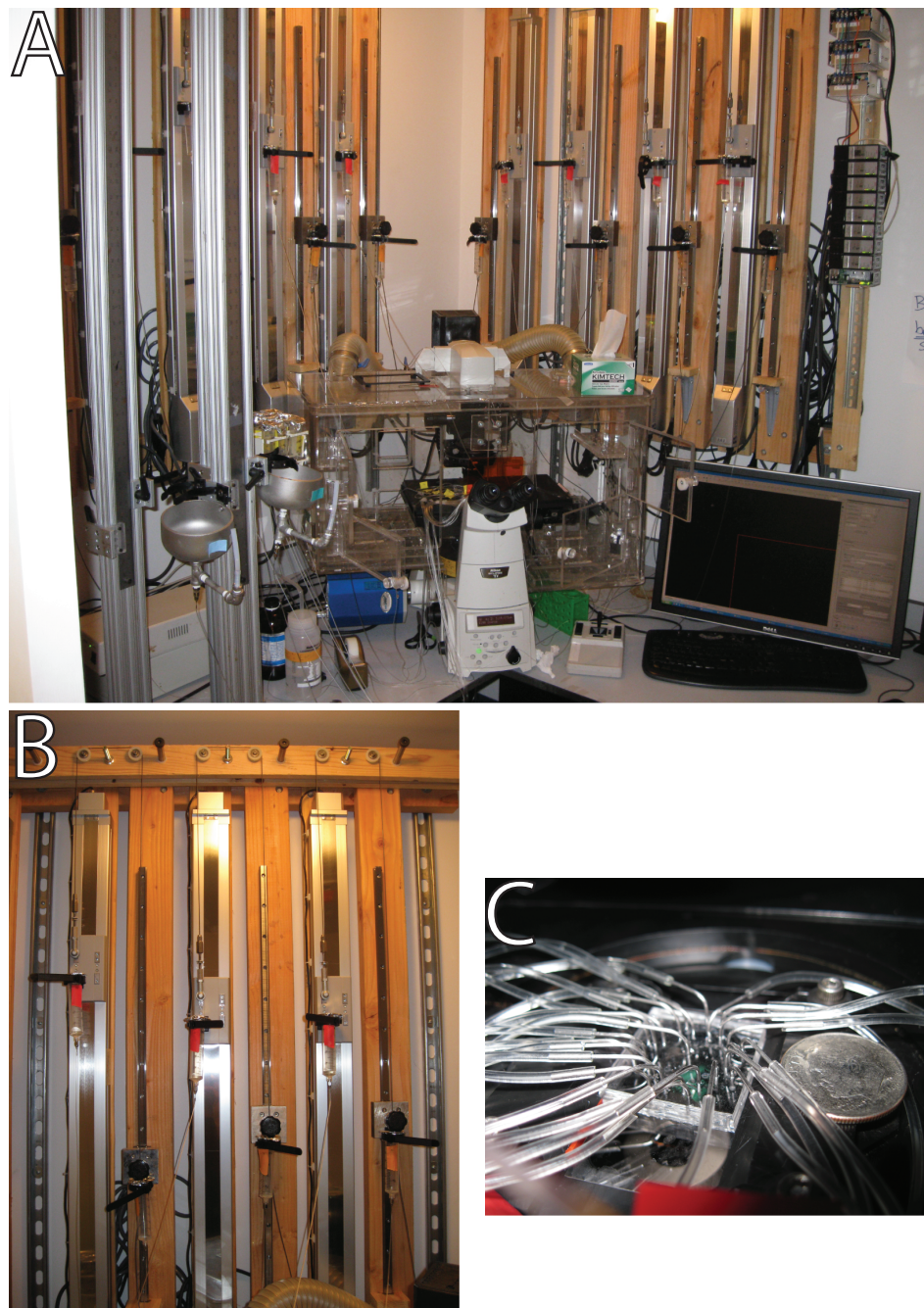


Figure B.9: Experimental setup. **A.** The equipment setup for mDAW experiments. In the background one can see the linear actuators, it is possible to fit all 8 actuators and 8 linear guides in a compact space behind the microscope. Fluorescent microscope with environmental chamber can be seen in the foreground of the image. **B.** 3 linear actuators with linear guides and pulley systems. This is a photograph of the system described in Figure 15B. **C.** An mDAW chip with all the connection pins and lines attached. US dime coin (diameter: 17.91mm) is shown for scale.

B.5.2 Cell growth

Dilute the overnight culture by a factor of 1:1000 into 50 ml of fresh media with appropriate antibiotics and inducers. Let the cells grow up to a culture density of OD₆₀₀ 0.05-1.0, we usually try for OD₆₀₀ 0.1. Depending on the cell type this step should take 2-3 hours. During this time perform steps 3-6.

B.5.3 Wetting the chip

Secure the chip in a chip holder, using rubber gaskets for additional contact. We have a custom chip holder, details for which can be provided by request. Basically, it securely holds a 24 x 40 mm cover slip, while allowing light access from the bottom, physical access from the top, and secure attachment to the microscope's stage. Place the chip under microscope at 4X magnification. It is important to examine the chip for dirt and collapsed channels. This is best done at lower magnification, as you can see a larger area. Make sure that there is no debris blocking the channels or the imaging areas. Collapsed traps or channels will look darker and generally resemble in shade bonded parts of the chip. If the chip looks good proceed to wetting. Wetting the chip can be done using hydrostatic or manual pressure applied through a syringe. Attach a luer stub, a microfluidic line and a connection pin to a syringe and fill with fresh media. Make sure there are no bubbles in the syringe or the line. Bubbles can be removed by flicking the syringe or the line with your finger. Carefully insert the pin into a port. The color of the channels should start to change as fluid fills them. If using hydrostatic pressure to wet, position the syringe on the towers as high as possible and let the fluid flow through the chip. If using manual pressure, make sure to apply gentle pressure as too much pressure will lift the chip off the coverslip. As media fills the chip it will come up through the open ports and start forming droplets on the surface of the chip. Repeat this process for all the ports and until there are no more air bubbles in the chip. Media removal from the surface of the chip is best accomplished using a kimwipe.

B.5.4 Preparing syringes

Attach a sterile 23 gauge leuc stub to a clean 60 ml syringe. Take 6 feet of Tygon tubing and gently slide it over the leuc stub. Attach a connection pin to the other side of the tubing. A connection pin is basically just the metal part of a 23 gauge leuc stub. We make them by pulling out the metal tips from the plastic part of the leuc stub using pliers. The phase condensers on some microscope may come in contact with the straight connection pins. To circumvent this issue we make L-shaped pins by bending them around the shank of a 10-32 wood screw using pliers, refer to Figure B.10 for exact instructions on making straight and L-shaped pins.

Depending on the intended use for the syringe, remove the plunger and extract 100 μl of media or dH_2O with a P200 pipetman. Insert the tip of the pipetman into the syringe and make contact with the inside of the leuc stub adapter. Slowly expel the fluid into the leuc stub adapter which should be enough to fill it, as shown in Figure B.11C-E. Adding fluid to the leuc stub adapter in this way greatly reduces bubble formation. Tilt the syringe slightly and gently pour the rest of the media or dH_2O into the top of the syringe, letting it run down the side before it reaches the base of the syringe. This also helps in preventing bubbles. Flick the leuc stub connector to cause media to flow into the microbore tubing. If difficult bubbles are present, partially unscrew the leuc stub adapter about one half turn and then retighten. This can help release bubbles. If fluid still will not enter the microbore tubing, use the syringe plunger to force the fluid in. Note if the plunger is necessary, it usually indicates a severe bubble problem. Make extra sure all bubbles are removed before proceeding. Watch the fluid flow carefully through the microbore tubing line to the exit point at the leuc stub. Carefully look over the line to ensure no bubbles are present. If bubbles are present flick the lines to release them and watch them flow to the end of the microbore tubing. Cover the syringe top using a piece of foil or parafilm, while leaving a small opening to the atmosphere. Label the syringes appropriately and make sure the connection tips do not touch any surface.

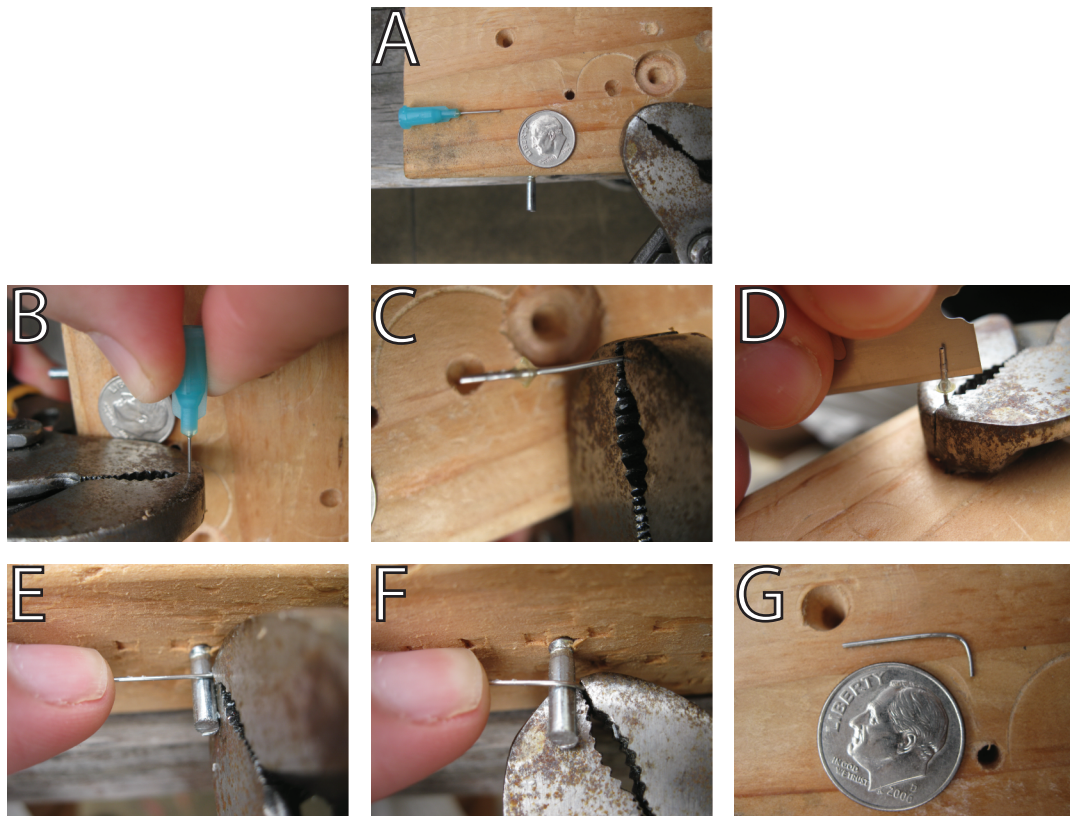


Figure B.10: Making connection pins. **A.** A non-sterile 23 gauge luer stub, dowel pin, and pliers are used to make the connection pins. **B.** Using pliers grab onto the metal part of the luer stub, while holding the plastic part with your fingers. Pull them in opposite direction until they separate. **C.** The metal pin alone, notice all the sealant and glue on it. **D.** Using a razor blade, carefully remove all the glue from the outside of the pin. To make straight connection pins the process is finished at this point and pins just need to be cleaned in a sonicator. **E.** Holding the pin with pliers, place it over the dowel pin. **F.** While holding one of the ends of the pin with you finger, gently rotate the other end around the dowel pin. **G.** Finished L-shaped connection pin. This method preserves the inner radius of the connection pin. Simple bending it will most likely pinch the pin. US dime (diameter: 17.91mm) shown for scale.

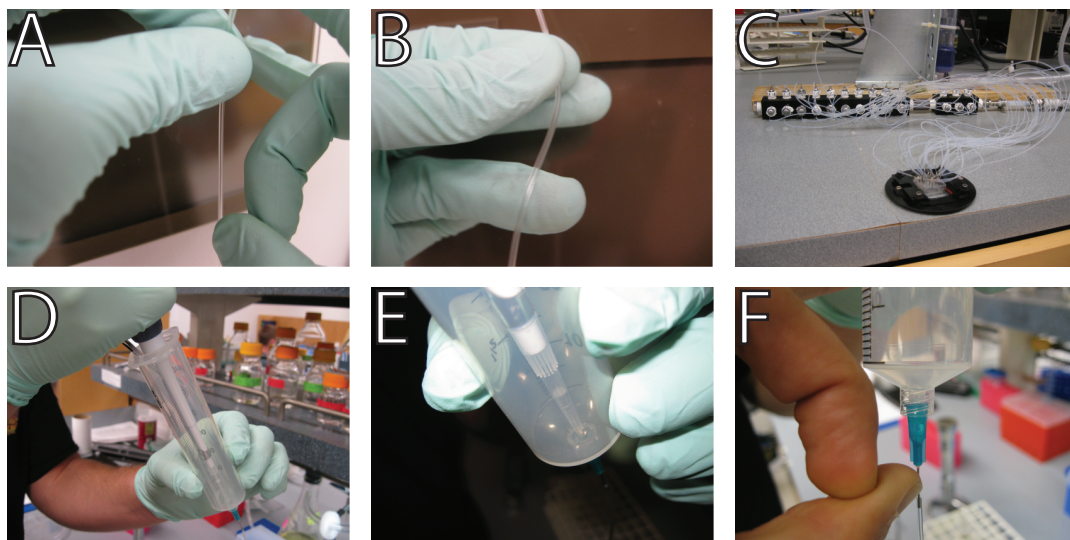


Figure B.11: Experimental line and syringe techniques. **A.** General guide for flicking a microfluidic line. Hold the line between the thumb and index finger of one hand, while flicking the downstream the line with a finger on your other hand. In the figure, the hands are placed on the line so that the left hand is closer to the syringe and the right hand is closer to the microfluidic chip. **B.** Technique for gentle agitation of fluid within the microfluidic device. Hold the line between thumb and index finger. Gently move the line back and forth using your ring finger. The ring finger is placed on the line towards the microfluidic device. **C.** The metal pin alone, notice all the sealant and glue on it. **D.** Technique for minimizing bubbles during syringe preparation. Using a P200 pipetman draw up 100 μl of desired liquid. Remove the plunger from the syringe. Insert the pipetman into the syringe and hold both at a slight angle. **E.** Insert the pipette tip all the way into the leur stub adapter and slowly expel the liquid. **F.** Flicking the bottom of the syringe to fill the connection pin with liquid.

B.5.5 Connecting syringes

Attach all the syringes to the sliders on the microfluidic tower, as seen in Figure B.8. Adjust syringe heights appropriately. To prevent contamination of the media source, make sure it is always the highest positioned syringe. One by one, starting with the media, connect each syringe to the chip. Since the cells are not ready yet, connect a syringe filled with DI water to the cell port. Examine that no bubbles were introduced into the chip during this process. If there are bubbles, see if they can slowly disappear on their own. However, it might be necessary flush the chip by disconnecting all the syringes and repeating Step 3. Once all the bubbles have been eliminated, using scotch tape secure each line to the chip holder. Tape far enough away from the chip, so that the bending of the tubing is not applying a force on the connection pin.

B.5.6 Setting up DAW software

Using the software, calibrate the syringe heights for correct mixing ratios. Create a desired profile for the syringe movement. Make sure that all the static syringes are in their “running” positions.

B.5.7 Spinning down cells

When the cells are ready, spin them down at 2700g for 10 minutes. As a backup, pour the supernatant media back into the flask and place it in incubator. Add 2-3 ml of fresh media to the pelleted cells and gently vortex them, until there are no cell clumps. Load the cells into a prepared syringe. Once again, make sure there are no bubbles.

B.5.8 Loading cells

Move all syringe to their “loading” positions. Disconnect the temporary cell syringe and plug in the actual cell syringe. At this point the flow from the media and the cell port both should be going towards the waste port. At 20X magnification you

should be able to see cells flowing through the channels. Adjust the height of the cell syringe so that the cells are slowly moving past the traps. Next, securely hold the cell line between the thumb and index finger of one hand, while flicking the line with a finger on your other hand as seen in Figure B.11A. Imagine that the pinching fingers divide the line into two parts: the syringe part and the connection pin part. The flicking should be done on the connection pin part of the line. The cells should rapidly move back and forth within the chip, as the flicking wave propagates down the line. Adjust the flicking strength to have enough force to load the traps. Once enough traps have been loaded, adjust the syringe heights to their “running” positions. Media flow should be 20-200 $\mu\text{m/s}$.

B.5.9 Starting experiment

Allow the cells to grow in the traps for 3-5 doublings, depending on you cell type this should take 1-2 hours. Setup the microscope software for you run. Start the imaging and the *iDAW* software at the same time.

B.5.10 Checking on cells

During the experiment it might be necessary to remove stuck cells from the channels. Hold the cell line between the thumb and index finger with your middle finger further away from the syringe. Gently move the line back and forth using your ring finger and watch as the cells smoothly mirror the motion, see Figure B.11B for a visual representation. This technique is useful for getting rid of stuck cells or controllably reducing cell density within a trap.

Table B.9: Experimental equipment, chemicals and supplies.

Equipment	Qty	Part No.	Vendor
Inverted fully automated microscope	1	Ti	Nikon
PDMS chip holder	1		Custom
Syringe towers			
Aluminum bread board, 12" x 12" x 1/2", 1/4-20 threaded	1	MB12	Thorlabs, Inc.
1" x 3" Extrusion 60" long	3	1030x60"	80/20, Inc.
8 Hole inside corner gusset	3	25-4138	80/20, Inc.
Slide-in T-nut	6	3382	80/20, Inc.
Double Slide-in T-nut	6	3280	80/20, Inc.
1/4-20 x 1/2" Flanged button head socket cap screw	6	3342	80/20, Inc.
1/4-20 x 1/2" Socket head cap screw	12	3062	80/20, Inc.
1/4-20 x 3/8" Socket head cap screw	6	3058	80/20, Inc.
1/4" washer - black zinc	20	3258	80/20, Inc.
Double flange linear bearing brake kit ready	8	6425	80/20, Inc.
Ratcheting L-handle	8	6850	80/20, Inc.
White UHMW Pads w/ brake hole	24	6490	80/20, Inc.
#8 x 3/8" SS standard bearing pad screw	24	3625	80/20, Inc.
48" stainless steel rule	3	2120A15	McMaster-Carr
1" adjustable strap	1 Pkg	7565K51	McMaster-Carr
Chip holder rubber gasket		7665K11	McMaster-Carr
Chemicals and supplies			
	Qty	Part No.	Manufacturer
Connection pins (23 gauge, ID 0.017", OD 0.025", 1/2" Long)		75165A684	McMaster-Carr
Single use, sterile leur stub (23 gauge)		14-826-19E	Fisher Scientific
Reusable leur stub (23 gauge, ID 0.017", OD 0.025", 1/2" Long)		JGM23-0.5D	Jensen Global Inc
Disposable syringe 10 ml w/ leur lock tip		14-823-2A	Fisher Scientific
Disposable syringe 30 ml w/ leur lock tip		14-829-48A	Fisher Scientific
Disposable syringe 60 ml w/ leur lock tip		13-689-8	Fisher Scientific
Tygon flexible microbore tubing (ID 0.020", OD 0.060")	1	14-170-15B	Fisher Scientific
Tween 80	1	P8074	Sigma-Aldrich
Alconox 1104	1	04-322-4	Fisher Scientific
Liquid cell media			
DI Water		Milli-Q or better	

B.6 Method to setup a MDAW microfluidic experiment

In this section we will describe how to setup a microfluidics experiment using the MDAW parallel DAW microchemostat chip since this chip presents challenges not seen for smaller chips.

B.6.1 Pre-experiment preparation

See Table B.9 for the catalog numbers of supplies listed here. The steps described in this section should be performed at least one day in advance of the experiment. The microfluidic devices themselves should be prepared as described in section B.4. Cut

26 lines using Tygon microbore tubing seven feet in length. Note the line length is dependent on the microscopy setup, there should be some slack to allow for movements of the syringe reservoirs. Obtain 26 sterile 30ml syringes. Note for the combined ports we use 4 inch stainless steel pipe caps fitted with leur stub adapters. If these pipe caps are used then only 24 30ml syringes are necessary. These pipe caps were manufactured by our university's machine shop, details can be provided by request. Due to their large diameter, the liquid height in the pipe caps changes very little for a given volume of accumulated fluid. This is important since the combined ports receive vastly more fluid than the individual ports during an experiment. If a 30ml syringe were used instead of a pipe cap, it is conceivable that the height increase would affect flows in the chip over the course of a long experiment (2-3 days). See Figure 3.5 and the accompanying text for an example of these issues.

To clean the metal parts, sonicate 26 reusable leur stub adapters, 26 90° curved connection pins (see B.10) and the pipe caps if they are to be used, for 60 min at 60°C in a 250 ml beaker containing 1% w/v Alconox. Sonication in 1% w/v Alconox does an excellent job of removing cell debris and residual media from small metal parts. After sonication rinse the parts in dH₂O. Flush water through the leur stub adapters and connection pins to remove residual Alconox. We use a manifold to flush all metal parts at once, see Figure B.11C. In general we flush 3 liters of dH₂O through the entire system for rinsing. After flushing with water, air can be flushed for drying. Autoclave the leur stubs, adapters and, if using them, pipe caps for 30 minutes on a dry cycle.

Prepare the 26 (24 if using pipe caps) syringe reservoirs as described in B.5.4. Cut 8 sections of red, orange and yellow tape. Write 1-8 on each of the colored tape sets and affix to the syringe bodies. The tape will help to identify the syringe reservoirs later in the setup. Each of the 8 subexperiments has two DAW input ports (A and B) and a cell port (C). We use the red tape to refer to A reservoirs, orange for B and yellow for C. Cut another three sets of colored tape and again write 1-8 on each set. Affix the tape near the end of the microbore tubing (just before the connection pin) for the appropriate reservoir. Labeling the end of the tubing helps to identify its connected

reservoir, a necessity when many lines are nested together. Use scotch tape to affix the loose microbore tubing end to the syringe.

B.6.2 Cell Growth

Determine how many cell cultures will be needed, a maximum of 8 can be used. Inoculate the cell cultures the day before the experiment with the appropriate media and additives. In the next morning check the culture optical density at 600nm (OD600) using a spectrophotometer. Grow cells at 30°C for ~4 hours, to an OD600 of ~1.0 upon cell loading.

B.6.3 Media preparation

Prepare 4 ml of media for each of the 16 input syringes (ports A and B for each of the 8 subexperiments). Generally the media is the same in the two inputs except for the tested component. See Table B.10 for an example of the media composition. Add dye to one of the two input reservoirs for each subexperiment to use as an inducer tracer. After the media has been prepared, add it to each of the A and B syringe reservoirs as described in section B.5.4. Add sterile dH₂O to the shunt and alternate waste reservoirs. If 30 ml syringes are used, add 4 ml of dH₂O. If pipe caps are used add ~100 ml.

Table B.10: Experimental equipment, chemicals and supplies.

	Ingredients	Stock	Final	units	Lot	1X (μ l)	FX (ml)	
1	2X SC - met media	2	1	X		2000	5	
2	Methionine	50000	500	μ M		40	0.1	
3	Galactose	2	0.2	% w/v		400	1	
4	Raffinose	20	2	% w/v		400	1	
5	ddH ₂ O	-	-	-		1160	2.9	
						total (μ l):	4000	10

B.6.4 Air removal from the chip

Note that this procedure differs from that of a smaller chip (such as MFD005_a). While removal of air can also be facilitated using a vacuum, we have found this to interfere with our cell's growth under some conditions. Affix a bonded MDAW chip onto a solid substrate, like a glass plate or a microscopy chip holder, as the one described in Step 3 of *E. coli* experimental section. Fill a 10 ml syringe with a sterile solution of 0.1% v/v Tween 80 and connect it to the central port of the chip (called the alternate waste port). Tween 80 is a surfactant that aids in clearing bubbles. It also acts as a lubricant that prevents cell clogging. Purge air from the chip by applying force to the syringe. Watch for droplets to appear at each port indicating that fluid has propagated through the chip's channel network.

We have a custom built 26 outlet manifold connected to a pressure reservoir filled with dH₂O. Each outlet of the manifold is connected to a half meter of teflon microbore tubing with a connection pin at the end. The manifold is fully autoclavable and by pressurizing all ports at once, achieves better clearance of air. Details of the manifold's construction can be provided upon request. To purge air from the manifold we pressurize it until water flows out of each connection pin. Next we connect each pin to a port on the chip, making sure a "fluidic connection" is made, i.e. there is a visible droplet of fluid above each port on the chip and fluid is leaving the connection pin of the manifold). When the manifold is fully connected it is then pressurized to 4 Psi for five minutes to flush all air from the system.

B.6.5 Connecting DAW reservoirs to the device

After the air has been purged from the system, place the chip in a microscopy holder if not done already. Secure both ends of the device with scotch tape. Place the chip above the microscope stage. Our microscope has an acrylic environmental chamber around it, whose top is about 25 cm above the stage height. We place the chip on top of this box. Attach the shunt and alternate waste port reservoirs to the syringe towers.

Adjust the height of the shunt reservoir to 30 cm above the stage. Adjust the height of the alternate waste reservoir to 37.5 cm above the stage. Take the connection pin from the shunt reservoir and place it several centimeters below the reservoir's fluid level. Wait for fluid to exit the end of the microbore tubing line and then connect the leur stub to the shunt port at the top of the device. Repeat this procedure to connect the alternate waste reservoir to the device. Connect the DAW input reservoirs for each subexperiment to each set of A and B ports on the device using the same procedure. After connecting the reservoirs attach them to the linear actuators. The linear actuators should be set so each reservoir is 60 cm above the stage height. Once all of the input reservoirs have been connected bundle the lines together with scotch tape so they do not become unwieldily.

B.6.6 Processing and loading cells

At this time remove the cell cultures from the incubator and record the final OD600 value if desired. Add Tween 80 to each cell culture to a final concentration of 0.1% v/v. Vortex on a medium setting to mix. Add each culture to the appropriate syringe reservoir as described in section B.5.4. Be extra careful there are no bubbles in any of the cell reservoirs. While using Tween 80 helps to prevent bubbles, any that remain in the reservoir will make it extremely difficult to load cells later on. The Tween 80 will also prevent clogging of the device by excess cells.

Adjust the height of the shunt port to 11.25 cm above the height of the stage and make sure the cell reservoir holder is set to 32.5 cm above stage height. This adjustment will ensure cells flow into the shunt and not other cell ports. At this time, all cell ports will contain a bead of fluid above them since they are the outlets for the other connected reservoirs. This bead of fluid will essentially function as a small reservoir. Since the device should still be placed at 25 cm above stage height, this will be the pressure of each cell port before its reservoir is connected. Once the shunt port is lowered there will be a net flow between the fluid bead of each cell port and the shunt. When the cell reservoirs are connected their pressure will increase to 32.5 cm. If the shunt port

were not lowered some flow would exit at the unconnected cell ports, possibly causing cross-contamination.

Once all cell ports have been connected, place the chip into the microscope and tape down all microbore tubing lines. Adjust the height of the cell ports to 40 cm and observe the cells entering the system at 4X magnification. If cells are not entering from the cell ports it is usually due to residual bubbles in the cell lines. Disconnect if necessary and make sure there are no bubbles. Adjust the height of the alternate waste port to force more cells into the central region of the trap if necessary. Flick the lines for each cell port to load cells into the trapping region. Continue this procedure until an adequate number of cells have been loaded (generally 20-40 yeast cells). Once the cells have been loaded adjust the heights of all reservoirs as follows: Cell ports: 15.5 cm, combined alternate waste: 14 cm, combined shunt: 11.25 cm. All heights above stage height. The level of the DAW inputs should remain at 60 cm above stage height. If desired move to the DAW junction of each subexperiment and record the height positions for 0% and 100% mixing ratios or use the calibration procedure described in section 3.1.5.

B.6.7 Microscope setup

Record the stage locations for each of the cell traps in the 8 subexperiments in the microscopy software. Switch to a 40X or 60X objective and add microscopy oil as necessary. Update the xy positions for each trap as they will have changed slightly. Setup the microscopy software for a multiple location experiment, using appropriate exposure settings for phase contrast and any fluorescence wavelengths. Make sure the autofocus routine is properly setup. Since the MDAW chip is quite large, there will likely be a z offset between the cell traps of each subexperiment. This z offset needs to be compensated for. Moreover, due to stage drift over the course of an experiment the z offset will shift in time. Some microscope software packages cannot cope with this properly and we have written a custom macro for the NI Elements software to compensate for this changing z offset. The macro uses the median of the last five focal

planes for each cell trap to calculate an updated z offset. This z offset is used as the best guess for where to start the next iteration's autofocus routine. Taking the median prevents a single poor autofocus result from causing a catastrophic loss of focus, which can happen if a bubble in oil droplet drifts into the field of view. We have had good success with this macro, retaining focus even after almost 72 hours of an experiment. Set the linear actuator controller software for the proper input waves as described in section B.1.2. Begin image acquisition.

Table B.11: Components of Nikon *Ti* automated fluorescence microscope.

Description	Qty	Part No.
Ti-E Inverted Microscope	1	MEA53100
Ti-HUBC/A Hub Controller A	1	MEF55030
Ti-AC/A AC Adapter for HUBC/A	1	MEF51010
Ti-AC120 Power Cord 120V	1	MEF51200
USB 2.0 Cable A-B 15', Required for DS-U2 Controller	1	97050
Ti-DH Dia Pillar Illuminator 100W	1	MEE59905
D-LH/LC Precentered Lamphouse with LC	1	MBE75221
Halogen Lamp 12V 100W L.L	3	84125
Ti-PS100W Power Supply 100-240V	1	MEF52250
Ti-100WRC 100W Lamphouse Remote Cable	1	MEF51001
Power Cord	3	79035
Filter 45mm GIF	1	MBN11200
Filter 45mm NCB11	1	MBN11710
45mm Heat Absorbing Filter	1	MBN11500
Eclipse Microscope Pad	1	92080
Eclipse Large Nylon Cover 14x26x32	1	92084
Package Lens Tissue 50 Sheets, 4X6	1	76997
CFI 10X Eyepiece F.N. 22mm	2	MAK10100
Ti-TD Eyepiece Tube D	1	MEB52320
Ti-T-B Eyepiece Base Unit	1	MEB55800
Ti-S-ER Motorized Stage With Encoders	1	MEC56100
Ti-SH Universal Holder for Motor Stage	1	MEC59110
Ti-S-C Motorized Stage Controller	1	MEF55710
Ti-S-EYOU Joystick for Motorized Stage	1	MEF55700
Ti-CT-E Motorized Condenser Turret	1	MEL51910
Ti-C-LWD LWD Lens Unit for System Condenser Turret	1	MEL56200
System LWD Ph L Annuli	1	MEH31040
TE-C LWD Ph1 Module	1	MEH41100
TE-C LWD Ph2 Module	1	MEH41200
TE-C LWD Ph3 Module	1	MEH41300
Ti-ND6-E Sextuple Motor Dic Nosepiece	1	MEP59310
CFI Plan Fluor DL 4XNA 0.13 WD 17.1mm	1	MRH20041
CFI Plan Fluor DL 10X NA 0.3 WD 16.0 mm	1	MRH20101
CFI Plan Fluor DLL 20X NA 0.5 WD2.1mm Sprg	1	MRH10201
CFI PLAN FLUOR DLL40X OIL NA 1.3/WD 0.2MM	1	MRY10018
CFI Plan APO DM 60X Oil	1	MRD31602
CFI Plan APO DM 100X Oil	1	MRD31901
50Cc Immersion Oil Each	2	MXA20234
C-FL GFP HC HISN Zero Shift	1	96362
C-FL TRITC HYQ	1	96321
C-FL YFP HC HISN Zero Shift	1	96363
C-FL CFP HC HISN Zero Shift	1	96361
C-FL Texas Red HC HISN Zero Shift	1	96365
Ti-FL Epi-Fl Illuminator for Ti-Series	1	MEE54100
Ti-FLC-E Motorized Epi-Fl Filter Turret for Ti-Series	1	MEV51110
Lumen 200 Illumination System	1	77011315
SmartShutter controller	1	77016099
35mm SmartShutter w/stand-alone housing	2	77016096
Excitation Adapter for SmartShutter	1	77016169
Transmitted Light Adapter for Ti, 35mm	1	77016168
Ti Shutter Trigger Cable for Sutter	2	MXA22088
Ti Emission Adapter	1	77016182
NIS-Elements software	1	MQS31000
NIS-Elements: Module 6D imaging	1	MQS42560
NIS-Elements: Hardware Module	1	MQS41220
C-Mount/ISO Adapter, 1X	1	MQD42000
CoolSNAP HQ2 Monochrome Camera	1	77018219
Nikon Environment-Chamber	1	77065000

References

- Acar, M., Becskei, A., and van Oudenaarden, A., 2005: Enhancement of cellular memory by reducing stochastic transitions. *Nature*, **435**(7039), 228–232.
- Acar, M., Pando, B. F., Arnold, F. H., Elowitz, M. B., and van Oudenaarden, A., 2010: A general mechanism for network-dosage compensation in gene circuits. *Science*, **329**(5999), 1656–1660.
- Adams, B. G., 1972: Induction of galactokinase in *saccharomyces cerevisiae*: kinetics of induction and glucose effects. *J Bacteriol*, **111**(2), 308–15.
- Alani, E., Cao, L., and Kleckner, N., 1987: A method for gene disruption that allows repeated use of *ura3* selection in the construction of multiply disrupted yeast strains. *Genetics*, **116**(4), 541–5.
- Amberg, D. C., Burke, D., Strathern, J. N., and Laboratory, C. S. H., 2005: *Methods in yeast genetics : a Cold Spring Harbor Laboratory course manual*. Cold Spring Harbor Laboratory Press, Cold Spring Harbor, N.Y., 2005 edition.
- Aramayo, R., and Metzenberg, R., 1996: Gene replacements at the *his-3* locus of *neurospora crassa*. *Fungal Genetics Newsletter*, **43**, 9–13.
- Aronson, B. D., Johnson, K. A., Loros, J. J., and Dunlap, J. C., 1994: Negative feedback defining a circadian clock: autoregulation of the clock gene frequency. *Science*, **263**(5153), 1578–84.
- Arpaia, G., Loros, J. J., Dunlap, J. C., Morelli, G., and Macino, G., 1993: The interplay of light and the circadian clock. independent dual regulation of clock-controlled gene *cgc-2(eas)*. *Plant Physiol*, **102**(4), 1299–305.
- Aschoff, J., 1965: Circadian rhythms in man. *Science*, **148**, 1427–32.
- Baganz, F., Hayes, A., Marren, D., Gardner, D. C., and Oliver, S. G., 1997: Suitability of replacement markers for functional analysis studies in *saccharomyces cerevisiae*. *Yeast*, **13**(16), 1563–73.

- Baker, C. L., Kettenbach, A. N., Loros, J. J., Gerber, S. A., and Dunlap, J. C., 2009: Quantitative proteomics reveals a dynamic interactome and phase-specific phosphorylation in the *neurospora* circadian clock. *Mol Cell*, **34**(3), 354–63.
- Bao, J. B., and Harrison, D. J., 2006: Measurement of flow in microfluidic networks with micrometer-sized flow restrictors. *Aiche Journal*, **52**(1), 75–85.
- Beebe, D. J., Mensing, G. A., and Walker, G. M., 2002: Physics and applications of microfluidics in biology. *Annu Rev Biomed Eng*, **4**, 261–86.
- Bell-Pedersen, D., Crosthwaite, S. K., Lakin-Thomas, P. L., Merrow, M., and Okland, M., 2001a: The *neurospora* circadian clock: simple or complex? *Philos Trans R Soc Lond B Biol Sci*, **356**(1415), 1697–709.
- Bell-Pedersen, D., Dunlap, J. C., and Loros, J. J., 1992: The *neurospora* circadian clock-controlled gene, *ccg-2*, is allelic to *eas* and encodes a fungal hydrophobin required for formation of the conidial rodlet layer. *Genes Dev*, **6**(12A), 2382–94.
- Bell-Pedersen, D., Dunlap, J. C., and Loros, J. J., 1996a: Distinct cis-acting elements mediate clock, light, and developmental regulation of the *neurospora crassa eas* (*ccg-2*) gene. *Mol Cell Biol*, **16**(2), 513–21.
- Bell-Pedersen, D., Garceau, N., and Loros, J., 1996b: Circadian rhythms in fungi. *Journal of Genetics*, **75**, 387–401.
- Bell-Pedersen, D., Lewis, Z. A., Loros, J. J., and Dunlap, J. C., 2001b: The *neurospora* circadian clock regulates a transcription factor that controls rhythmic expression of the output *eas(ccg-2)* gene. *Mol Microbiol*, **41**(4), 897–909.
- Bell-Pedersen, D., Shinohara, M. L., Loros, J. J., and Dunlap, J. C., 1996c: Circadian clock-controlled genes isolated from *neurospora crassa* are late night- to early morning-specific. *Proc Natl Acad Sci U S A*, **93**(23), 13096–101.
- Belli, G., Gari, E., Piedrafita, L., Aldea, M., and Herrero, E., 1998: An activator/repressor dual system allows tight tetracycline-regulated gene expression in budding yeast. *Nucleic Acids Res*, **26**(4), 942–7.
- Benemann, J., and Oswald, W., 1996: Systems and economic analysis of microalgae ponds for conversion of co₂ to biomass. Final report, Pittsburgh Energy Technology Center.
- Bennett, M. R., Pang, W. L., Ostroff, N. A., Baumgartner, B. L., Nayak, S., Tsimring, L. S., and Hasty, J., 2008: Metabolic gene regulation in a dynamically changing environment. *Nature*, **454**(7208), 1119–22.

- Bhat, P. J., and Murthy, T. V., 2001: Transcriptional control of the gal/mel regulon of yeast *saccharomyces cerevisiae*: mechanism of galactose-mediated signal transduction. *Mol Microbiol*, **40**(5), 1059–66.
- Bhat, P. J., and Venkatesh, K. V., 2005: Stochastic variation in the concentration of a repressor activates gal genetic switch: implications in evolution of regulatory network. *FEBS Lett*, **579**(3), 597–603.
- Brody, J. P., Yager, P., Goldstein, R. E., and Austin, R. H., 1996: Biotechnology at low reynolds numbers. *Biophysical Journal*, **71**(6), 3430–3441.
- Brody, S., and Harris, S., 1973: Circadian rhythms in neurospora: spatial differences in pyridine nucleotide levels. *Science*, **180**(85), 498–500.
- Castro-Longoria, E., Brody, S., and Bartnicki-Garcia, S., 2007: Kinetics of circadian band development in neurospora crassa. *Fungal Genet Biol*, **44**(7), 672–81.
- Chang, D.-E., Leung, S., Atkinson, M. R., Reifler, A., Forger, D., and Ninfa, A. J., 2010: Building biological memory by linking positive feedback loops. *Proc Natl Acad Sci U S A*, **107**(1), 175–180.
- Cheng, P., He, Q., Wang, L., and Liu, Y., 2005: Regulation of the neurospora circadian clock by an rna helicase. *Genes Dev*, **19**(2), 234–41.
- Cheng, P., Yang, Y., Heintzen, C., and Liu, Y., 2001: Coiled-coil domain-mediated frq-frq interaction is essential for its circadian clock function in neurospora. *EMBO J*, **20**(1-2), 101–8.
- Colot, H. V., Loros, J. J., and Dunlap, J. C., 2005: Temperature-modulated alternative splicing and promoter use in the circadian clock gene frequency. *Mol Biol Cell*, **16**(12), 5563–71.
- Cookson, S., Ostroff, N., Pang, W. L., Volfson, D., and Hasty, J., 2005: Monitoring dynamics of single-cell gene expression over multiple cell cycles. *Mol Syst Biol*, **1**, 2005 0024.
- Crosthwaite, S. K., 2004: Circadian clocks and natural antisense rna. *FEBS Lett*, **567**(1), 49–54.
- Danino, T., Mondrago-Palomino, O., Tsimring, L., and Hasty, J., 2010: A synchronized quorum of genetic clocks. *Nature*, **463**(7279), 326–330.
- del Campo, A., and Greiner, C., 2007: Su-8: a photoresist for high-aspect-ratio and 3d submicron lithography. *Journal of Micromechanics and Microengineering*, **17**(6).
- Denault, D. L., Loros, J. J., and Dunlap, J. C., 2001: Wc-2 mediates wc-1-frq interaction within the pas protein-linked circadian feedback loop of neurospora. *EMBO J*, **20**(1-2), 109–17.

- Dertinger, T., Pacheco, V., von der Hocht, I., Hartmann, R., Gregor, I., and Enderlein, J., 2007: Two-focus fluorescence correlation spectroscopy: A new tool for accurate and absolute diffusion measurements. *Chemphyschem*, **8**(3), 433–443.
- Diernfellner, A. C. R., Querfurth, C., Salazar, C., Hfer, T., and Brunner, M., 2009: Phosphorylation modulates rapid nucleocytoplasmic shuttling and cytoplasmic accumulation of neurospora clock protein frq on a circadian time scale. *Genes Dev*, **23**(18), 2192–2200.
- Douglas, H. C., and Hawthorne, D. C., 1966: Regulation of genes controlling synthesis of the galactose pathway enzymes in yeast. *Genetics*, **54**(3), 911–6.
- Duffy, D. C., McDonald, J. C., Schueller, O. J. A., and Whitesides, G. M., 1998: Rapid prototyping of microfluidic systems in poly(dimethylsiloxane). *Anal. Chem.*, **70**, 4974–4984.
- Dunlap, J. C., 1993: Genetic analysis of circadian clocks. *Annu Rev Physiol*, **55**, 683–728.
- Dunlap, J. C., 1996: Genetics and molecular analysis of circadian rhythms. *Annu Rev Genet*, **30**, 579–601.
- Dunlap, J. C., 1999: Molecular bases for circadian clocks. *Cell*, **96**(2), 271–90.
- Dunlap, J. C., 2006: Proteins in the neurospora circadian clockworks. *J Biol Chem*, **281**(39), 28489–93.
- Dunlap, J. C., and Loros, J. J., 2006: How fungi keep time: circadian system in neurospora and other fungi. *Curr Opin Microbiol*, **9**(6), 579–87.
- Dunlap, J. C., Loros, J. J., and DeCoursey, P. J., 2004: *Chronobiology : biological timekeeping*. Sinauer Associates, Sunderland, Mass.
- Elowitz, M. B., and Leibler, S., 2000: A synthetic oscillatory network of transcriptional regulators. *Nature*, **403**(6767), 335–8.
- Elowitz, M. B., Levine, A. J., Siggia, E. D., and Swain, P. S., 2002: Stochastic gene expression in a single cell. *Science*, **297**(5584), 1183–6.
- Feldman, J. F., and Hoyle, M. N., 1973: Isolation of circadian clock mutants of neurospora crassa. *Genetics*, **75**(4), 605–13.
- Ferea, T. L., Botstein, D., Brown, P. O., and Rosenzweig, R. F., 1999: Systematic changes in gene expression patterns following adaptive evolution in yeast. *Proc Natl Acad Sci U S A*, **96**(17), 9721–9726.

- Froehlich, A. C., Liu, Y., Loros, J. J., and Dunlap, J. C., 2002: White collar-1, a circadian blue light photoreceptor, binding to the frequency promoter. *Science*, **297**(5582), 815–9.
- Froehlich, A. C., Loros, J. J., and Dunlap, J. C., 2003: Rhythmic binding of a white collar-containing complex to the frequency promoter is inhibited by frequency. *Proc Natl Acad Sci U S A*, **100**(10), 5914–9.
- Gancedo, J. M., 1998: Yeast carbon catabolite repression. *Microbiol Mol Biol Rev*, **62**(2), 334–361.
- Garceau, N. Y., Liu, Y., Loros, J. J., and Dunlap, J. C., 1997: Alternative initiation of translation and time-specific phosphorylation yield multiple forms of the essential clock protein frequency. *Cell*, **89**(3), 469–76.
- Gari, E., Piedrafitra, L., Aldea, M., and Herrero, E., 1997: A set of vectors with a tetracycline-regulatable promoter system for modulated gene expression in *saccharomyces cerevisiae*. *Yeast*, **13**(9), 837–48.
- Gooch, V. D., Mehra, A., Larrondo, L. F., Fox, J., Touroutoudis, M., Loros, J. J., and Dunlap, J. C., 2008: Fully codon-optimized luciferase uncovers novel temperature characteristics of the *neurospora* clock. *Eukaryot Cell*, **7**(1), 28–37.
- Grilly, C., Stricker, J., Pang, W. L., Bennett, M. R., and Hasty, J., 2007: A synthetic gene network for tuning protein degradation in *saccharomyces cerevisiae*. *Mol Syst Biol*, **3**, 127.
- Guarente, L., 1993: Synthetic enhancement in gene interaction: a genetic tool come of age. *Trends Genet*, **9**(10), 362–366.
- Gustafsson, C., Govindarajan, S., and Minshull, J., 2004: Codon bias and heterologous protein expression. *Trends Biotechnol*, **22**(7), 346–53.
- Hartman, J. L., Garvik, B., and Hartwell, L., 2001: Principles for the buffering of genetic variation. *Science*, **291**(5506), 1001–1004.
- Hasty, J., Dolnik, M., Rottschäfer, V., and Collins, J. J., 2002a: Synthetic gene network for entraining and amplifying cellular oscillations. *Phys Rev Lett*, **88**(14), 148101.
- Hasty, J., McMillen, D., and Collins, J. J., 2002b: Engineered gene circuits. *Nature*, **420**(6912), 224–30.
- He, Q., Cheng, P., Yang, Y., Yu, H., and Liu, Y., 2003: Fwd1-mediated degradation of frequency in *neurospora* establishes a conserved mechanism for circadian clock regulation. *EMBO J*, **22**(17), 4421–30.

- He, Q., and Liu, Y., 2005: Degradation of the neurospora circadian clock protein frequency through the ubiquitin-proteasome pathway. *Biochem Soc Trans*, **33**(Pt 5), 953–6.
- Heintzen, C., Loros, J. J., and Dunlap, J. C., 2001: The pas protein vivid defines a clock-associated feedback loop that represses light input, modulates gating, and regulates clock resetting. *Cell*, **104**(3), 453–464.
- Hersen, P., McClean, M. N., Mahadevan, L., and Ramanathan, S., 2008: Signal processing by the hog map kinase pathway. *Proc Natl Acad Sci U S A*, **105**(20), 7165–7170.
- Hickey, S. S. R. M. R. N., P.C., 2005: Live-cell imaging of filamentous fungi using vital fluorescent dyes and confocal microscopy. In *Methods Microbiol*, editor P. C. Savidge, T., volume 35 of *Microbial Imaging*, 63–87. Elsevier, London.
- Holden, H. M., Rayment, I., and Thoden, J. B., 2003: Structure and function of enzymes of the leloir pathway for galactose metabolism. *J Biol Chem*, **278**(45), 43885–8.
- Horak, J., and Wolf, D. H., 1997: Catabolite inactivation of the galactose transporter in the yeast *saccharomyces cerevisiae*: ubiquitination, endocytosis, and degradation in the vacuole. *J Bacteriol*, **179**(5), 1541–9.
- Janke, C., Magiera, M. M., Rathfelder, N., Taxis, C., Reber, S., Maekawa, H., Moreno-Borchart, A., Doenges, G., Schwob, E., Schiebel, E., and Knop, M., 2004: A versatile toolbox for pcr-based tagging of yeast genes: new fluorescent proteins, more markers and promoter substitution cassettes. *Yeast*, **21**(11), 947–62.
- Jansen, R. P., Dowzer, C., Michaelis, C., Galova, M., and Nasmyth, K., 1996: Mother cell-specific ho expression in budding yeast depends on the unconventional myosin myo4p and other cytoplasmic proteins. *Cell*, **84**(5), 687–697.
- Johnston, M., 1987: A model fungal gene regulatory mechanism: the gal genes of *saccharomyces cerevisiae*. *Microbiol Rev*, **51**(4), 458–76.
- Kinnaird, J. H., Burns, P. A., and Fincham, J. R., 1991: An apparent rare-codon effect on the rate of translation of a neurospora gene. *J Mol Biol*, **221**(3), 733–6.
- Klar, A. J., and Halvorson, H. O., 1974: Studies on the positive regulatory gene, gal4, in regulation of galactose catabolic enzymes in *saccharomyces cerevisiae*. *Mol Gen Genet*, **135**(3), 203–12.
- Kurth, F., Schumann, C. A., Blank, L. M., Schmid, A., Manz, A., and Dittrich, P. S., 2008: Bilayer microfluidic chip for diffusion-controlled activation of yeast species. *J Chromatogr A*, **1206**(1), 77–82.
- Lagunas, R., 1979: Energetic irrelevance of aerobiosis for *s. cerevisiae* growing on sugars. *Mol Cell Biochem*, **27**(3), 139–146.

- Lakin-Thomas, P. L., and Brody, S., 2004: Circadian rhythms in microorganisms: new complexities. *Annu Rev Microbiol*, **58**, 489–519.
- Lauter, F. R., Russo, V. E., and Yanofsky, C., 1992: Developmental and light regulation of *eas*, the structural gene for the rodlet protein of neurospora. *Genes Dev*, **6**(12A), 2373–81.
- Lee, K., Loros, J. J., and Dunlap, J. C., 2000: Interconnected feedback loops in the neurospora circadian system. *Science*, **289**(5476), 107–10.
- Lee, P. J., Helman, N. C., Lim, W. A., and Hung, P. J., 2008: A microfluidic system for dynamic yeast cell imaging. *Biotechniques*, **44**(1), 91–95.
- Lide, D., 2004: *CRC handbook of chemistry and physics: a ready-reference book of chemical and physical data*. CRC Pr I Llc.
- Liu, Y., Garceau, N. Y., Loros, J. J., and Dunlap, J. C., 1997: Thermally regulated translational control of *frq* mediates aspects of temperature responses in the neurospora circadian clock. *Cell*, **89**(3), 477–86.
- Liu, Y., He, Q., and Cheng, P., 2003: Photoreception in neurospora: a tale of two white collar proteins. *Cell Mol Life Sci*, **60**(10), 2131–8.
- Liu, Y., Loros, J., and Dunlap, J. C., 2000: Phosphorylation of the neurospora clock protein frequency determines its degradation rate and strongly influences the period length of the circadian clock. *Proc Natl Acad Sci U S A*, **97**(1), 234–9.
- Lohr, D., Venkov, P., and Zlatanova, J., 1995: Transcriptional regulation in the yeast gal gene family: a complex genetic network. *Faseb J*, **9**(9), 777–87.
- Loros, J., 1995: The molecular basis of the neurospora clock. *Seminars in Neuroscience*, **7**(1), 3–13.
- Loros, J. J., and Dunlap, J. C., 2001: Genetic and molecular analysis of circadian rhythms in neurospora. *Annu Rev Physiol*, **63**, 757–94.
- Luo, C., Loros, J. J., and Dunlap, J. C., 1998: Nuclear localization is required for function of the essential clock protein *frq*. *EMBO J*, **17**(5), 1228–35.
- Lupton, S. D., Brunton, L. L., Kalberg, V. A., and Overell, R. W., 1991: Dominant positive and negative selection using a hygromycin phosphotransferase-thymidine kinase fusion gene. *Mol Cell Biol*, **11**(6), 3374–8.
- Malthus, T., 1817: *An essay on the principle of population, as it affects the future improvement of society. With remarks on the speculations of mr. Godwin, m. Condorcet, and other writers. By TR Malthus.*

- Margolin, B., Freitag, M., and Selker, E., 1997: Improved plasmids for gene targeting at the his-3 locus of neurospora crassa by electroporation. *Fungal Genetics Newsletter*, **44**, 34–36.
- Martin, V. J. J., Pitera, D. J., Withers, S. T., Newman, J. D., and Keasling, J. D., 2003: Engineering a mevalonate pathway in escherichia coli for production of terpenoids. *Nat Biotechnol*, **21**(7), 796–802.
- Mather, W., Mondragon-Palomino, O., Danino, T., Hasty, J., and Tsimring, L. S., 2010: Streaming instability in growing cell populations. *Physical Review Letters*, **104**(20), –.
- McClung, C. R., Fox, B. A., and Dunlap, J. C., 1989: The neurospora clock gene frequency shares a sequence element with the drosophila clock gene period. *Nature*, **339**(6225), 558–62.
- MicroChem, 2010: Microchem corporation. su-8 photoresist product line.
- Miura, K., 2005: Tracking movement in cell biology. *Adv Biochem Eng Biotechnol*, **95**, 267–295.
- Morgan, L. W., Greene, A. V., and Bell-Pedersen, D., 2003: Circadian and light-induced expression of luciferase in neurospora crassa. *Fungal Genet Biol*, **38**(3), 327–32.
- Mosig, A., Jager, S., Wang, C., Nath, S., Ersoy, I., Palaniappan, K., and Chen, S., 2009: Tracking cells in life cell imaging videos using topological alignments. *Algorithms for Molecular Biology*, **4**(1), 10.
- Mundkur, B. D., 1952: Long term adaptation to galactose by yeast. *Genetics*, **37**(5), 484–99.
- Nakashima, H., 1981: A liquid culture method for the biochemical-analysis of the circadian clock of neurospora-crassa. *Plant and Cell Physiology*, **22**(2), 231–238.
- Nasmyth, K., Adolf, G., Lydall, D., and Seddon, A., 1990: The identification of a second cell cycle control on the ho promoter in yeast: cell cycle regulation of sw15 nuclear entry. *Cell*, **62**(4), 631–647.
- Nelson, D. E., Ihekweba, A. E. C., Elliott, M., Johnson, J. R., Gibney, C. A., Foreman, B. E., Nelson, G., See, V., Horton, C. A., Spiller, D. G., Edwards, S. W., McDowell, H. P., Unitt, J. F., Sullivan, E., Grimley, R., Benson, N., Broomhead, D., Kell, D. B., and White, M. R. H., 2004: Oscillations in nf-kappab signaling control the dynamics of gene expression. *Science*, **306**(5696), 704–708.
- Nguyen, N., and Wereley, S., 2002: *Fundamentals and applications of microfluidics*. Artech House Publishers.

- Oldenburg, K. R., Vo, K. T., Michaelis, S., and Paddon, C., 1997: Recombination-mediated pcr-directed plasmid construction in vivo in yeast. *Nucleic Acids Res*, **25**(2), 451–2.
- Oswald, W., 1995: Ponds in the twenty-first century. *Water Science and Technology*, **31**(12), 1 – 8.
- Owens, J., Houston, M., Luebke, D., Green, S., Stone, J., and Phillips, J., 2008: Gpu computing. *Proceedings of the IEEE*, **96**(5), 879–899.
- Ozbudak, E. M., Thattai, M., Lim, H. N., Shraiman, B. I., and Oudenaarden, A. V., 2004: Multistability in the lactose utilization network of escherichia coli. *Nature*, **427**(6976), 737–740.
- Perlman, J., Nakashima, H., and Feldman, J. F., 1981: Assay and characteristics of circadian rhythmicity in liquid cultures of neurospora crassa. *Plant Physiol*, **67**(3), 404–407.
- Pratt, R. J., and Aramayo, R., 2002: Improving the efficiency of gene replacements in neurospora crassa: a first step towards a large-scale functional genomics project. *Fungal Genet Biol*, **37**(1), 56–71.
- Ramsdale, M., and Lakin-Thomas, P. L., 2000: sn-1,2-diacylglycerol levels in the fungus neurospora crassa display circadian rhythmicity. *J Biol Chem*, **275**(36), 27541–50.
- Raser, J. M., and O’Shea, E. K., 2004: Control of stochasticity in eukaryotic gene expression. *Science*, **304**(5678), 1811–4.
- Robert, L., Paul, G., Chen, Y., Taddei, F., Baigl, D., and Lindner, A. B., 2010: Predispositions and epigenetic inheritance in the escherichia coli lactose operon bistable switch. *Mol Syst Biol*, **6**, 357.
- Rohde, J. R., Trinh, J., and Sadowski, I., 2000: Multiple signals regulate gal transcription in yeast. *Mol Cell Biol*, **20**(11), 3880–6.
- Rowat, A. C., Bird, J. C., Agresti, J. J., Rando, O. J., and Weitz, D. A., 2009: Tracking lineages of single cells in lines using a microfluidic device. *Proc Natl Acad Sci U S A*, **106**(43), 18149–18154.
- Rubio-Teixeira, M., 2005: A comparative analysis of the gal genetic switch between not-so-distant cousins: Saccharomyces cerevisiae versus kluyveromyces lactis. *FEMS Yeast Res*, **5**(12), 1115–28.
- Sambrook, J., and Russell, D. W., 2001: *Molecular cloning : a laboratory manual*. 3. Cold Spring Harbor Laboratory Press, Cold Spring Harbor, N.Y., 3rd edition.

- Sargent, M. L., Briggs, W. R., and Woodward, D. O., 1966: Circadian nature of a rhythm expressed by an invertaseless strain of *neurospora crassa*. *Plant Physiol*, **41**(8), 1343–9.
- Schafmeier, T., Diernfellner, A., Schfer, A., Dintsis, O., Neiss, A., and Brunner, M., 2008: Circadian activity and abundance rhythms of the *neurospora* clock transcription factor *wcc* associated with rapid nucleo-cytoplasmic shuttling. *Genes Dev*, **22**(24), 3397–3402.
- Schafmeier, T., Kaldi, K., Diernfellner, A., Mohr, C., and Brunner, M., 2006: Phosphorylation-dependent maturation of *neurospora* circadian clock protein from a nuclear repressor toward a cytoplasmic activator. *Genes Dev*, **20**(3), 297–306.
- Shaner, N. C., Campbell, R. E., Steinbach, P. A., Giepmans, B. N., Palmer, A. E., and Tsien, R. Y., 2004: Improved monomeric red, orange and yellow fluorescent proteins derived from *discosoma* sp. red fluorescent protein. *Nat Biotechnol*, **22**(12), 1567–72.
- Sheff, M. A., and Thorn, K. S., 2004: Optimized cassettes for fluorescent protein tagging in *saccharomyces cerevisiae*. *Yeast*, **21**(8), 661–70.
- Sia, S. K., and Whitesides, G. M., 2003: Microfluidic devices fabricated in poly(dimethylsiloxane) for biological studies. *Electrophoresis*, **24**(21), 3563–76.
- Sohngen, N. L., and Coolhaas, C., 1924: The fermentation of galactose by *saccharomyces cerevisiae*. *J Bacteriol*, **9**(2), 131–41.
- St John, T. P., and Davis, R. W., 1981: The organization and transcription of the galactose gene cluster of *saccharomyces*. *J Mol Biol*, **152**(2), 285–315.
- Stephanopoulos, G., 2007: Challenges in engineering microbes for biofuels production. *Science*, **315**(5813), 801–804.
- Stricker, J., Cookson, S., Bennett, M. R., Mather, W. H., Tsimring, L. S., and Hasty, J., 2008: A fast, robust and tunable synthetic gene oscillator. *Nature*, **456**(7221), 516–519.
- Stroock, A. D., Dertinger, S. K., Ajdari, A., Mezic, I., Stone, H. A., and Whitesides, G. M., 2002: Chaotic mixer for microchannels. *Science*, **295**(5555), 647–51.
- Sveen, J., 2004: An introduction to *matpiv* v. 1.6.1. *eprint series (Department of Mathematics, University of Oslo, Oslo, Norway, 2004)*. Author Affiliations Bruno Moullia Biomechanics Group, Institut National de la Recherche Agronomique, **234**.
- Taylor, R. J., Falconnet, D., Niemisto, A., Ramsey, S. A., Prinz, S., Shmulevich, I., Galitski, T., and Hansen, C. L., 2009: Dynamic analysis of *mapk* signaling using a high-throughput microfluidic single-cell imaging platform. *Proc Natl Acad Sci U S A*, **106**(10), 3758–63.

- Timson, D. J., Ross, H. C., and Reece, R. J., 2002: Gal3p and gal1p interact with the transcriptional repressor gal80p to form a complex of 1:1 stoichiometry. *Biochem J*, **363**(Pt 3), 515–520.
- Vann, D., 1995: Electroporation-based transformation of freshly harvested conidia of *neurospora crassa*. *Fungal Genetics Newsletter*, **42A**, 53.
- Vincent, S. F., Bell, P. J., Bissinger, P., and Nevalainen, K. M., 1999: Comparison of melibiose utilizing baker's yeast strains produced by genetic engineering and classical breeding. *Lett Appl Microbiol*, **28**(2), 148–52.
- Vogel, H., 1956: A convenient growth medium for *neurospora crassa*. *Microbiol. Genet. Bull*, **13**, 42–43.
- Wach, A., 1996: Pcr-synthesis of marker cassettes with long flanking homology regions for gene disruptions in *s. cerevisiae*. *Yeast*, **12**(3), 259–65.
- Wendland, J., 2003: Pcr-based methods facilitate targeted gene manipulations and cloning procedures. *Curr Genet*, **44**(3), 115–23.
- Whitesides, G. M., Ostuni, E., Takayama, S., Jiang, X., and Ingber, D. E., 2001a: Soft lithography in biology and biochemistry. *Annu Rev Biomed Eng*, **3**, 335–73.
- Whitesides, G. M., Otuni, E., Takayama, S., Jiang, X., and Ingber, D. E., 2001b: Soft lithography in biology and biochemistry. *Annu. Rev. Biomed. Eng*, **3**, 335–73.
- Wilkinson, J. F., 1949: The pathway of the adaptive fermentation of galactose by yeast. *Biochem J*, **44**(4), 460–7.
- Williams, M. S., Longmuir, K. J., and Yager, P., 2008: A practical guide to the staggered herringbone mixer. *Lab on a Chip*, **8**(7), 1121–1129.
- Xia, Y., and Whitesides, G. M., 1998: Soft lithography. *Annu. Rev. Mater. Sci.*, **28**, 153–84.
- Young, M. E., Carroad, P. A., and Bell, R. L., 1980: Estimation of diffusion-coefficients of proteins. *Biotechnology and Bioengineering*, **22**(5), 947–955.